Computational Electrochemistry

Dzianis (Denis) Menshykau

St John's College

University of Oxford

A thesis submitted for the degree of DPhil in chemistry

Trinity Term 2010

“The purpose of computing is insight, not numbers”

Richard W Hamming

This thesis addresses simulation of electrochemical experiments, with an emphasis on processes of diffusional mass transport to the electrode surface. The following topics have been studied:

- By applying theoretical modeling and experimentation it is shown that even significant surface roughness produced by deliberate polishing or scratching is not sufficient to be distinguished in cyclic voltammetry experiments. In stripping voltammetry the shape of the voltammograms strongly depends on the model of the electron transfer, but is not always sensitive to the model of the electrode surface; the conditions under which this is the case are identified, and generic roughness effects on stripping voltammetry are quantified.

- We first consider two different models of electrodes covered with electroinactive layers: where the electrode is covered with a uniform layer and where the layer contains pinholes. Both models are simulated and then compared to identify conditions under which they can be distinguished. We further proposed a generic model to predict the influence of electroactive layers on the cyclic voltammetry. The conditions where deviation can be seen from the ordinary behavior of a clean planar electrode are predicted.

- We consider one electron, one proton and next two electron, two proton reduction of surface bound species. Two mechanisms of reaction are considered: stepwise and concerted. Voltammetry is modelled under three regimes of proton transport: infinitely fast (fully buffered solution), infinitely slow (infinitely high surface coverage of electrode) and the intermediate case of a finite rate of diffusional mass transport to electrode surface. The types of voltammograms observed in each case are presented and discussed.

- Theory of chronoamperometry on disc and ring-recessed microelectrodes and their arrays is reported. Three and four different regimes of transient current versus time can be observed at microelectrode arrays of disc and ring electrodes, accordingly. A generic, accurate and easy to use method of experimental chronoamperometric data analysis is proposed. It is shown that the method can be applied to the simultaneous measurement of the diffusion coefficient D and the product nC, where n is the number of electrons transferred and C is the concentration of electroactive analyte.

- The fabrication, characterization, and use of arrays of ring-recessed disk generator-colector microelectrodes are reported. Experiments and simulations relating to time- of-flight experi-

ments in which material electrogenerated at a disk is diffusionally transported to the ring are reported. We further report voltammetry of electrochemically active species which undergo first and second order chemical reactions. Current transients are found to be sensitive to the diffusion coefficient of both the reduced and oxidised species as well as to the rate of the chemical reaction and its mechanism.

Acknowledgements

I would like to thank:

- Professor Richard G Compton, for allowing me to undertake my DPhil as part of his research group and for his guidance and encouragement throughout.
- The experimental researchers who I collaborated with: Aoife M. O'Mahony, Javier del Campo, Neil V. Rees, Christopher Batchelor-McAuley, Xing-Jiu Huang, Leigh Aldous, Yao Meng.
- Ian Streeter for introducing me to C++ and LaTeX.
- Computational fellows: Ian J. Cutress, Edmund J.F. Dickinson, Stephen R. Belding and Martin C. Henstridge.
- All members of the Compton group for keeping me entertained over the duration of my work.
- St John's College for funding and hospitality.

Contents

Chapter 1

Introduction

This chapter considers the basics of electrochemical thermodynamic and kinetics as well as electrochemical methods. More detailed information can be found in various textbooks[1–3] and the other references provided here.

1.1 Fundamentals of Electrochemical Thermodynamics

Electrochemical thermodynamics considers an electrochemical potential $\overline{\mu}$ instead of a chemical potential μ. The electrochemical potential for species A is given by the following equation:

$$\overline{\mu_{\mathrm{A}}} = \mu_{\mathrm{A}} + Z_{\mathrm{A}} F \phi \tag{1.1}$$

where Z_{A} is the charge of species A, F is the Faraday constant and ϕ is the potential of the phase where species A is situated. Note that absolute values of ϕ cannot be measured.

As can be seen from equation 1.1 the electrochemical potential is a sum of two terms: a chemical potential, μ_{A} and the molar electrical energy, $Z_{\mathrm{A}} F \phi$.

Let's consider the simple one electron reduction reaction:

$$A + e \rightleftharpoons B \tag{1.2}$$

As known from the chemical thermodynamics at equilibrium the sum of electrochemical potentials of reactants are equal to that of products:

$$\overline{\mu_{\mathrm{A}}} + \overline{\mu_e} = \overline{\mu_{\mathrm{B}}} \tag{1.3}$$

Substituting of the electrochemical potential in this equation by expression 1.1 we obtain:

$$F(\phi_{\mathrm{M}} - \phi_{\mathrm{S}}) = \mu_{\mathrm{A}} + \mu_e - \mu_{\mathrm{B}} \tag{1.4}$$

where ϕ_M and ϕ_S are the electrical potentials of the metal electrode and the solution respectively.

It is also known from chemical thermodynamics that the chemical potential and it's standard value are linked by the equation:

$$\mu_A = \mu_A^0 + RT \ln \frac{[A]}{[A]^*} \tag{1.5}$$

where $[A]^* = 1 \times 10^3$ mol m^{-3} is a standard concentration.

Substitution of the potential with their standard values in equation 1.4 allows the following equation to be derived:

$$\phi_M - \phi_S = \frac{\mu_A^0 + \mu_e^0 - \mu_B}{F} - \frac{RT}{F} \ln \frac{[B]}{[A]} \tag{1.6}$$

Equation 1.6 is known as the Nernst equation. It also should be noted here that the absolute value of $\phi_M - \phi_S$ cannot be measured. The Nernst equation can be easily generalised for any chemical reaction:

$$\sum_i v_i A_i + e = \sum_j v_j B_j \tag{1.7}$$

in the following way:

$$\phi_M - \phi_S = \frac{\sum_i v_i \mu_{A_i}^0 + n\mu_e^0 - \sum_j v_j \mu_{B_j}}{F} - \frac{RT}{F} \ln \frac{\sum_j [B_j]^{v_j}}{\sum_i [A_i]^{v_i}} \tag{1.8}$$

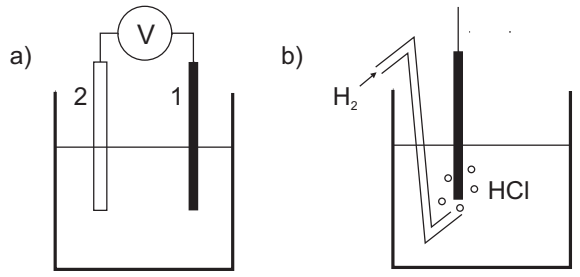

Figure 1.1: Schematic diagram of a) a typical two electrode electrochemical cell and b) a hydrogen electrode.

It was pointed out above that neither ϕ_M, ϕ_S nor $\phi_M - \phi_S$ can be measured experimentally. However the difference of $(\phi_M - \phi_S)_{\text{electrode 1}} - (\phi_M - \phi_S)_{\text{electrode 2}}$ between two electrodes is measurable experimentally. Figure 1.1 a) shows a schematic diagram of a typical two electrode electrochemical cell. Assuming that the reaction given by equation 1.2 happens at electrode 1 and reaction at electrode 2 are independent of reagents involved in the electrochemical reaction at electrode 1 the potential difference between the two electrodes is given by

the equation:

$$E = (\phi_{\mathrm{M}} - \phi_{\mathrm{S}})_{\mathrm{el}\ 1} - (\phi_{\mathrm{M}} - \phi_{\mathrm{S}})_{\mathrm{el}\ 2} = \frac{\Delta\mu_1^0 - \Delta\mu_2^0}{F} - \frac{RT}{F}\ln\frac{[\mathrm{B}]}{[\mathrm{A}]} = E^0 - \frac{RT}{F}\ln\frac{[\mathrm{B}]}{[\mathrm{A}]} \tag{1.9}$$

In practice such measurements are made when only a tiny current is passing through electrodes. The current is assumed to be so small that deviation of the chemicals concentrations from their initial values are negligible. It is clear now that some standard electrode should be chosen to measure potentials of other electrodes against it. According to the International Union of Pure and Applied Chemistry the hydrogen electrode is chosen as a standard reference electrode. Figure 1.1 b) shows a schematic diagram of the hydrogen reference electrode. It consists of a Pt wire immersed into 1.18 M HCl at 25^0 C and the hydrogen gas pressure is kept at 1.01×10^5 N m^{-2}. The concentration of hydrochloric acid differ from 1 M due to solution non-ideality; the protons activity in a solution of 1.18 M HCl is equal to 1 M. Equation 1.9 was derived assuming the solution to be ideal and that concentrations are equal to activities; in reality this is not always the case. Furthermore the relation between activity and concentration is often unknown. To overcome this problem we introduce here the formal potential E_f^0. This quantity is a measured potential versus a standard hydrogen electrodes under certain specified conditions, such as particular concentration of electrolyte, concentrations of red/ox species and other components in solution. The formal potential loses the thermodynamic generality of the standard potential being only applicable to certain conditions, but is very useful from a practical point of view.

1.2 Electrode Kinetics

Here again we consider simple one electron reduction given by equation 1.2. Early studies done by Tafel[4] showed that at small overpotentails current is often related exponentially to the overpotential $\eta = \frac{(E-E_f^0)F}{RT}$:

$$i = ae^{b\eta} \tag{1.10}$$

We further assume that the rate of an electrochemical reaction is analogous to the rate of a chemical reaction and can be written according to the mass action law:

$$\frac{i}{FA} = \frac{d[\mathrm{A}]}{dt} = -k_{\mathrm{f}}[\mathrm{A}] + k_{\mathrm{b}}[\mathrm{B}] \tag{1.11}$$

where A is electrode area.

Assuming that rate constant of the electron transfer k_f and k_b depend on overpotential according to the Tafel law the following equation can be formulated:

$$\frac{d[\mathrm{A}]}{dt} = -[\mathrm{A}]a_\mathrm{f}e^{b_\mathrm{f}\eta} + [\mathrm{B}]a_\mathrm{b}e^{b_\mathrm{b}\eta} \tag{1.12}$$

Consider equation 1.12 at the $E = E_f$, assuming that equilibrium has been reached and that the concentration of electrochemically active species are equal; [A]=[B]. In this case concentrations are constant in time and the current is equal to zero. Hence we can conclude that $a_\mathrm{f} = a_\mathrm{b} = k_0$, where k_0 is a rate constant for electron transfer and has dimensions of m s^{-1}. Further we consider equation 1.12 at the equilibrium at an arbitrary overpotenital η_1 when the concentration is constant with time and are in agreement with Nernst equation:

$$\frac{[\mathrm{B}]_1}{[\mathrm{A}]_1} = \frac{k_0e^{b_\mathrm{f}\eta_1}}{k_0e^{b_\mathrm{b}\eta_1}} = e^{-\eta_1} \tag{1.13}$$

So we have $b_\mathrm{f} - b_\mathrm{b} = -1$, conventionally $-b_\mathrm{f}$ is labeled as α and $b_\mathrm{b} = 1-\alpha = \beta$. Using this notation equation 1.13 can be rewritten in the form known as the Butler-Volmer equation, named in honour of J.A.V. Butler[5] and M. Volmer[6]

$$\frac{i}{FA} = \frac{d[\mathrm{A}]}{dt} = -[\mathrm{A}]k_0e^{-\alpha\frac{(E-E_f^0)F}{RT}} + [\mathrm{B}]k_0e^{(1-\alpha)\frac{(E-E_f^0)F}{RT}} \tag{1.14}$$

Typically measured values of k_0 are in the interval from 10^{-11} m s^{-1} to 0.1 m s^{-1}. High values for the rate constant of the electron transfer are observed for reduction and/or oxidation of various hydrocarbons and the formation of metal amalgams.[7–9] Complicated reactions involving significant molecular rearrangements accompanying electron transfer can demonstrate very slow kinetics.[10] The physical meaning of the coefficients α and β, known as transfer coefficients, can be understood by considering an energy profile of reaction along a reaction coordinate at two different potentials (Figure 1.2). Assuming that the energy curves for both A+e and B are linear near to the point of their intersection and the shape of the energy curves are independent of the potential, the value of α can be found according to the equation:

$$\alpha = \frac{\tan\theta}{\tan\theta + \tan\phi} \tag{1.15}$$

It is clear now that $0 < \alpha, \beta < 1$. If $\theta > \phi$ then $\tan\theta > \tan\phi$ and $\alpha < 0.5$; this case describes the reaction where the transition state is situated close to reagents (A+e) where is for the opposite case, when $\theta < \phi$, $\alpha > 0.5$ the transition state situated closer to the reaction product (B). Experimentally it was found that for a large number of electrochemical reactions, $\alpha \approx 0.5$ and therefore the curve intersection is symmetrical.

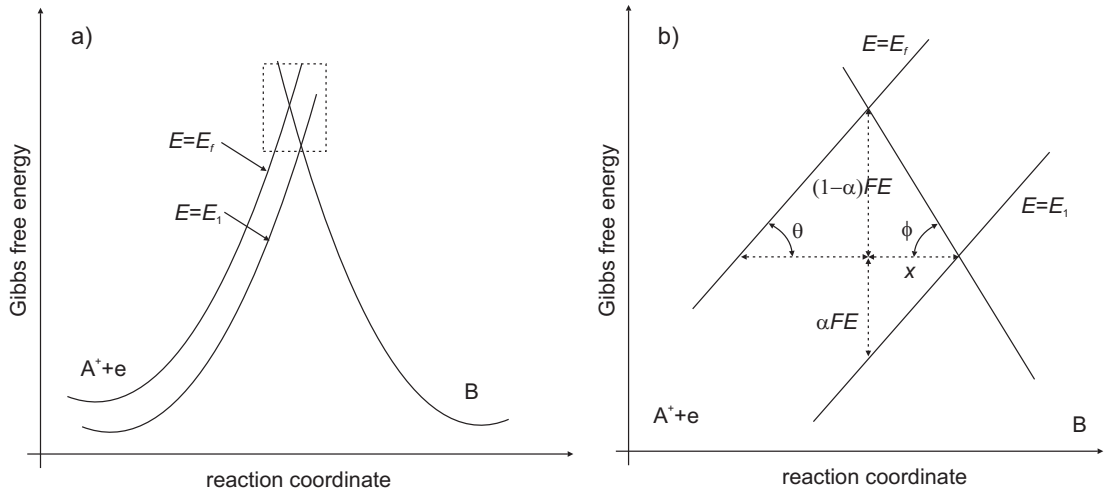

Figure 1.2: (a) Energy profile of a simple one electron reduction, b) magnified picture of boxed area in the frame a).

1.3 Mass Transfer

Mass transport is the net movement of mass from one spatial location to another. It usually arises from difference in chemical concentrations, potentials or movement of an element of a solution. There are three key mechanisms of mass transport: diffusion, migration and convection.

1.3.1 Diffusion

Diffusion is a result of random molecular motion. Macroscopically diffusion is described by Fick's first and second laws:

$$J = -D\nabla C \tag{1.16}$$

and

$$\frac{\partial C}{\partial t} = \nabla(D\nabla C) \tag{1.17}$$

where ∇ are differential operators and their particular mathematical expression depend on the symmetry of the coordinate system used and will be discussed later in this chapter.

Fick's first law states that the diffusional flux is proportional to the concentration gradient with a constant of proportionality D, known as a diffusion coefficient. The dimensions of the diffusion coefficient are $m^2\ s^{-1}$. Diffusional flux is directed from the region with a higher concentration to a region with a lower concentration. Hence systems with initially observed concentration gradients, if left alone for a sufficiently long time will reach a homogeneous state where the concentrations are equal at every point in solution. Experimental studies of diffusion shows that values of diffusion coefficient in nonviscous solvents, like water and acetonitrile are around $10^{-9}\ m^2s^{-1}$. For more viscous solvents like room temperature ionic liquids diffusion coefficients are around $10^{-11}\ m^2s^{-1}$. Values of diffusion coefficient can be estimated by the Einstein-Stokes equation:

$$D = \frac{k_B T}{6\pi\nu r} \tag{1.18}$$

where k_B is Boltzmann's constant, ν is the viscosity and r is the radius of the diffusing molecule, assuming it is spherical.

Experimental studies show that in diluted solutions the diffusion coefficient is independent of concentration, so Fick's second law of diffusion (equation 1.17) can be simplified: Fick's second law of diffusion

$$\frac{\partial C}{\partial t} = D\nabla^2 C \tag{1.19}$$

Fick's laws treat the concentration of species in solution as being a continuous mathematical function. Hence, correctly, it might be expected Fick's laws to break down at microscopic distances. Nevertheless molecular dynamic simulations show that Fick's laws accurately describe diffusional mass transport in pores with radii as small as several molecular radius.[11,12]

1.3.2 Migration

Migration is the mass transport of a charged species due to an electric field in solution. Often electrochemical experiments are conducted in a fully supported media[13] where the effect of migration can be neglected, but some experiments are performed in conditions where migration are important and cannot be neglected.[13–16]

The flux of a charged species caused by am electric field is given by the following equation:

$$J = -z_{\mathrm{i}} u_{\mathrm{i}} C_{\mathrm{i}} \nabla \phi \tag{1.20}$$

where z_{i} is the charge, C_{i} is the concentration, ϕ is electric potential and u_{i} is the ion mobility. Ion mobility is related to the diffusion coefficient by the Einstein-Smoluchowski equation:

$$u_{\mathrm{i}} = \frac{F}{RT} D_{\mathrm{i}} \tag{1.21}$$

Equation 1.20 shows that the flux caused by the electric field is proportional to the electric field gradient $\nabla\phi$ and depends on the charge of the species. Negatively and positively charged ions are forced in opposite directions. Equation 1.20 cannot be solved on it is own and should be accompanied by the Poisson equation to form a closed system of mathematical equations:

$$\nabla^2 \phi = -\frac{\rho}{\varepsilon_{\mathrm{r}} \varepsilon_0} \tag{1.22}$$

where ρ is the local charge density, ε_{r} is the dielectric constant of the medium and ε_0 is the permittivity of space. The charge density is expressed in terms of the local concentrations of the charged species in solution:

$$\rho = F \sum_{\mathrm{i}} z_{\mathrm{i}} C_{\mathrm{i}} \tag{1.23}$$

1.3.3 Convection

Convection can be generally classified as “natural” or “forced”. Natural convection occurs due to thermal and density gradients in a system and is generally irreproducible. Therefore it is undesirable in electrochemical experiments. Natural convection limits the duration of electrochemical experiments which can be quantitatively interpreted over no more then 10-30 s in nonviscous solvents like water or 1-2 minutes in room temperature ionic liquids.

Forced convection is a type of mass transport in which fluid motion is generated by an external source such as fan, jet, ultrasound etc. The simplest type of convection is a one dimensional laminar flow and is described by the equation:

$$\frac{\partial C}{\partial t} = -v \frac{\partial C}{\partial x} \tag{1.24}$$

where v is flow velocity.

Forced convection provide enhanced mass transport and is an essential part of various electrochemical techniques such as voltammetry at rotating disk electrodes, channel electrodes and well jet electrodes.

1.4 Electrode Geometry and Symmetry

Here we discus some common types of electrode geometries and the symmetry associated with them. Table 1.1 show electrodes of various geometries and associated with them systems of coordinate as well as expressions for related differential operator ∇^2. Correct choice of coordinate system is very important for quantitative and qualitative descriptions of electrochemical processes, and furthermore leads to the reduction of the dimensions of a system. Classical electrochemical experiments are conducted with a flat electrode of linear dimensions of several millimeters. Assuming y and x the axis are along the electrode surface and the axis z is perpendicular to the electrode surface we obtain a three dimensional Cartesian system of coordinates. As discussed above the timescales of a typical electrochemical experiment are around 10 s and a typical diffusion coefficient is 10^{-9} m^2 s^{-1}, so the length scale of the diffusional layer can be approximated as $l = 2\sqrt{Dt} = 2 \times 10^{-4}$ m$= 0.02$ mm, that is two orders of magnitude smaller than characteristic length scale of the electrode. Consequently the electrode can be considered as infinitely large and the only coordinate that is essential is the z coordinate perpendicular to the electrode surface. Here we have just reduced a three dimensional problem to one of only one dimension.

Table 1.1: Coordinate systems for various electrode geometries.

Electrode	Schematic	Coordinate system	∇^2
Planar (macro)	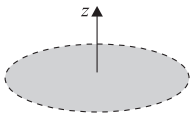	Cartesian	$\frac{\partial^2}{\partial z^2}$
Sphere	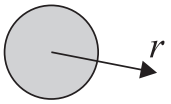	Spherical polar	$\frac{\partial^2}{\partial r^2}+\frac{2}{r}\frac{\partial}{\partial r}$
Cylinder	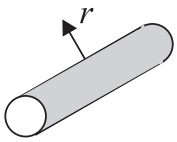	Cylindrical	$\frac{\partial^2}{\partial r^2}+\frac{1}{r}\frac{\partial}{\partial r}$
Disk	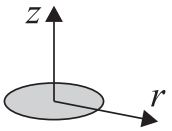	Cylindrical	$\frac{\partial^2}{\partial r^2}+\frac{1}{r}\frac{\partial}{\partial r}+\frac{\partial^2}{\partial z^2}$
Ring	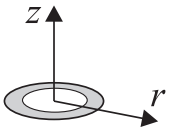	Cylindrical	$\frac{\partial^2}{\partial r^2}+\frac{1}{r}\frac{\partial}{\partial r}+\frac{\partial^2}{\partial z^2}$
Rotating body	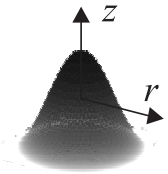	Cylindrical	$\frac{\partial^2}{\partial r^2}+\frac{1}{r}\frac{\partial}{\partial r}+\frac{\partial^2}{\partial z^2}$
Band	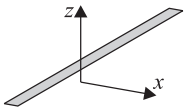	Cartesian	$\frac{\partial^2}{\partial x^2}+\frac{\partial^2}{\partial z^2}$
Rectangular	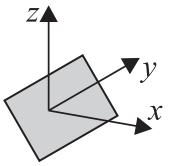	Cartesian	$\frac{\partial^2}{\partial x^2}+\frac{\partial^2}{\partial y^2}+\frac{\partial^2}{\partial z^2}$

1.5 Electrochemical Techniques

Here and further in this thesis we discuss potential step and potential sweep methods; in particular we consider chronoamperometry and cyclic voltammetry. Information about other electrochemical methods such as stripping voltammetry, pulse methods, current controlled methods and impedance methods can be found in refs.[2,3]

Before we start discussion of electrochemical methods, brief information about electrochemical cell used in electroanalysis. In practise a three electrode cell is usually used instead of two electrode cell discussed earlier. The three electrodes are named the working, counter and reference electrodes. In such an experimental setup the reaction occurring at a working electrode is under investigation. Some other electrochemical reaction (counter reaction) happens at the counter electrode and no chemical reaction is assumed to occur at the reference electrode. The reference electrode is used to measure the potential at the working electrodes. A hydrogen reference electrode is usually substituted by an easy to use reference electrodes such as a saturated calomel electrode or silver chloride electrode. The standard electrode potential of the silver chloride electrode and the potential of the saturated calomel electrode against standard hydrogen electrode are 0.230V and 0.250V respectively.

1.5.1 Chronoamperometry

Here we consider the simple one electron reduction:

$$A + e \rightarrow \text{products} \tag{1.25}$$

In this experimental technique the potential rapidly changes from a region where no electrochemical reaction occurs to a potential sufficiently large to assume infinitely fast electron transfer. The current dependence on time is a function of the electrode geometry used in the experiment. Here we first consider chronoamperometry at a macroelectrode. This problem is one of the few in electrochemistry which has analytical solution. Such problems and their solutions are of great importance both for experimentalists and theoreticians. It provides with a perfect tool and concept with which to interpret experimental data and let to validate more complicated models and numerical simulations. The

diffusional current to macroelectrode is given by the Cottrell equation:[2]

$$i = \frac{nFAD^{1/2}C}{\pi t^{1/2}} \tag{1.26}$$

where n is number of electron transferred, F is the Faradaic constant, C is the concentration in the bulk of the solution and A is the electrode area.

An analytical solution also exist for the diffusional current to spherical and hemispherical electrodes:

$$i = nFADC(\frac{1}{\sqrt{\pi Dt}} + \frac{1}{r_0}) \tag{1.27}$$

where r_0 is a sphere radius.

The current at a spherical electrode at infinitely long times reaches a steady state value:

$$i_{ss} = \frac{nFADC}{r_0} \tag{1.28}$$

Next we consider chronoamperometric experiments at microdisk, microring and microband electrodes, where no analytical solutions are available for these cases. However asymptotic solutions for short time behavior exists and are given by the following equations:[17,18]

$$\text{Disk}: \ j = \frac{\pi}{4} + \frac{\pi^{1/2}}{\tau^{1/2}} + 0.188\tau^{1/2} \tag{1.29}$$

where, $\tau = \frac{tD}{r_0^2}$ and $j = \frac{i}{4nFDCr}$.

$$\text{Ring}: \ j = \frac{\pi}{4} + \frac{\pi^2(1-R_a^2)}{4\tau^{1/2}} \tag{1.30}$$

Correspondingly at long times:[19]

$$\text{Disc}: \ j = 1 + 0.392\tau^{-1/2} + .00703\tau^{-3/2} \tag{1.31}$$

$$\text{Ring}: \ j = \frac{l_0}{4}(1 + \frac{l_0}{2\pi^{3/2}\tau^{1/2}}) \tag{1.32}$$

where, $l_0 = \frac{\pi^2(1+R_a)}{\ln\frac{32R_a}{1-R_a} + \exp\frac{\pi^2}{4}}$.

$$\text{Band}: \ j = \frac{1}{2\ln(64\tau)} \tag{1.33}$$

A very widely applied empirical equation in analytical chemistry was derived by Shoup and Sz-

abo. This equation describes the current at a microdisk electrode at all times with an accuracy better than 0.6%:[20]

$$j = 0.7854 + 0.4432\tau^{-1/2} + 0.2148e^{-0.391\tau^{-1/2}} \tag{1.34}$$

An empirical equation for the diffusional current to a cylindrical electrode valid at any time with an accuracy of 1.3% was also reported:[2]

$$j = \frac{2e^{-0.1\sqrt{\pi\tau}}}{2\sqrt{\pi\tau}} + \frac{1}{\ln(5.29 + 1.5\sqrt{\tau})} \tag{1.35}$$

Comparison of equations 1.26 - 1.30 and 1.35 shows, that independent of the particular electrode geometry, at short times the current is approximately equal to that at planar macroelectrode of equivalent area. This can be rationalised by noting that the thickness of diffusional layer is proportional to $l \approx \sqrt{Dt}$ and if l significantly less that geometrical features of electrode diffusion can be assumed planar. Detailed analyses of long time behavior reveals fundamental differences between diffusion of different types: planar diffusion is observed at macroelectrode, cylindrical convergent diffusion observed at microband and cylindrical electrodes and spherical convergent diffusion is observed at spherical and microdisk electrodes. The efficiency of mass transport provided by various types of diffusion is different and decrease in the order: spherical, cylindrical, planar. Decrease of the efficiency in the order: spherical, cylindrical, planar is observed due to change of the symmetry of the problem and depicted by the change of the differential operator ∇^2, as shown in Table 1.1.

1.5.2 Cyclic Voltammetry

Here we consider the cyclic voltammetry experiment applied to a simple one electron reduction of A according to scheme 1.25. The experiment records the current flowing through the working electrode as function of the applied potential and a plot of current versus potential is displayed, which is known as a voltammogram. The potential changes in agreement with Equation 1.36a before a switching potential (E_s) and E and follows equation 1.36b after the switching potential.

$$E = E_{in} - vt \tag{1.36a}$$

$$E = E_s + vt \tag{1.36b}$$

where E_{in} is the initial potential and v is a voltage scan rate.

Cyclic Voltammetry of Adsorbed Species

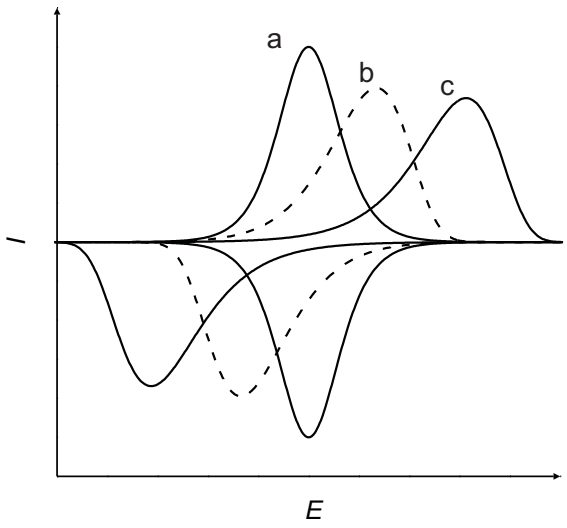

Figure 1.3: Schematic cyclic voltamogram of surface bound species, infinite fast electron transfer (a), finite rate of electron transfer (b) and irreversible electron transfer (c).

The potential step experiment considered above was designed in such a way that the rate of electron transfer has assumed infinitely fast and provided information about the diffusion of electrochemically active species to the electrode surface. Here we consider cyclic voltammetry of surface bound electrochemically active species so no mass transport to the electrode surface needs to be considered and effects associated with rates of electron transfer can be considered independent of mass transfer effects.

We consider a simple one electron reduction as given by the equation 1.2. Figure 1.3 schematically shows cyclic voltammograms of surface bound species. We see that a decrease of rate of electron transfer cause a change of symmetry of the peak and an increase of the peak to peak separation. We first consider infinitely fast electron transfer, so equilibrium at electrode surface can always be assumed and the concentration of the electrochemically active species are linked by the Nernst equation:

$$\Gamma_{\text{A}} = \Gamma_{\text{B}} e^{\frac{(E-E_f^0)F}{RT}} \tag{1.37}$$

where Γ_{A} and Γ_{B} are surface coverages of compounds A and B accordingly.

This equation is accompanied by the mass conservation law:

$$\Gamma_{\text{A}} + \Gamma_{\text{B}} = \Gamma_0 \tag{1.38}$$

where Γ_0 is a total coverage of surface bound species A and B. Current to the electrode during the

cyclic voltammetry experiment can be calculated according to the equation:[21]

$$i = -AF\frac{d\Gamma_A}{dt} = AFv\frac{d\Gamma_A}{dE} = \frac{F^2vA\Gamma_A}{RT}\frac{e^{\frac{(E-E_f^0)F}{RT}}}{(1+e^{\frac{(E-E_f^0)F}{RT}})^2} \tag{1.39}$$

with the peak current given by the equation:

$$i_p = \frac{F^2}{4RT}Av\Gamma_A^0 \tag{1.40}$$

and the peak potential is equal to $E_p = E^0$. We can see from figure 1.3 and the equations above that in the case of infinitely fast electron transfer the voltammogram has a symmetrical bell like shape.

Finite rates of electron transfer are described by the Butler-Volmer equation 1.14 discussed above. This equation cannot be solved for the general case, but assuming that the rate constant of electron transfer is low, and only one term for the either forward or backward reaction can be left in the equation:

$$\frac{d\Gamma_A}{dt} = -\Gamma_A k_0 e^{-\alpha\frac{(E-E_f^0)F}{RT}} \tag{1.41}$$

This equation has a solution which is given by the formula:

$$i = AFk_0\Gamma_A^0 e^{-\alpha\eta}e^{\frac{k_0RT}{\alpha vF}}\exp(-\alpha\eta) \tag{1.42}$$

with a peak current and peak potential given by equations 1.43 and 1.44, accordingly:

$$i_p = \frac{\alpha v\Gamma_A^0F^2}{2.718RT} \tag{1.43}$$

$$E_p = E^0 + \frac{RT}{\alpha F}\ln\frac{kRT}{\alpha vF} \tag{1.44}$$

Diffusional Cyclic Voltammetry

Here we consider diffusional cyclic voltammetry when electrochemically active species can freely diffuse in solution. Figure 1.4 shows typical cyclic voltammograms registered at a macroelectrode.

The mathematical model of diffusional cyclic voltammetry experiment is given by the Butler-

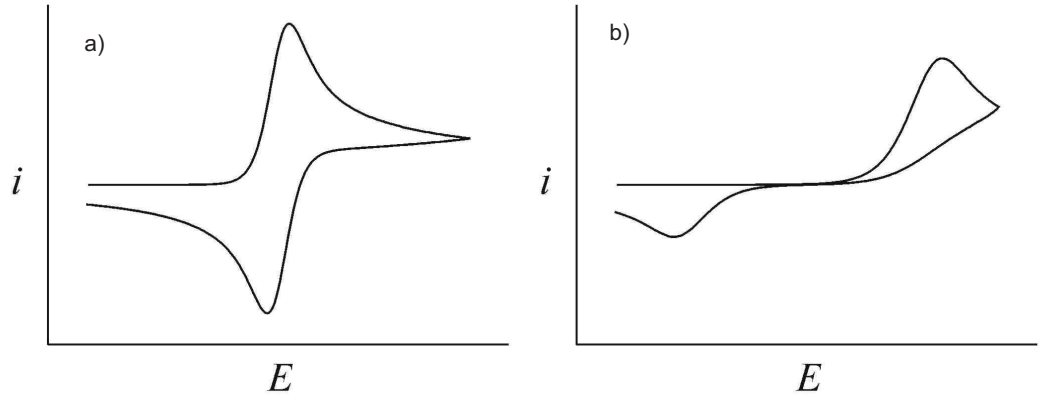

Figure 1.4: Schematic cyclic voltamograms of freely diffusion electrochemically active species, a) infinite fast electron transfer, b) and irreversible electron transfer.

Volmer equation 1.2 accompanied by the Fick's second law of diffusion:

$$\frac{\partial[\mathrm{A}]}{\partial t} = D\frac{\partial^2[\mathrm{A}]}{\partial z^2} \tag{1.45}$$

Accompanied by the assumption that concentration is assumed to be constant in the bulk of the solution.

There is no simple analytical equation which describes entire shape of the voltammogram. However equations for the peak current values for the cases of reversible and irreversible electron transfer exist, and are known as Randles-Sevcik equations:[1]

$$I_\mathrm{p} = 2.69 \times 10^5 AC\sqrt{Dv} \tag{1.46}$$

$$I_\mathrm{p} = 2.99 \times 10^5 AC\sqrt{\alpha Dv} \tag{1.47}$$

The peak to peak separation for the cases of reversible and irreversible electron transfer are given by the expressions 1.48 and 1.49:

$$\Delta E_\mathrm{pp} = 2.218\frac{RT}{F} = 57 \text{ mV} \tag{1.48}$$

$$\Delta E_\mathrm{pp} = \frac{59.4}{\alpha}\log v + Const \tag{1.49}$$

The criteria of reversibility or irreversibility of reaction was introduced by Natsuda and Ayabe[22]

and is characterised by the dimensionless parameter Λ, which is a ratio of the efficiency of electron transfer characterised by the k_0 to that of mass transport:

$$\Lambda = \frac{k_0}{\sqrt{\frac{FDv}{RT}}} \tag{1.50}$$

High values of Λ ($\Lambda > 15$) correspond to reversible reactions when the rate of the electron transfer is significantly higher than that of the diffusion to the electrode surface; low values of Λ ($\Lambda < 1 \times 10^{-3}$) corresponds to the irreversible reaction when the diffusional transport is significantly faster than the electron transfer; at intermediate values of Λ ($1 \times 10^{-3} < \Lambda < 15$) rates of electron transfer and diffusional transport are comparable and reaction is assumed to be quasi-reversible.

References

[1] Compton, R. G.; Banks, C. E. *Understanding Voltammetry;* World Scientific: 2007.

[2] Bard, A. J.; Faulkner, L. R. *Electrochemical Methods, Fundamentals and Applications;* John Wiley and Sons: New York, 2001.

[3] Damaskin, B.; Petriy, O.; Tsirlina, G. *Electroxchimia;* Xchimia: Moscow, 2006.

[4] Tafel, J. *Z Phys Chem* **1905,** *50A,* 641-712.

[5] Butler, J. A. V. *Trans Faraday Soc* **1924,** *19,* 729–724.

[6] Erdey-Gruz, T.; Volmer, T. *Z Phys Chem* **1930,** *150A,* 203-213.

[7] Peover, M.; White, B. *J Electroanal Chem* **1967,** *13,* 93-99.

[8] Koizumi, N.; S., A. *J Electroanal Chem* **1974,** *55,* 452-454.

[9] Kojima, H.; Bard, A. *J Amer Chem Soc* **1975,** *97,* 6317–6324.

[10] Tanaka, N.; Tamamushi, R. *Electrochim Acta* **1964,** *9,* 963–989.

[11] Cui, S. T. *J Chem Phys* **2005,** *123,* 054706.

[12] Xue, J.; Zou, X.; Xie, Y.; Wang, Y. *J Phys D: Appl Phys* **2009,** *42,* 105308.

[13] Dickinson, E. J. F.; Limon-Petersen, J. G.; Rees, N. V.; Compton, R. G. *J. Phys. Chem. C* **2009,** *113,* 11157-11171.

[14] Limon-Petersen, J. G.; Streeter, I.; Rees, N. V.; Compton, R. G. *J Phys Chem C* **2009,** *113,* 333–337.

[15] Limon-Petersen, J. G.; Dickinson, E. J. F.; Rees, N. V.; Compton, R. G. *J Phys Chem C* **2009,** *113,* 15320–15325.

[16] Limon-Petersen, J. G.; Han, J. T.; Rees, N. V.; Dickinson, E. J. F.; Streeter, I.; Compton, R. G. *J Phys Chem C* **2010,** *114,* 2227–2236.

[17] Aoki, K.; Osteryoung, J. *J. Electroanal. Chem.* **1981,** *122,* 19–35.

[18] Oldham, K. B. *J. Electroanal. Chem.* **1981,** *122,* 1–17.

[19] Szabo, A. *J. Phys. Chem.* **1987,** *91,* 3108–3111.

[20] Shoup, D.; Szabo, A. *J. Electroanal. Chem.* **1982,** *140,* 237-245.

[21] Srinivasan, S.; Gileadi, E. *Electrachim Acta* **1966,** *11,* 321-335.

[22] Matsuda, H.; Ayabe, *Z Electrochem* **1955,** *59,* 494-503.

Chapter 2

Influence of Electrode Roughness on Cyclic and Stripping Voltammetry

2.1 Introduction

The development of lithographic, nanoprinting,[1] plasma etching,[2] laser microstructuring[3] and other techniques allows the fabrication of surfaces with a precisely defined geometry at the micro- or nano-scale. Such surfaces find many applications.[4–7] The modeling of electrochemical responses from surfaces of a well-defined geometry is well advanced.[8–13]

Despite such progress in the fabrication of surfaces with defined morphology, electrodes with rough surfaces will likely always be considered as cheap and realistic alternatives for many applications.[14–17] Moreover, rough electrodes have been reported to be advantageous over flat electrodes. For example, the intensity of the stripping peak from some oligodeoxynucleotides on rough glassy carbon electrodes is more then ten times that of a flat glassy carbon electrode.[15] Also rough glassy carbon electrodes show higher activity in ascorbic acid oxidation.[17] Furthermore, in practice flat electrodes, even after polishing have some surface roughness. Deliberately roughened surfaces can be fabricated in number of ways: by scratching,[15] by electrodeposition,[18–20] by electrochemical roughening[14,21,22] and by etching,[23] etc.

To describe the electrochemical response of rough electrodes two different approaches exist in the literature: the fractal approach[24–28,28–34] and the description of the surface in terms of exact mathematical functions.[35–38] The fractal approach provides a general description without the need for precise definition of the surface morphology. In early papers the electrodes were considered as self-similar fractal surfaces. Special electrodes, e.g. with Sierpinsky pattern, were fabricated for experimental[24–28,39] verification of the theoretical predictions. In this way it was proved theoretically that in potential step experiments the current is given by a generalized Cottrell equation $I \propto t^{-\alpha_f}$ where I is the current, t is the time and $\alpha_f = (D_f - 1)/2$, where D_f is the fractal dimension of the surface

$2 < D_f < 3$. In potential sweep experiments the peak current is found to vary as $I_{peak} \propto v^{\alpha_f}$, where v is the voltage scan rate. These relations were observed experimentally and rationalized by modeling. The peak to peak separation in cyclic voltammetry was shown to be strongly dependent on the surface fractal dimension. To characterize more realistic surfaces the idea of self-affine fractals[29–31,31,32] and fractals with a higher and lower cut-off frequencies[40] were utilized in later works. In particular should be noted that whilst fractal like surfaces can be specially prepared for the experimental validation[20,25,28,39,41] of the theoretical predictions, it is the case that most experimentally used electrodes, such as those made of carbon, platinum or gold show a surface topography which reflects the polishing regime used to prepare the electrode. AFM and other images and their frequency analysis[14,31,42–45] show that the dominant surface features are these of a size linked to polishing powder or grid used for surface preparation or other characteristic length scale. Moreover where diffusion to and from the surface is under study consideration of the Einstein equation relates the distance diffused in time t to $\sqrt{\pi D t}$, where D is the diffusion coefficient and this suggest that the larger sized irregularity on the surface will contribute most since at the typical scan rates in linear sweep voltammetry (10 - 1000 mV/s) the distance diffused are at least microns; in contrast the fractal description will likely only describe roughness effects near the mean roughness of the surface but not at the maximum roughness.

A second approach which can be found in the literature includes a detailed description of the geometry of the surface in terms of exact mathematical functions.[35–38,46] This allows diffusional equations to be solved analytically taking complex boundary conditions into account. However, due to the complexity of the problem only asymptotic solutions were obtained for potential step experiments.[35–37] The current was described by a generalized Cottrell equation: $I = at^{-1/2}$, where a depends on time and the surface roughness.

In this chapter we adopt a computational approach used earlier to successfully model diffusional voltammetry on electrodes with non-uniform surfaces,[9–11,13] particularly regular and random arrays of microdisks and cones electrodes, nanoparticle arrays and partially blocked electrodes. The applicability of the approach was also confirmed[47] with the three dimensional simulation and the only limitation of the approach is that electrodes in the array should be of equal area. Further we apply the diffusion domain approach to consider stripping voltammetry at rough and scratched electrodes. Note that the present work compliments an approach to non-fractal surfaces in which chronoamperometry is used to measure the roughness of electrode.[38,48,49] Note however that such an approach is con-

strained by the fact that the short time data is overwhelmingly masked by the double layer charging effect. In contrast the present study focused entirely on experimentally accessible timescales.

We first present theory for cyclic voltammetry of rough electrode, specifically the influence of the electrode morphology on the peak current and peak to peak separation. The $Ru(NH_3)_6^{2+}$/ $Ru(NH_3)_6^{3+}$ and N,N,N',N'-tetramethyl-p-phenylenediamine(TMPD) redox couples are used to characterize glassy carbon electrodes with different surface morphologies. The conclusion is drawn that rough electrodes are remarkably insensitive to purely diffusional effects when studied with cyclic voltammetry. Further we investigate stripping voltammetry on rough and scratched (V-shaped) electrodes. We consider stripping of a monolayer, a thin layer and finally stripping of a bulk layer. We conclude that the stripping of bulk layer is extremely sensitive to the electrode roughness.

2.2 Models of Electrode Surface

We consider two models for the electrode surface - "rough" and "scratched" (V-shaped) electrodes.

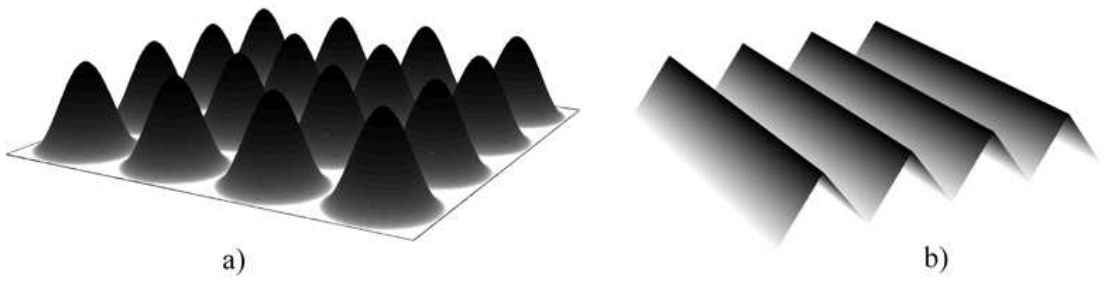

Figure 2.1: Models of the electrode surface: (a) rough electrode and (b) scratched electrode

2.2.1 Rough electrodes (bell shaped roughness).

An electrode with an idealized rough surface is shown in Figure 2.1a. The idealized surface is composed of a regular "array" of peak-shaped protrusions conferring a significant surface roughness. The diffusion of an electrochemically active species to such a surface is complicated because it is intrinsically a three dimensional problem. However, the problem can be simplified by noting that each peak belongs to a diffusionally independent region known as a diffusion domain.[9–12,50,51] The diffusion domain approximation treats these zones as being cylindrical with a peak situated at the axis

of symmetry, thus reducing the problem of diffusion to one of only two dimensions. The area of the diffusional domain in cylindrical coordinates has an equivalent area to the unit cell in Cartesian coordinates. The approximation is illustrated in Figure 2.2. Figures 2.2a and b shows the surface with cubic and hexagonal symmetry in Cartesian coordinates.

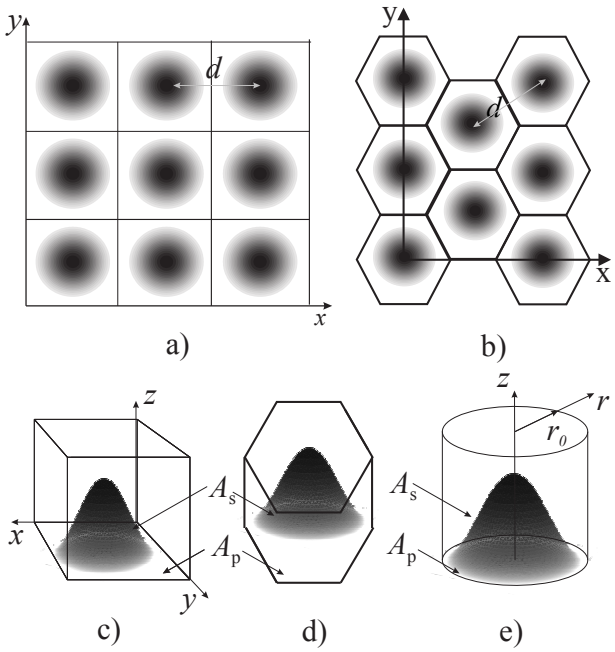

Figure 2.2: Schematic diagram of the unit cell for (a) cubic and (b) hexagonal arrays of peaks; (c) cubic and (d) hexagonal unit cell in Cartesian coordinates; and (e) equivalent diffusion domain in cylindrical coordinates

Figures 2.2c and d identify the unit cell with cubic and hexagonal symmetry correspondingly and Figure 2.2e shows the diffusional domain in cylindrical coordinates (r,z). The cylindrical coordinate system is defined relative to the single diffusion domain. The cylindrical radial coordinate, r, is defined as the distance from the axis of the symmetry that runs through the center of the electrode domain. The peak-to-peak separation is d. The area of the cylindrical domain is chosen to be equal to the area of the unit cell in Cartesian coordinates:

$$\frac{\sqrt{3}}{2}d^2 = \pi r_0^2 \tag{2.1}$$

for hexagonal and

$$d^2 = \pi r_0^2 \tag{2.2}$$

for cubic arrays.

2.2.2 Scratched electrodes (triangular corrugation).

An electrode with an idealised scratched surface as shown in Figure 2.1b. The idealised surface is composed of a regular "array" of V-shaped bands. Each V-shaped band has planes of symmetry along the top and the bottom. There is a condition of zero flux across these planes. These planes of symmetry therefore form the boundaries of a diffusionally independent unit cell, which is repeated across the

surface of the electrode.[8] The diffusionally independent unit cell is presented in Figure 2.3. In the numerical simulation of diffusion to a scratched electrode, only a single unit cell needs to be considered. Furthermore the length of the band is assumed to significantly exceed the width and height, so the concentration of electrochemical species are constant along the band length. Consequently the complicated three-dimensional problem can again be reduced to that of only two dimensions.

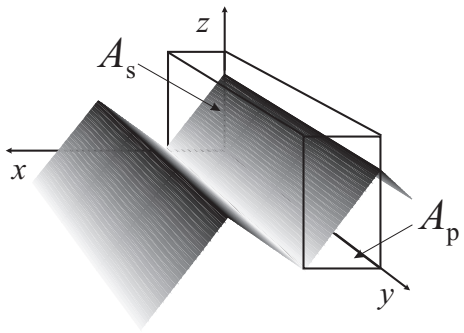

Figure 2.3: Schematic diagram of the diffusionally independent unit cell used to simulate voltammograms on scratched electrodes.

Two different areas are considered in this paper: A_p is the area of the electrode projected onto the flat surface at Z=0 (area above the peak on Figures 2.2) and 2.3)), whereas A_s is the real area of the electrode (area of the peak on Figure 2.2) and 2.3)). The total number of the diffusion domains N_p at the macroelectrode is given by formulas:

$$N_p = \frac{2A_p}{\sqrt{3}d^2} = \frac{A_p}{\pi r_0^2} \tag{2.3}$$

for hexagonal and

$$N_p = \frac{A_p}{d^2} = \frac{A_p}{\pi r_0^2} \tag{2.4}$$

for cubic array.

Hence the total current from the macroelectrode "array" is given by simple multiplication of the current from single diffusion cell to the total number of domains N_p

2.3 Mathematical Model

Equation 2.5 shows the electrochemical reaction considered in numerical simulations of cyclic and stripping voltammetry experiments.

$$\mathrm{A(aq)} + \mathrm{e} \underset{k_b}{\overset{k_f}{\rightleftharpoons}} \mathrm{B(aq)} \tag{2.5}$$

here we assume that electron transfer is described by the Butler-Volmer kinetics:

$$k_{\mathrm{f}} = k_{\mathrm{f}}^{0} \exp\left(-\frac{\alpha F}{RT}(E - E_{\mathrm{f}}^{0}) \right) \tag{2.6}$$

$$k_{\mathrm{b}} = k_{\mathrm{b}}^{0} \exp\left(\frac{(1-\alpha) F}{RT}(E - E_{\mathrm{f}}^{0}) \right) \tag{2.7}$$

2.3.1 Cyclic Voltammetry

Here both species A and B are soluble, but only species A is assumed to be present in bulk solution. Electron transfer is given by the following equation:

$$\frac{\partial [\mathrm{A}]}{\partial t} = k_0([\mathrm{A}] \exp - \frac{\alpha F}{RT}(E - E_{\mathrm{f}}^{0}) - [\mathrm{B}] \exp \frac{(1-\alpha)F}{RT}(E - E_{\mathrm{f}}^{0})) \tag{2.8}$$

where, as was derived in Chapter 1, $k_{\mathrm{f}}^{0} = k_{\mathrm{b}}^{0} = k_0$.

2.3.2 Stripping Voltammetry

In stripping voltammetry experiment only species A is soluble and assumed to be present in bulk solution and species B is assumed to be deposited on the electrode surface, k_{f} is the rate constant for the deposition and k_{b} is the rate constant for the dissolution. The rate constant for the deposition and dissolution are linked via the Nernst equation. Assuming that the solution is ideal and taking into account that activity of the solid phase is equal to unity, the Nernst equation for the electron transfer considered above can be written as:

$$E = E^{0} + \frac{RT}{F} \ln \frac{[A]}{[A]^{*}} \tag{2.9}$$

where $[\mathrm{A}]^{*}$ is a standard concentration. At equilibrium the following equation is valid:

$$0 = [A] k_{\mathrm{f}}^{0} \exp\left(-\frac{\alpha F}{RT}(E - E_{\mathrm{f}}^{0}) \right) - k_{\mathrm{b}}^{0} \exp\left(\frac{(1-\alpha)F}{RT}(E - E_{\mathrm{f}}^{0}) \right) \tag{2.10}$$

combining equations 2.9 and 2.10 the following can be derived:

$$k_{\mathrm{b}}^{0} = k_{\mathrm{f}}^{0} \times [A]^{*} = k_{\mathrm{f}}^{0} \times 1 \times 10^{-3} \text{ mol cm}^{-3} \tag{2.11}$$

Three different models of electron transfer[52] will be considered here:

$$\text{model A} \quad \Gamma_{\max}\frac{\partial\Gamma}{\partial t} = k_{\mathrm{f}}(\Gamma_{\max}-\Gamma)[\mathrm{A}]_{\mathrm{surf}} - k_{\mathrm{b}}\Gamma \tag{2.12}$$

$$\text{model B} \quad \Gamma_{\max}\frac{\partial\Gamma}{\partial t} = \Gamma_{\max}k_{\mathrm{f}}[\mathrm{A}]_{\mathrm{surf}} - k_{\mathrm{b}}\Gamma \tag{2.13}$$

$$\text{model C} \quad \Gamma_{\max}\frac{\partial\Gamma}{\partial t} = \Gamma_{\max}k_{\mathrm{f}}[\mathrm{A}]_{\mathrm{surf}} - k_{\mathrm{b}} \tag{2.14}$$

where, Γ is the surface coverage of B (mol cm^{-2}), $\Gamma_{\max}$ is maximal surface coverage, t is time (s) and $[\mathrm{A}]_{\mathrm{surf}}$ concentration of electroactive species A at electrode surface. Model C has the additional condition that the value of Γ is not permitted to go below zero. These equations are accompanied by the condition:

$$\frac{\partial\Gamma}{\partial t} = D\frac{\partial[\mathrm{A}]}{\partial N} \tag{2.15}$$

where D is diffusion coefficient of species A and $\frac{\partial[\mathrm{A}]}{\partial N}$ is flux of A normal to the electrode surface which is defined later and given by the equation 2.34 (see below). The problem can be also formulated in terms of a thin layer deposited on the electrode surface, rather than an adsorption layer:

$$\text{model A} \quad lB_{\max}\frac{\partial[\mathrm{B}]}{\partial t} = k_{\mathrm{f}}([\mathrm{B}]_{\max}-[\mathrm{B}])[\mathrm{A}]_{\mathrm{surf}} - k_{\mathrm{b}}[\mathrm{B}] \tag{2.16}$$

$$\text{model B} \quad lB_{\max}\frac{\partial[\mathrm{B}]}{\partial t} = k_{\mathrm{f}}[\mathrm{A}]_{\mathrm{surf}} - k_{\mathrm{b}}[\mathrm{B}] \tag{2.17}$$

$$\text{model C} \quad lB_{\max}\frac{\partial[\mathrm{B}]}{\partial t} = k_{\mathrm{f}}[\mathrm{A}]_{\mathrm{surf}} - k_{\mathrm{b}} \tag{2.18}$$

In this case equation 2.15 becomes:

$$l\frac{\partial[\mathrm{B}]}{\partial t} = D\frac{\partial[\mathrm{A}]}{\partial N} \tag{2.19}$$

where, l is the layer thickness and [B] is the concentration of the electrochemically active specie in the layer. Model C again has the additional condition that the value of σ is not permitted to go below zero.

The models are normalized with the use of the dimensionless parameters presented in Table 2.1. Equations 2.12 - 2.14 and 2.16 - 2.18 have following forms in terms of dimensionless variables:

$$\text{model A} \quad \frac{\partial b}{\partial\tau} = \beta\Lambda e^{-\alpha\theta}a_{\mathrm{surf}}(1-\gamma) - \Lambda\beta e^{(1-\alpha)\theta}\gamma \tag{2.20}$$

$$\text{model B} \quad \frac{\partial b}{\partial \tau} = \Lambda\beta e^{-\alpha\theta} a_{\text{surf}} - \Lambda\beta e^{(1-\alpha)\theta}\gamma \tag{2.21}$$

$$\text{model C} \quad \frac{\partial b}{\partial \tau} = \beta\Lambda e^{-\alpha\theta} a_{\text{surf}} - \Lambda\beta e^{(1-\alpha)\theta} \tag{2.22}$$

together with the expression:

$$\frac{\partial b}{\partial \tau} = \beta \frac{\partial a}{\partial N} \tag{2.23}$$

Models A, B and C describe the stripping of a monolayer, of a thin layer and of a bulk metal respectively.

Table 2.1: Dimensionless parameters used for numerical simulation.

parameter	rough	scratched (or flat)
radial (x) coordinate	$R = r/r_0$	$X = x/x_0$
normal (z) coordinate	$Z = z/(Sr_0)$	$Z = z/(Sx_0)$
time	$\tau = \frac{Dt}{r_0^2}$	$\tau = \frac{Dt}{x_0^2}$
scan rate	$\sigma = \frac{Fvr_0^2}{RTD}$	$\sigma = \frac{Fvx_0^2}{RTD}$
potential	$\theta = \frac{F(E-E_f^0)}{RT}$	$\theta = \frac{F(E-E_f^0)}{RT}$
concentration of species A	$a = [\text{A}]/[\text{A}]^*$	$a = [\text{A}]/[\text{A}]^*$
concentration of species B	$b = [\text{B}]/[\text{B}]_{\max}$	$b = [\text{B}]/[\text{B}]_{\max}$
coverage	$\gamma = \Gamma/\Gamma_{\max}$	$\gamma = \Gamma/\Gamma_{\max}$
surface coverage parameter	$\beta = \frac{[\text{A}]^* r_0}{\Gamma_{\max}}$	$\beta = \frac{[\text{A}]^* x_0}{\Gamma_{\max}}$
surface concentration parameter	$\beta = \frac{[\text{A}]^* r_0}{[\text{B}]_{\max} l}$	$\beta = \frac{[\text{A}]^* x_0}{[\text{B}]_{\max} l}$
constant of electron transfer	$\Lambda = \frac{k_0 r_0}{D}$	$\Lambda = \frac{k_0 x_0}{D}$
layer thickness	$L = \frac{l}{r_0}$	$L = \frac{l}{x_0}$
total charge	$Q = \frac{\pi q r_0^2}{\Gamma_{\max} F}$	$Q = \frac{q x_0^2}{\Gamma_{\max} F}$
electrode flux (CV)	$j = \frac{-i}{FDr_0[\text{A}]^*}$	$j = \frac{-i}{FDx_0[\text{A}]^*}$
electrode flux (stripping)	$j = \frac{-i}{2\pi FDr_0[\text{A}]^*}$	$j = \frac{-i}{FDx_0[\text{A}]^*}$

2.3.3 Flat macroelectrodes.

Mass transport to a flat macroelectrode is described by the one dimensional Fick's Second law of diffusion:

$$\frac{\partial[\mathrm{A}]}{\partial t} = D_{\mathrm{A}} \frac{\partial^2[\mathrm{A}]}{\partial z^2} \tag{2.24}$$

In normalised space mass transport equation 2.24 is given by the equation:

$$\frac{\partial \mathrm{a}}{\partial \tau} = \frac{\partial^2 a}{\partial Z^2} \tag{2.25}$$

2.3.4 Rough electrodes.

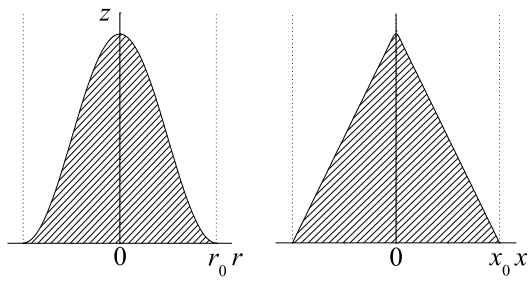

Figure 2.4: Slice in the $r-z$ plane of diffusional domains of the rough electrode in cylindrical coordinates (a) and slice in the $x-z$ plane of diffusional cell of the scratched electrode in Cartesian coordinates (b).

Figure 2.4a shows a slice on the $r-z$ plane of the diffusional domain (Figure 2.2a) in cylindrical coordinates. The shape of each single electrode domain in cylindrical coordinates is given by the function:

$$z = S r_0 \cos^2\left(\frac{\pi r}{2 r_0}\right) \tag{2.26}$$

where r_0 is the radius of the diffusion domain and S is a scale factor. This scale factor S is the main parameter characterising surface roughness: the larger its value, the more rough the surface. The mass transport in cylindrical coordinates is described by the Fick's second law of diffusion, which is presented in eq 2.27

$$\frac{\partial[\mathrm{A}]}{\partial t} = D_{\mathrm{A}} \left(\frac{\partial^2[\mathrm{A}]}{\partial r^2} + \frac{1}{r}\frac{\partial[\mathrm{A}]}{\partial r} + \frac{\partial^2[\mathrm{A}]}{\partial z^2} \right) \tag{2.27}$$

In the normalised space the mass transport equation is given by the dimensionless variant of eq 2.27

$$\frac{\partial a}{\partial \tau} = \frac{\partial^2 a}{\partial R^2} + \frac{1}{R}\frac{\partial^2 a}{\partial R} + \frac{\partial^2 a}{\partial Z^2} \tag{2.28}$$

and the electrode surface is described by a locus:

$$Z \equiv f = \cos^2\left(\frac{\pi R}{2}\right) \tag{2.29}$$

2.3.5 Scratched electrodes.

Figure 2.4b shows a slice on the $x-z$ plane of the diffusional domain (Figure 2.2a) in Cartesian coordinates. The shape of each diffusion cell is given by the function:

$$z = S(x_0 - x) \tag{2.30}$$

The mass transport in Cartesian coordinates is described by the Fick's second law of diffusion, which is presented in eq 2.31

$$\frac{\partial[\mathrm{A}]}{\partial t} = D_{\mathrm{A}}\left(\frac{\partial^2[\mathrm{A}]}{\partial x^2} + \frac{\partial^2[\mathrm{A}]}{\partial z^2}\right) \tag{2.31}$$

In the normalised space the mass transport equation is given by the dimensionless variant of eq 2.31

$$\frac{\partial a}{\partial \tau} = \frac{\partial^2 a}{\partial X^2} + \frac{\partial^2 a}{\partial Z^2} \tag{2.32}$$

and the electrode surface is described by a locus:

$$Z \equiv f = 1 - X \tag{2.33}$$

The electrochemical experiment is assumed to be conducted in the fully supported media, so the mass transport is fully described by Fick's Second law of diffusion 2.28 and 2.32.

2.3.6 Boundary Conditions and Calculation of the Flux Normal to the Surface

Table 2.2: Boundary and initial conditions

Boundary	Condition (CV)	Condition (ASV)
Initial condition	a=1, b=0	$a = e^{-\theta}, b = 1$
Bulk solution	a=1, b=0	$a = e^{-\theta}$
Diffusion domain border	$\frac{\partial a}{\partial R} = 0$ or $\frac{\partial a}{\partial X} = 0$	$\frac{\partial a}{\partial R} = 0$ or $\frac{\partial a}{\partial X} = 0$

The electrode surface boundary conditions are given in Table 2.2. The flux normal to the electroactive surface $\frac{\partial a}{\partial N}$, which controls the current, is calculated as a composite of fluxes in the $R-$ and

$Z-$directions:[46]

$$J = \frac{\partial a}{\partial N} = -\frac{\partial a}{\partial R}\frac{f'(R)}{\sqrt{1+f'(R)^2}} + \frac{1}{S}\frac{\partial a}{\partial Z}\frac{1}{\sqrt{1+f'(R)^2}} \tag{2.34}$$

where,

$$f'(R) = -\pi S\cos(\frac{\pi R}{2})\sin(\frac{\pi R}{2}) \tag{2.35}$$

for the rough electrode and

$$f'(R) = -S \tag{2.36}$$

for the scratched electrode. Equation 2.34 provides a local flux density, which is converted to dimensionless flux j by integrating across the surface area of the diffusional domain. The flux to the diffusion domain is given by equation 2.37 for the rough electrode and equation 2.38 for the scratched electrode.

$$j = 2\pi\int_0^1 \frac{\partial a}{\partial N}\sqrt{1+f'(R)^2}RdR = 2\pi\int_0^1 \left(\pi S\frac{\partial a}{\partial R}\cos(\frac{\pi R}{2})\sin(\frac{\pi R}{2}) + \frac{1}{S}\frac{\partial a}{\partial Z}\right)RdR \tag{2.37}$$

$$j = \int_0^1 \frac{\partial a}{\partial N}\sqrt{1+f'(X)^2}dX = \int_0^1 \left(S\frac{\partial a}{\partial X} + \frac{1}{S}\frac{\partial a}{\partial Z}\right)dX \tag{2.38}$$

The flux to the flat macroelectrode is given by the equation 2.11

$$j = \frac{\partial a}{\partial Z} \tag{2.39}$$

2.4 Experimental and Computational Details

2.4.1 Macroelectrode Cyclic Voltammetry of Soluble A/B Species

One dimensional simulations macroelectrode cyclic voltammogram were performed using DigiSim (BASi, IN, USA)[53] to extract kinetic parameters from experimental data and to verify the convergence or otherwise of the computation procedures defined below.

2.4.2 Computation Procedure of Cyclic and Stripping Voltammograms at Rough and V-Shaped Electrodes

Equations 2.28 and 2.32 and their accompanying boundary conditions (Table 2.2) were discretised and solved by the alternating direction implicit (ADI) finite difference method[54] in conjunction with

the Thomas algorithm.[55] Equations 2.40 and 2.41 are similar to those used in previous works[10,46] and are used to calculate the flux to the electrode. Electrode boundary condition 2.40 is used when the ADI method is implicit in the R-direction, and boundary condition 2.41 is used when it is implicit in the Z-direction. The Newton algorithm[55] was implemented to solve the non-linear equation of the model A of the electron transfer. Programs were written in C++.

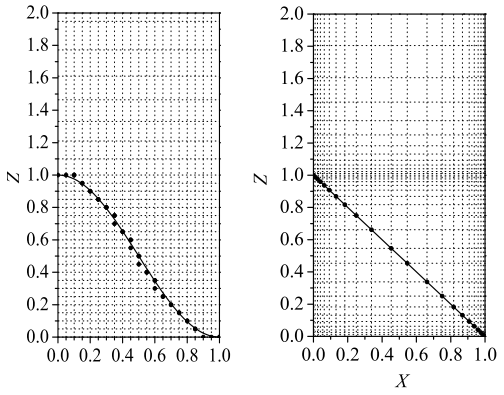

Figure 2.5: Schematic view of the grid used in this work for simulation of the stripping voltammetry at (a) rough and (b) scratched electrodes

Figure 2.5 shows the expanding simulation grids, which are based on the grids used in previous simulations of electrodes with a curved shape.[9–13,46,50,56] The black curve represents the idealised electrode surface. The dots represents the discretised electrode surface. In the case of the scratched electrode, grid points are fitted precisely to the sloping surface of the electrode (fig 2.5b); however, in the case of the rough electrode, the grid points fit only approximately to the actual electrode surface (fig 2.5a).

$$\frac{\partial a}{\partial N} = \frac{\partial a}{\partial Z} \Big/ \frac{f'(R)}{\sqrt{1+f'(R)^2}} \tag{2.40}$$

$$\frac{\partial a}{\partial N} = \frac{\partial a}{\partial R} \Big/ \frac{1}{\sqrt{1+f'(Z)^2}} \tag{2.41}$$

where

$$f'(Z) = -\pi S \sqrt{(1-Z)Z} \tag{2.42}$$

and $f'(R)$ is given by equation 2.35 for the rough electrode and

$$f'(Z) = f'(R) = -S \tag{2.43}$$

for the scratched electrode.

The spacing of mesh lines in the expanding region is given by equations 2.44 and 2.45.

$$\Delta z_{\mathrm{i}} = \gamma_{\mathrm{z}} \Delta z_{\mathrm{i}-1} \tag{2.44}$$

$$\Delta r_{\mathrm{i}} = \gamma_{\mathrm{r}} \Delta r_{\mathrm{i}-1} \tag{2.45}$$

2.4.3 Computational Accuracy

To check the convergence of the simulation procedure numerous simulations with different space grids and time steps were run. An example is presented in Figure 2.6. The calculated current converges with a decrease of the space step Δz_0 and Δr_0 and on increase in the number of the steps per unit of dimensional potential θ. The whole range of parameters was tested to achieve an accuracy of better than 0.2%. The standard values of parameters used for simulations are $\Delta z_0 = \Delta r_0 = 4 \times 10^{-4}$, $\gamma =$ 1.125, and number of steps per potential is 400.

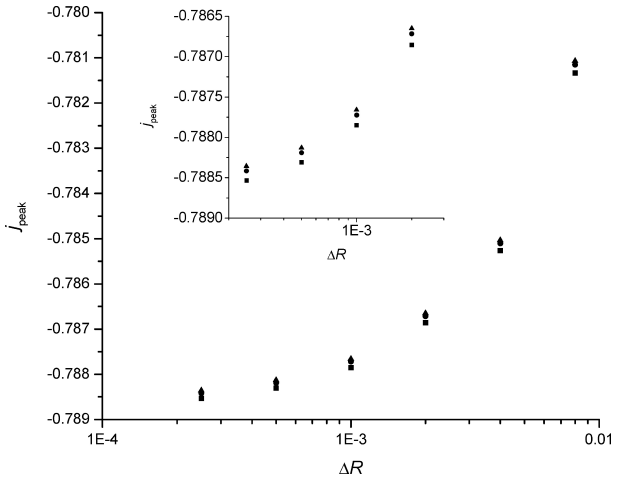

Figure 2.6: Values of the dimensionless peak current j at different space grids and time steps. $\sigma = 0.3893$, $\Lambda = 1$; squares, dots, and triangles show data calculated with 50, 100, and 200 number of time steps per unit of dimensionless potential θ.

Results from the two dimensional simulation of diffusional cyclic voltammetry at a rough electrode with small values of scale factor S are presented in Table 2.3. The deviation of the calculated dimensionless current from the current given by equation 2.46[57] for broad range of scan rates is less than 0.2%:

$$j_{\mathrm{peak}} = 1.402\sigma^{1/2} \tag{2.46}$$

Calculation of stripping voltammograms on scratched electrodes according to model C were done on a mesh expanding only in Z-direction from the electrode surface. At low

Table 2.3: Simulated and Theoretical Peak Current Values for Macrodisk Electrode

σ	$S = 0.16$	$S = 0.08$	$S = 0.04$	$S = 0.02$	$S = 0.01$	eq 2.46
0.1	0.4425	0.4436	0.4438	0.4439	0.4439	0.4434
1	1.402	1.403	1.404	1.404	1.404	1.402
10	4.455	4.442	4.440	4.439	*S*4.439	4.434

values of the scale factor S the electrode can be considered effectively flat. The peak current and peak potential values calculated by two dimensional model at low values of the scale factor S were in quantitative agreement with that calculated by the one dimensional model for a flat electrode. The total charge passed through the electrode is given by equation 2.47

$$q = A_s F \Gamma_{\max} = \int_0^{t_f} i dt = \int_{E_i n}^{E_f} \frac{i}{v} dE \tag{2.47}$$

In dimensionless variables this equation is formulated as follows

$$Q = A_s \sigma = \beta \int_{\theta_i n}^{\theta_f} j d\theta \tag{2.48}$$

where A_s is dimensionless area of the electrode surface. Calculated numerically values of the total charge transfered through electrode were in agreement with that given by equation 2.48.

2.4.4 Chemical Reagents and Instrumentation

All chemicals were of analytical grade and were used as received without any further purification, unless stated. All aqueous solutions were prepared with deionised water of resistivity not less than 18.2 MΩ cm at 25^0 C (Millipore water systems, UK).

Voltammetric measurements were carried out using an Autolab (ECO-Chemie, The Netherlands) potentiostat connected to a PC. All measurements were conducted using a three electrode cell. The counter electrode was a bright platinum wire. A saturated calomel electrode was used as the reference electrode in water solutions and a silver wire was used as a pseudo-reference electrode in acetonitrile solutions.

A flat glassy carbon electrode (GC, 3 mm diameter, BAS Technicol, U.K.) was first polished with diamond spray (Kemet Int. Ltd., UK) with size of particles 3, 1 and finally 0.1 m. Rough GC electrodes were fabricated from flat electrodes by scratching with Silicon-Carbide P1000 (3M, U.K.) paper. After polishing and scratching the GC electrode was sonicated for at least 15 minutes. The GC electrode was additionally cleaned by treatment with concentrated sulfuric acid with potassium permanganate. The GC electrode was activated by cycling between -0.8 - 0.4 V in 0.1M KCl subsequently the $Ru(NH_3)_6Cl_3$/0.1 M KCl was studied. All experiments in aqueous solutions were conducted at 25 ± 1^0C. In the case that experiments were conducted in non-aqueous solutions the

GC electrode was activated by applying a potential of -3 V and then cycling between -0.2 - 0.6 V in 0.1 M tetra(n-butyl)ammonium perchlorate (TBAP). Then N,N,N,N-tetramethyl-p-phenylenediamine (TMPD)/0.1 M TBAP in acetonitrile was studied. TMPD was recrystallized from petroleum ether before use.47 Acetonitrile was dried above molecular sieves before use. All experiments in acetonitrile solutions were conducted at 2 $\pm$ 0.5 0C. All solutions were degassed with high purity nitrogen in accordance with standard electrochemical practice.

An AFM was used to image the surface. This was a Digital Instruments Multimode SPM, operating in TappingMode. A model "J" scanner was used, having a lateral range of 125$\times$125 μm and a vertical range of 5 μm.

2.5 Cyclic Voltammetry: Results and Discussion

2.5.1 Fast Kinetics (Nernst Case): Theoretical Considerations

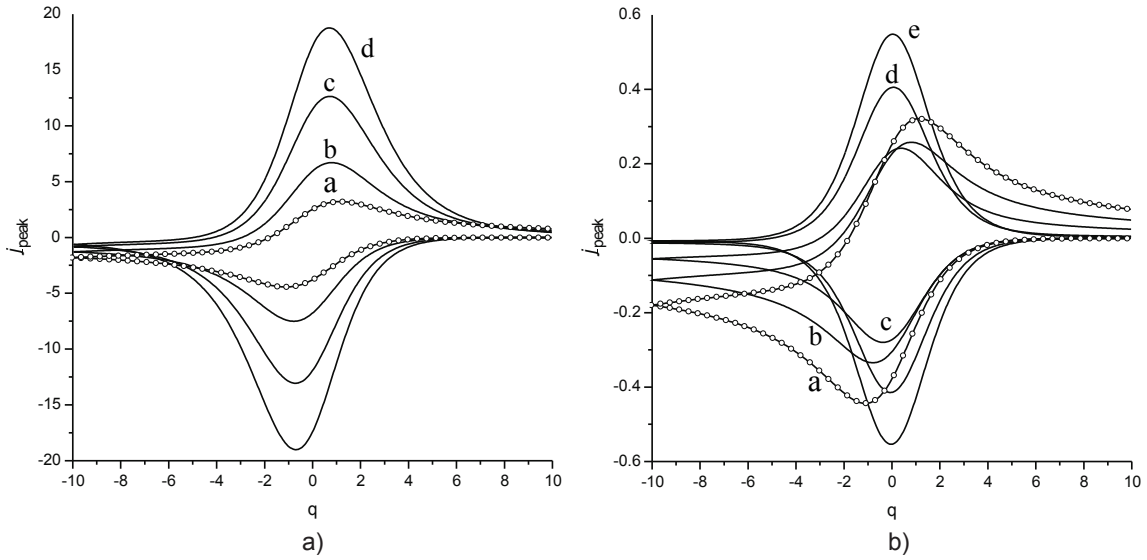

Figure 2.7: Cyclic voltammograms at different values of scale factor *S*: (a) σ = 10, *S* has the following values (a) 0.1, (b) 2, (c) 4, (d) 6; (b) σ = 0.1, *S* has the following values (a) 0.1, (b) 2, (c) 4, (d) 10, (e) 14. The open dots show the planar diffusion cyclic voltammograms calculated with DigiSim.

To characterize surface roughness the scale factor *S* has been introduced by equation 2.26. Voltammograms simulated at different values of the scale factor *S* are presented in Figure 2.7. Figure 2.7a shows cyclic voltammograms simulated at the dimensionless scan rate σ = 10 and Figure 2.7b shows that simulated at σ= 0.1. The cyclic voltammograms of the rough electrode must converge to the limiting case of the flat macrodisk as the scale factor *S* decreases. The difference in surface area of

the flat and rough electrodes is less than 5% until the scale factor S reaches a value of $S = 0.3$. Voltammograms simulated with values of the scale factor $S < 0.3$ are similar to those of a flat macrodisk. In parts a and b of Figure 2.7 the voltammograms labeled a were simulated for $S = 0.1$ and very closely match the voltammograms simulated with DigiSim in the limit of a flat macrodisk electrode. Figure 2.7a shows that on increase of the scale factor S the peak current increases, and the peak in the $j - \theta$ curves become sharper and more pronounced in shape. The concentration profiles for different values of the scale factor S are presented in Figure 2.9. The current is almost absent after the peak (Figure 2.7a,b) at high values of the scale factor S, because diffusion is too slow to bring much new material from the bulk solution and the concentration of the electroactive substance is very low at the bottom of the electrode in the valleys between the protrusions at high values of S (Figure 2.9c,d). At low values of the scale factor S the diffusion is more efficient (Figure 9a). Peak current and peak current density versus the scale factor S is presented in Figure 2.8a, and surface area versus the scale factor S is presented in Figure 2.8b. Figure 2.8a shows that on increase the scale factor S the peak current goes through a minimum. However, the peak current density decreases gradually with increasing scale factor S as shown in Figure 2.8a. At low values of the scale factor S ($S < 1$) the electrode area is approximately constant (Figure 2.8b), but the complex electrode shape decreases the efficiency of diffusional mass transport (Figure 2.9b) to the bottom of the electrode. At high values of the scale factor S ($S > 10$) the surface of the electrode is approximately proportional to S and significantly bigger than in the case of a plane electrode; because of this a large peak current is observed. The thickness of the diffusion layer l_{D} decreases in agreement with expression:

$$l_{\mathrm{D}} \propto \tau^{1/2} \propto \frac{1}{\sigma}$$

on increase of the scan rate. At high scan rates the thickness of the diffusional layer becomes small and diffusional fluxes to the bottom of the electrode and to the top do not interfere with each other. Hence peak current increases proportionally to the surface area. In Figure 2.8 peak current and peak-to-peak separation $\Delta\theta_{\mathrm{pp}}$ versus the scale factor S are presented. Comparing Figures 2.8b with 2.10a, it is seen that at high scan rates peak current increases proportionally to the surface area of the electrode. At low values of the scale factor S the peak current density is equal to the peak current density at a macrodisk electrode under planar one-dimensional diffusion as shown in Figures 2.7a,b and 2.10a and Table 2.3. At high values of the scale factor S, the peak current density goes to a limiting value.

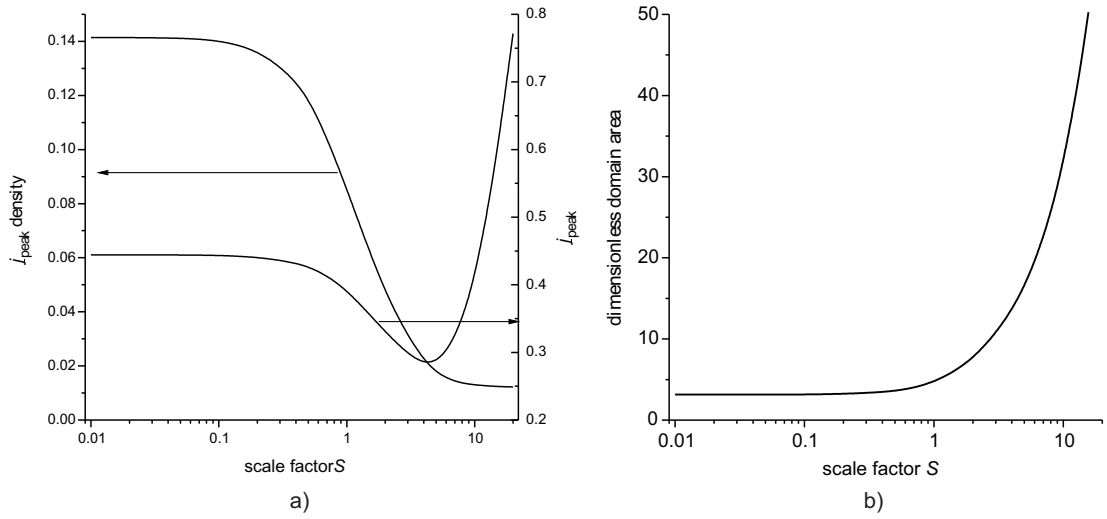

Figure 2.8: (a) σ = 0.1 peak current and peak current density at different values of the scale factor S; (b) electrode domain area at different values of the scale factor S. x-Axes are plotted with a logarithmic scale.

The peak current to a cylindrical electrode is given by equation 2.49.[58] Equation 2.49 becomes linear in the coordinates $j\sigma^{-1/2}$ versus $\sigma^{-0.425}$. The peak current for electrodes with a high scale factor S = 20 and different values of scan rate is presented in Figure 2.10. At high values of scan rates $j\sigma^{-1/2}$ is linearly dependent on $\sigma^{-0.425}$, which shows that the diffusion is effectively radial and one-dimensional.

The behavior of the electroactive compound may be characterized by both the peak current and the peak-to-peak separation. Peak current values at different scan rates and scale factor S are presented in Figure 2.10a. Calculated peak current values for low scale factor S values are in good agreement with those calculated with DigiSim at the planar diffusion limit for a flat electrode. From Figure 2.10a it can be seen that at low scan rates a minimum in the peak current value is observed. At high scan rates the peak current is proportional to the surface area (Figure 2.10b). The peak-to-peak separation gradually decreases with increase of the scale factor S; the faster the scan rate, the larger the peak-to-peak separation (Figure 2.10b).

$$j_{\text{peak}} = 0.446\sigma^{1/2} + 0.355\sigma^{0.075} \tag{2.49}$$

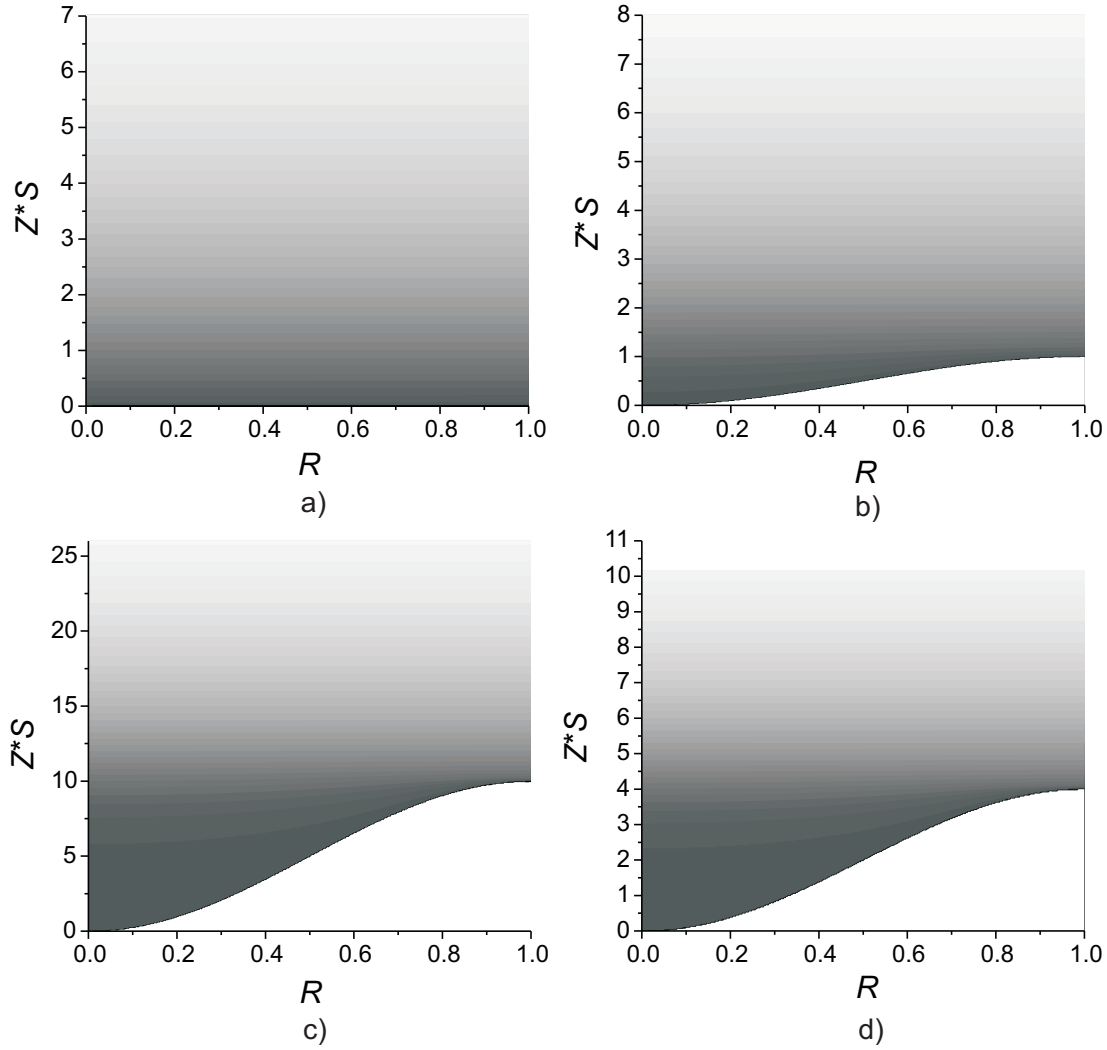

Figure 2.9: Concentration profiles taken at θ = -2, σ = 0.1: (a) scale factor S = 0.01; (b) S = 1; (c) S = 4; (d) S = 10.

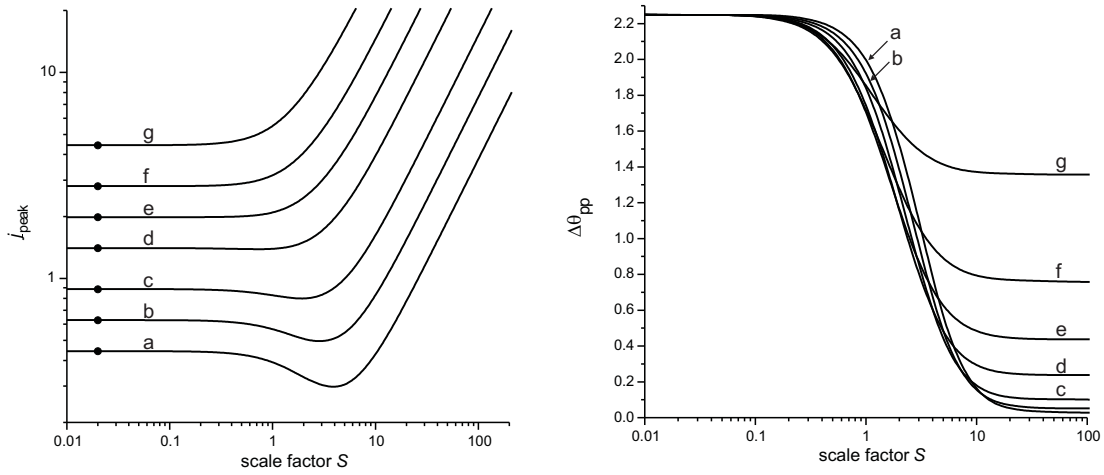

Figure 2.10: Peak current (a) and peak to peak separation (b) at different scan rates and scale factor S values, Nernst equilibrium at the electrode surface: (a) $\sigma = 0.1$, (b) $\sigma = 0.2$, (c) $\sigma = 0.4$, (d) $\sigma = 1$, (e) $\sigma = 2$, (f) $\sigma = 4$, (g) $\sigma = 10$. Dots at (a) show the planar diffusion peak current calculated with DigiSim.

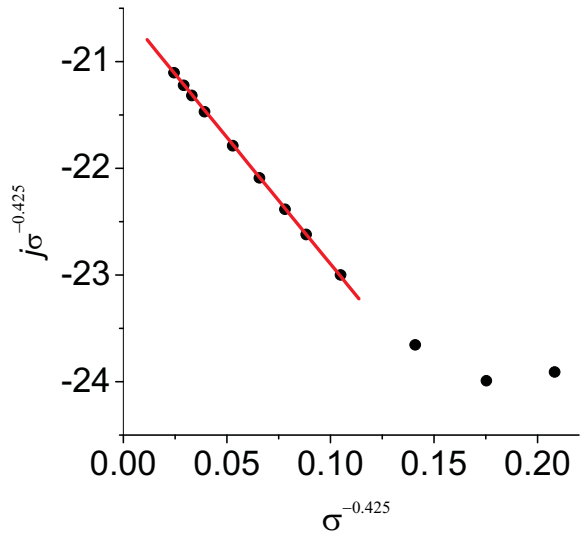

Figure 2.11: Peak current values at a high value of scale factor $S = 20$.

2.5.2 Scratched (V-shaped) Electrodes

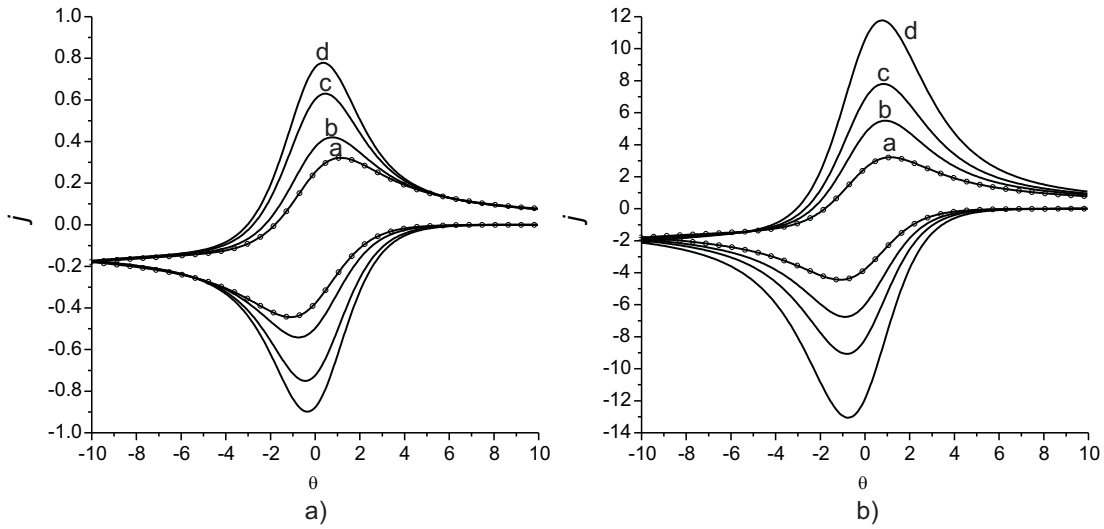

Figure 2.12: Cyclic voltammograms at different values of scale factor S: (a) σ = 0.1, S has the following values (a) 0.1, (b) 4, (c) 10, (d) 14; (b) σ = 10, S has the following values (a) 0.1, (b) 1.6, (c) 2.5, (d) 4. The open dots show the planar diffusion cyclic voltammograms calculated with DigiSim.

Figure 2.12 shows voltammograms calculated at different values of scale factor S. Peak current and peak potential values versus scale factor S at various scan rates are presented in Figure 2.13. At low values of scale factor S calculated voltammograms are similar to that on a flat macroelectrode. Noticeable deviations of voltammograms calculated on a V-shaped electrode form that on a rough electrodes are observed at $S > 0.4$. Similar to rough electrodes at high scan rates increase of scale factor S causes gradual increase of peak current and decrease of peak to peak separation. However at V-shaped electrodes at slow scan rates contrary to rough electrodes no minimum is observed at curves j_{peak}-S, such a difference can possibly be explained by various symmetry of rough and V-shaped electrodes and consequently various diffusional regimes of mass-transport towards electrode surface.

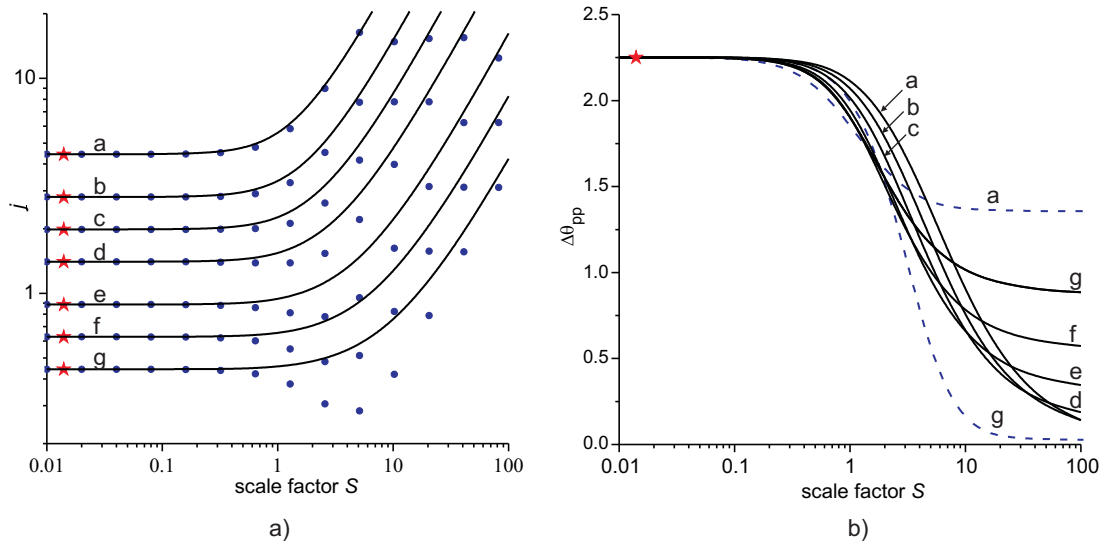

Figure 2.13: Peak current (a) and peak to peak separation (b) at different scan rates and scale factor S values, Nernst equilibrium at the electrode surface: (a) $\sigma = 0.1$, (b) $\sigma = 0.2$, (c) $\sigma = 0.4$, (d) $\sigma = 1$, (e) $\sigma = 2$, (f) $\sigma = 4$, (g) $\sigma = 10$. Solid lines and blue dashed lines (dots) corresponds to V-shaped and rough electrodes accordingly. Stars shows values calculated with DigiSim for the case of flat macroelectode.

2.5.3 Butler-Volmer Kinetics: Theoretical Considerations

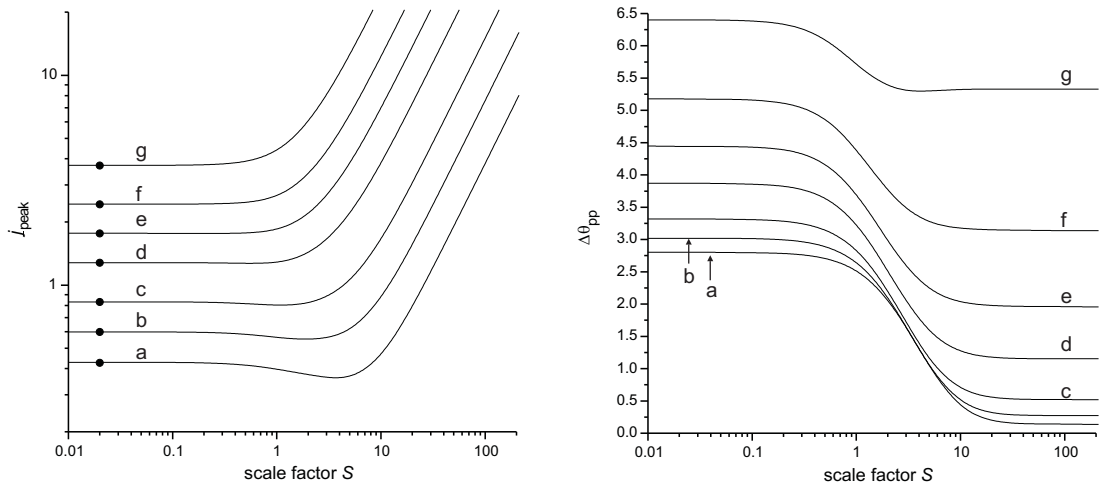

Figure 2.14: Peak current (a) and peak-to-peak separation (b) at different scan rates and scale factor S values, $\lambda = 1$: (a) $\sigma = 0.1$, (b) $\sigma = 0.2$, (c) $\sigma = 0.4$, (d) $\sigma = 1$, (e) $\sigma = 2$, (f) $\sigma = 4$, (g) $\sigma = 10.8$. (b). Dots at a show the planar diffusion peak current calculated with DigiSim.

The rate of the electron transfer in the Butler-Volmer model (eq 2.6) is characterized by the dimensionless parameter λ defined in Table 2.1. Figures 2.14a and 2.15a show the peak current dependence

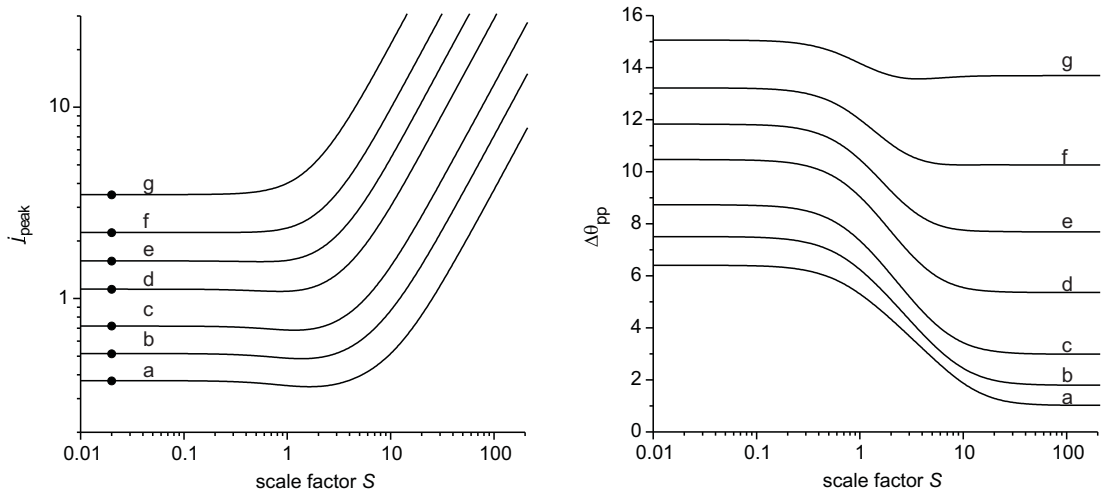

Figure 2.15: Peak current (a) and peak-to-peak separation (b) at different scan rates and scale factor S values, $\lambda = 0.1$: (a) $\sigma = 0.1$, (b) $\sigma = 0.2$, (c) $\sigma = 0.4$, (d) $\sigma = 1$, (e) $\sigma = 2$, (f) $\sigma = 4$, (g) $\sigma = 10.8$. (b). Dots at a show the planar diffusion peak current calculated with DigiSim.

on the scale factor S and on the scan rate at $\lambda = 1$ and 0.1. The calculated peak current values at low values of scale factor S are in good agreement with those calculated with DigiSim in the planar diffusion limit for a flat electrode. A minimum is seen on the plots of peak current versus scale factor S. The minimum decreases when the rate of electron transfer decreases, since the current is limited by electron transfer kinetics but not by the rate of mass transport. Comparing Figure 2.8b with Figures 2.14a and 2.15a, it is seen that at high scan rates peak current increases proportionally to the surface area of the electrode. Figures 2.14b and 2.15b show the peak-to-peak separation dependence on the scale factor S and on the scan rate at $\sigma = 1$ and 0.1. The peak-to-peak separation decreases as the scale factor S increase for all values of electron transfer rate (Figures 2.10b, 2.14b, and 2.14b), since diffusion is relatively slow to bring electrochemical species from bulk solution at high values of scale factor S.

2.5.4 Domain Size Influence

Above we have calculated the dimensionless current $j(\sigma, S, \lambda)$ from a single domain. The dimensional peak current from a rough macroelectrode of N_p domains can be calculated from Equation 2.50:

$$I = nfDA_0 r_0 j_p(\sigma, S, \lambda) N_p = nfDA_0 r_0 j_p(\frac{nFr_0^2 v}{RTD}, S, \frac{r_e}{r_0})(\frac{r_e}{r_0})^2 \tag{2.50}$$

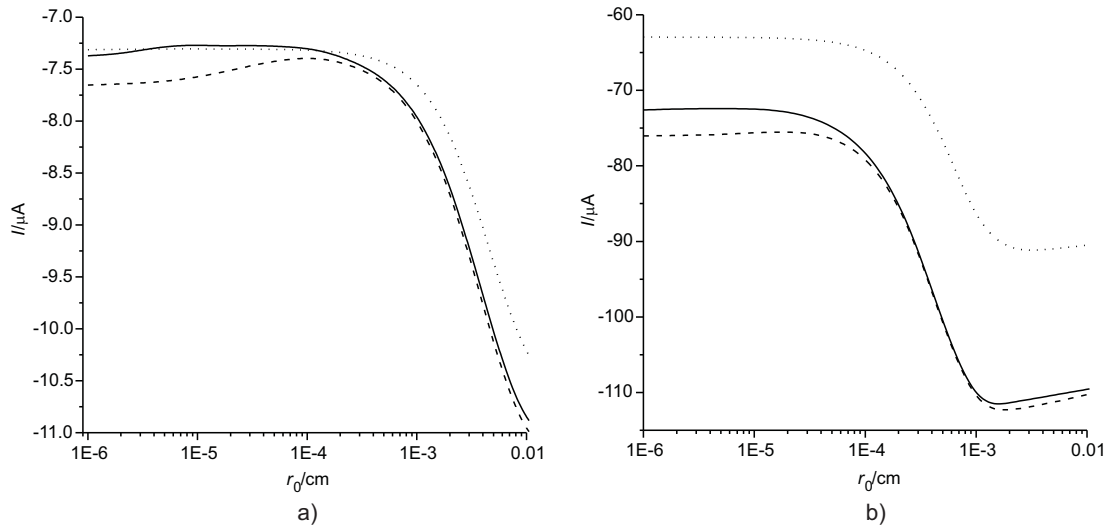

Figure 2.16: Influence of the size of diffusional domain on the peak current. The following parameters were used in simulation: $D = 1 \times 10^{-5}$ cm^2/s, $\alpha = 0.5$, scan rate 0.1 V/s (a) and scan rate 10 V/s (b). Solid and dash, dot lines represent infinitely fast and k_0= 1 cm$^-$1, k_0 = 0.01 cm^{-1}.

At low values of the scale factor S the current from a rough electrode is approximately equal to the current from a flat electrode (Figures 2.10, 2.14, and 2.15) and eq 2.50 reduces to the Randles-Sevcik equation for the peak current value at macroelectrode. The dependence of the peak current on the domain size is presented in parts a and b of Figure 2.16. The peak current is almost independent of electrode domain size if the diffusion length is many times less than the domain size or if it is many times greater than the domain size. Both cases are shown in Figure 2.16b. In Figure 2.16a the flat region is absent at high values of r_0, since the domain size is not big enough to be diffusionally independent.

2.5.5 AFM Surface Characterization

Tapping mode AFM images of a flat GC electrode and roughened GC electrode are presented in Figure 2.17. To characterize the surface roughness and to estimate diffusional domain sizes a Fourier power spectrum (Figure 2.18) was calculated with the AFM microscope software package. The power is related to the roughness amplitude squared. The roughness amplitude for the used shape of diffusion domain shape used in the above theory is given by equation 2.51:

$$R_a = \frac{1}{\pi r_0^2}[2\pi \int_0^{r_0} (Sr_0 \cos^2(\frac{\pi r}{2r_0}) - R_a)^2 dr]^{1/2} = \frac{Sr_0}{\rho} \tag{2.51}$$

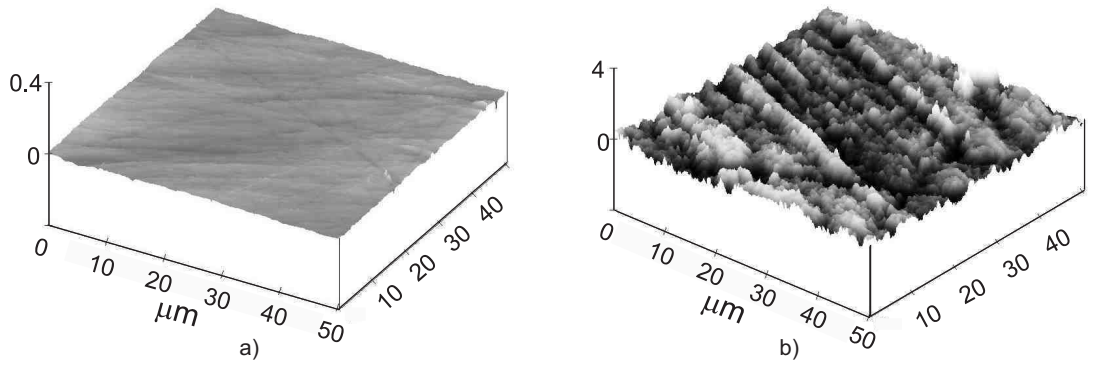

Figure 2.17: Tapping mode AFM image of flat (a) and rough (b) GC electrode.

where, ρ=3.45 cm^{-1} and R_a is the average height of an electrode domain, which is given by expression 2.52

$$R_a = \frac{1}{\pi r_0^2} 2\pi \int_0^{r_0} S r_0 \cos^2 \frac{\pi r}{2 r_0} dr = 2 S r_0 (\frac{1}{4} - \frac{1}{\pi^2}) \tag{2.52}$$

The scale factor S can be calculated from these data employing the formula 2.53:

$$S = \frac{\rho \sqrt{power}}{\lambda} \tag{2.53}$$

where, λ is the wavelength in the power spectrum. The value of the scale factor S versus domain size is presented in Figure 16b. The highest value of scale factor S = 0.23 is reached at a domain size 7 μm. This is the highest scale factor value obtained with a rough glassy carbon electrode.

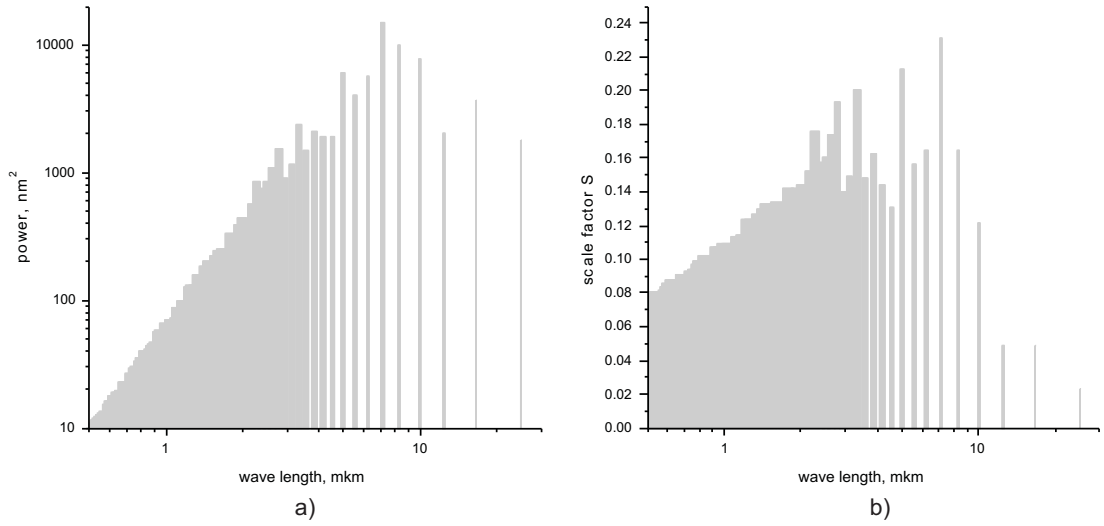

Figure 2.18: (a) Power spectrum and (b) scale factor S of rough electrode versus diffusional domain size.

2.5.6 Cyclic Voltammetry Experiments at Flat and Rough Glassy Carbon Electrodes

To characterize voltammetrically the flat and rough glassy carbon electrodes, two model experimental systems were used. The first was 3.95 mM TMPD/0.1 TBAP in acetonitrile at 2 ^{0}C and the second was 4.03 mM $Ru(NH_3)_6Cl_3$/0.1 M KCl in water at 25 ^{0}C.

Cyclic voltammograms of $Ru(NH_3)_6Cl_3$/0.1 in 0.1 M KCl are presented in Figure 2.2018. Cyclic voltammograms obtained at flat GC electrodes were fitted with DigiSim (Figure 2.19) and the following kinetic parameters were extracted: $D = 8.1 \times 10^{-6}$ cm^2 s^{-1}, $k_0 = 0.010$ cm s^{-1}, and $\alpha = 0.51$. These values are in good agreement with literature data.[59–62] Note the rate constant of electron transfer for the redox couple $Ru(NH_3)_6^{3+/2+}$ depends on the surface coverage of the glassy carbon with oxides. Therefore the reported values vary over a range of values according to electrode pretreatments.[63,64] The dimensionless parameters corresponding to the experimental data are the following: $\Lambda = 0.86$, $\sigma = 2.35\times$ (scan rate V s^{-1}). Figure 2.14 shows that at a scale factor of $S = 0.23$ the cyclic voltammograms of the flat and rough electrodes should be identical. These theoretical predictions are in a good agreement with the experimental data presented in Figure 2.19. Over a broad range of scan rates from 0.1 V s^{-1} to 10 V s^{-1} cyclic voltammograms of the redox couple $Ru(NH_3)_6^{3+}$ are similar on the flat and roughened GC electrodes.

Rough and flat GC electrodes were also characterized with 3.95 mM TMPD/0.1 M TBAP in

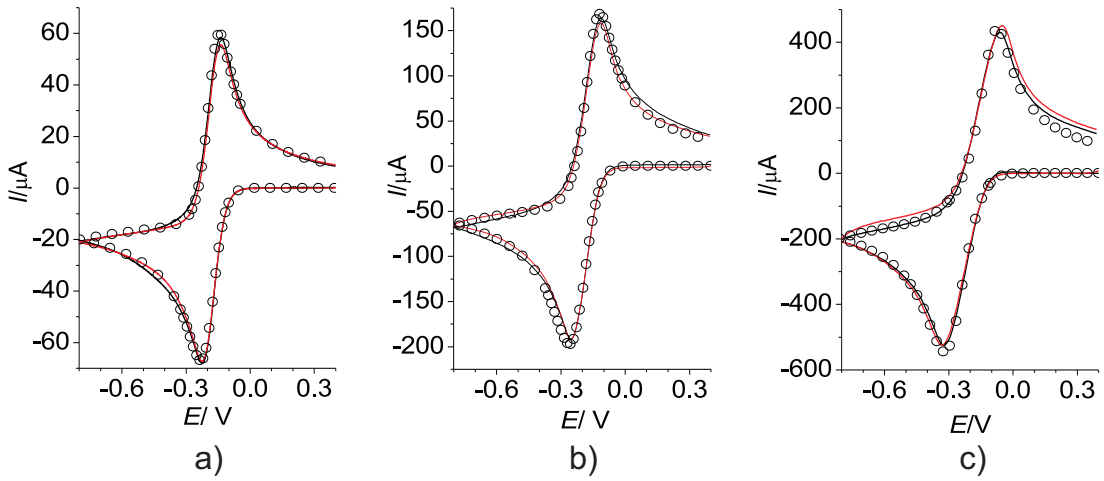

Figure 2.19: Cyclic voltammograms obtained at flat (black line) and rough (red line) GC electrodes in 4.2 mM $Ru(NH_3)_6Cl_3$/0.1 M KCl, background current is subtracted. Circles represent the planar diffusion cyclic voltammograms simulated with DigiSim. Scan rate: (a) 0.1, (b) 1, and (c) 10 V/s.

acetonitrile at 2^0C. Results of the cyclic voltammetry experiments are presented in Figure 2.20a,b. It is clear that cyclic voltammograms and peak current values are identical for rough and flat GC electrodes. Cyclic voltammograms obtained at the flat GC electrode were fitted with DigiSim (Figure 2.20a), and the following kinetic parameters were extracted: $D = 1.75 \times 10^{-5}$ cm^2 s-1, k_0 = 0.0083 cm/s, and α = 0.47. This diffusion coefficient is in perfect agreement with that calculated from the data in previous studies of the TPMD redox couple.[65] The rate constant for electron transfer is similar to that reported in previous studies,[66] but we note the high sensitivity of electron transfer rates to the state of glassy carbon electrode surfaces and the difference between various supporting electrolytes.

Consequently, significant deliberate polishing and scratching of the glassy carbon electrode does not change the surface morphology sufficiently to give observable effects in cyclic voltammetry experiments.

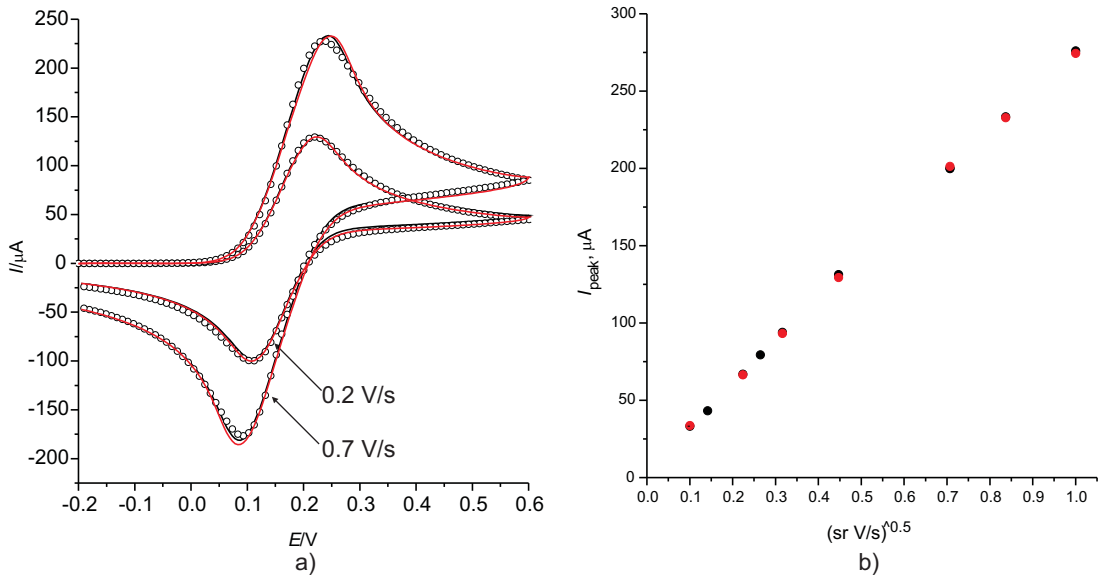

Figure 2.20: (a) Cyclic volatmmograms obtained at a flat (black line) and a rough (red line) GC electrode in 3.95 mM TMPD/0.1 M TBAP scan rate 0.2 and 0.7 V/s, background current is subtracted. Circles represent the planar diffusion simulation results with DigiSim (b) peak current versus (scan rate V/s)0.5; black dots, flat electrode; red, rough electrode.

2.6 Cyclic Voltammetry: Conclusions

Electrode roughness only has a significant effect on the shape of cyclic voltammograms and peak currents at extremely high values of electrode roughness. The reversibility of the electron transfer reaction can influence the sensitivity of the peak current to electrode roughness. Electrode roughness has the biggest influence on cyclic voltammograms under electrochemically reversible conditions where the kinetics are fully controlled by mass transport.

The independence of the electrode roughness in relation to the peak current was verified experimentally and the data obtained are in perfect agreement with the theoretical predictions. The most rough GC electrode obtained by scratching had a scale factor of $S = 0.23$. Cyclic voltammograms of redox couples $Ru(NH_3)_6^{3+}$ and TMPD obtained on such rough electrodes were similar to those obtained on flat electrodes.

We conclude that deliberate surface roughness produced by significant polishing or scratching is not sufficient to be distinguished in cyclic voltammetry experiments conducted under normal conditions.

2.7 Stripping Voltammetry

Stripping voltammetry is widely used in electroanalysis and often offers high sensitivity.[57,67,68] It is a two-step method. The first step is preconcentration which is achieved by the electro-deposition. The second step is the electrochemical dissolution of the deposited substance by a cathodic sweep (cathodic stripping voltammetry, CSV) or anodic sweep (anodic stripping voltammetry, ASV). The charge passed in this second step reflects the concentration of the substance in the solution. The preconcentration leads to a low detection limit compared to conventional direct electroanalysis. Concentrations as low 10^{-10}M and 10^{-11}M can be achieved in favorable circumstances.[69–71]

Classical ASV was conducted at mercury electrodes where the reduction of the metal ion leads to the formation of an amalgam. The theory of the ASV has been developed both for mercury film electrodes (MFEs)[72–76] and for mercury drop electrodes (MDEs).[77–79] More recently however the need for environmentally friendly measurements has resulted in the use of the solid electrodes such as boron-doped diamond,[80–87] edge plane pyrolytic graphite electrodes[88,89] and screen-printed electrodes.[90,91] The theory of stripping voltammetry on electrodes other than mercury has been considered for both paste electrodes[76,92–98] and for solid electrodes modified with particles.[52,99] Those studies use highly simplified assumptions such as neglecting mass transport effects.[94–96] Where mass transport has been considered, one dimensional models have been employed.[92,93,97] Only recently have more sophisticated approaches been examined.[12,73–75,87,100,101] Nevertheless the theory of stripping voltammetry on non-flat electrodes has never been developed, despite multiple experimental evidence showing measurable roughness effect on many electrodes.[102] Accordingly in this paper we present a study of the influence of roughness on stripping voltammetry.

2.8 Stripping Voltammetry: Results and discussions

2.8.1 Stripping voltammetry at flat macroelectrodes

Stripping voltammograms calculated for the case of flat macroelectrode are presented in Figure 2.21. Model C gives voltammograms with very sharp peaks, and the current grows exponentially over most of the wave until all material is stripped of from the surface 2.22. Models A and B give voltammograms with a broader shape of peak, however model B demonstrates exponential growth of the current at the beginning of the wave (Figure 2.22). The scan rate does not qualitatively affect the shape of

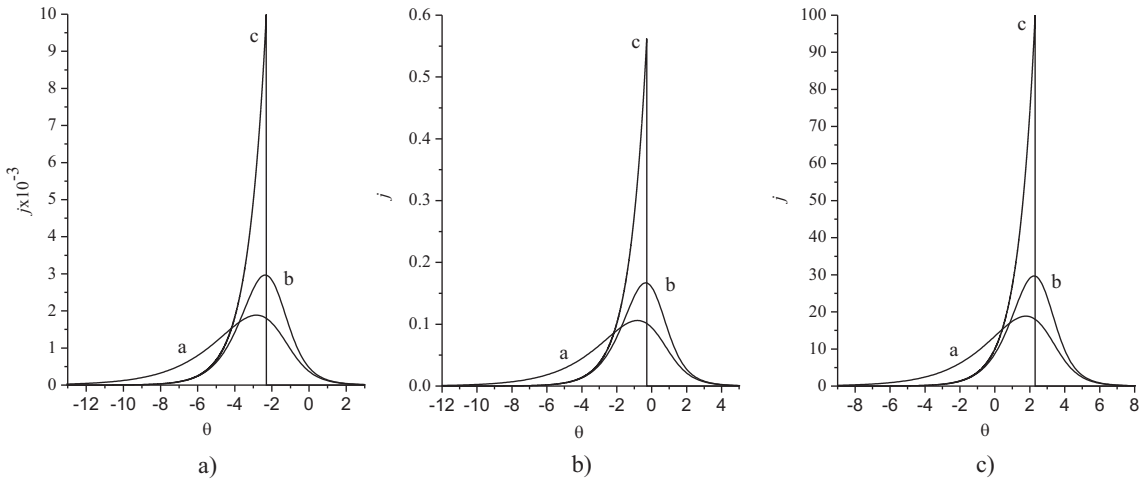

Figure 2.21: Stripping voltammograms simulated for $\beta = 1$. $\sigma = 0.01$ a, $\sigma = 1$ b, $\sigma = 100$ c. Voltammograms a, b and c are simulated with models A, B and C respectively

the voltammograms, but causes shifts of the voltammograms along the abscissa axis. Analysis of the voltammograms in the range of scan rate (σ) from 0.01 to 100, and surface coverage parameter β from 0.01 to 100 shows that the peak current is given by the equations:

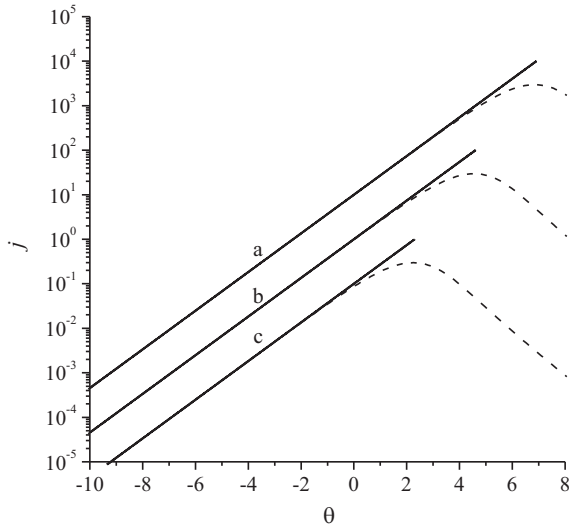

Figure 2.22: Stripping voltammograms in logarithmic coordinates simulated for $\beta = 0.01$. $\sigma = 100$ a, $\sigma = 1$ b, $\sigma = 0.01$ c. Solid and dashed lines represent voltammograms simulated with model C and B respectively.

$$j_{\text{peak}} = 0.1886\sigma/\beta \tag{2.54}$$

$$j_{\text{peak}} = 0.2969\sigma/\beta \tag{2.55}$$

$$j_{\text{peak}} = \sigma/\beta \tag{2.56}$$

for the models A, B and C respectively. The peak potential is given by the equations:

$$\theta_{\text{peak}} = 0.5\ln\sigma - \ln\beta - 0.529 \tag{2.57}$$

$$\theta_{\text{peak}} = 0.5\ln\sigma - \ln\beta - 0.0559 \tag{2.58}$$

$$\theta_{\text{peak}} = 0.5\ln\sigma - \ln\beta \tag{2.59}$$

These develop the approximate equations of Brainina whose works approximates diffusion as fully planar and an uses empirical relationship between activity of the solid phase and the charge passed in stripping.[93,103]

2.8.2 Model A

Stripping voltammograms calculated for different values of the scale factor S are presented in Figure 2.23. Increase of the electrode roughness (curves a, b, c, d, e and f) causes an increase of the peak current and a shift of the peak potential to more positive values. The peak becomes broader as well on an increase of electrode roughness. An increase of the scan rate causes a shift of the stripping voltammogram to more positive potential values, but their shape does not change significantly. The peak current changes proportionally to the scan rate. Such behavior is in agreement with that predicted by the one-dimensional flat electrode model (equation 2.54 and 2.57). At low (Figure 2.23a and d) and moderate (Figure 2.23b and e) values of the scan rate σ, deviation between voltammograms calculated for the rough and scratched electrodes is observed, but the difference (Figure 2.23c and f) almost vanishes at high scan rates (Figure 2.23c and f). Decrease of the surface coverage parameter β does not affect the shape of the voltammograms, but causes a shift of the voltammograms to more negative values of the potential and decreases the peak current (compare Figure 2.23 a), b), c) and d), e), f)) which is again in agreement with flat electrode model. Figure 2.24 shows the concentration of the deposited (adsorbed) species at different points of the electrode versus potential. At low values of the scale factor $S = 0.01$ the electrode can be considered nearly flat and material must strip uniformly at all scan rates. An increase of the electrode roughness results in the observation that deposited(adsorbed) material no longer strips uniformly (Figure 2.24). Deposited material firstly strips

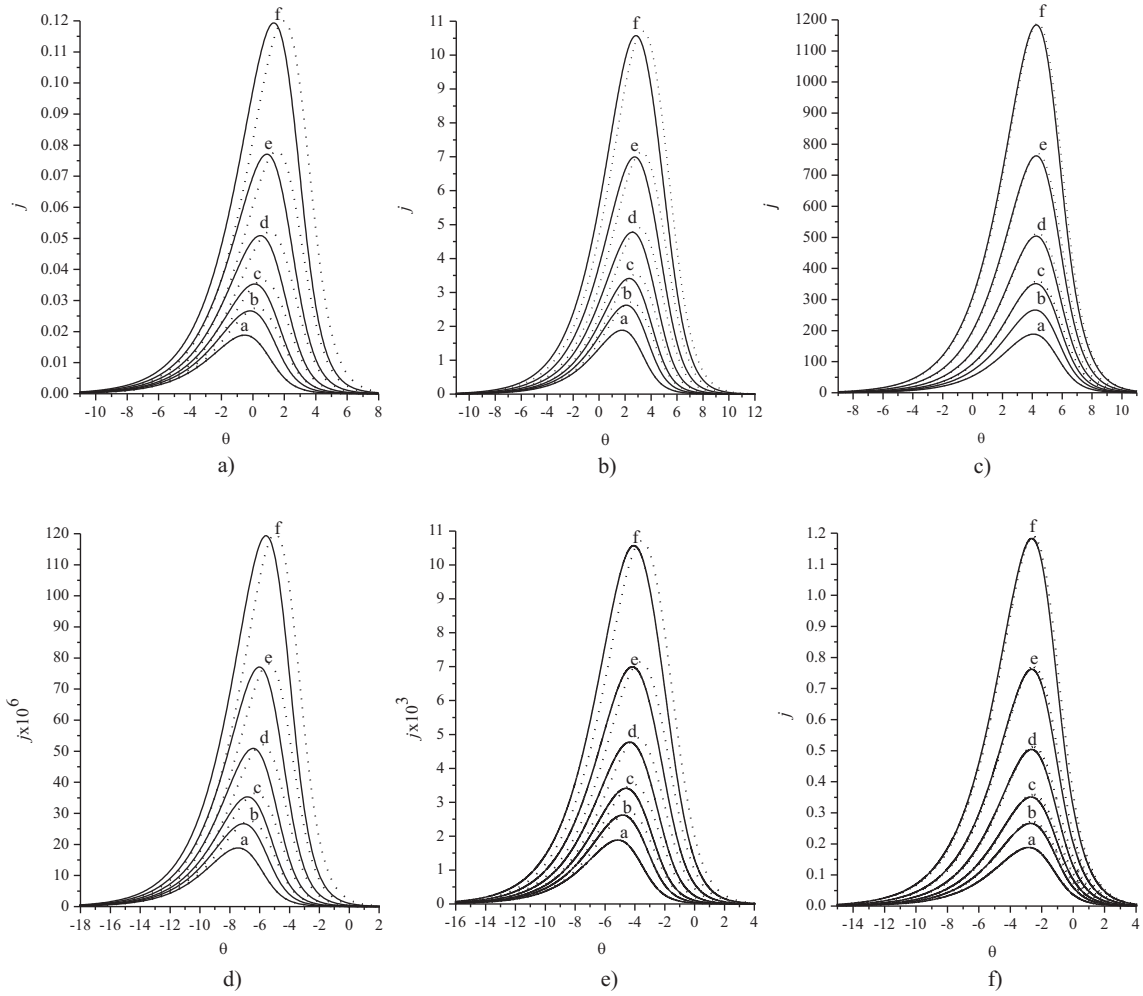

Figure 2.23: Stripping voltammograms simulated for model A, $\beta = 0.1$, $\sigma = 0.01$ (a), $\sigma = 1$ (b), $\sigma = 100$ (c) and $\beta = 100$, $\sigma = 0.01$ (d), $\sigma = 1$ (e), $\sigma = 100$ (f). Scale factor $S = 0.01$ a, $S = 1$ b, $S = 1.58$ c, $S = 2.51$ d, $S = 3.98$ e, $S = 6.3$ f. Solid line and dots represents voltammograms calculated for the model of the scratched and rough electrode respectively.

off from the top of the electrode ($R = 0$ and $X = 0$ at rough and scratched electrode, respectively) and last from the troughs between the peaks ($R = 1$ and $X = 1$ at rough and scratched electrodes, respectively). The effect is more pronounced at high and moderate scan rates (Figure 2.24 b), c) and d), e)) than at low scan rates (Figure 2.24 a) and d)). No significant difference between rough and scratched electrodes is observed. At some hydrodynamic electrodes with non-uniform surface accessibility the phenomenon of redeposition is observed .[104] However on electrodes with rough and scratched surfaces and model A of electron transfer no such redeposition was observed. Figure 2.25 shows the current density defined by the equation 2.34 at electrode surface versus potential. The current density at scratched and rough electrodes does not differ significantly. The current density is almost inde-

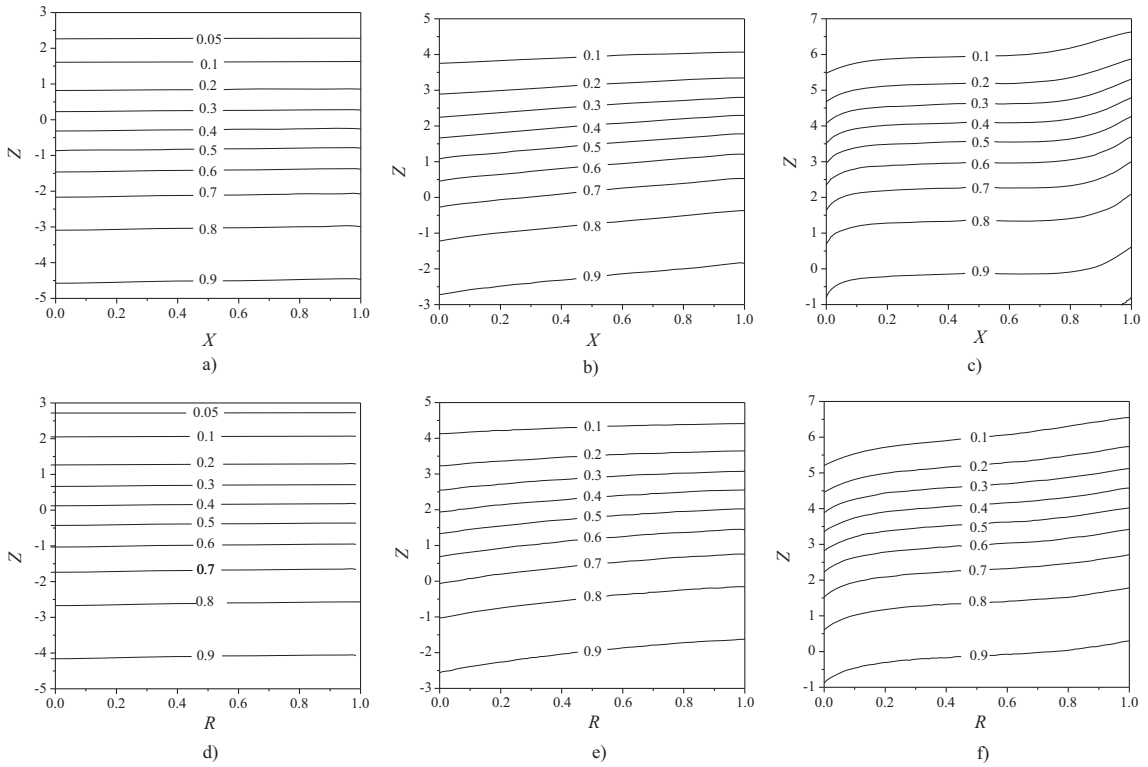

Figure 2.24: Concentration of the adsorbed (deposited) compound at electrode surface versus potential. Contour lines show points of equal concentration. $\beta = 0.1$, $S = 1$. Scratched electrode: (a) $\sigma = 0.01$, (b) $\sigma = 1$, (c) $\sigma = 100$. Rough electrode: (d) $\sigma = 0.01$, (e) $\sigma = 1$, (f) $\sigma = 100$

pendent on the coordinate at low scan rates, increase of scan rate cause inequality of current density at different points of the electrode. The current density at the top of the electrode is higher than at the bottom until significant amount of material strips off from the surface. At high scan rates current density is almost independent on the coordinate, except bottom and the top of the electrode. Again current density is higher at the top of the electrode than at the bottom. Figure 2.26 shows concentration profiles at the rough electrode for low and high scan rates. At high scan rates the length of the diffusional layer is less than the length scale of the electrode roughness and the concentration profiles follow the electrode shape (Figure 2.26 c and f). The length of diffusional layer is proportional to $\sqrt{\frac{1}{\sigma}}$. At slow scan rates the length of the diffusional layer is higher than the length scale of electrode surface curvature and diffusion is almost planar (Figure 2.26 a) and d)), wheres at high scan rate the the diffusional length is low and the concentration profile follows the electrode surface. No significant qualitative differences between the concentration profiles on rough and scratched electrodes was observed. Voltammograms can be characterized by the peak current and peak potential. The

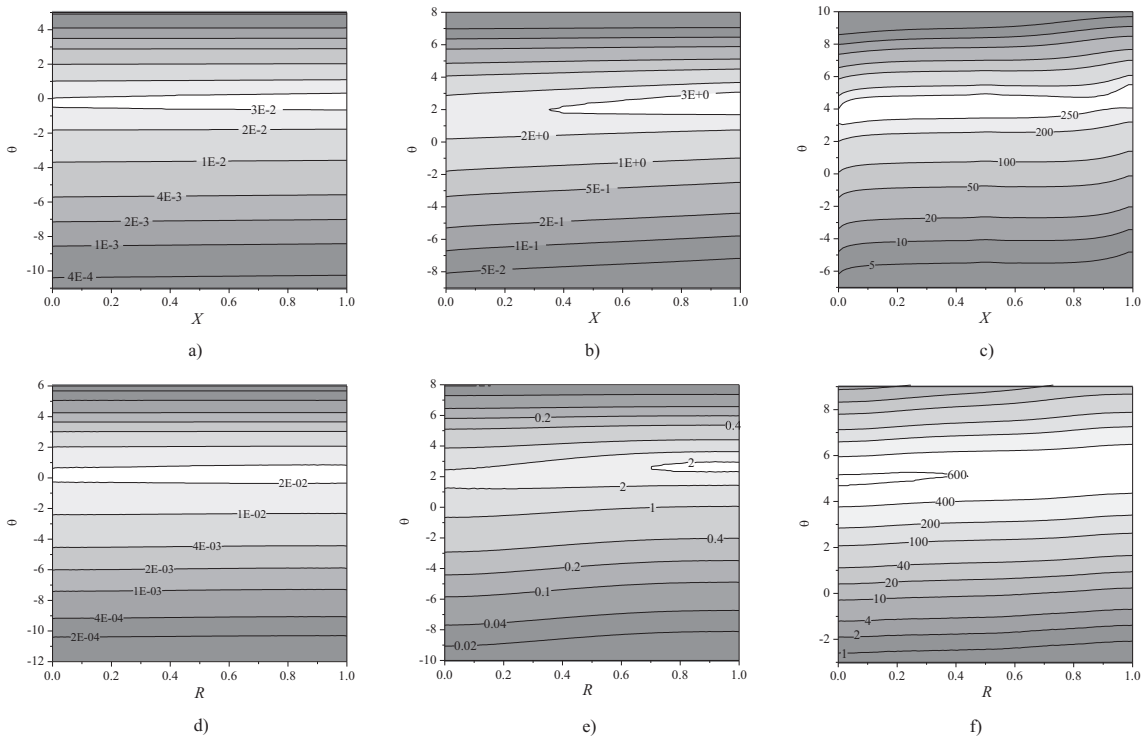

Figure 2.25: Current density at electrode surface versus potential. Contour lines show points of equal local flux. $\beta = 0.1$, $S = 1$. Scratched electrode: (a) $\sigma = 0.01$, (b) $\sigma = 1$, (c) $\sigma = 100$. Rough electrode: (d) $\sigma = 0.01$, (e) $\sigma = 1$, (f) $\sigma = 100$

variation of the dimensionless peak current versus scan rate σ and the scale factor S are presented in Figure 2.27. At low values of the electrode roughness calculated values of the peak current and the peak potential are in the good agreement with those predicted by flat electrode model (equations 2.54 and 2.57, respectively). The increase of the electrode roughness causes an increase of the peak current and a shift of peak potential to positive values. The shift of the peak potential is bigger at lower scan rates than at higher scan rates. The peak potential at rough electrodes is more sensitive to the scale factor S that on scratched electrodes. The peak current is almost independent of the model of the electrode surface. Figure 2.27 shows the dependence of the peak current and the peak potential at two different values of the surface coverage parameter β. The surface coverage parameter β does not change the shape of the peak current (potential) versus scale factor S plot, but shifts the whole curve in agreement with the flat electrode model. The influence of the surface coverage parameter β was studied in more detail. Figure 2.28 shows the influence of the surface coverage parameter β and scan rate σ on the peak current and peak potential. In figure 2.28 (a) the peak current at a scratched electrode divided by the value of the peak current at the flat electrode (equation 2.54) is plotted versus

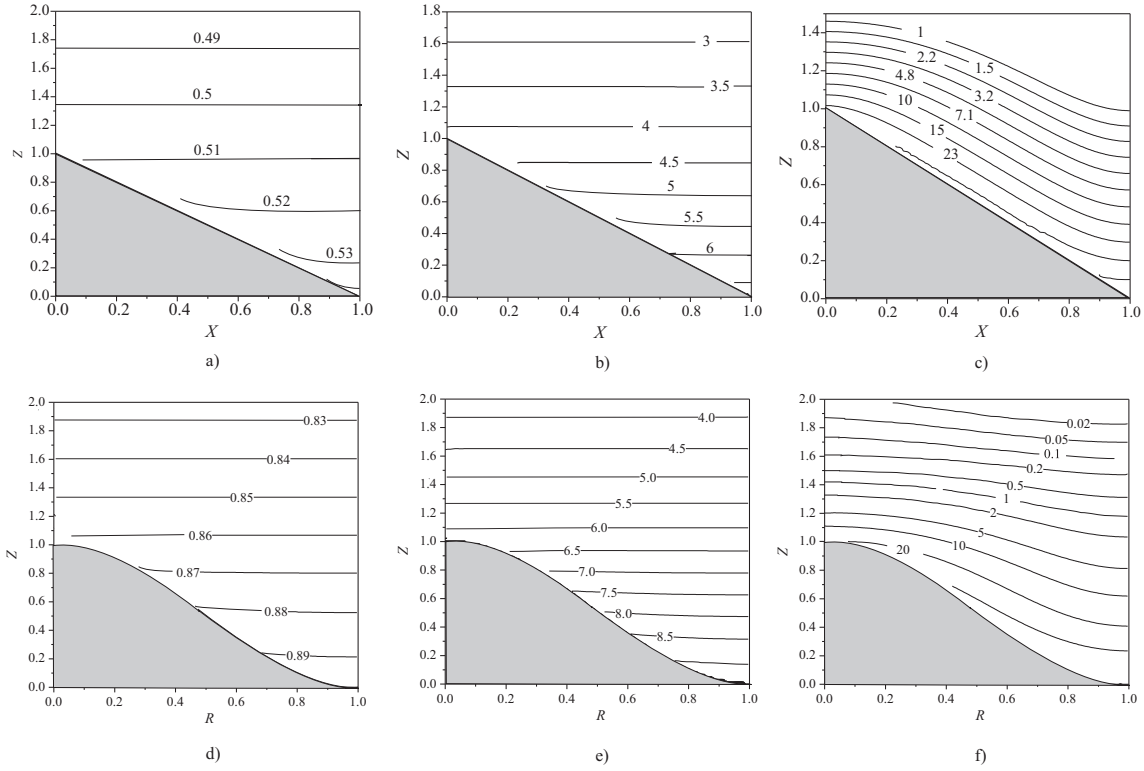

Figure 2.26: Concentration profiles of stripped compound straight after the peak potential. Contour lines show points of equal concentration. $\beta = 0.1, S = 1$. Scratched electrode: (a) $\sigma = 0.01$, (b) $\sigma = 1$, (c) $\sigma = 100$. Rough electrode: (d) $\sigma = 0.01$, (e) $\sigma = 1$, (f) $\sigma = 100$

σ and β. In Figure 2.28 (b) the peak potential at a scratched electrode minus the value of the peak potential at a flat electrode (equation 2.57) is plotted versus σ and β. On the full range of tested scan rates the normalised peak current and peak potential did not depend on the surface coverage parameter β. So the peak current and peak potential at scratched electrodes depend on the surface coverage parameter β according to equations 2.54 and 2.55, respectively. However, neither the peak current nor the peak potential depend linearly on the scan rate on rough electrodes; the higher the value of the scale factor S the higher the deviation from the flat electrode model.

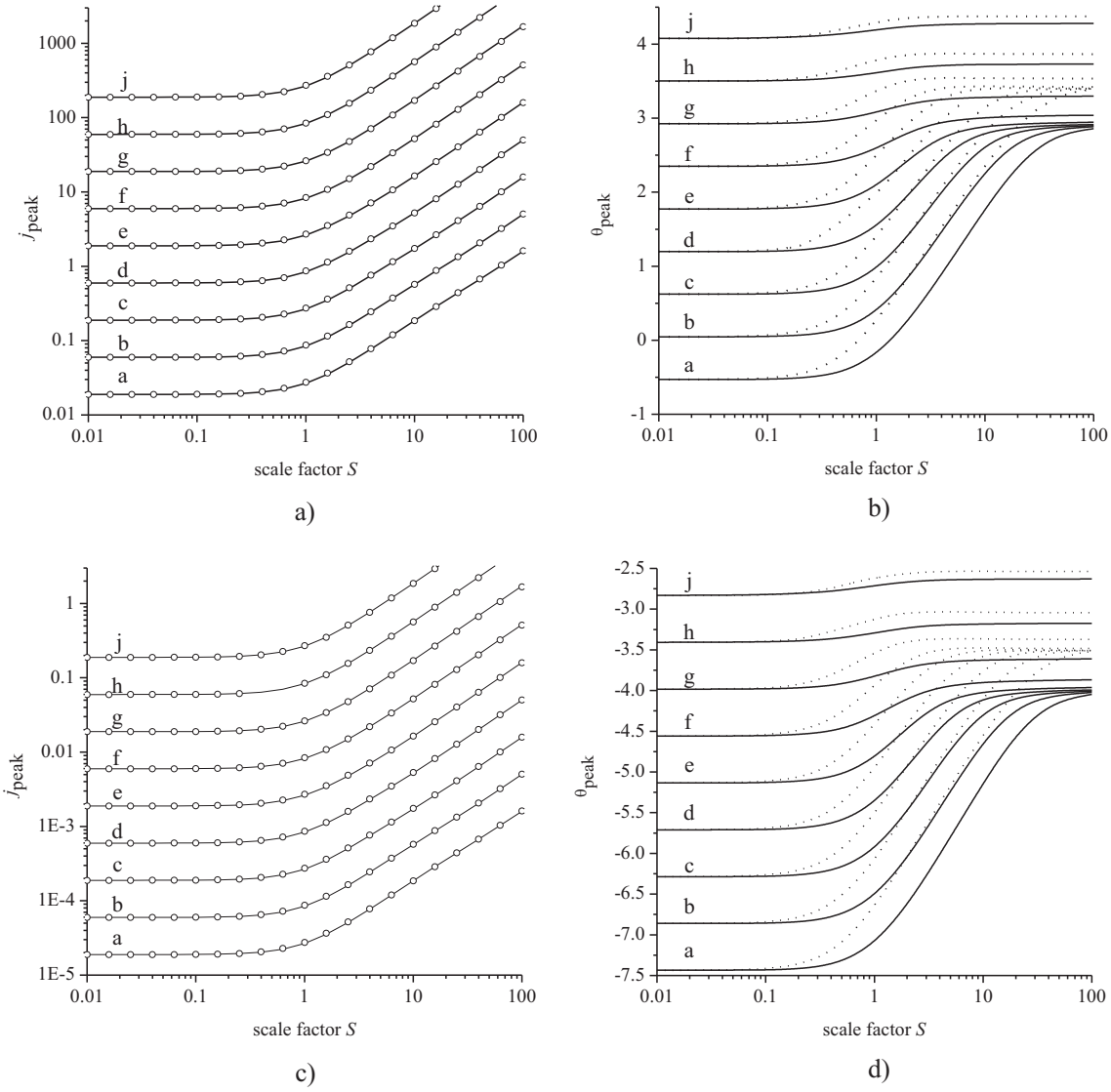

Figure 2.27: Peak current (a), (c) and peak potential (b), (d) versus scale factor S simulated for model A. (a), (b) - $\beta = 0.1$ and (c), (d) - $\beta = 100$. $\sigma = 10^{-2}$ a, $\sigma = 10^{-1.5}$ b, $\sigma = 10^{-1}$ c, $\sigma = 10^{-0.5}$ d, $\sigma = 10^{0}$ e, $\sigma = 10^{0.5}$ f, $\sigma = 10^{1}$ g, $\sigma = 10^{1.5}$ h, $\sigma = 10^{2}$ j. Solid line and dots represents values calculated for the model of the scratched and rough electrodes respectively.

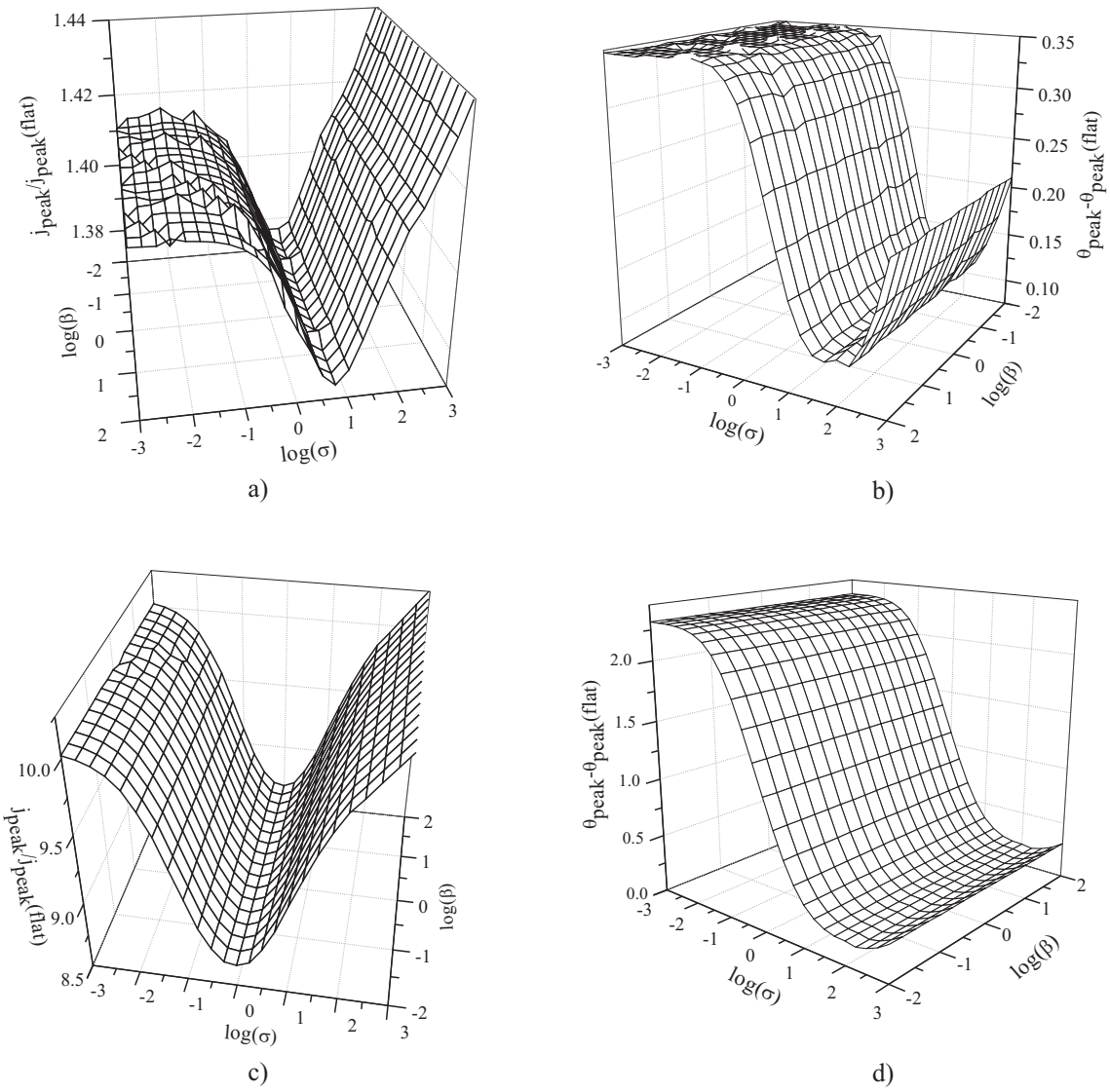

Figure 2.28: Normalised peak current and peak potential calculated on the scratched electrodes, model A. Normalised peak current a) $S = 1$ and c) $S = 10$ and normalized peak potential b) $S = 1$, d) $S = 10$

2.8.3 Model B

Stripping voltammograms calculated for different values of the scale factor S are presented in Figure 2.29. Similar to the stripping voltammograms calculated for the model A an increase of the electrode roughness (curves a, b, c, d and e) causes an increase of the peak current and a shift of the peak potential to more positive values. The difference between voltammograms calculated on the rough and scratched electrodes decreases when the scan rate increases (figure 2.29a, b and c). Figure 2.30 shows the concentration of the deposited (adsorbed) species at different points of the electrode versus potential. At low values of the scale factor S the electrode can be considered flat and material must strip uniformly at any scan rate. An increase of the electrode roughness results in the deposited(adsorbed) material not stripping uniformly (Figure 2.30). Deposited material firstly strips off from the top of the highest point of the electrode ($R = 0$ and $X = 0$ at rough and scratched electrode, respectively) and finally from the bottom of the peak ($R = 1$ and $X = 1$ at rough and scratched electrode, respectively). The effect is pronounced over the whole range of tested scan rates, not only at high scan rates as in case of the model A (compare Figure 2.24 a) and 2.30 a)). On scratched electrodes adsorbed species strip very non-uniformly. However the phenomena of redeposition was again not observed. Figure 2.31 shows the current density at electrode surface versus potential. The current density at scratched and rough electrodes does not differ significantly at all range of scan rates. At low and moderate scan rates current density is higher at the top of the electrode than at the bottom at

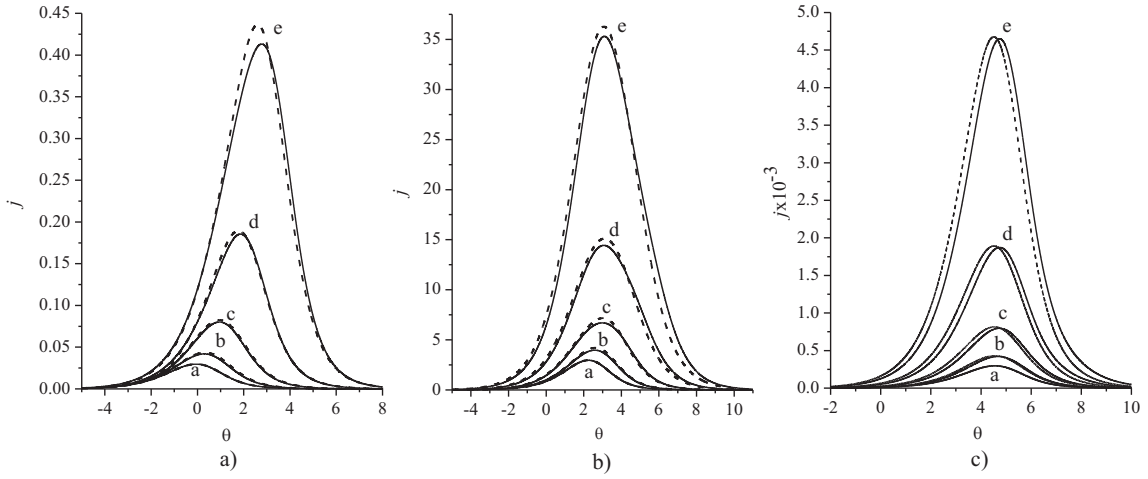

Figure 2.29: Stripping voltammograms simulated for model B $\sigma = 0.01$ a), $\sigma = 1$ b), $\sigma = 100$ c). $\beta = 0.1$; scale factor $S = 0.01$ a, $S = 1$ b, $S = 2.5$ c, $S = 6.3$ d, $S = 16$ e. Solid and dashed lines represent voltammograms calculated for scratched and rough electrodes respectively.

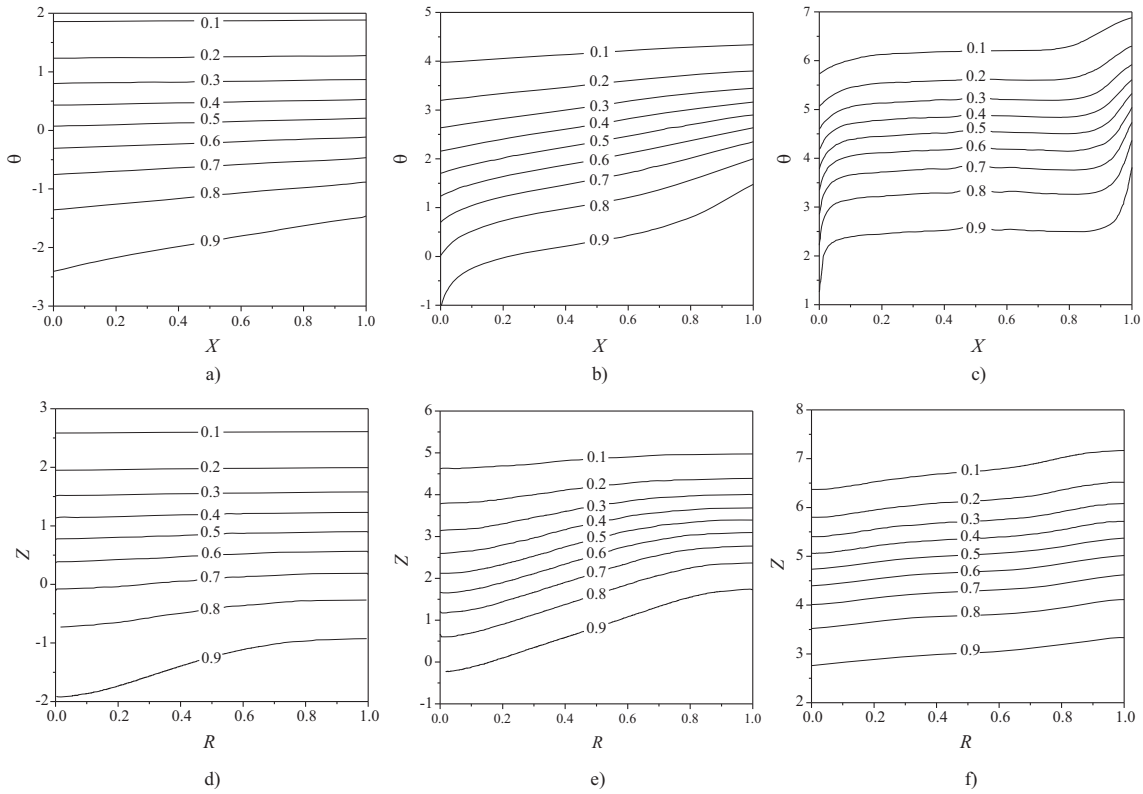

Figure 2.30: Concentration of the adsorbed (deposited) compound at electrode surface versus potential, model B, $\beta = 0.1$, $S = 1$. Contour lines show points of equal concentration. Scratched electrode: $\sigma = 0.01$ a), $\sigma = 1$ b), $\sigma = 100$ c) and rough electrode: $\sigma = 0.01$ d), $\sigma = 1$ e), $\sigma = 100$ f)

low overpotentials. At high scan rates flux density almost independent on the coordinate. Figure 2.32 shows the concentration profiles at a rough electrode for low and high scan rates. At high scan rates the length of the diffusional layer is less than the length scale of the electrode roughness and concentration profiles follow the electrode shape (Figure 2.32 c and f). At slow scan rates the length of the diffusional layer is higher than length scale of electrode roughness and diffusion is almost planar (Figure 2.32 a) and d)). The concentration profiles for the rough and scratched electrodes are qualitatively similar. The variation of the dimensionless peak current with scan rate σ and the scale factor S is presented in Figure 2.33. At low values of electrode roughness the calculated values of the peak current and the peak potential are in the good agreement with those predicted by the flat electrode model (equations 2.55 and 2.58 respectively). The increase of the electrode roughness causes an increase of the peak current and a shift of the peak potential to more positive values. The shift of the peak potential is bigger at lower scan rates than at higher scan rates. No significant difference was observed between rough and scratched electrodes. As with model A the peak current and the

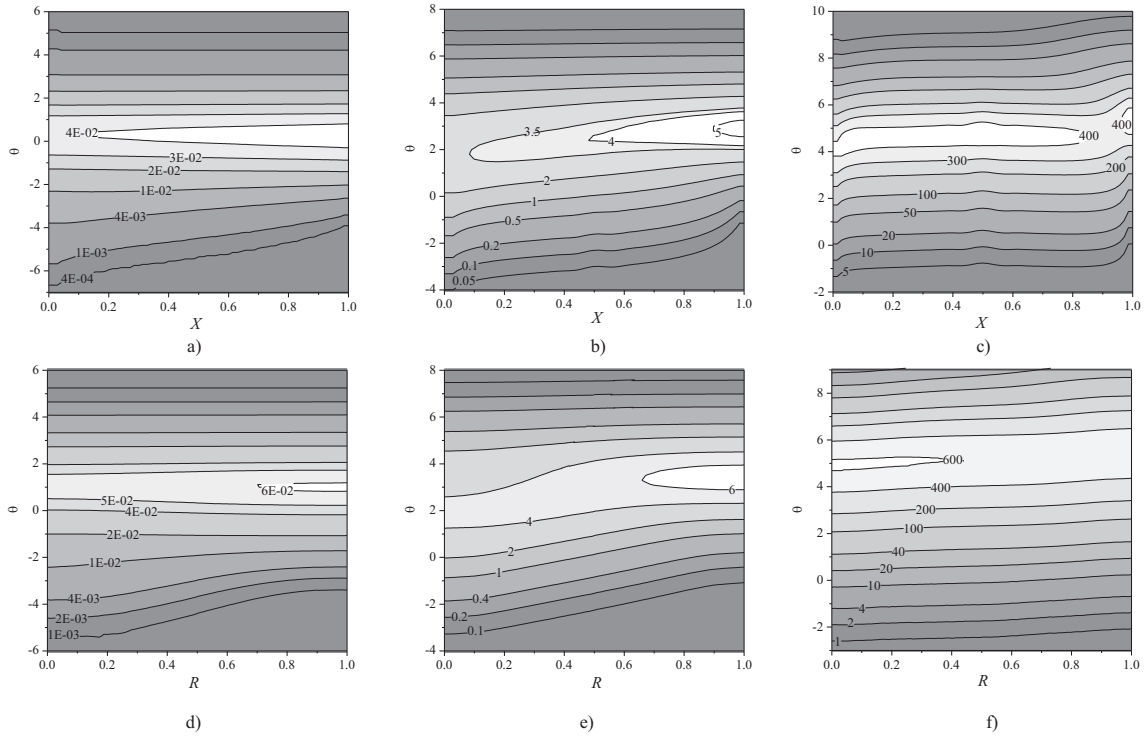

Figure 2.31: Current density at electrode surface versus potential. Contour lines show points of equal local flux. $\beta = 0.1$, $S = 1$. Scratched electrode: (a) $\sigma = 0.01$, (b) $\sigma = 1$, (c) $\sigma = 100$. Rough electrode: (d) $\sigma = 0.01$, (e) $\sigma = 1$, (f) $\sigma = 100$

peak potential depend on the surface coverage parameter in agreement with one-dimensional model (equation 2.55 and equation2.58). Figure 2.34 shows the variation of the normalised peak current and peak potential versus scan rate. The normalised peak potential and peak current depend non-linearly on the scan rate.

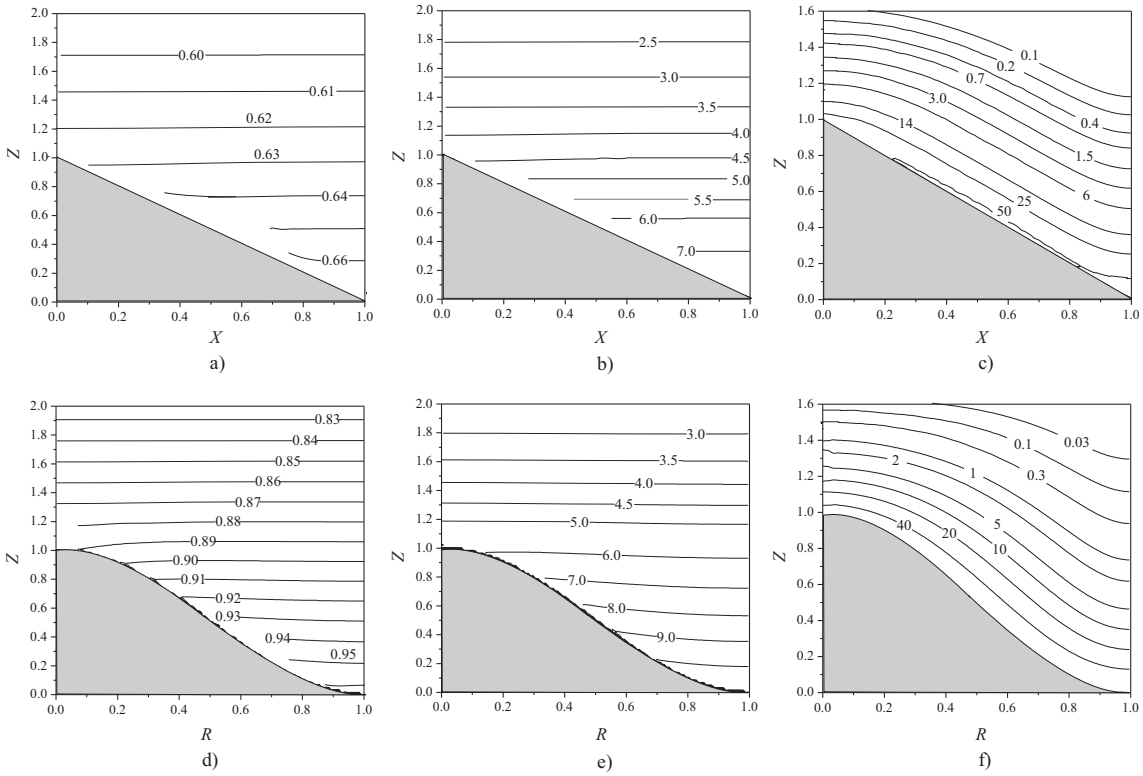

Figure 2.32: Concentration profiles of stripped compound straight after the peak potential, model B, $\beta = 0.1$, $S = 1$. Contour lines show points of equal concentration. Scratched electrode: $\sigma = 0.01$ a), $\sigma = 1$ b), σ=100 c) and rough electrode $\sigma = 0.01$ d), $\sigma = 1$ e), σ=100 f)

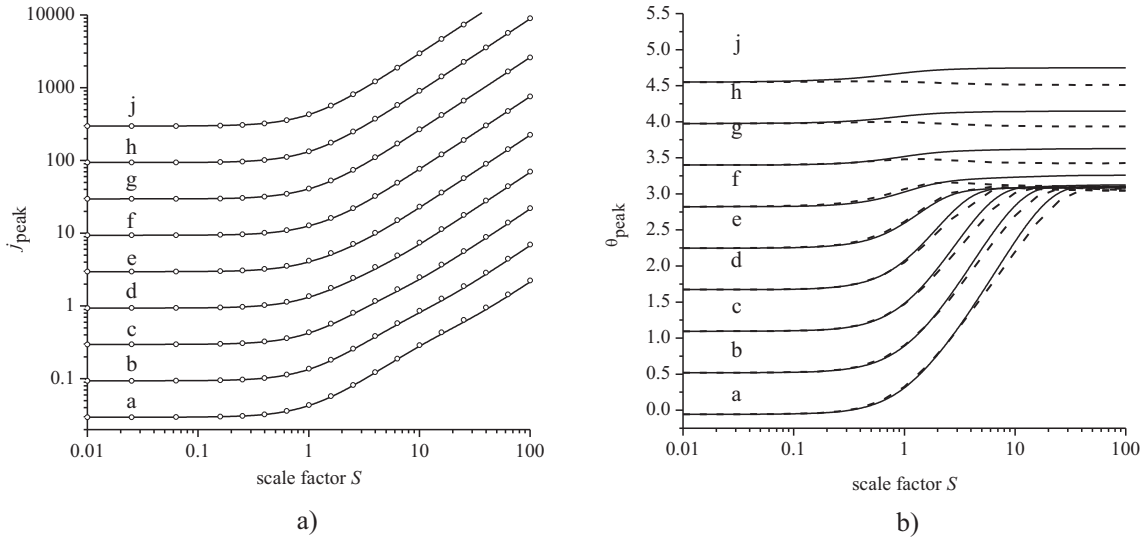

Figure 2.33: Peak current (a) and peak potential (b) versus scale factor S simulated for model B. $\beta = 0.1$; $\sigma = 10^{-2}$ a, $\sigma = 10^{-1.5}$ b, $\sigma = 10^{-1}$ c, $\sigma = 10^{-0.5}$ d, $\sigma = 10^{0}$ e, $\sigma = 10^{0.5}$ f, $\sigma = 10^{1}$ g, $\sigma = 10^{1.5}$ h, $\sigma = 10^{2}$ j. Solid line and dots represents values calculated for the model of the scratched and rough electrodes respectively.

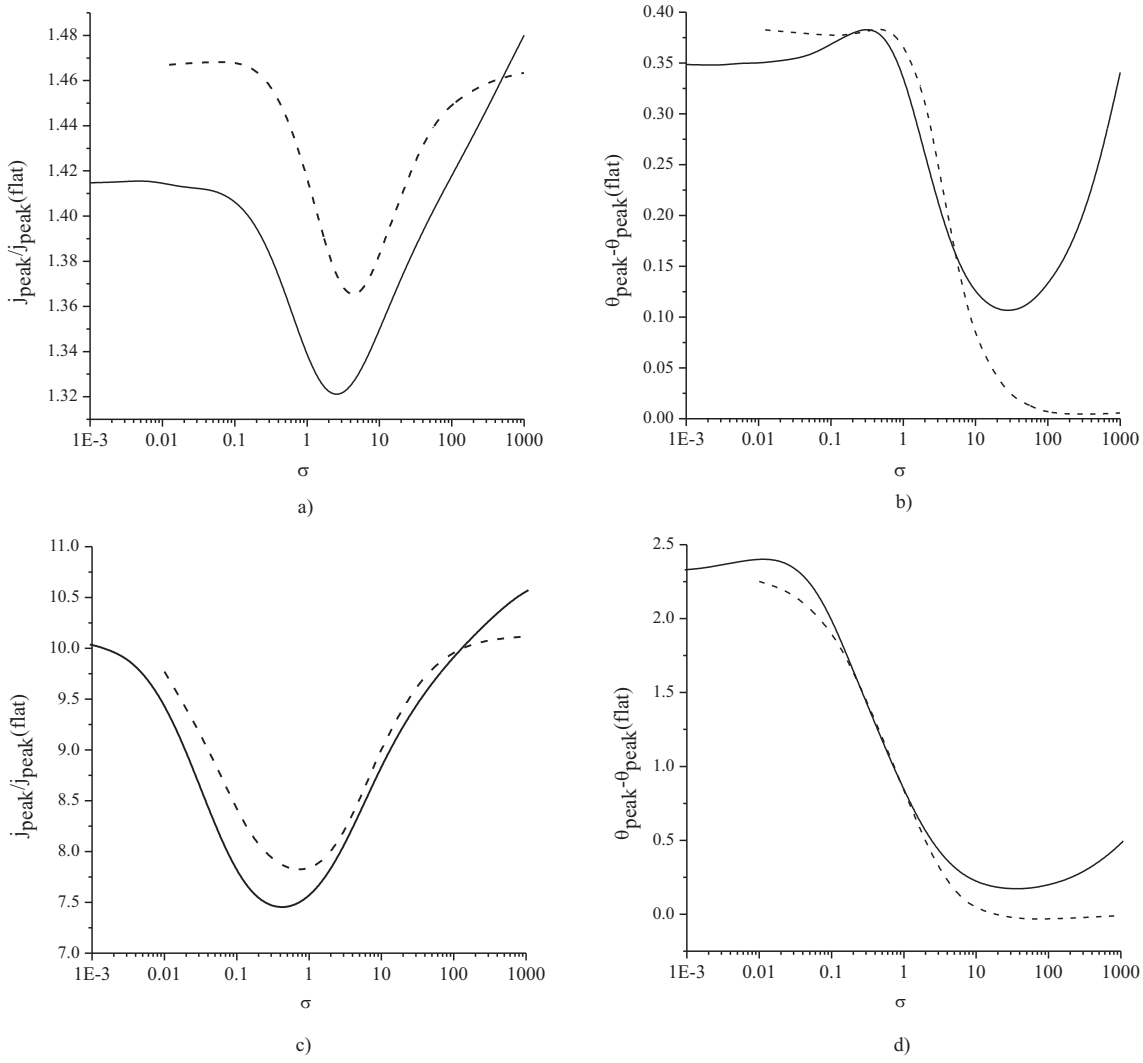

Figure 2.34: Normalised peak current and peak potential calculated on the rough electrode for model B. Normalised peak current a) $S = 1$ and c) $S = 10$ and normalized peak potential b) $S = 1$, d) $S = 10$

2.8.4 Model C

Stripping voltammograms calculated for different values of the scale factor S are presented in Figure 2.35. Voltammograms are very sharp at the flat electrode and are very sensitive to the surface roughness. At small values of the electrode roughness the peak current and the peak potential decrease (curves a, b, c and d at Figure 2.35) (a), (d) and (g)) and the voltammograms becomes less sharp. A further increase of the electrode roughness causes a dramatic change of the shape of voltammograms. The shape of the voltammograms depends not only on the scale factor S, but also on the scan rate σ. Figure 2.38 shows the concentration of the deposited (adsorbed) species at different points of the electrode versus potential. Similar to models A and B an increase of the electrode roughness causes the deposited(adsorbed) material not to strip uniformly (Figure 2.38). Deposited material firstly strips off from the top of the highest point of the electrode ($R = 0$ and $X = 0$ at rough and scratched electrode, respectively) and finally from the bottom of the peak ($R = 1$ and $X = 1$ at rough and scratched electrode, respectively). The effect is pronounced at all tested scan rates, $0.01 < \sigma < 100$. On scratched electrodes the adsorbed species strips very non-uniformly: the concentration of the adsorbed species becomes zero on the top of the electrode rapidly, but the concentration at the bottom of the electrode remains constant until very positive potentials reached. Similar to models A and B the phenomenon of redeposition was not observed. Figure 2.37 shows the current density at electrode surface versus potential. Both on rough and scratched electrodes flux density strongly depend on coordinate at all values of the scanrates and higher at the top of the electrode than at the bottom until significant amount of the adsorbed compound has been stripped of the surface. Figure 2.8.4 shows the concentration profiles at a rough electrode at low and high scan rates. Contrary to models A and B at low scan rates diffusion is not linear since the deposited layer strips very fast and non-uniformly. For the same reason the concentration at the bottom of the electrode is high. Similar to models A and B redeposition was not observed for model C. The variation of the dimensionless peak current and peak potential versus scan rate σ and the scale factor S are presented in Figure 2.36. At low values of electrode roughness the calculated values of peak current and peak potential are in the good agreement with those predicted by the flat electrode model (equations 2.56 and 2.59 respectively). Stripping voltammograms calculated for model C on the rough and scratched electrode are significantly different from each other and should be considered separately. First we consider voltammetry on the scratched electrode. The peak current and particular peak potential start to deviate from that

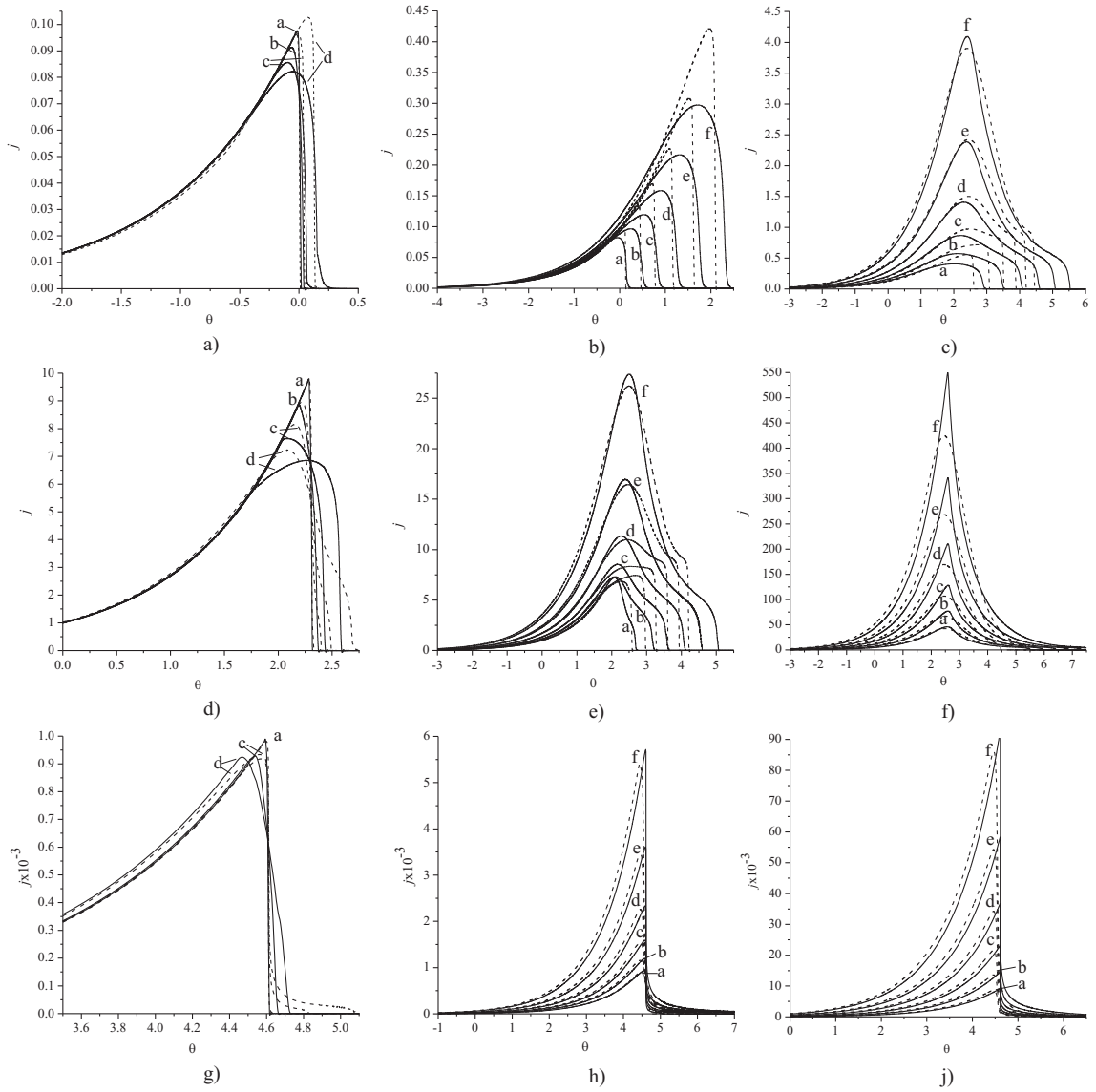

Figure 2.35: Stripping voltammograms simulated for model C $\sigma = 0.01$ (a),(b),(c); $\sigma = 1$ (d),(e),(f) $\sigma = 100$ (j),(h),(j). $\beta = 0.1$;. Scale factor $S = 0.01$ a, $S = 0.16$ b, $S = 0.40$ c, $S = 1$ d at Figures (a), (d), (g); $S = 1$ a, $S = 1.6$ b, $S = 2.5$ c, $S = 4.0$ d, $S = 6.3$ e, 15.8 f at figures (b), (e), (f); $S = 2.5$ a, $S = 6.3$ b, $S = 10$ c, $S = 16$ d, $S = 25$ e, 63 f at Figures (c), (f), (j). Solid and dashed lines represents voltammograms calculated for the model of the scratched and rough electrode respectively.

predicted for the flat electrode at values of scale factor $S = 0.1$ (Figure 2.36). At slow and moderate scan rates the peak current and peak potential decrease since the shape of the voltammograms become less sharp (Figure 2.35 (a),(d) and (g)). Further increase of the scale factor S causes an increase of the peak current and the peak potential and the shape of voltammograms changes continuously. At high values of the scale factor S the peak potential reaches a limiting value. At high scan rates the peak current and peak potential are less sensitive to the value of scale factor S. The shape of the voltam-

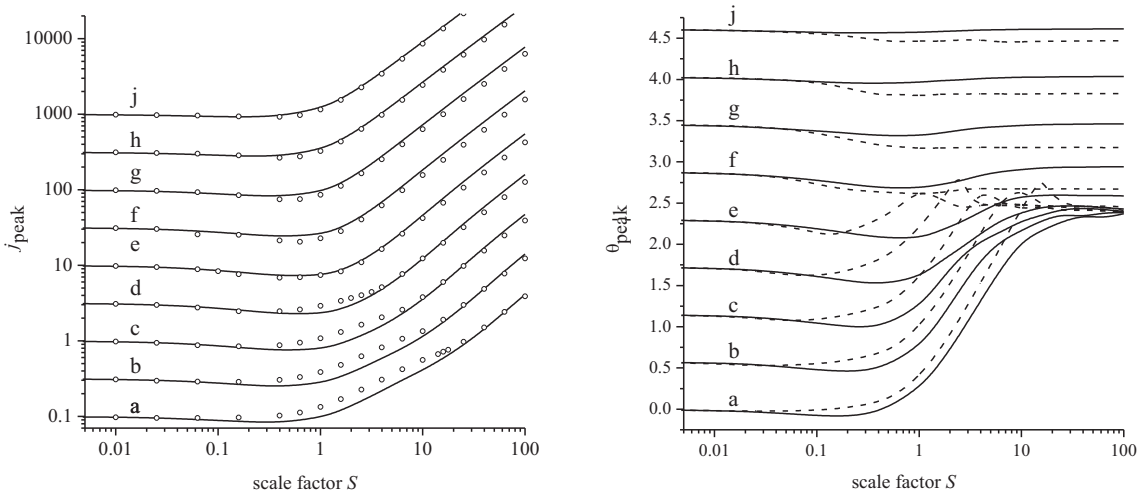

Figure 2.36: Peak current (a) and peak potential (b) versus scale factor S simulated for the model C. $\beta = 0.1$; $\sigma = 10^{-2}$ a, $\sigma = 10^{-1.5}$ b, $\sigma = 10^{-1}$ c, $\sigma = 10^{-0.5}$ d, $\sigma = 10^{0}$ e, $\sigma = 10^{0.5}$ f, $\sigma = 10^{1}$ g, $\sigma = 10^{1.5}$ h, $\sigma = 10^{2}$ j. Solid line and dots (dashed line) represents values calculated for scratched and rough electrodes respectively.

mograms do not change significantly, but the peak current increases proportionally to the increase of the electrode area, A_s. Secondly we consider stripping voltammetry on the rough electrode. An increase of the scale factor S causes an increase of the peak current. The decreases of the peak current is only observed at moderate values of the scan rate. At low values of the scan rate an increase of the scale factor S causes an increase of the peak potential. At high values of the scale factor S the peak potential reaches a limiting value, but before it has a complicated dependence on the scale factor S which is reflected in significant changes in the shape of the voltammogrames (Figure 2.35 (b), (c), (e), (f)). At high scan rates the peak potential does not significantly depend on the scan rate, the peak current increase proportionally to the electrode area and the shape of the voltammogram does not change significantly. Similar for the models A and B the peak current and the peak potential depend on the surface coverage parameter in agreement with the flat electrode model (eq. 2.56 and 2.59). Figure 2.40 shows the peak current and the peak potential versus scan rate σ at value of scale factor $S = 1$ $S = 10$. The dependence of the peak potential versus scan rate has a complicated shape since the shape of the voltammograme changes with the scan rate (compare curves a and d at Figure 2.35 (a), (d) and (g)).

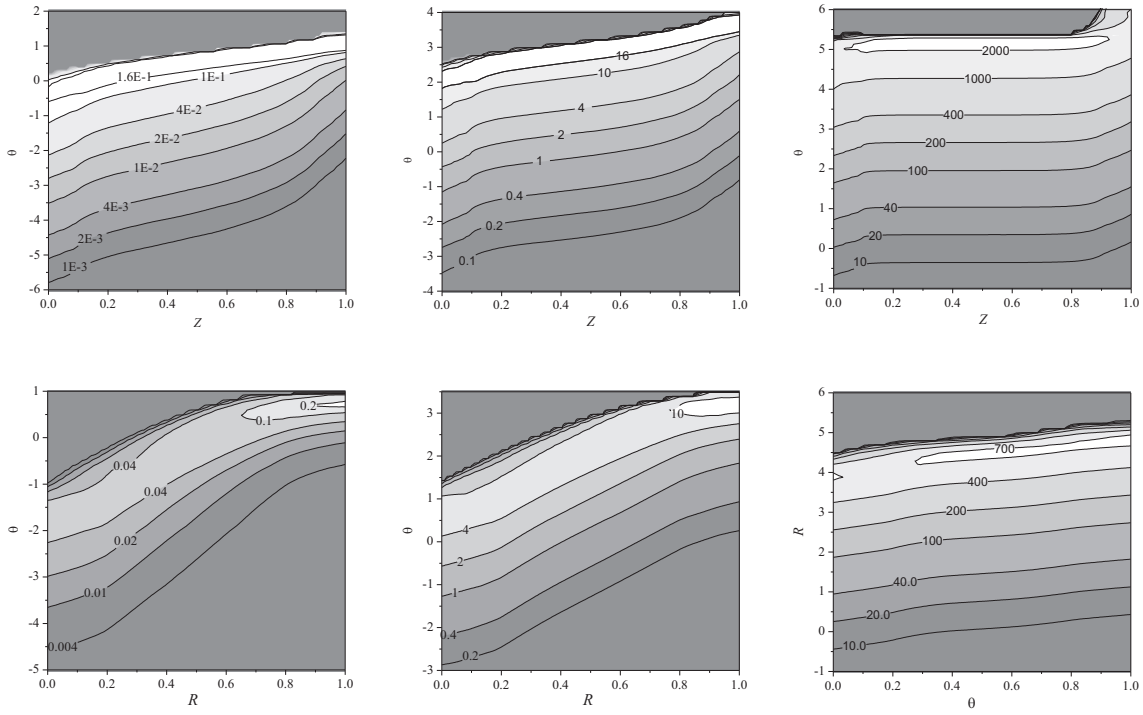

Figure 2.37: Current density at electrode surface versus potential simulated for model C. Contour lines show points of equal local flux. $\beta = 0.1$, $S = 1$. Scratched electrode: (a) $\sigma = 0.01$, (b) $\sigma = 1$, (c) $\sigma = 100$. Rough electrode: (d) $\sigma = 0.01$, (e) $\sigma = 1$, (f) $\sigma = 100$

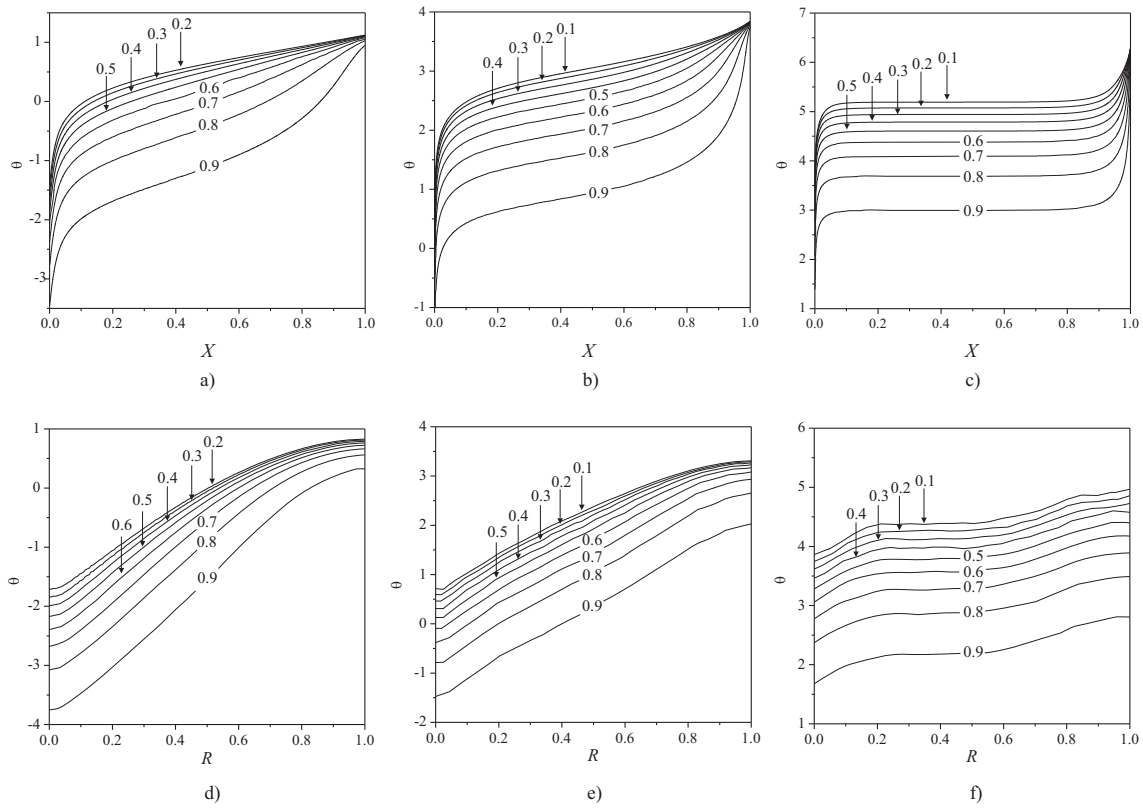

Figure 2.38: Concentration of the adsorbed (deposited) compound at electrode surface versus potential, model C, $\beta = 0.1$, $S = 1$. Contour lines show points of equal concentration. Scratched electrode: $\sigma = 0.01$ a), $\sigma = 1$ b), $\sigma = 100$ c) and rough electrode: $\sigma = 0.01$ d), $\sigma = 1$ e), $\sigma = 100$ f)

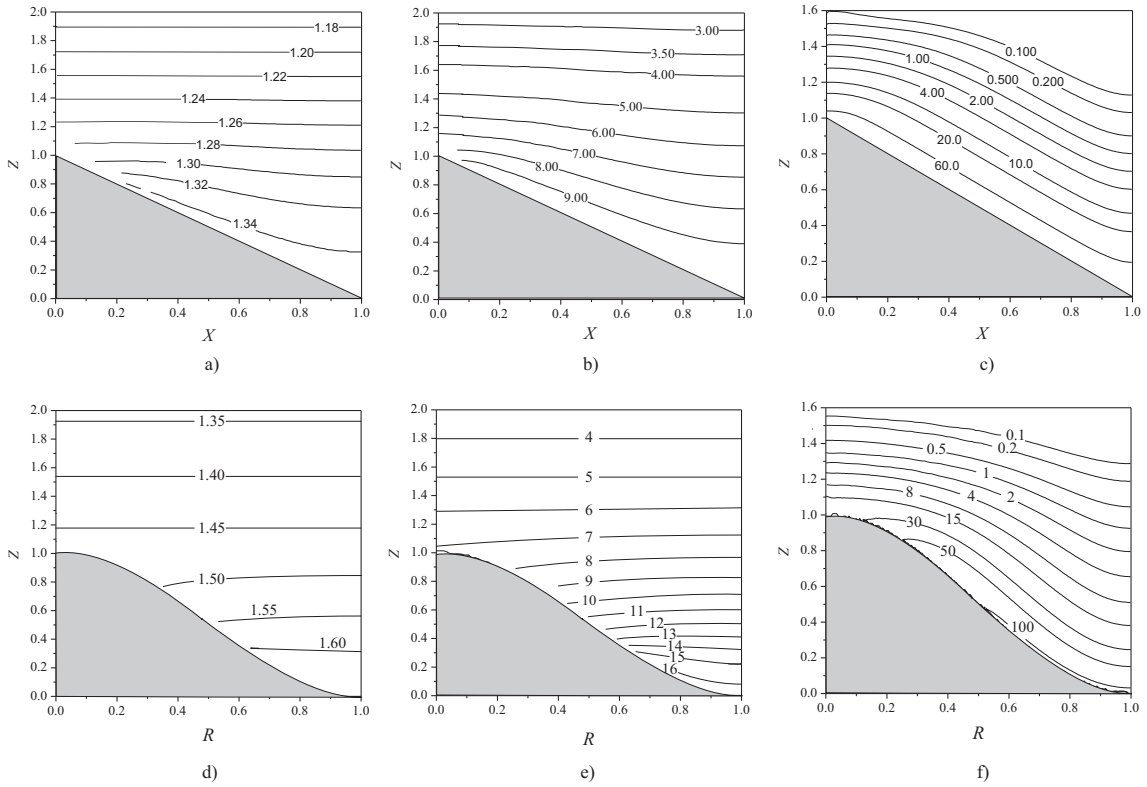

Figure 2.39: Concentration profiles of stripped compound straight after the peak potential, model C, β=0.1, S=1. Contour lines show points of equal concentration. Scratched electrode: σ=0.01 a), σ=1 b), σ=100 c) and rough electrode σ=0.01 d), σ=1 e), σ=100 f)

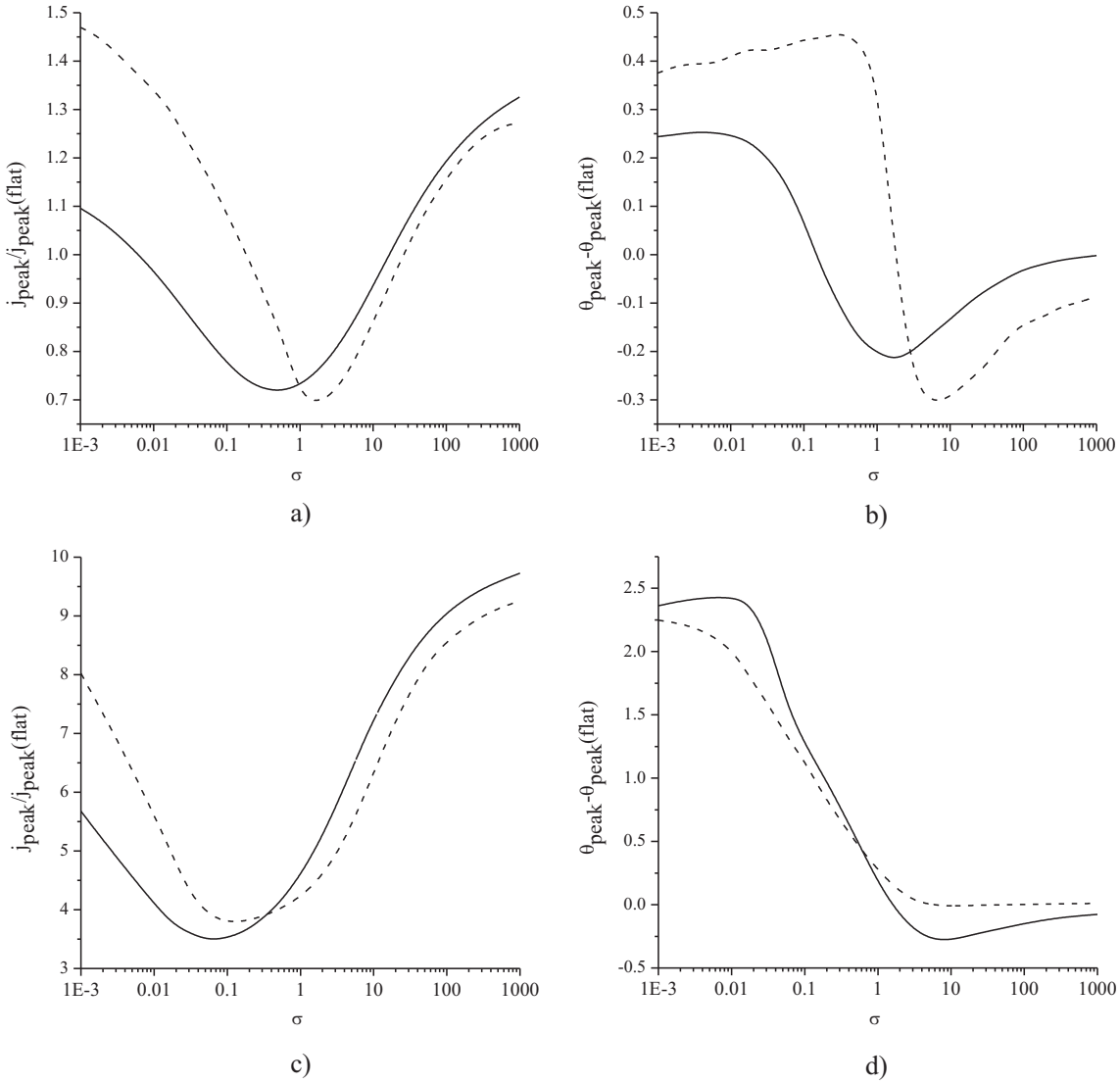

Figure 2.40: Normalised peak current (a) S=1 and (c) S=10 and peak potential (b) S=1 and (d) S=10 calculated on the scratched (solid line) and rough (dashed line) electrodes. $S = 1$

2.8.5 Comparison of the models

In our previous work[46] we investigated surface roughness influences on diffusional cyclic voltammetry. Experimentally it was found that values of scale factor S that can be realised by physical scratching of an electrode is about 0.2. Both theory and experiment showed that diffusional voltammmograms at electrodes with such a value of the electrode roughness were indistinguishable from that of a truly flat electrode. Considering anodic stripping voltammetry, the data reported above shows a much greater generic similarity in particular Figures 2.27, 2.33, 2.36 show that model C is the most sensitive to the surface morphology - the peak potential and peak current start to deviate from that on the flat electrode at values of the scale factor as small as 0.05. Model C corresponds to the stripping of bulk metals from the solid electrodes, so this the type of the experiment which is the most sensitive to the electrode morphology.

2.9 Stripping Voltammetry: Conclusions

Analytical expressions are derived for the peak current and the peak potential at flat electrodes for three models of the electrode transfer. Electrode roughness has a greater impact on stripping voltammetry than on diffusional voltammetry. The influence of electrode roughness on stripping voltammetry depends on the model of the electron transfer. However the peak current and the peak potential on the rough electrodes depend on the surface coverage parameter in a similar manner to that seen on a flat electrode for all considered models. In case of the models A and B voltammograms are sensitive to the electrode roughness only at high values of the scale factor S, which are not easy to achieve experimentally by the polishing and scratching of the electrode. Furthermore this models are not sensitive to the particular type of the surface roughness. On the other hand influence of the electrode roughness in Model C is significantly different from the previous models: observable voltammetric changes occur $S = 0.05$, which are easily realised experimentally. Furthermore in case of model C the stripping voltammogram significantly depend on the topology of the surface.

References

[1] Ozin, G. A.; Arsenault, A. C. *Nanochemistry;* Royal Society of Chemistry: Cambridge, UK, 2005.

[2] Masuda, H.; Watanabe, M.; Yasni, K.; Tryk, D.; Rao, T.; Fiijishima, A. *Advanced Materials* **2000,** *12,* 444–447.

[3] Nayak, B. K.; Gupta, M. C.; Kolasinski, K. W. *Nanotechnology* **2007,** *18,* 195302.

[4] Honda, K.; Yoshimura, M.; Rao, T. N.; Tryk, D. A.; Fujishima, A.; Yasui, K.; Sakamoto, Y.; Nishio, K.; Masuda, H. *J Electroanal Chem* **2001,** *514,* 35–50.

[5] La O, G. J.; In, H. J.; Crumlin, E.; Barbastathis, G.; Shao-Horn, Y. *International Journal of Energy Research* **2007,** *31,* 548–575.

[6] Soh, K. L.; Kang, W. P.; Davidson, J. L.; Basu, S.; Wong, Y. M.; Cliffel, D. E.; Bonds, A. B.; Swain, G. M. *Diamond Relat Mater* **2004,** *13,* 2009–2015.

[7] Peng, W.; Wang, E. *Anal Chim Acta* **1993,** *281,* 663–671.

[8] Streeter, I.; Compton, R. G. *J Phys Chem C* **2007,** *111,* 18049–18054.

[9] Streeter, I.; Baron, R.; Compton, R. G. *J Phys Chem C* **2007,** *111,* 17008–17014.

[10] Dickinson, E. J. F.; Streeter, I.; Compton, R. G. *J Phys Chem C* **2008,** *112,* 11637–11644.

[11] Dickinson, E. J. F.; Streeter, I.; Compton, R. G. *J Phys Chem B* **2008,** *112,* 4059–4066.

[12] Chevallier, F. G.; Jiang, L.; Jones, T. G. J.; Compton, R. G. *J Electroanal Chem* **2006,** *587,* 254–262.

[13] Britz, D.; Strutwolf, J. *Electrochim Acta* **2006,** *52,* 33–41.

[14] Liu, Z.; Yang, Z. L.; Cui, L.; Ren, B.; Tian, Z. Q. *Journal of Physical Chemistry C* **2007,** *111,* 1770–1775.

[15] Fojt, L.; Hason, S. *J Electroanal Chem* **2006,** *586,* 136–143.

[16] Leopold, M. C.; Bowden, E. F. *Langmuir* **2002,** *18,* 2239–2245.

[17] Hanwen, S.; Kaoqi, L.; Shuxuan, L.; Zhanfeng, L. *Chem. J. Internet* **2004,** *6,* 06a065pe.

[18] Afshar, A.; Dolati, A. G.; Ghorbani, M. *Mater Chem Phys* **2002,** *88,* 352–358.

[19] Otero, T. F.; Rodrguez-Jimnez, J. L.; Martin, H.; Carro, P.; Krijer, S. M.; Hernndez-Creus, A. *J Electrochem Soc* **2000,** *147,* 4546–4553.

[20] Foster, D. G.; Shapir, Y.; Jorne, J. *J Electrochem Soc* **2003,** *150,* C375–C380.

[21] Liu, Y. C.; Hwang, B. J.; Jian, W. J. *Mater Chem Phys* **2002,** *73,* 129–134.

[22] Hoogvliet, J. C.; Dijksma, M.; Kamp, B.; Van Bennekom, W. P. *Anal Chem* **2000,** *72,* 2016–2021.

[23] Cakir, O.; Temel, H.; Kiyak, M. *Journal of Materials Processing Technology* **2005,** *162-163,* 275–279.

[24] Nyikos, L.; Pajkossy, T. *Electrochim Acta* **1986,** *31,* 1347–1350.

[25] Pajkossy, T.; Nyikos, L. *Electrochim Acta* **1989,** *34,* 181–186.

[26] Stromme, M.; Niklasson, G. A.; Granqvist, C. G. *Physical Review B* **1995,** *52,* 14192–14197.

[27] Stromme, M.; Niklasson, G. A.; Granqvist, C. G. *Solid State Commun* **1995,** *96,* 151–154.

[28] Dassas, Y.; Duby, P. *J Electrochem Soc* **1995,** *142,* 4175–4180.

[29] Outsuka, I.; Iwasaki, T. *Journal of Vacuum Science and Technology B: Microelectronics and Nanometer Structures* **1996,** *14,* 1153–1156.

[30] Kant, R. *J Phys Chem B* **1997,** *101,* 3781–3787.

[31] Go, J. Y.; Pyun, S. I.; Hahn, Y. D. *J Electroanal Chem* **2003,** *549,* 49–59.

[32] Jha, S. K.; Sangal, A.; Kant, R. *J Electroanal Chem* **2008,** *615,* 180–190.

[33] Kant, R.; Jha, S. K. *J Phys Chem C* **2007,** *111,* 14040–14044.

[34] Kant, R.; Kumar, R.; Yadav, V. K. *J Phys Chem C* **2008,** *112,* 4019–4023.

[35] Kozaderov, O. A.; Vvedenskii, A. V. *Russ J Electrochem* **2001,** *37,* 798–802.

[36] Louch, D. S.; Pritzker, M. D. *J Electroanal Chem* **1991,** *319,* 33–53.

[37] Nolen, T. R.; Fedkiw, P. S. *J Electroanal Chem* **1989,** *258,* 265–280.

[38] Kant, R.; Rangarajan, S. K. *J Electroanal Chem* **1994,** *368,* 1–21.

[39] Pajkossy, T.; Nyikos, L. *Electrochim Acta* **1989,** *34,* 171–179.

[40] Jha, S. K.; Kant, R. *J Electroanal Chem* **2010,** *641,* 78-82.

[41] Ocon, P.; Herrasti, P.; Vzquez, L.; Salvarezza, R. C.; Vara, J. M.; Arvia, A. J. *J Electroanal Chem* **1991,** *319,* 101–110.

[42] Davies, T. J.; Hyde, M. E.; Compton, R. G. *Angewandte Chemie - International Edition* **2005,** *44,* 5121–5126.

[43] Barkey, D. P.; Muller, R. H.; Tobias, C. W. *J Electrochem Soc* **1989,** *136,* 2199–2207.

[44] Simm, A. O.; Ji, X.; Banks, C. E.; Hyde, M. E.; Compton, R. G. *ChemPhysChem* **2006,** *7,* 704–709.

[45] Hyde, M. E.; Jacobs, R.; Compton, R. G. *J Phys Chem B* **2002,** *106,* 11075–11080.

[46] Menshykau, D.; Streeter, I.; Compton, R. G. *J Phys Chem C* **2008,** *112,* 14428–14438.

[47] Guo, J.; Lindner, E. *Anal Chem* **2009,** *81,* 130–138.

[48] Kant, R. *Phys Rev Lett* **1993,** *70,* 4094–4097.

[49] Oldham, K. B. *J Electroanal Chem* **1991,** *297,* 317–348.

[50] Streeter, I.; Fietkau, N.; Del Campo, J.; Mas, R.; Mnoz, F. X.; Compton, R. G. *J Phys Chem C* **2007,** *111,* 12058–12066.

[51] Amatore, C.; Saveant, J. M.; Tessier, D. *J Electroanal Chem* **1983,** *147,* 39–51.

[52] Ward Jones, S. E.; Chevallier, F. G.; Paddon, C. A.; Compton, R. G. *Anal Chem* **2007,** *79,* 4110–4119.

[53] Rudolph, M.; Reddy, D. P.; Feldberg, S. W. *Anal Chem* **1994,** *66,* –.

[54] Peaceman, D. W.; Rachford, H. H. *J. Soc. Ind. Appl. Math.* **1955,** *3,* 28–41.

[55] Atkinson, K. *Elementary Numerical Analysis;* John Wiley & Sons, INC: 1993.

[56] Menshykau, D.; Compton, R. G. *Electroanalysis* **2008,** *20,* 2387–2394.

[57] Bard, A. J.; Faulkner, L. R. *Electrochemical Methods, Fundamentals and Applications;* Wiley: New York, 2nd ed.; 2001.

[58] Aoki, K.; Honda, K.; Tokuda, K.; Matsuda, H. *J Electroanal Chem* **1985,** *182,* 267–279.

[59] Chen, Q.; Swain, G. M. *Langmuir* **1998,** *14,* 7017–7026.

[60] Deakin, M. R.; Stutts, K. J.; Wightman, R. M. *J Electroanal Chem* **1985,** *182,* 113–122.

[61] Marken, F.; Eklund, J. C.; Compton, R. G. *J Electroanal Chem* **1995,** *395,* 335–339.

[62] Antiochia, R.; Lavagnini, I.; Magno, F.; Valentini, F.; Palleschi, G. *Electroanalysis* **2004,** *16,* 1451–1458.

[63] Chen, P.; McCreery, R. L. *Anal Chem* **1996,** *68,* 3958–3965.

[64] Chen, P.; Fryling, M. A.; McCreery, R. L. *Anal Chem* **1995,** *67,* 3115–3122.

[65] Jacob, S. R.; Hong, Q.; Coles, B. A.; Compton, R. G. *J Phys Chem B* **1999,** *103,* 2963–2969.

[66] Fernandez, H.; Zon, M. A. *J Electroanal Chem* **1990,** *283,* 251–270.

[67] Brainina, K.; Neyman, E. *Electroanalytical Stripping Methods;* volume John Wiley & Sons John Wiley & Sons: New York, 1993.

[68] Wang, J. *Analytical Electrochemistry;* Wiley: New York, 2nd ed.; 1994.

[69] Adeloju, S. B.; Brown, K. A. *Analyst* **1987,** *112,* 221–226.

[70] Adeloju, S. B. O.; Pablo, F. *Anal Chim Acta* **1994,** *288,* 157–166.

[71] Norouzi, P.; Ganjali, M. R.; Larijani, B.; Karamdoust, S. *Croat Chem Acta* **2008,** *81,* 423–430.

[72] De Vries, W. T.; Van Dalen, E. *J Electroanal Chem* **1964,** *8,* 366–377.

[73] Ball, J. C.; Cooper, J. A.; Compton, R. G. *J Electroanal Chem* **1997,** *435,* 229–239.

[74] Ball, J. C.; Compton, R. G. *J Phys Chem B* **1998,** *102,* 3967–3973.

[75] Ball, J. C.; Compton, R. G. *Electroanalysis* **1997,** *9,* 1305–1310.

[76] Nazarov, B. F.; Stromberg, A. G. *Russ J Electrochem* **2005,** *41,* 49–62.

[77] Reinmuth, W. H. *Anal Chem* **1961,** *33,* 1793–1794.

[78] Reinmuth, W. H. *J Am Chem Soc* **1957,** *79,* 6358–6360.

[79] DeMars, R. D.; Shain, I. *J Am Chem Soc* **1959,** *81,* 2654–2659.

[80] Goeting, C. H.; Marken, F.; Gutierrez-Sosa, A.; Compton, R. G.; Foord, J. S. *New Diamond Front Carbon Technol* **1999,** *9,* 207–228.

[81] Compton, R. G.; Foord, J. S.; Marken, F. *Electroanalysis* **2003,** *15,* 1349–1363.

[82] Manivannan, A.; Kawasaki, R.; Tryk, D. A.; Fujishima, A. *Electrochim Acta* **2004,** *49,* 3313–3318.

[83] Manivannan, A.; Tryk, D. A.; Fujishima, A. *Electrochem Solid-State Lett* **1999,** *2,* 455–456.

[84] Prado, C.; Wilkins, S. J.; Marken, F.; Compton, R. G. *Electroanalysis* **2002,** *14,* 262–272.

[85] Ward-Jones, S.; Banks, C. E.; Simm, A. O.; Jiang, L.; Compton, R. G. *Electroanalysis* **2005,** *17,* 1806–1815.

[86] Simm, A. O.; Banks, C. E.; Ward-Jones, S.; Davies, T. J.; Lawrence, N. S.; Jones, T. G. J.; Jiang, L.; Compton, R. G. *Analyst* **2005,** *130,* 1303–1311.

[87] Ward Jones, S. E.; Compton, R. G. *Anal Chem* **2008,** *4,* 170–176.

[88] Banks, C. E.; Compton, R. G. *Analyst* **2006,** *131,* 15–21.

[89] Wantz, F.; Banks, C. E.; Compton, R. G. *Electroanalysis* **2005,** *17,* 655–661.

[90] Honeychurch, K. C.; Hart, J. P. *TrAC - Trends in Analytical Chemistry* **2003,** *22,* 456–469.

[91] Wang, J.; Tian, B. *Anal Chem* **1992,** *64,* 1706–1709.

[92] Brainina, K. Z.; Lesunova, R. P. *Zh. Analit. Khimyi* **1974,** *29,* 1302.

[93] Brainina, K. Z.; Vydrevich, M. B. *J Electroanal Chem* **1981,** *121,* 1–28.

[94] Mouhandess, M. T.; Chassagneux, F.; Vittori, O.; Accary, A.; Reeves, R. M. *J Electroanal Chem* **1984,** *181,* 93–105.

[95] Mouhandess, M. T.; Chassagneux, F.; Vittori, O. *J Electroanal Chem* **1982,** *131,* 367–371.

[96] Mouhandess, M. T.; Chassagneux, F.; Durand, B.; Sharara, Z. Z.; Vittori, O. *J Mater Sci* **1985,** *20,* 3289–3299.

[97] Grygar, T. *J Solid State Electrochem* **1998,** *2,* 127–136.

[98] Grygar, T.; Marken, F.; Schroder, U.; Scholz, F. *Collect Czech Chem Commun* **2002,** *67,* 163–208.

[99] Chevallier, F. G.; Goodwin, A.; Banks, C. E.; Jiang, L.; Jones, T. G. J.; Compton, R. G. *J Solid State Electrochem* **2006,** *10,* 857–864.

[100] Ward Jones, S. E.; Zheng, S. H.; Jeffrey, C. A.; Seretis, S.; Morin, S.; Compton, R. G. *J Electroanal Chem* **2008,** *616,* 38–44.

[101] Powell, M.; Ball, J. C.; Tsai, Y. C.; Surez, M. F.; Compton, R. G. *J Phys Chem B* **2000,** *104,* 8268–8278.

[102] Trasatti, S.; Petrii, O. A. *J Electroanal Chem* **1992,** *327,* 353–376.

[103] Brainina, K. Z. *Talanta* **1971,** *18,* 513–539.

[104] Ball, J. C.; Compton, R. G.; Brett, C. M. A. *J Phys Chem B* **1998,** *102,* 162–166.

Chapter 3

Voltammetry at Electrodes Covered with Electroactive and Electro-Inactive Layers

3.1 Introduction

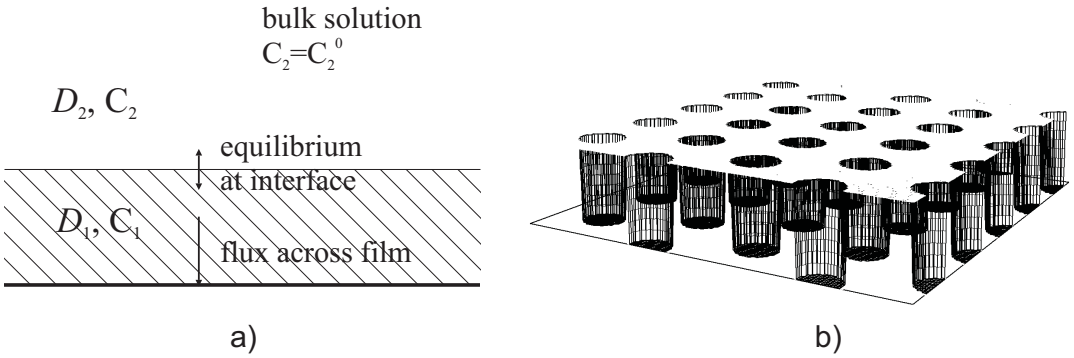

Figure 3.1: Schematic diagram of electrode surface: a) a uniform electro-inactive layer; b) porous layer can be either electroactive or electro-inactive.

The surface modification of electrodes is currently an area of intense activity worldwide with the promise of "designer - interfaces" offering improved or optimized electrochemical responses in diverse areas such as fuel cells, analysis, synthetic and biomimetic chemistry.[1–3] Electrode modification surface vary from deposition of self-assembled monolayers to introduction of layer of a significant thickness where the critical scale is that of the diffusion length on the timescale of the experiment, almost invariably voltammetry or chronoamperometry, used to investigate the beneficial or otherwise effects of surface modification. Such layers might diversely be composed of small organic molecules, polymers, nanotubes, buckyballs, ionic liquids, etc. These electrodes can exhibit mass transport properties that are very different from those observed for unmodified planar electrodes. A number of approaches have been developed in the literature to investigate the relationship between the electrochemical response and the film structure.[2–5]

The aim of this chapter is to consider both electro- active and inactive films. The red/ox chemistry

on electrodes covered with electro-inactive films occurs at the underlying electrode surface rather than within the film. Whilst electron tunneling through the film has been considered,[6–8] here we consider relatively thick films so that the transport to the electrode occurs either via dissolution of the solute into the film followed by Fickian diffusion to the electrode[5,9] or via diffusion through non-connecting pin holes within the film.[10] Such conditions relate both to polymer-modified electrodes and to electrodes covered with self-assembled monolayers[11–14] and have relevance to fuel cells, batteries and sensors.[1–3] We note that approximate treatments for pinhole diffusion based on transmission line equivalent circuits have been reported,[15–17] as have approximations based on assuming a negligible film thickness so that the surface behaves as an array of microelectrodes.[18–21,21–23] Here we generalize this latter approach to a film of arbitrary thickness and in particular consider via simulation how the presence of pinhole diffusion can be experimentally distinguished from the case of through-film diffusion, presenting results of general applicability subject to the assumption that the pin holes are wide enough to allow a description of the mass transport in term of the Fickian diffusion and that there is sufficient supporting electrolyte in both the pin hole and the solution phase suppress any migration effects. Similar models were applied by the Savéant[24] to study the electrochemical response of rotating disc electrodes modified with electro-inactive layers. A comparison with our work is made below.

Contrary to electrodes covered with electro-inactive films where electron transfer occur only at underlying electrode surface the entire porous surface of the electroactive electrode is electrochemically active. In many applications the sought effect of the modification is enhanced “electrocatalysis” so as for example, to promote fast electrode reactions at the surface of fuel cell electrodes or to allow the analytical viability of a target analyte within the available solvent window. Typically fast “catalyzed” electrode reactions are characterized by a cyclic voltammetry signal in which the peak to peak separation is reduced in comparison with the uncatalyzed process. The behavior of porous electrodes has received intermittent attention. Of particular note are approaches based on transmission lines and their impedance behavior[15,16,25] and methods which presume, often inappropriately, that the electrode surface has a fractal character.[26,27] Diverse other strategies have been adopted.[28–33] The purpose of this chapter is to demonstrate that the surface modification of an electrode with a porous layer can under certain conditions cause the false impression of “electrocatalysis”. That is to say that the modified layer can show a cyclic voltammetry response in which the peak to peak separation is

reduced compared to that of the unmodified electrode. However, the sole reason for this can be a purely the mass transport effect rather than an alteration of the fundamental electrode kinetics. Here we utilize a simple diffusion domain approach to investigate the transition, which corresponds to that from a "porous" to a "flat" electrode.

3.2 The Models of Electrode Surface

3.2.1 Electrodes Covered with a Uniform Layer

We consider a macroelectrode covered with an electro-inactive layer, as shown in Figure 3.1a, through which a species has to diffuse to reach the electrode surface. The diffusion coefficient and solubility of the species in the film are likely different from those in bulk solution.

3.2.2 Electrodes Covered with an Electro-Inactive Layer Containing Uniformly Distributed Cylindrical Pores or Pinholes

We consider an electrode with an idealized surface as shown in Figure 3.1b. The surface is composed of an "array" of cylindrical pores or pinholes. Material is assumed to reach the electrodes via diffusion through the pore and negligibly otherwise. The diffusion of the electrochemically active species is complicated because it is intrinsically a three dimensional problem. However, the problem can be simplified by noting that each cylindrical pore belongs to a diffusionally independent region known as diffusion domain.[23,34] The diffusional domain approximation treats these zones as being cylindrical with a pore situated at the axis of symmetry, thus reducing the problem to one of only two dimensions. The approximation is illustrated in Figure 3.2. Figure 3.2 a) and b) show the surface in Cartesian coordinates and Figure 3.2 c) identifies the unit cell in cylindrical coordinates (r,z). The cylindrical radial coordinate, r, is defined as the distance from the axis of symmetry that runs through the center of the electrode domain. The cylindrical domain is of equal area to the hexagonal unit cell. The total current from the macroelectrode "array" is given by simple multiplication of the current from single diffusion domain to that from the total number of domains N_{p}.

3.2.3 Electrodes Covered with Electroactive Layer

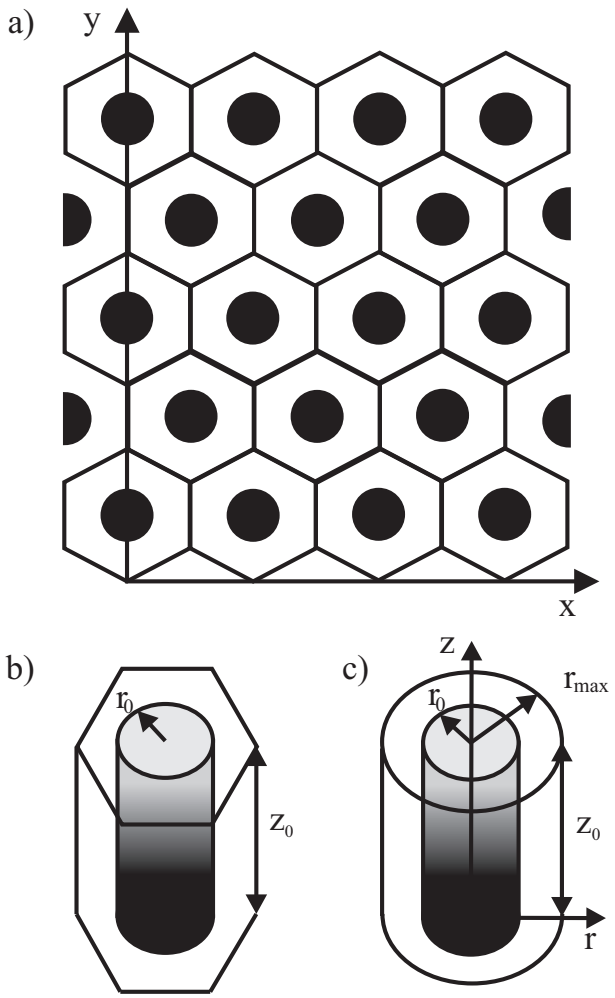

Figure 3.2: Schematic diagram of the unit cell for an array of cylindrical pores; b) single unit cell in Cartesian coordinates; c) equivalent diffusion domain in cylindrical coordinates.

species A is assumed to be present in bulk solution.

Similar to model of an electrode covered with electro-inactive layer we consider an electrode with an idealized surface as shown in Figure 3.1b. Contrary to the model of an electrode covered with electro-inactive layer electron transfer occurs at all the surface of the electrode: the top surface, walls and bottom of pores. Two different areas are considered when discussing voltammetry at electroactive electrode: A_p is the projection area or area of an equivalent flat electrode whereas A_s is the total area of the rough electrode surface. Here again diffusional domain approximation applied (Figure 3.2) to simplify an intrinsically three dimensional problem to that of only two dimensions.

3.3 Mathematical model

Equation 3.1 shows the electron transfer reaction considered in these numerical simulations. Both species A and B are soluble, but only

$$A + e^- \rightleftharpoons B \tag{3.1}$$

We assume that species A and B have equal diffusion coefficients:

$$D_A = D_B = D \tag{3.2}$$

so that at each point of the solution the concentrations of species A and B satisfy relationship:

$$[\mathrm{A}] + [\mathrm{B}] = [\mathrm{A}]_0 \tag{3.3}$$

where $[\mathrm{A}]_0$ is the bulk concentration of A. In such a situation the concentration profile of species A may be simulated independently from that of species B. We next consider the cyclic voltammetry experiment applied to the reduction of A. The potential changes in agreement with equation 3.4 before a switch potential and equation 3.5 after a switch potential.

$$E = E_{\mathrm{in}} - vt; t < |E_{\mathrm{s}} - E_{\mathrm{in}}|/v \tag{3.4}$$

$$E = E_{\mathrm{s}} + vt; t > |E_{\mathrm{s}} - E_{\mathrm{in}}|/v \tag{3.5}$$

where E_{in} is the initial potential, E_{s} is the switch potential and v is a voltage scan rate. The electron transfer process is considered for the two cases: the first case is infinitely fast electrode kinetics, so that Nernst equilibrium is established at the electrode surface:

$$[\mathrm{B}] = [\mathrm{A}]\exp[-\frac{F(E - E_{\mathrm{f}}^0)}{RT}] \tag{3.6}$$

where T is the absolute temperature, R is the molar gas constant, and E_{f}^0 is the formal potential of the half reaction.

The second case corresponds to electron transfer described by Butler-Volmer kinetics:

$$\frac{\partial [A]}{\partial t} = k_0([\mathrm{A}]e^{-\alpha\theta} - [\mathrm{B}]e^{(1-\alpha)\theta}) \tag{3.7}$$

where, k_0 is a rate constant of electron transfer and α is a transfer coefficient.

3.3.1 Electrodes Covered with a Uniform Layer

The mass transport of species A is described by Fick's second law of diffusion, which is given by equation 3.8:

$$\frac{\partial [\mathrm{A}]}{\partial t} = D_{\mathrm{i}} \frac{\partial^2 [\mathrm{A}]}{\partial z^2}; \tag{3.8}$$

Table 3.1: Dimensionless parameters used for numerical simulation of electrodes covered with uniform layer.

Parameter	Expression
Normal coordinate	$Z = z/z_0$
Time	$\tau = \frac{D_2 t}{z_0^2}$
Scan rate	$\sigma = \frac{F v z_0^2}{RTD_2}$
Potential	$\theta = \frac{F(E-E_f^0)}{RT}$
Concentration of species A_i	$a_i = [A]_i/[A]_2^0$
Concentration of species B_i	$b_i = [B]_i/[A]_2^0$
Diffusion coefficient ratio	$\gamma_i = \frac{D_1}{D_2} = \gamma, z < z_0$ and $\gamma_i = 1, z > z_0$
Electrode flux	$j = \frac{-iz_0}{FD_2[A]_2^0 A}$

where D_i=D_1 if $z < z_0$ and $D_i = D_2$, if $z \geq z_0$ (Figure 3.1). Equilibrium is assumed at the film/solution border:[5]

$$K_{eq} = \frac{[A]_1}{[A]_2} \tag{3.9}$$

where the subscript 1 refers to the film and the subscript 2 refers to the bulk solution. The model is normalized using the dimensionless parameters in Table 3.1. The mass transport is then described by the dimensionless variant of equation 3.8

$$\frac{\partial a_i}{\partial \tau} = \gamma_i \frac{\partial^2 a_i}{\partial Z^2}; \tag{3.10}$$

were γ_i is defined in Table 3.1. Note that in experimental practice measurement at too high voltage scan rates may compromise the assumption in the equation 3.9.

Table 3.2: Boundary and initial conditions for model describing electrodes covered with a uniform layer

Boundary	Condition
Initial condition	$a_1 = K_{eq}; a_2 = 1; b_1 = 0; b_2 = 0$
Layer's border	$K_{eq} = \frac{a_1}{a_2}$
Bulk solution	$a_2 = 1$
Electrode surface	$\frac{a_1}{b_1} = \exp[\theta(\tau)]$

3.3.2 Electrodes Covered with a Layer Containing Uniformly Distributed Cylindrical Pores: Electroactive and Electro-Inactive Layers

Table 3.3: Dimensionless parameters used for numerical simulation of electrodes covered with a layer containing uniformly distributed cylindrical pores of pinholes.

Parameter	Expression normalized to r_0	Expression normalized to z_0
Radial coordinate	$R = r/r_0$	$R = r/z_0$
Normal coordinate	$Z = z/r_0$	$Z = z/z_0$
Time	$\tau = \frac{Dt}{r_0^2}$	$\tau = \frac{Dt}{z_0^2}$
Scan rate	$\sigma = \frac{F\nu r_0^2}{RTD}$	$\sigma' = \frac{F\nu z_0^2}{RTD}$
Potential	$\theta = \frac{F(E-E_f^0)}{RT}$	$\theta = \frac{F(E-E_f^0)}{RT}$
Concentration of species A	$a = [\mathrm{A}]/[\mathrm{A}]_0$	$a = [\mathrm{A}]/[\mathrm{A}]_0$
Concentration of species B	$b = [\mathrm{B}]/[\mathrm{A}]_0$	$b = [\mathrm{B}]/[\mathrm{As}]_0$
Pore depth	$L_{\mathrm{cyl}} = \frac{z_0}{r_0}$	$L_{\mathrm{cyl}} = \frac{z_0}{r_0}$
Radius of diffusion domain	$R_{\max} = \frac{r_{\max}}{r_0}$	$R_{\max} = \frac{r_{\max}}{r_0}$
Electrode flux*	$j = \frac{-i}{4FD[\mathrm{A}]_0 r_0}$	$j = \frac{-i}{4FD[\mathrm{A}]_0 r_0}$
Electrode flux**	$j = \frac{-i}{FD[\mathrm{A}]_0 r_0}$	

* Electrode covered with electro-inactive layer. ** Electrode covered with electroactive layer.

The mass transport of species A in cylindrical coordinates is described by Fick's second law of diffusion given by equation 3.11

$$\frac{\partial[\mathrm{A}]}{\partial t} = D\left(\frac{\partial^2[\mathrm{A}]}{\partial r^2} + \frac{1}{r}\frac{\partial[\mathrm{A}]}{\partial r} + \frac{\partial^2[\mathrm{A}]}{\partial z^2}\right) \tag{3.11}$$

For convenience of subsequent data presentation the model is normalized using two different sets of the dimensionless parameters. In the first the case pore radius r_0 is used to normalize all variables and parameters; in the second pore depth z_0 is used instead. Dimensionless parameters and variables are summarized in Table 3.3, in both cases the current is normalized to the pore radius r_0. The mass transport in cylindrical coordinates is given by the dimensionless version of equation 3.11:

$$\frac{\partial a}{\partial \tau} = \frac{\partial^2 a}{\partial R^2} + \frac{1}{R}\frac{\partial a}{\partial R} + \frac{\partial^2 a}{\partial Z^2} \tag{3.12}$$

The boundary conditions for equation 3.12 are summarized in Table 3.4. There is a no-flux condition at the axis of symmetry ($R = 0$) and the diffusion domain border $R = R_{max}$. The bulk solution condition is implemented at a distance $6\sqrt{\tau_{\max}}$ from the highest point of the electrode, where $\tau_{\max}$ is a time of experiment. Beyond this the effects of diffusion are not important on the experimental voltammetric timescale.[35]

Table 3.4: Boundary and initial conditions for model describing electrodes covered with a layer containing uniformly distributed cylindrical pores or pinholes

Boundary	Condition
Initial condition	$a = 1; b = 0$
Axis of symmetry	$\frac{\partial a}{\partial R} = 0; \frac{\partial b}{\partial R} = 0$
Diffusion domain border	$\frac{\partial a}{\partial R} = 0; \frac{\partial b}{\partial R} = 0$
Bulk solution	$a = 1; b = 0$
Electrode surface	$\frac{a}{b} = \exp[\theta(\tau)]$

3.4 Computational Details

3.4.1 Computational procedure

Planar One Dimensional Diffusion to Naked Macroelectrode

One dimensional simulations of macroelectrode cyclic voltammograms were performed using DigiSim(BASi, IN, USA)[36] to verify the convergence or otherwise of the computational procedures defined below.

Electrodes Covered with a Uniform Layer

Equation 3.10 and its accompanying conditions (Table 3.2) were discretized and solved by the fully implicit finite difference method in conjunction with Thomas algorithm.[37] The program was written in C++. A high mesh density is required in the region of the electrode surface and film/solution border. The expanding grid is implemented to decrease the computational time.

Electrodes Covered with a Layer Containing Uniformly Distributed Cylindrical Pores or Pinholes

Because of the symmetry of the model, the mass transport equation 3.12 and its accompanying conditions (table 3.4) were solved in the two dimensional space in the region $0 < R < R_{\max}$ and $Z > 0$. A rectangular expanding grid (defined by equations 3.13 - 3.16) similar to the used in previous simulations of electrodes with complicated surfaces[38–40] is used to discretize the mass transport equation 3.12.

$$R_{i+1} - R_i = h_i \tag{3.13}$$

$$Z_{i+1} - Z_i = k_i \tag{3.14}$$

$$h_i = \gamma_R \times h_{i-1} \tag{3.15}$$

$$k_i = \gamma_Z \times k_{i-1} \tag{3.16}$$

Standard values of the mesh used in computations were $h_0 = k_0 = 10^{-5}$ and $\gamma_R = \gamma_Z = 1.125$ The alternating direction implicit finite difference method[41] in conjunction with Thomas algorithm[37] was used to solve the discretized form of the mass transport equation 3.12. The program was written in C++.

3.4.2 Computational accuracy

To check the convergence of simulation procedure numerous simulations were run with different space grids and time steps. The calculated current converges with decrease of the space step and an increase in the number of steps per dimensionless potential θ. The whole range of parameters were tested to achieve an accuracy of 0.2% or better when calculating voltammograms registered at electrodes covered with electro-inactive layers. To validate the procedure, a comparison to the known results for a flat macrodisk were made. Results calculated by the models where the electrode was assumed to be covered with a uniform or porous layer converges to the results predicted by model assuming only planar one dimensional diffusion.[5] Furthermore at low scan rates and small values of the pore depth L_{cyl} the steady state current calculated in the model where the electrode is assumed to be covered with porous layer is equal to unity, in agreement with the analytical steady state current at a microdisk electrode.[5] Votammograms at electrode covered with electroactive layer were calculated

with an accuracy of 0.1%. To validate the procedure, a comparison to the known results for a flat macrodisk were made. Results from the two dimensional simulation of electrode with cylindrical pores for small values of L_{cyl} are presented in Table 3.5. The deviation of calculated dimensionless current from current given by equation 3.17[5] for a broad range of scan rates were less than 0.1%:

$$j_{peak} = 1.401 \times \sqrt{\sigma} \tag{3.17}$$

Table 3.5: Boundary and initial conditions for model describing electrodes covered with a uniform layer

σ	$L_{cyl} = 0.16$	$L_{cyl} = 0.08$	$L_{cyl} = 0.04$	$L_{cyl} = 0.02$	$L_{cyl} = 0.01$	Eq. 3.18
0.1	0.4447	0.4441	0.4438	0.4437	0.4437	0.4434
1	1.412	1.406	1.404	1.403	1.403	1.402
10	4.508	4.459	4.443	4.438	4.437	4.434

3.5 Electro-Inactive Layers: Results and Discussions

3.5.1 Electrodes covered with a uniform layer

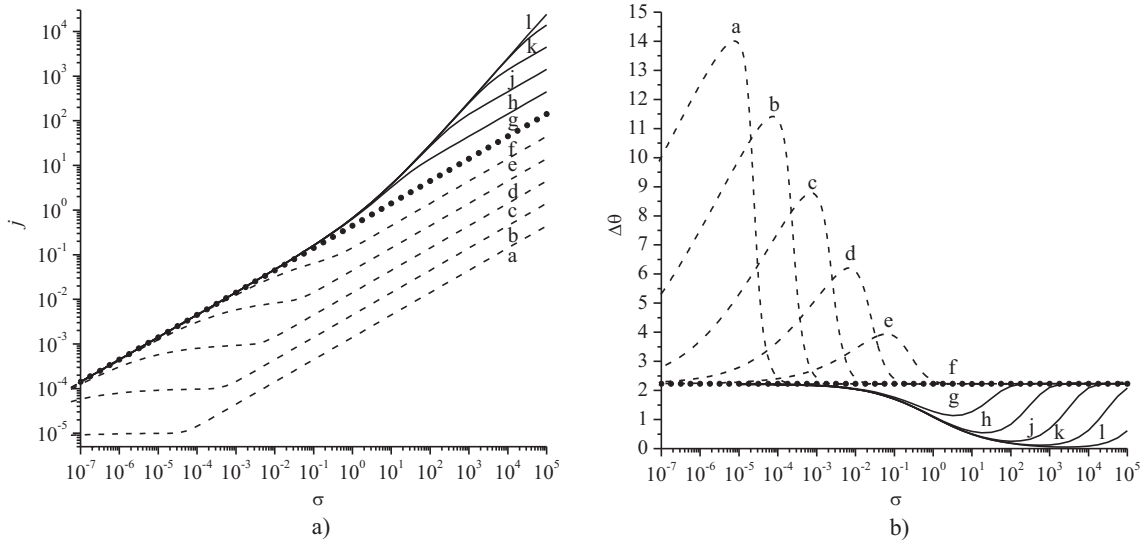

Figure 3.3: Peak current a) and peak to peak separation b) versus dimensionless scan rate σ, $K_{eq} = 1$, $\gamma = 10^{-5}$ a; 10^{-4} b; 10^{-3} c; 10^{-2} d; 10^{-1} e; 1 f; 10^{1} g; 10^{2} h; 10^{3} j; 10^{4} k; 10^{5} l;

Cyclic voltammograms can be characterized by the peak current and the peak to peak separation.[42] The variation of peak current versus the dimensionless scan rate σ is presented in Figure 3.3 a) for $K_{eq} = 1$ and for a range of different values of γ. Figure 3.3 b) shows the corresponding values of

the peak to peak separation $\Delta\theta$. The calculated peak current follows the Randles-Ševčík equation[5] perfectly:

$$j_{\text{peak}} = 0.4463 \times \sqrt{\sigma} \tag{3.18}$$

for $\gamma = 1$. The peak to peak separation is $\Delta\theta = 2.23$ which corresponds to 56.5 mV at 298K and is in agreement with the known theory for one dimensional planar diffusion to a macrodisk electrode.[5] If $\gamma \neq 1$ the dependence of peak current and peak to peak separation on the scan rate is more complicated. Let us consider the case where diffusion in the film is slower than diffusion in the solution above it ($\gamma < 1$). At high scan rates when the diffusion layer is thinner than the film and condition

$$\sqrt{\frac{\gamma}{\sigma}} << 1 \tag{3.19}$$

is fulfilled the peak current scales with scan rate as $j_{\text{peak}} \sim \sqrt{\sigma}$ (Figure 3.3 a), curves a - f) and is given by the generalized Randles-Ševčík equation 3.20, and a peak to peak separation of $\Delta\theta = 2.23$ (Figure 3.3 b), lines a-f) that is characteristic for planar one dimensional diffusion.

$$j_{\text{peak}} = 0.4463 \times \sqrt{\sigma \times \gamma} \tag{3.20}$$

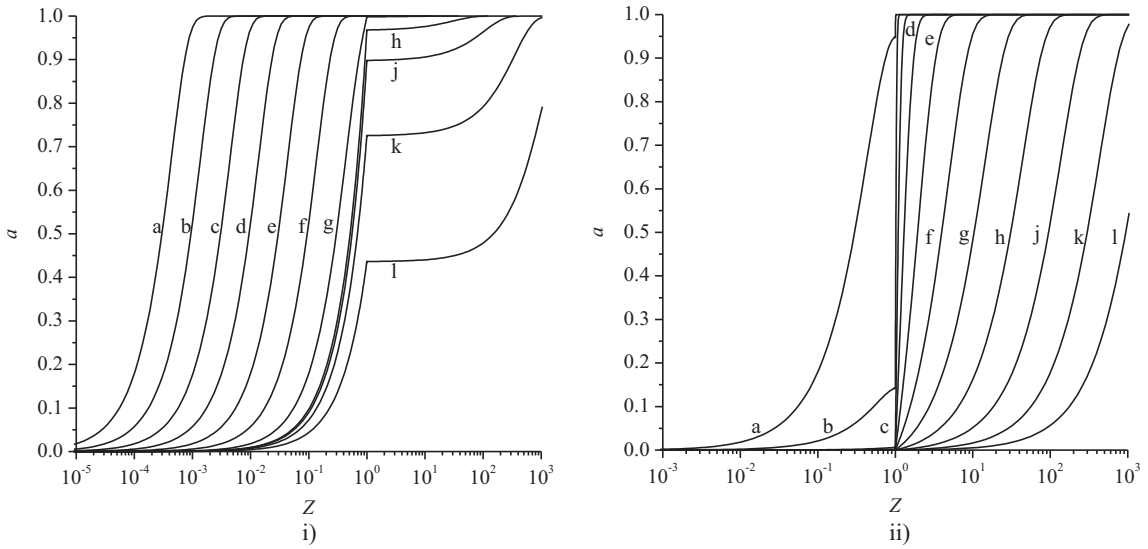

Figure 3.4: Concentration profiles i) $\gamma = 10^{-3}$, ii) $\gamma = 10^{3}$; $K_{\text{eq}} = 1$, $\sigma = 10^{-5}$ a; 10^{-4} b; 10^{-3} c; 10^{-2} d; 10^{-1} e; 1 f; 10^{1} g; 10^{2} h; 10^{3} j; 10^{4} k; 10^{5} l;

Concentration profiles simulated for the parameters $\gamma = 1 \times 10^{-3}$ and $K_{\text{eq}} = 1$ are presented in Figure 3.4 i), it is clearly seen that at high scan rates (curves a-f) the thickness of diffusion layer

is less than that of the film. Cyclic voltammograms simulated for the parameters $\gamma = 1 \times 10^{-3}$ and $K_{eq} = 1$ are presented in Figure 3.5. A decrease of the scan rate causes an increase of diffusion layer thickness. When the diffusion layer thickness reaches the size of the layer (Figure 3.4 i) curves g and h) and if the diffusion coefficient in the layer is significantly less than in bulk solution steady state behavior is observed (Figure 3.5, curve d). Figure 3.3 shows the peak current and the peak to peak separation versus scan rate at different values of γ. The region of parameters where steady state cyclic voltammograms are observed is presented in Figure 3.3 a) corresponding the plateaus on curves a-e and in Figure b) to the region of high values of peak to peak separation. Note that in these region of parameters where the cyclic voltammograms have a steady state shape the peak to peak separation value cannot be located precisely, consequently values of peak to peak separations, $\Delta\theta$, higher that 6 have some degree of aproximation. The steady state current is given by equation:

$$j_{ss} = \gamma \tag{3.21}$$

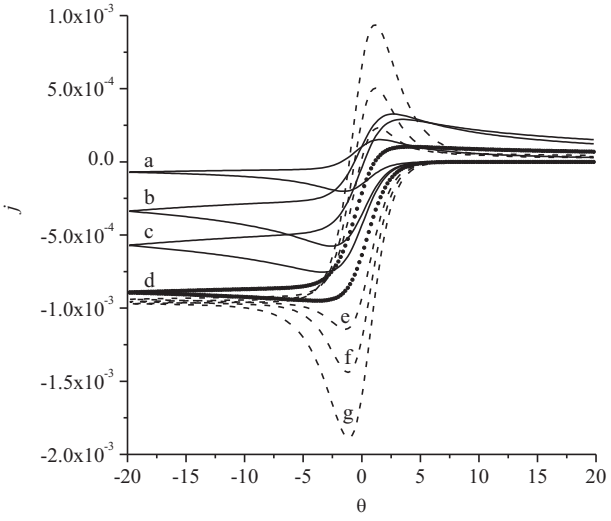

Figure 3.5: Cyclic voltammograms simulated for $\gamma = 10^{-3}, K_{eq} = 1$, $\sigma = 3.2 \times 10^{-7}$ a; 10^{-5} b; 5.6×10^{-3} c; 1.8×10^{-2} d; 5.6×10^{-3} e; 1×10^{-2} f; 1.8×10^{-2} g;

A further decrease of scan rates causes an increase in diffusional layer thickness and it penetrates far into the solution (Figure 3.4, curves j - l). The shape of the cyclic voltammograms gradually changes from steady state to planar one dimensional diffusion (Figure 3.5, curves d - g). Under the latter conditions the peak to peak separation reaches a value of $\Delta\theta = 2.23$ (F 3.3) and the peak current is given by the Randles-Ševčík equation 3.18.

Let us consider the case when diffusion in the film is faster than in solution, $\gamma > 1$ at $Z > 1$. The diffusion layer thickness is larger than the film thickness at low scan rates (Figure 3.4 ii), lines g-l) and the current is limited by transport of the electroactive species from the bulk solution to the film surface and the peak current is equal to that given by Randles-Ševčík equation 3.18, with a peak to peak separation of $\Delta\theta = 2.23$ (Figure 3.3). An increase of scan rate causes a decreases of the

peak to peak separation, so that the peak current is given by a generalized equation for the thin layer model (Figure 3.3, lines g-l).[5]

$$j_{\text{peak}} = \sigma/4 \tag{3.22}$$

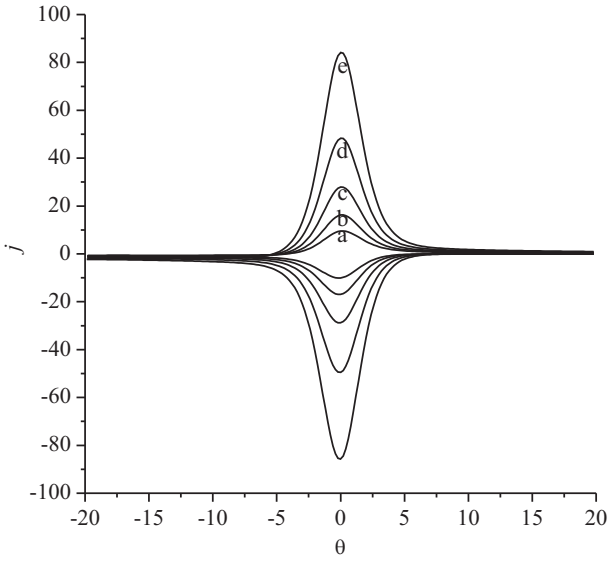

Figure 3.6: Cyclic voltammograms simulated for $\gamma = 10^4, K_{\text{eq}} = 1$, $\sigma = 32$ a; 56 b; 100 c; 180 d; 320 e.

Cyclic voltammograms for $\gamma = 1 \times 10^4$ and $K_{\text{eq}} = 1$ are presented in Figure 3.6. The cyclic voltammograms have a shape typical for a one dimensional thin layer model.[5] Further increase of scan rate causes an increase of the peak to peak separation to a value of $\Delta\theta = 2.23$. The peak current values are given by the generalized Randles-Ševčík equation 3.20 (Figure 3.3, curves g-l) and the cyclic voltammograms have then the shape typical of planar one dimensional diffusion.

Let us consider the influence of the equilibrium constant K_{eq}. The peak current and peak to peak separation versus scan rate for $K_{\text{eq}} = 0.1$ and $K_{\text{eq}} = 10$ are presented in Figure 3.7 and Figure 3.8 respectively. Similar to the case considered above an increase of scan rate causes a change in the type of cyclic voltammograms. The shape of the cyclic voltammograms changes gradually from that characteristic of planar one dimensional diffusion to a shape characteristic of thin layer, one dimensional diffusion and further to planar one dimensional diffusion at high values of γ. At low values γ increase of scan rate causes change of shape of cyclic voltammogram from characteristic of planar one dimensional diffusion to steady state and further to planar one dimenisonal diffusion. At high scan rates the peak current values are given by a generalized Randles-Ševčík equation:

$$j_{\text{peak}} = 0.4463 \times K_{\text{eq}} \times \sqrt{\sigma \times \gamma} \tag{3.23}$$

A similar type of current scaling was found for chronoamperometry on electrodes modified with thin films.[5] The peak current is given by equation 3.24 in a parameter region where thin layer behavior

is observed.

$$j_{\text{peak}} = K_{\text{eq}} \times \sigma/4 \tag{3.24}$$

The steady state current is given by equation 3.21 in a parameter region where steady state behavior is observed.

$$j_{\text{ss}} = K_{\text{eq}} \times \gamma \tag{3.25}$$

For $K_{\text{eq}} = 0.1$, $\gamma = 100$ and $K_{\text{eq}} = 10$, $\gamma = 0.01$ peak to peak separation $\Delta\theta = 2.23$ and peak current is given by equation 3.18 at all scan rate values (Figure 3.7, curve h and Figure 3.8 curve d).

The different types of cyclic voltammograms which can be observed in model describing electrodes covered with uniform layer are presented in Figure 3.9. Cyclic voltammograms with a shape characteristic for planar one dimensional diffusion are observed in region I, and the peak current is given by the generalized Randles-Ševčík equation 3.23. Cyclic voltammograms with a shape typical of one dimensional thin layer model are observed in zone II, with a peak to peak separation tending to zero and a peak current given by equation 3.24. Cyclic voltammograms have a shape characteristic of planar one dimensional diffusion in zone III, and the peak current is given by Randles-Ševčík equation 3.18. Cyclyc voltammograms are steady-state on character in zone IV, and the steady state current is given by equation 3.21. Note, of course the transitions from part of to another in Figure 3.9 are gradual, not abrupt (Figure 3.5).

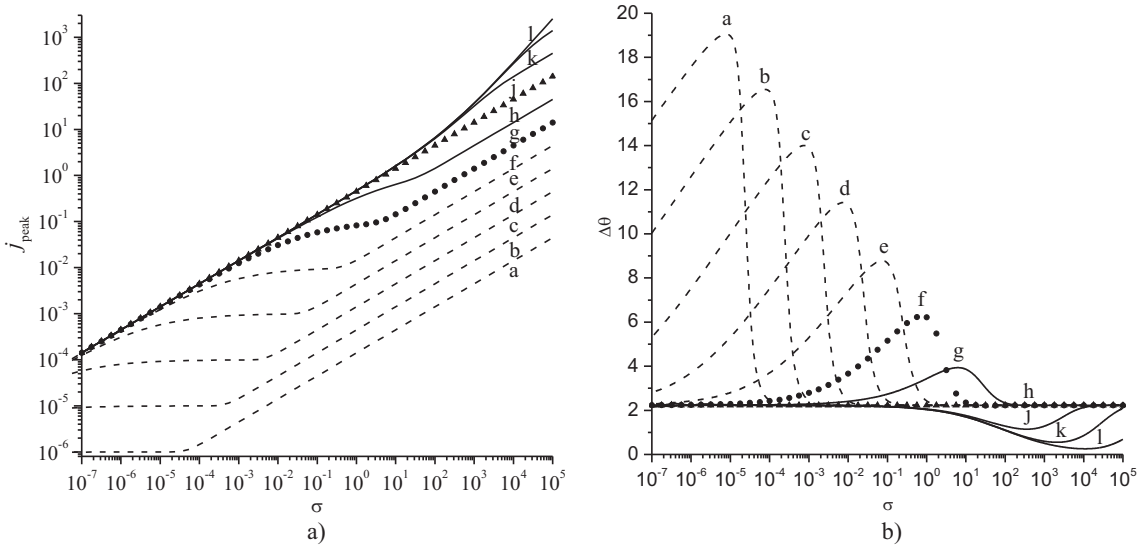

Figure 3.7: Peak current a) and peak to peak separation b) versus dimensionless scan rate σ, $K_{\text{eq}} = 0.1$, $\gamma = 10^{-5}$ a; 10^{-4} b; 10^{-3} c; 10^{-2} d; 10^{-1} e; 1 f; 10^{1} g; 10^{2} h; 10^{3} j; 10^{4} j; 10^{5} k;

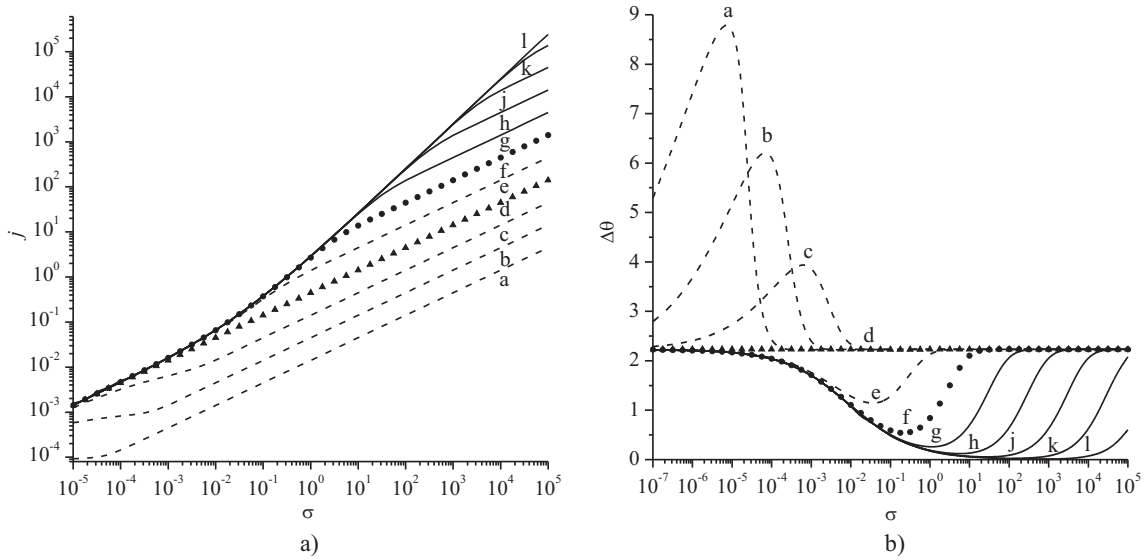

Figure 3.8: Peak current a) and peak to peak separation b) versus dimensionless scan rate σ, $K_{eq} = 10$, $\gamma = 10^{-5}$ a; 10^{-4} b; 10^{-3} c; 10^{-2} d; 10^{-1} e; 1 f; 10^{1} g; 10^{2} h; 10^{3} j; 10^{4} k; 10^{5} l;

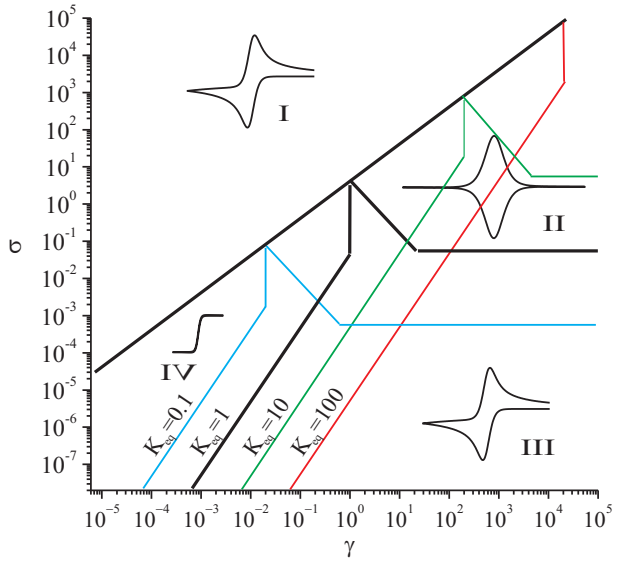

Figure 3.9: Zone diagram for an electrode covered with a uniform film. Types of behavior I-IV is described in text.

3.5.2 Electrodes Covered with a Layer Containing Uniformly Distributed Cylindrical Pores or Pinholes

Dimensionless parameters normalized to r_0

Let us first consider the case when the dimensionless parameters and variables (Table 3.3) are normalized to r_0. The peak current versus dimensionless scan rate σ is presented in Figure 3.10. The

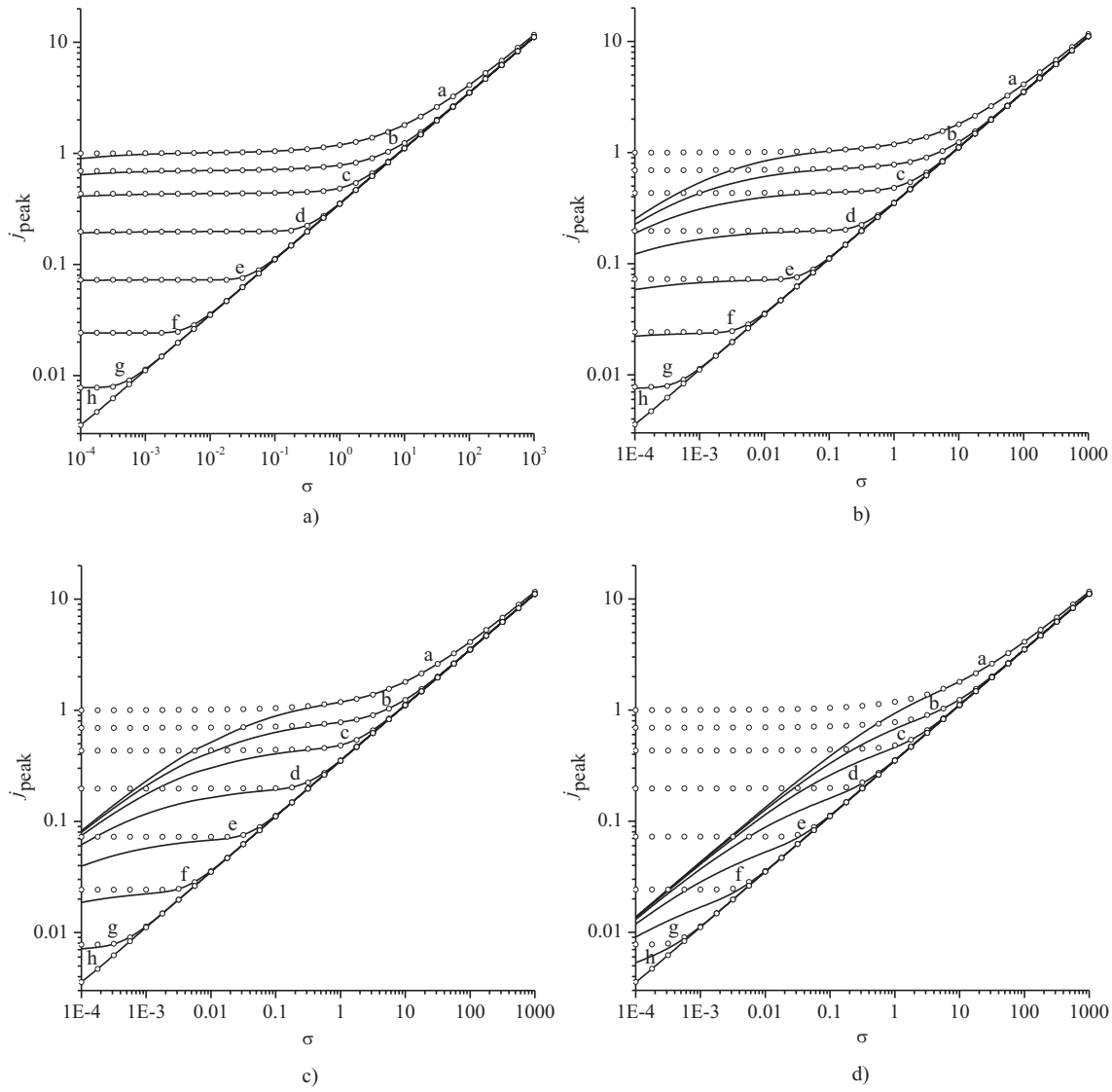

Figure 3.10: Peak current versus dimensionless scan rate σ. For all plots the dots represent data for single diffusionally independent pore. The lines represent data for a single pore in an array $R_{max} = 50$ a), $R_{max} = 10$ b), $R_{max} = 5$ c), $R_{max} = 2$ d). L_{cyl} is 0.001 - curve a, 0.32 - b, 1 - c, 3.2 - d, 10 - e, 32 - f, 56 - g, 100 - h

peak to peak separation versus dimensionless scan rate σ is presented in Figure 3.11. Here and elsewhere it should be understood that in the region of parameters where the cyclic voltammograms have steady state character, the peak to peak separation cannot be located precisely, and consequently for values of the peak to peak separation $\Delta\theta$ higher than 6 should not be considered as exact. Let us consider a case of single diffusionally independent pore. At high scan rates the calculated peak current perfectly follows Randles-Ševčík equation 3.18 and shows a peak to peak separation of $\Delta\theta = 2.3$; the cyclic voltammograms have the shape characteristic of one dimensional planar diffusion. At low

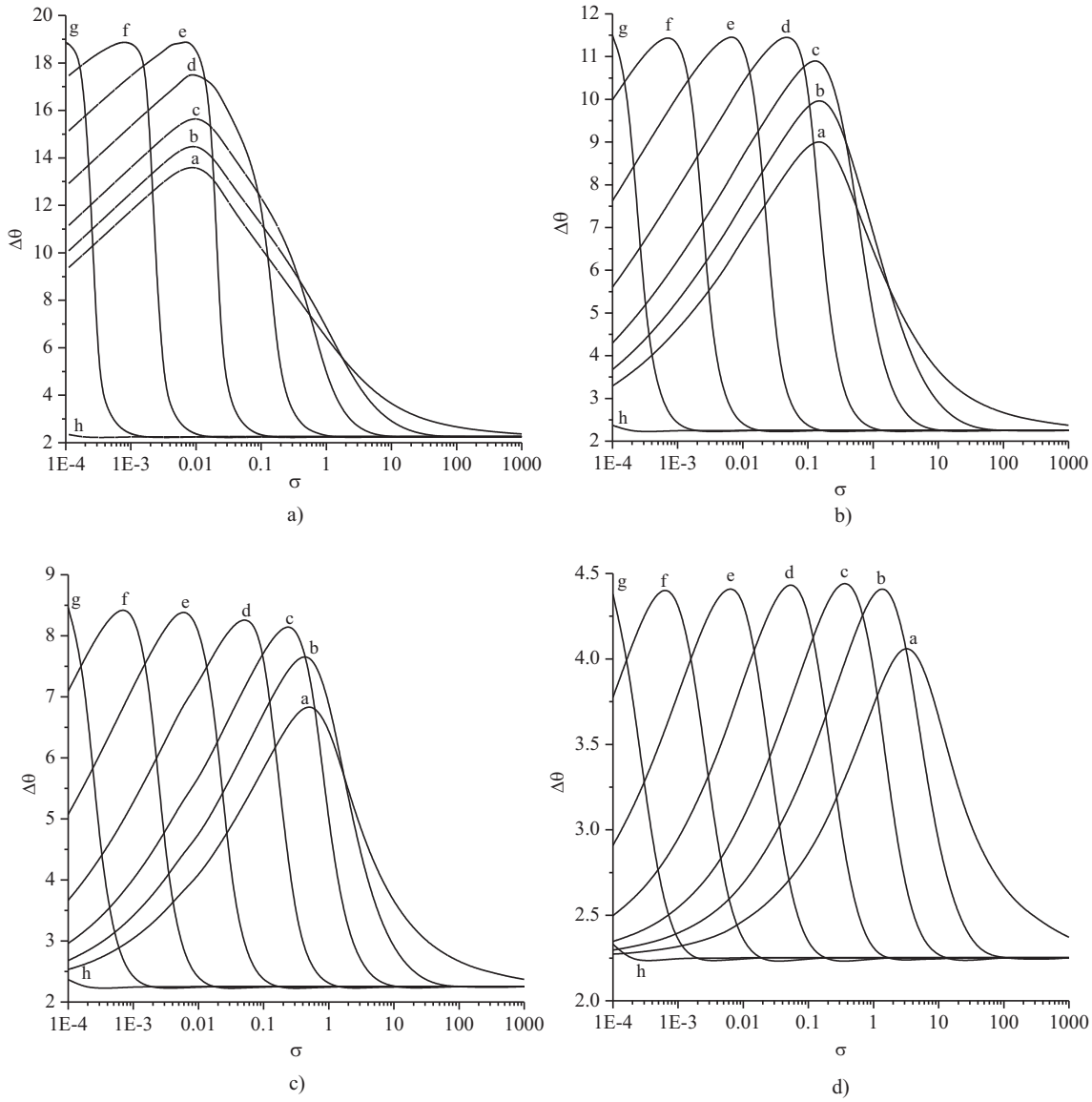

Figure 3.11: Peak to peak separation, $\Delta\theta$, versus dimensionless scan rate σ. $R_{\max} = 50$ a), $R_{\max} = 10$ b), $R_{\max} = 5$ c), $R_{\max} = 2$ d). L_{cyl} is 0.001 - curve a, 0.32 - b, 1 - c, 3.2 - d, 10 - e, 32 - f, 56 - g, 100 - h

scan rates and low L_{cyl}=0.001 when the electrode can be considered flat steady state voltammograms are observed. The steady state current is $j_{\text{ss}} = 1$, in agreement with results for a microdisk.[5] The concentration profiles for different values of L_{cyl} are presented in Figure 3.12. An increase of the pore depth causes a switch of diffusion type from convergent two dimensional diffusion to planar one dimensional (Figure 3.12). Diffusion again becomes two dimensional when the diffusion length l_{D} reaches the value of the pore depth L_{cyl}

$$L_{\text{cyl}} \approx \sqrt{\frac{1}{\sigma}} \tag{3.26}$$

If the pores separation is less than the diffusion length $\sqrt{\frac{1}{\sigma}}$, the pores cannot be considered as independent due to overlapping of their diffusion layers (compare Figure 3.12 a) and c)). Figure 3.13 shows cyclic voltammograms modeled for a porous electrode with $R_{max} = 10$ and $L_{cyl} = 10$. At high scan rates we observe one dimensional planar diffusion to the "microelectrode" at the base of the pore (Figure 3.12 b) and Figure 3.13 a) curve f). A decrease of scan rate causes an increase of the diffusion layer thickness, and the diffusion type switches from one dimensional to two dimensional and steady state cyclic voltammograms are observed Figure 3.13 b) curve a). Figure 3.10 shows that when diffusional layers from adjacent pores overlap the peak current deviates from steady state and the peak to peak separation decrease (Figure 3.11). Peak current versus scan rate in bi-logarithmic coordinates has a slope of $-\frac{1}{2}$, and peak to peak separation has the value $\Delta\theta = 2.23$. Both of these are characteristic for planar one dimensional diffusion. Cyclic voltammograms in this region of parameters can be fitted with the commercial simulation package DigiSim (Figure 3.13).[36]

Dimensionless parameters normalized to z_0

Here we consider the two dimensional model with dimensionless parameters normalized to z_0. This consideration is necessary since the experimental measurement of film thickness is more reliable than the measurements of pore radius and so comparison of one and two dimensional models are clearer if the variables have a common normalization to this variable. The peak currents versus scan rates at different values of the pore depth L_{cyl} and diffusional domain radius are presented in Figure 3.15. In the case of well separated pores (Figure 3.15 a)) three types of cyclic voltammograms can be observed on a porous electrode: planar one dimensional diffusion to an array of microelectrodes reflecting the pores opening, convergent two dimensional steady state diffusion to an array of microelectrodes and planar one dimensional diffusion to a macroelectrode. In the first region the peak current is given by the generalized Randles-Ševčík equation:

$$j_{\mathrm{peak}} = 0.3505 \times \sqrt{\sigma'} \times \frac{1}{L_{\mathrm{cyl}}} \tag{3.27}$$

In the second region the steady state current at low values of pore depth L_{cyl} is close to unity and at high values it inversely proportional to pore depth. The range of scan rates where convergent two dimensional diffusion take place dramatically depend on the diffusion domain radius R_{max} (compare the length of the flat regions in Figures 3.15 a)-d)).

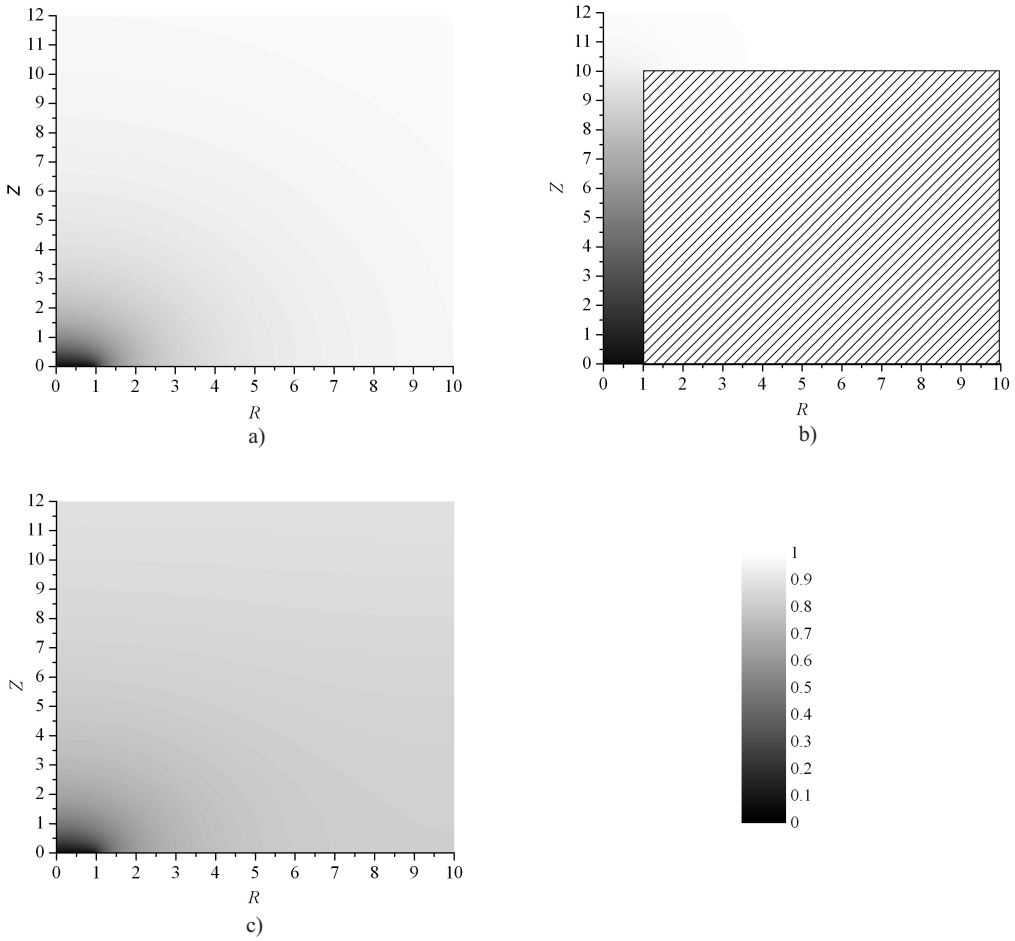

Figure 3.12: Concentration profiles captured on the forward scan of the voltage at, $\theta = -3$. a) $L_{\text{cyl}} = 0.001$, single diffusionally independent pore; b) $L_{\text{cyl}} = 10$, single diffusionally independent pore;) c) $L_{\text{cyl}} = 0.001$, $R_{\text{max}} = 10$s

Finally at very slow scan rates when the diffusion layers from adjacent pores overlaps the peak current is given by the generalized Randles-Ševčík equation:

$$j_{\text{peak}} = 0.3505 \times R_{\text{max}}^2 \times \sqrt{\sigma'} \times \frac{1}{L_{\text{cyl}}} \tag{3.28}$$

The types of cyclic voltammograms which can be observed in the two dimensional model are presented in Figure 3.14. Planar one dimensional diffusion to a microelectrode is observed in region I, and the peak current is given by the generalized Randles-Ševčík equation 3.27. Steady state cyclic voltammograms are observed in region II; the lowest value of scan rate at which steady state behavior

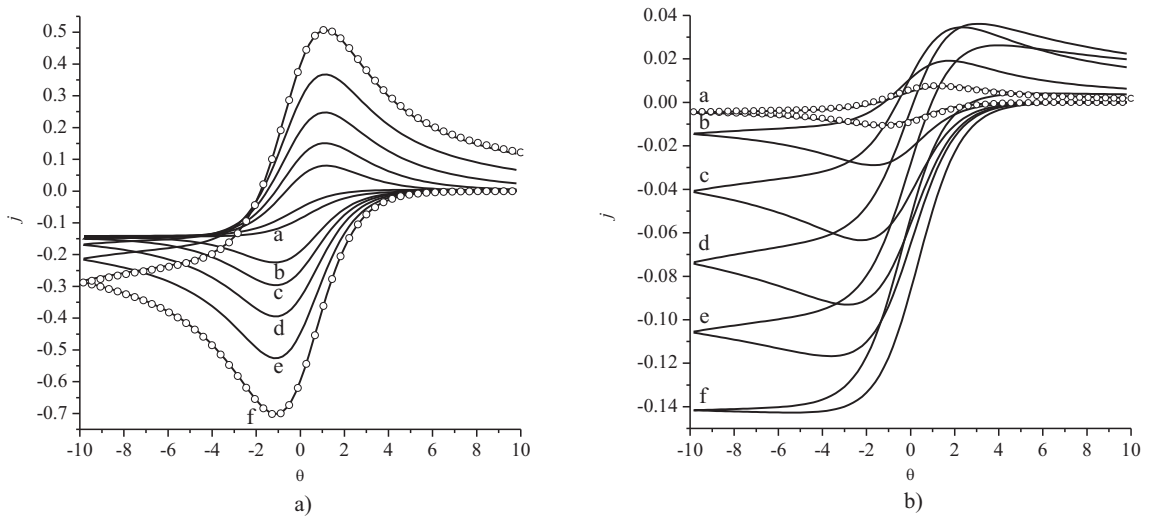

Figure 3.13: Cyclic voltammograms simulated in two dimensional model with $R_{cyl} = 10$, L_{cyl}=10 at a) high scan rates σ'=1 a; σ'=10 b; σ'=17.8 c; σ'=31.6 d; σ'=56.2 e; σ'=100 f; and b) low scan rates $\sigma' = 3.16 \times 10^{-6}$ a; $\sigma' = 3.16 \times 10^{-5}$ b; $\sigma' = 3.16 \times 10^{-4}$ c; $\sigma' = 3.16 \times 10^{-3}$ d; $\sigma' = 0.01$ e; $\sigma' = 1$ f. Circles shows cyclic voltammograms modeled with DigiSim

is observed is strongly depend on pore separation R_{cyl}. Finally in zone III planar one dimensional diffusion to macroelectrode is observed; the peak current is given by the generalized Randles-Ševčík equation 3.28.

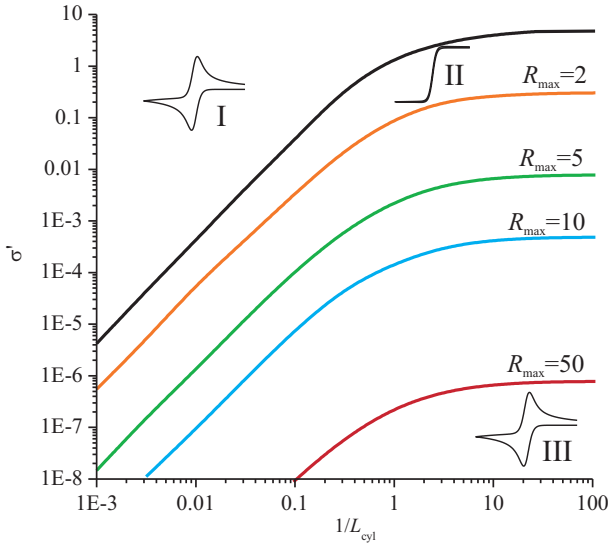

Figure 3.14: Zone diagram for electrode covered with a layer containing uniformly distributed cylindrical pores or pinholes. Types of behavior I-III is described in text.

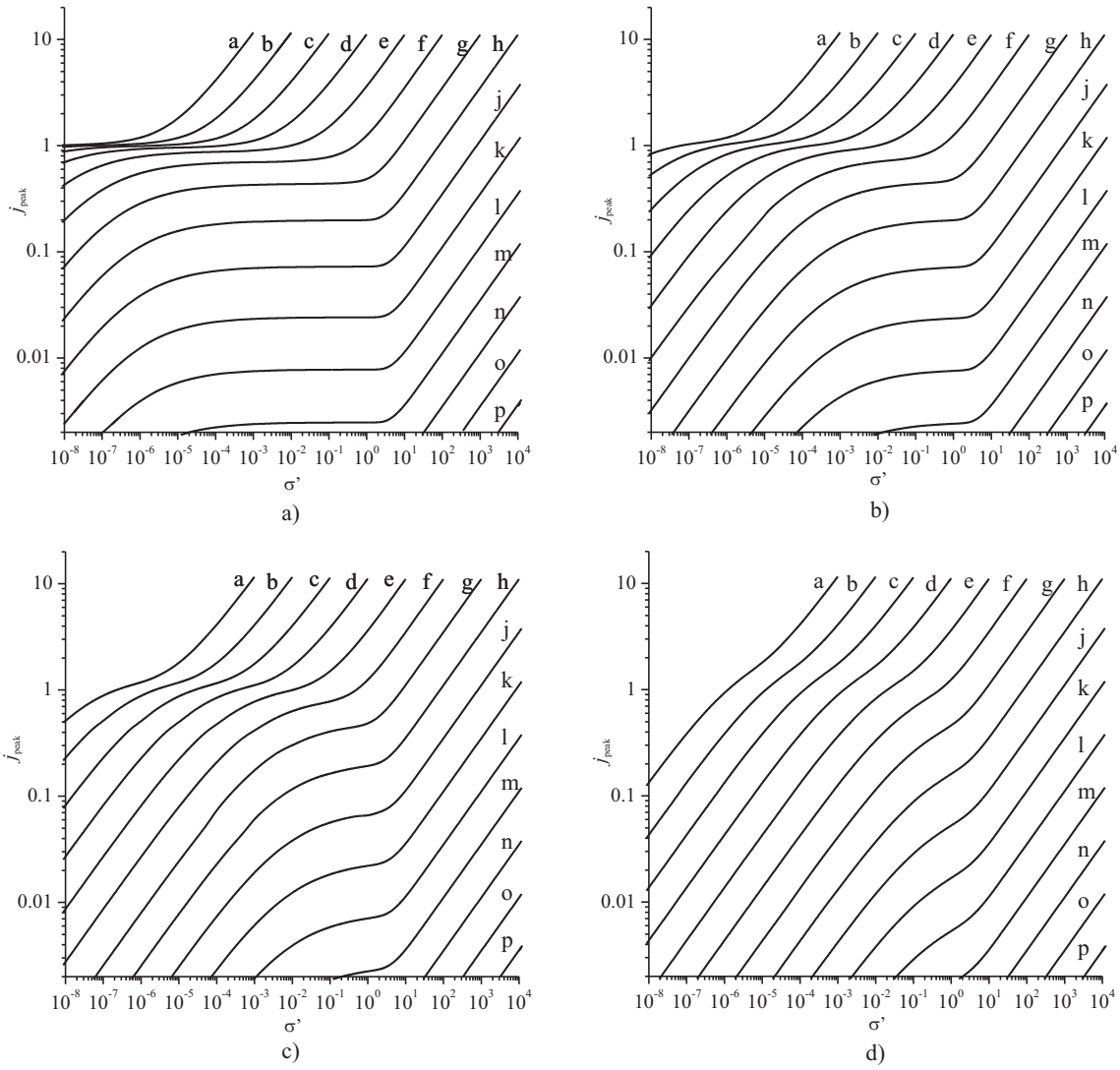

Figure 3.15: Peak current versus dimensionless scan rate σ'. a) $R_{max} = 50$; b) $R_{max} = 10$; c) $R_{max} = 5$; d) $R_{max} = 2$. a $L_{cyl} = 10^{-3}$; b $L_{cyl} = 10^{-2.5}$; c $L_{cyl} = 10^{-2}$; d $L_{cyl} = 10^{-1.5}$; e $L_{cyl} = 10^{-1}$; f $L_{cyl} = 10^{-0.5}$; g $L_{cyl} = 10^{0}$; h $L_{cyl} = 10^{0.5}$; j $L_{cyl} = 10^{1}$; k $L_{cyl} = 10^{1.5}$; l $L_{cyl} = 10^{2}$; m $L_{cyl} = 10^{2.5}$; n $L_{cyl} = 10^{3}$; o $L_{cyl} = 10^{3.5}$; p $L_{cyl} = 10^{4}$;

3.5.3 Comparison of the models and mechanistic resolution of the two cases using experimental data

Figure 3.9 and Figure 3.14 show that similar types of voltammetric behavior can be observed in both the uniform and porous layer models, except for thin layer behavior, which is observed only in the uniform layer model. Consequently if thin layer behavior is observed experimental parameters can immediately be extracted with equation 3.24. Otherwise in standard electrochemical experiments the scan rate can be changed over more than three orders of magnitude;[5,42] this is only sufficient to

distinguish models on the basis of Figures 3.3, 3.7, 3.8 and Figures 3.15 and the equations presented in text if there is a transition between voltammograms types for example from Randles-Ševčík to steady state. To illustrate this in Figure 3.16 the dimensionless peak current calculated according to the model of an electrode covered with a porous layer is presented as a function of scan rate σ'.

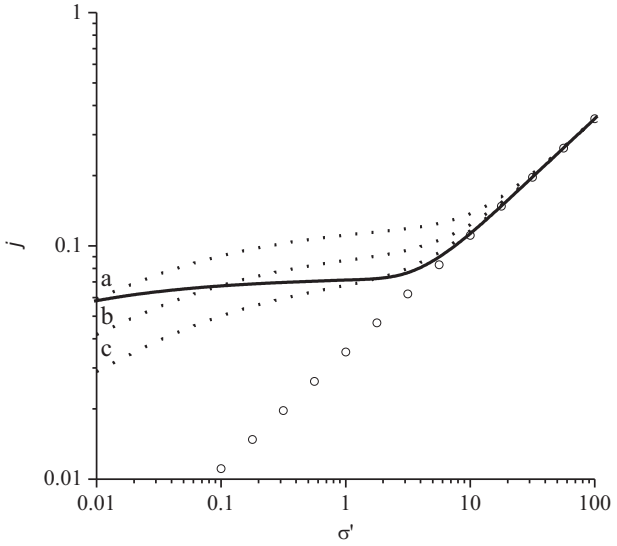

Figure 3.16: Peak current versus scan rate. Solid line - two dimensional porous electrode model. Next dimensional parameters were used for modeling $D = 10^{-5}$ cm^2/s, $z_0 = 10$ μm, $r_0 = 1$ μm, $[\mathrm{A}]_0 = 10^{-6}$ mol/cm^3 and $v = 0.01 - 10$ V/s, that corresponds to dimensional parameters $L_{\mathrm{cyl}} = 10$, radius of diffusion domain is $R_{\max} = 10$. Dots - one dimensional two layer model at curve a $K_{\mathrm{eq}} = 0.079, \gamma = 0.98$, at curve b $K_{\mathrm{eq}} = 0.1, \gamma = 0.62$ and at curve c $K_{\mathrm{eq}} = 0.13, \gamma = 0.39$. Open circles - peak current values calculated by generalized Randles-Ševčík equation

Also shown are attempts to fit this behavior with a uniform layer model. It is clear that the model of electrode covered with a uniform layer fails to reproduce the dependence of the peak current versus scan rate (Figure 3.16). Similarly in Figure 3.17 the dimensionless peak current versus scan rate is presented for the model of the electrode covered with a uniform layer. Here again the model of an electrode covered with a porous layer fails to reproduce the peak current at slow scan rates. Consequently if change of diffusion type occurs in the experimentally available range of scan rates then the two models can be distinguished. It is apparent that if the voltage scan range can be varied so as to change between different zones in Figures 3.9 and 3.14 then experimental resolution can be achieved.

It is interesting to compare the conclusion of the present work in respect of cyclic voltammetric investigation of the pin hole diffusion versus film permeation problem with that using classical rotating disc voltammetry. The latter problem has been elegantly and rigorously analyzed by Savéant with the conclusion that the dynamics of film permeation cannot readily be dissected from those of pin hole diffusion. The contrast with our conclusions arises because in the rotating disc system the rotation will most likely, as realistically assumed by Savéant,[24] even out any concentration variations in the solution phase except those normal to the electrode (z coordinate in the Figure 3.12). Accordingly since no concentration variation radially

from, or angularly around, the pore is permitted it follows that in the rotating disc system all diffusion is necessarily linear. In contrast, for the cyclic voltammetric case considered in our theory, the interplay or comparison between linear and convergent diffusion regimes, illustrated in Figures 3.9 and 3.14 and summarized in the zone diagrams allows the experimental distinction, at least in principle, between the two models.

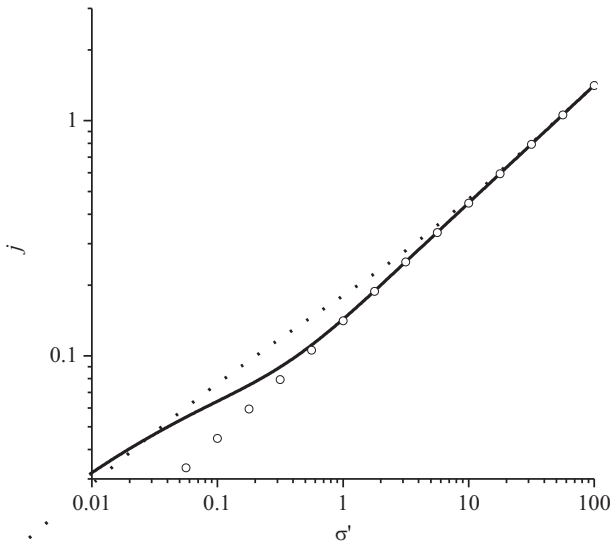

Figure 3.17: Peak current versus scan rate. Solid line - one dimensional two layer model. Next parameters were used for modeling $D_1 = 10^{-6}$ cm^2/s, $D_2 = 10^{-5}$ cm^2/s, $[A]_2^0 = [A]_1^0 = 10^{-6}$ mol/cm^3, $z_0 = 10\ \mu$m, and $v = 0.01 - 10\ V/s$, that is correspond to dimensional parameters $K_{eq} = 1, \gamma = 0.1$. Dots - two dimensional porous electrode model $L_{cyl} = 2.48$, $R_{max} = 1.5$. Open circles - peak current values calculated by generalized Randles-Ševčík equation

In short the use of cyclic voltammetry in the pin hole case can probe convergent diffusion regimes which are necessarily absent in the film permeation model. Whereas the rotating disc system removes this diffusion limit, the cyclic voltammetry does not and hence provides more sensitive mechanistic resolution.

3.6 Electro-Inactive Layers: Conclusions

The presence of electro-inactive layer on a macro or micro electrodes has a significant effect on diffusional cyclic voltammograms measured at the electrode. Different types of cyclic voltammograms can be observed on modified electrodes: generalized Randles-Ševčík, steady state and thin layer. The type of observed voltammogram depends strongly on the geometrical parameters of layer thickness and voltage scan rate. Model parameters can be extracted from cyclic voltammetry experiment if a transition from one type of voltammogram to another is observed. A change of scan rate over three orders of magnitude is easily viable experimentally and often sufficient to observe the transition. In practice uniform and porous layers can be distinguished experimentally if such a transition observed.

3.7 Electroactive Layers: Results and Discussion

3.7.1 Electrode Geometry Influence on Cyclic Voltammetry

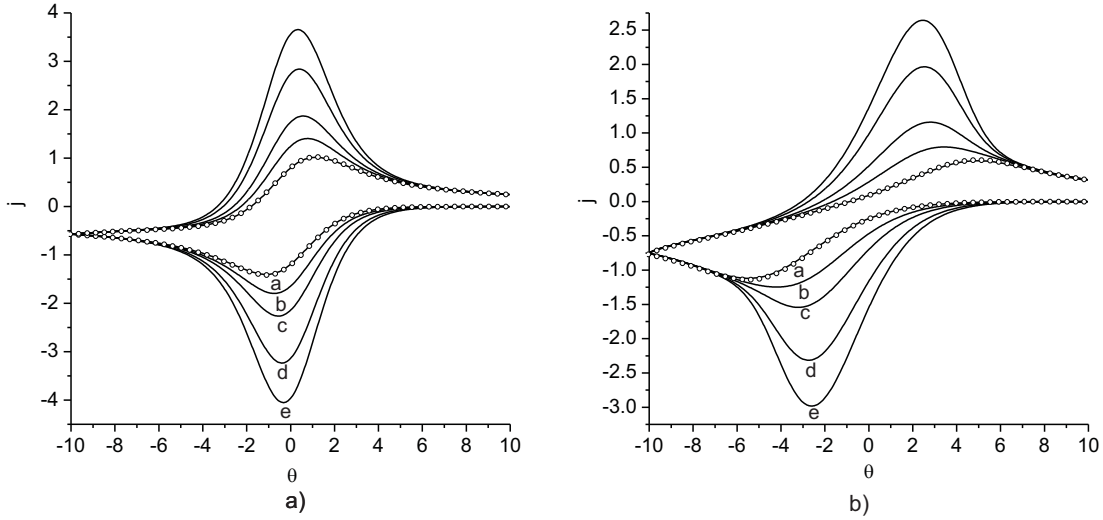

Figure 3.18: Cyclic voltammograms at different values L_{cyl}, R_{max}=2, σ=1, L_{cyl} have the following values a - 0.08 , b - 2.56, c - 10.2, d - 14.5; a) infinitely fast electron transfer b) Λ=0.1. The open dots show the cyclic voltammograms of a flat macrodisk electrode calculated with DigiSim.

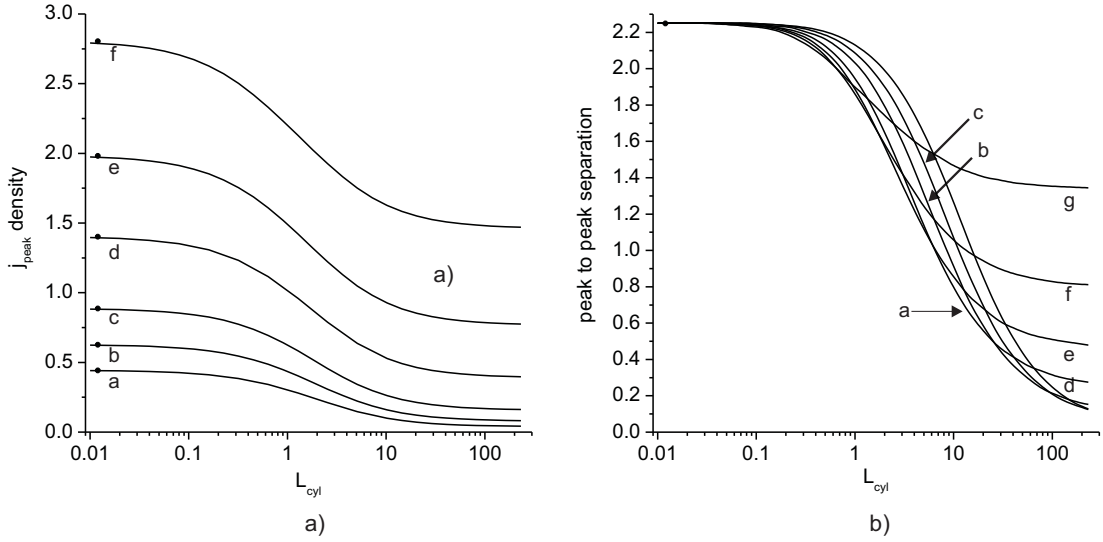

Figure 3.19: Peak current a) and peak to peak separation b) at different scan rates and cylinder depth L_{cyl} values, infinitely fast rate of electrode transfer; a - σ=0.1, b - σ=0.2, c - σ=0.4, d - σ=1, e - σ=2, f - σ=4, g - σ=10. Dots show the values calculated for the flat macroelectrode limit with DigiSim.

Cyclic voltammograms simulated at different values of the cylindrical pore depth L_{cyl} are pre-

sented in Figure 3.18. Figure 3.18 a) shows cyclic voltammograms simulated in the limit of infinitely fast electron transfer, Figure 3.18 b) shows that in case of the Butler-Volmer kinetics with dimensionless constant of electron transfer Λ=0.1. The cyclic voltammograms of electrode with cylindrical pores must converge to the limiting case for an the flat macrodisk as L_{cyl} goes to zero. The difference in a area of the flat electrode and one with cylindrical pores is

$$1 + \frac{L_{\text{cyl}}}{R_{\text{max}}^2} \tag{3.29}$$

and is less than 5% for R_{max}=2 until cylinder depth L_{cyl} reaches a value $L_{\text{cyl}} = 0.1$. Voltammograms simulated with values of cylinder depth $L_{\text{cyl}} < 0.1$ are similar for those of a flat macrodisk. In Figures 3.18 a) and b) the voltammograms labeled a were simulated for L_{cyl}=0.08 and perfectly match voltammograms simulated with DigiSim in a limit of a flat macrodisk electrode. Figure 3.18 a) and b) shows that an increase of the cylinder depth causes L_{cyl} the peak current increases and peak to peak separation decreases. The peak current density and the peak to peak separation for infinitely fast kinetics of electron transfer are presented in Figures 3.19 a) and b). The peak current density and the peak to peak separation converge to limiting values of a flat macroelectrode at low values of the cylindrical pore depth L_{cyl} for the whole range of tested scan rates. Figure 3.19 a) shows that an increase of the pore depth L_{cyl} causes the peak current density to decrease. Figure 3.22 b) shows that an increase of the pore depth L_{cyl} causes the peak to peak separation to decrease, the higher the scan rate the less the effect. Figure 3.20 shows concentration profiles calculated at different values of the cylindrical pore depth L_{cyl}: a) $L_{\text{cyl}} = 0.01$, b) $L_{\text{cyl}} = 0.1$, c) $L_{\text{cyl}} = 1$, a) $L_{\text{cyl}} = 10$. It is clearly seen from Figure 3.20 that on increase of cylindrical pore depth L_{cyl} diffusion mass transport is not efficient enough to bring electroactive species from the bulk solution and it concentration goes to zero in the pore. Wherefore decrease of peak current density and peak to peak separation are observed. The thickness of the diffusion layer l_{D} decreases in agreement with expression:

$$l_{\text{D}} \propto \sqrt{\tau} \propto \frac{1}{\sqrt{\sigma}} \tag{3.30}$$

on increase of the scan rate. At high scan rates the thickness of the diffusional layer becomes small and diffusional fluxes to the bottom of the electrode and to the top do not interfere with each other, in other words efficiency of diffusional mass transport increase. Peak current density and peak to peak

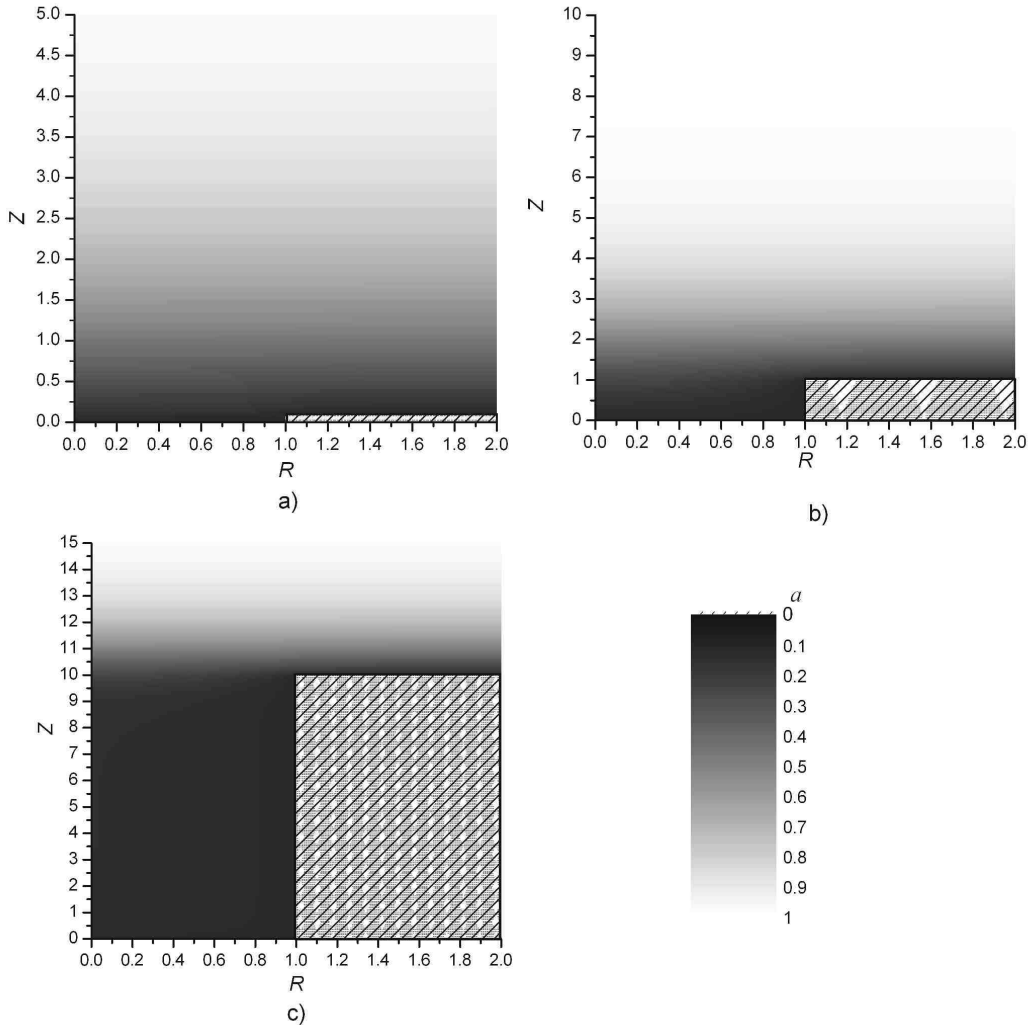

Figure 3.20: Concentration profiles taken at θ=-2, σ=1, $R_{\max}$ infinitely fast electron transfer a) L_{cyl}=0.1; b) $L_{\text{cyl}} = 1$; c) $L_{\text{cyl}} = 10$.

separation for Butler-Volmer kinetics with dimensionless constant of electron transfer $\Lambda = 0.1$ versus the depth of cylindrical pore L_{cyl} are presented in Figures 3.21 a) and b). In the case of Buler-Volmer kinetics the peak to peak separation and peak current density depend on L_{cyl} and scan rate similarly to infinitely fast electron transfer.

Figure 3.22 shows the influence of the ratio of an electrode domain radius to that of a pore on the peak to peak separation. Infinitely fast electron transfer (Figure 3.22 a)) and Butler-Volmer (Figure 3.22 b)) kinetics are considered. On increase of $R_{\max}$, the peak to peak separation goes to the limiting values of a flat macrodisk electrode.

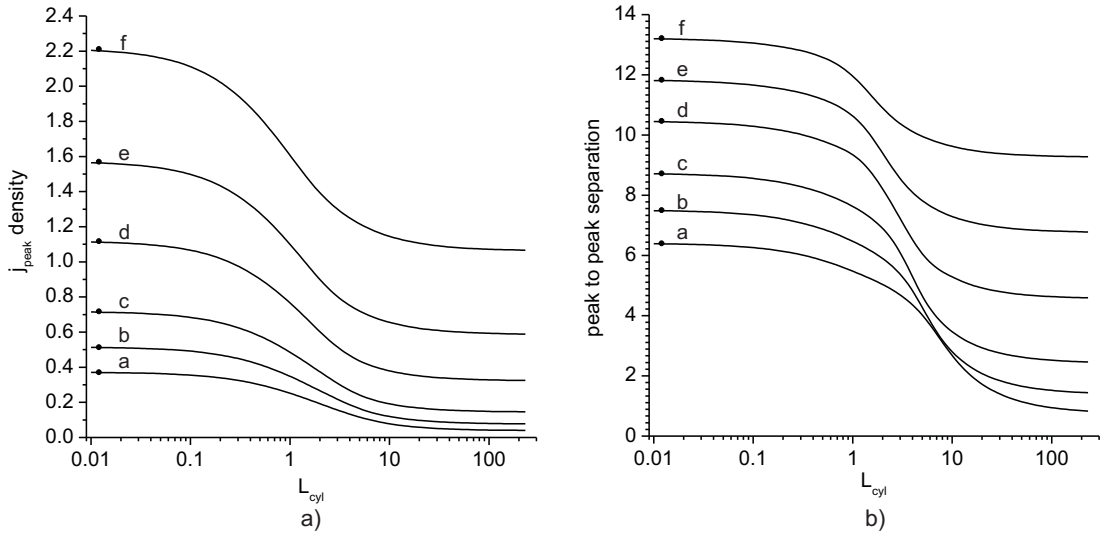

Figure 3.21: Peak current a) and peak to peak separation b) at different scan rates and cylinder depth L_{cyl} values, Λ=0.1; a - σ=0.1, b - σ=0.2, c - σ=0.4, d - σ=1, e - σ=2, f - σ=4. Dots show the values calculated for the flat macroelectrode limit with DigiSim.

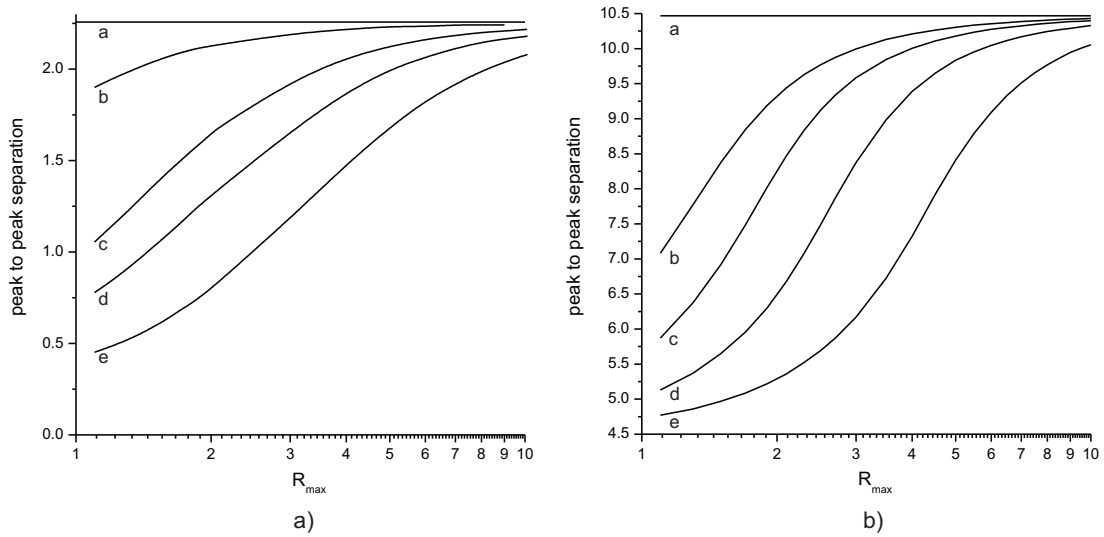

Figure 3.22: Peak to peak separation versus domain size R_{max} a) Infinitely fast electrode transfer b) Λ=0.1. a corresponds to the flat macrodisk limit; b - L_{cyl}=1; c - L_{cyl}=2; d - L_{cyl}=4; e - L_{cyl}=10;

Figure 3.23 shows Randles-Sevcik plots for infinitely fast electron transfer and Butler-Volmer kinetics, Λ =0.1. From Figures 3.23 a) and b) is seen that the deeper the pore, L_{cyl}, the higher deviation from linear curve. The deviation from the linear curve in coordinates j_{peak} is observed because an increase in the dimensionless scan rate causes the efficiency of mass transport to increase

(see Figure 3.20).

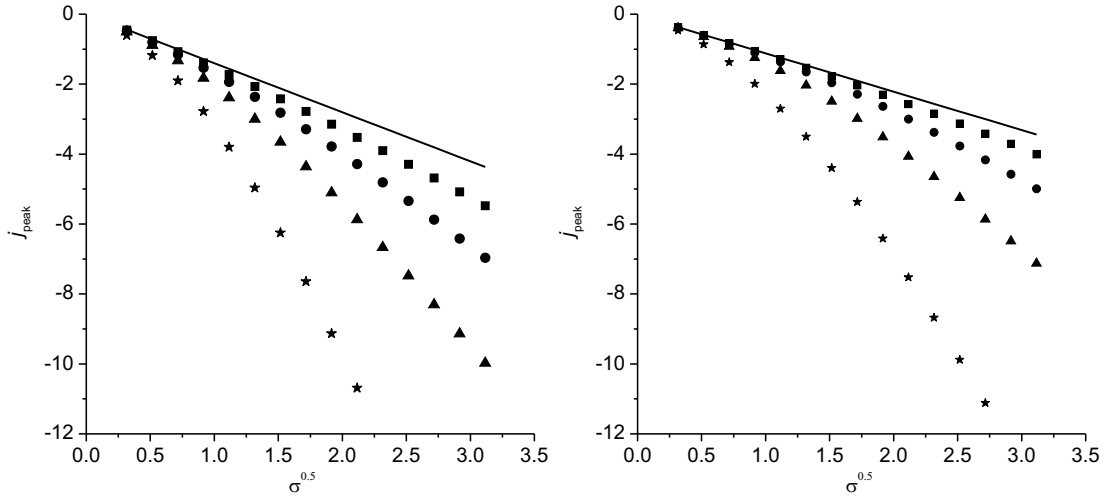

Figure 3.23: Peak current versus $\sigma^{-0.5}$ a) infinitely fast electrode transfer b) $\Lambda = 0.1$. Square, dots, triangles and stars correspond to values L_{cyl} equal to 1, 2, 4 and 10. Lines show the values calculated for the planar diffusion flat macroelectrode limit with DigiSim.

3.7.2 Extracting Kinetic Data from Cyclic Voltammogram

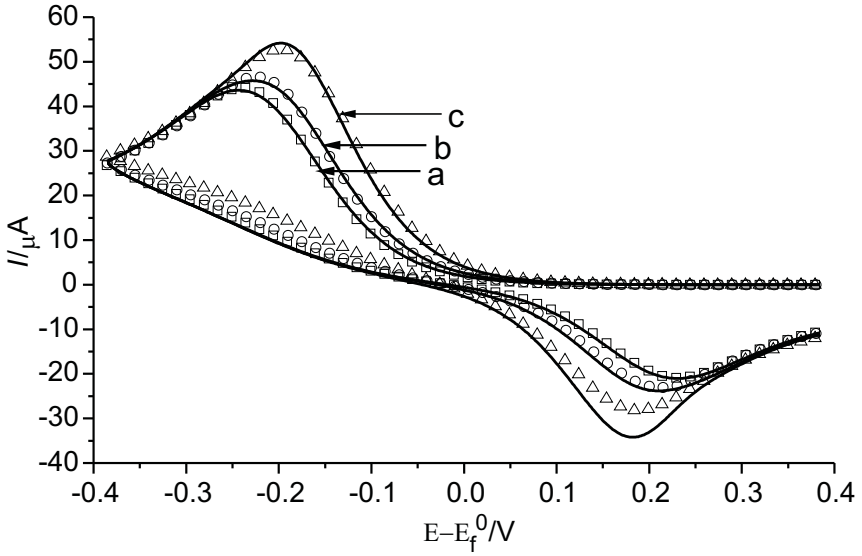

Figure 3.24: Cyclic voltammograms simulated at different values of the cylindrical pore depth L_{cyl}: a - $L_{\text{cyl}} = 1.28$, b - L_{cyl}=2.56, c - $L_{\text{cyl}} = 5.12$. Symbols show the best fit with DigiSim: squares - $L_{\text{cyl}} = 1.28$, circles - L_{cyl}=2.56, triangles - L_{cyl}=5.12. The parameters of the model: $r_0 = 1 \times 10^{-3}$ cm, $r_e = 0.1$ cm, R_{max}=2, $D = 1 \times 10^{-5}$ cm^2 s^{-1}, k_0=1×10^{-3} cm s^{-1}, α=0.5, scan rate is 0.26 V s^{-1}.

Table 3.6: Boundary and initial conditions for model describing electrodes covered with a uniform layer

L_{cyl}	D(cm^2 s^{-1})	k_0 cm s^{-1}
0.01	1.1×10^{-5}	1×10^{-3}
1.28	1.1×10^{-5}	1.6×10^{-3}
2.56	1.2×10^{-5}	2.3×10^{-3}
5.12	1.5×10^{-5}	5.3×10^{-3}

The peak to peak separation is a common criterion of the reversibility of electron transfer.[43] This criteria is applicable only in case of semi-infinite diffusion to flat macrodisk, because if the surface of electrode is not flat peak to peak separation depends not only on the rate of electron transfer, but also on the surface geometry (Figures 3.18, 3.19, 3.21). Quantitative values of the electron transfer rate can be extracted from cyclic voltammograms measured at flat electrodes by fitting data with commercial packages e.g. DigiSim. However, this should be done with attention to the type of diffusion and to the morphology of the surface. Figure 3.24 shows cyclic voltammograms simulated for the macroelectrode with an array of cylindrical pores and their fit with DigiSim. The parameters of the model: r_0=1×10^{-3} cm, $r_e = 0.1$ cm, $R_{max} = 2$, $D = 1 \times 10^{-5}$ cm^2 s^{-1}, $k_0 = 1 \times 10^{-3}$ cm s^{-1}, $\alpha = 0.5$, scan rate is 0.26 V s^{-1}. The fits of cyclic voltammograms are of reasonable quality, however the kinetic data extracted from then are incorrect (Table 3.6).

3.8 Electroactive Layers: Conclusions

The presence of the array of cylindrical pores on a macrodisk electrode has a significant effect on cyclic voltammograms, particularly on the peak current and the peak to peak separation. On increase of the cylinder depth the peak current density decreases and the peak to peak separation increases. Standard methods of electron transfer rate determination are not applicable in this case. The results presented above allow the inference of kinetic parameters for the case of a porous layer on a macroelectrode subjected to planar diffusion. Note that the case of porous layer on microelectrode under convergent diffusion conditions remains unexplored.

References

[1] Winter, M.; Brodd, R. J. *Chem Rev* **2004,** *104,* 4245-4270.

[2] Yao, K. Z.; Karan, K.; McAuley, K. B.; Oosthuizen, P.; Peppley, B.; Xie, T. *Fuel Cell* **2004,** *4,* 3-29.

[3] Blanco-Lopez, M. C.; Gutierrez-Fernandez, S.; Lobo-Castanon, M. J.; Miranda-Ordiere, A. J.; Tunon-Blanco, P. *Anal Bioanal Chem* **2004,** *378,* 1922-1928.

[4] Lyons, M. E. G.; Greer, J. C.; Fitzeraland, C. A.; Bannon, T.; Barlett, P. N. *The Analyst* **1996,** *121,* 715-731.

[5] Bard, A. J.; Faulkner, L. R. *Electrochemical Methods: Fundamentals and Application;* John Wiley and Sons: New York, 2001.

[6] Miller, C.; Cuendet, P.; Graetzel, M. *J Phys Chem* **1991,** *85,* 877-886.

[7] Ganesh, V.and Lakshminarayanan, V. *Langmuir* **2006,** *22,* 1561-1570.

[8] Fan, F.-R.; Yang, J.; Cai, L.; Price, D. W.; Dirk, S. M.; Kosynkin, D. V.; Yao, Y.; Rawlett, A. M.; Tour, J. M.; Bard, A. J. *J Am Chem Soc* **2002,** *124,* 5550-5560.

[9] Leddy, J.; Bard, A. J. *J Electroanal Chem* **1983,** *153,* 223-242.

[10] Chevallier, F. G.; Jiang, L.; Jones, T. G. J.; Compton, R. G. *J Electroanal Chem* **1983,** *153,* 223-242.

[11] Finklea, H. O.; A., S. D.; Fedyk, J. *Langmuir* **1990,** *6,* 371-376.

[12] Finklea, H. O.; Avery, S.; Lynch, M.; Furtsch, T. *Langmuir* **1987,** *3,* 409-413.

[13] Finklea, H. O.; Snider, D. A.; Fedyk, J.; Sabatani, E.; Gafni, Y.; Rubinstein, I. *Langmuir* **1993,** *9,* 3660-3667.

[14] Calvente, J. J.; Lopez-Perez, G.; Ramirez, P.; Fernandez, H.; Zon, M. A.; Mulder, W. H.; R., A. *J Am Chem Soc* **2005,** *127,* 6476-6486.

[15] de Levie, R. *Electrochim Acta* **1964,** *9,* 1231-1245.

[16] de Levie, R. *Adv Electrochem Electrochem Eng* **1967,** *6,* 329-398.

[17] Raistrick, I. D. *Electrochim. Acta.* **1990,** *35,* 1579-1586.

[18] Davies, T. J.; Ward-Jones, S.; Banks, C. E.; Del Campo, J.; Mas, R.; Munoz, F. X.; Compton, R. G. *J Electroanal Chem* **2005,** *585,* 51-62.

[19] Davies, T. J.; Compton, R. G. *J Electroanal Chem* **2005,** *585,* 63-82.

[20] Beriet, C.; Ferrigno, R.; Girault, H. H. *J Electroanal Chem* **2000,** *486,* 56-64.

[21] Lee, H. J.; Beriet, C.; Ferrigno, R.; Girault, H. H. *J Electroanal Chem* **2001,** *502,* 138-145.

[22] Scharikfer, B. R. *J Electroanal Chem* **1988,** *240,* 61-76.

[23] Amatore, C.; Saveant, J. M.; Tessier, D. *J Electroanal Chem* **1983,** *147,* 39-51.

[24] Saveant, J.-M. *J Electroanal Chem* **1991,** *302,* 91-101.

[25] Raistrick, I. *Electrochim Acta* **1990,** *35,* 1579-1586.

[26] Chirkov, Y.; Rostokin, V. *Rus. J. Electrochem* **2002,** *12,* 1437.

[27] Pajkossy, T.; Borosy, A.; Imre, A.; Martemyanov, S.; Nagy, G.; Schiller, R.; Nyikos, L. *J Electroanal Chem* **1994,** *366,* 69-73.

[28] Chevallier, F.; Jiang, L.; Jones, T.; Compton, R. *J Electroanal Chem* **2006,** *587,* 254-262.

[29] Viner, A. S.; Fedkiw, P. S. *J Electrochem Soc* **1990,** *137,* 1435-1444.

[30] Weidner, J. W.; Fedkiw, P. S. *J Electrochem Soc* **1991,** *138,* 2514-2526.

[31] Pollard, R.; Newman, J. *Electrochim Acta* **1980,** *25,* 315-321.

[32] Austin, L.; Lerner, H. *Electrochim Acta* **1964,** *9,* 1469-1481.

[33] Ksenzhek, O. *Electrochim Acta* **1964,** *9,* 629-637.

[34] Brookes, B. A.; Davies, T. J.; Fisher, A. C.; Evans, R. G.; Wilkins, S. J.; Yunus, K.; Wadhawan, J. D.; Compton, R. G. *J Phys Chem B* **2003,** *107,* 1616-1627.

[35] Svir, I. B.; Klymenko, O. V.; Compton, R. G. *Radiotekhnika* **2001,** *118,* 92-101.

[36] Rudolph, M.; Reddy, D. P.; Feldberg, S. W. *Anal Chem* **1994,** *66,* 589A-600A.

[37] Atkinson, K. *Elementary Numerical Analysis, 3rd ed;* John Wiley and Sons: New York, 2004.

[38] Gavaghan, D. *J Electroanal Chem* **1998,** *456,* 1-12.

[39] Dickinson, E. J. F.; Streeter, I.; Compton, R. G. *J Phys Chem B* **2008,** *112,* 4059-4066.

[40] Dickinson, E. J. F.; Streeter, I.; Compton, R. G. *J Phys Chem C* **2008,** *112,* 11637-11644.

[41] Peaceman, J.; Rachford, H. *J Soc Ind Appl Math* **1955,** *3,* 28-41.

[42] Compton, R. G.; Banks, C. E. *Understanding Voltammetry;* World Scientific: Singapore, 2007.

[43] Davies, T.; Banks, C.; Compton, R. *J Solid State Electrochem* **2005,** *9,* 797-808.

Chapter 4

Voltammetry of Proton Coupled Electrochemical Reduction of Surface Bound Species

4.1 Introduction

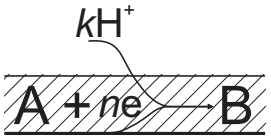

Figure 4.1: Schematic diagram of an electrode covered with a uniform layer of surface confined molecules which react electrochemically with solution phase protons.

Electron transfer reactions coupled with a proton transfer are ubiquitous in chemistry and biology. Two recent reviews are devoted to these reactions.[1,2] The majority of quantitative electrochemical studies of proton-coupled electron transfer are done for molecules freely diffusing in fully buffered solutions, this includes various organic molecules: anthracene,[3] thiol/disulfide,[4] methyl isonicotinate,[5] p-diacetylbenzene,[6] isonicotinic acid,[7] 1-methyl-4-carboxy pyridinium[8] 4-nitropyridine,[9] 4-nitropyridine N-oxide,[10] p-nitrobenzophenone;[11] molecules or their syntethetic analogs which play key roles in biosystems: thionicotinamide,[12] isonicotinamide,[13] vitamin E,[14] dopamine and ascorbic acid,[15] synthetic analogues of dihydronicotamide adenine dinucleotide;[16] metal complexes designed for water oxidation.[17–19] Theory as proposed by Laviron[20,21] have been successfully used to interpret experimental data, including modeling of experimental data in a full range of pH available in aqueous solution.[22] In contrast very few works are dedicated to studies of freely diffusing molecules in unbuffered media.[23,24] Surface bound molecules which undertake proton-coupled electron transfer has also been studied electrochemically, including self assembled monolayers of quinones with a long alkaline chains,[25,26] hydroquinone derivatives,[27] poly(vinyl hydroquinone)s,[28] poly(vinyl benzoquinone)s,[29] adsorbed mercaptohydroquinon,[30] adsorbed anthraquinone-2,7-disulfonic acid,[31] azobenzene SAM,[32] anthraquinone-2,7-disulfonic acids[33] and various osmium complexes.[34–36] Most of the voltammetric studies of surface bound molecules has been done in a fully buffered solutions[27,29,31–33,35,36] It was found that in

an unbuffered media shape of the cyclic voltamograms of adsorbed 2-mercaptohydroquinone strongly depends on the scanrate.[30] A full theory for such processes has not hitherto been developed.

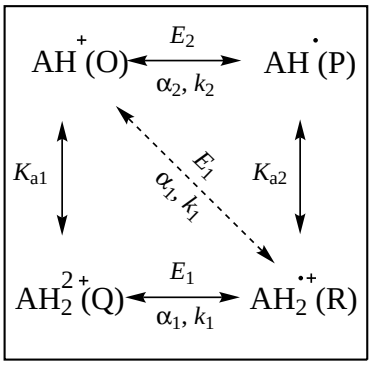

Figure 4.2: "Scheme of squares" for $1H^+$, $1e$ reduction. Solid horizontal and vertical arrows show stepwise mechanism: horizontal reactions are electrochemical transformations and vertical reactions are protonation/deprotonation of surface bound species. The concerted mechanism is shown by dashed arrows.

Here we establish a general theory for the voltammetry of surface confined molecules which electrochemical transformation are coupled with protonation/deprotonation reactions, building on the pioneering work by Jacq[37] and later works by Laviron[20,21] which assumed the protonation reaction to be infinitely fast. However in this study proton mass transfer is considered for three cases: the limiting case of infinitely fast proton mass transport (fully buffered solution) studied earlier, the limiting case of electrodes with infinitely high coverage in which only the protons which are situated in the proximity of electrode surface may be consumed and finally the general case where proton mass transport to the electrode has a finite rate and is described by Fick's laws of diffusion. Moreover in our theory we are not limited to the assumption of equality of all transfer coefficients $\alpha_i = 0.5$ made by Laviron. Finally we also consider a concerted mechanism of proton-coupled electron transfer in buffered and unbuffered media. Concerted mechanism of proton-coupled electron transfer is complex at microscopic level, since involves simultaneous transfer of electron and proton from donor(s) orbitals to that of acceptor(s), however it might be energetically more favorable than stepwise pathways.[1,2,38,39] Recently Costenin *et al.* reported concerted proton-coupled electron transfer during electrochemical reactions of phenols and osmium complexes.[40,41]

4.2 Theoretical Model

We consider a macroelectrode covered with a uniform layer of surface confined molecules as shown in Figures 4.1. Surface bound molecules react electrochemically according to scheme 4.1:

$$A + ne + kH^+ \leftrightarrow B \tag{4.1}$$

Here we first in detail consider the stepwise and concerted mechanisms for the one electron one, proton reduction of species A (Figure 4.2). We assume that the protonation/deprotonation reactions are infinitely fast and are characterised by the acid dissociation constant, K_a. In both cases of stepwise and concerted mechanisms the rate of the electron transfer is assumed to be described by Butler-Volmer kinetics.[42] Further we consider the stepwise and concerted mechanisms for two proton, two electron reductions as shown in Figure 4.3.

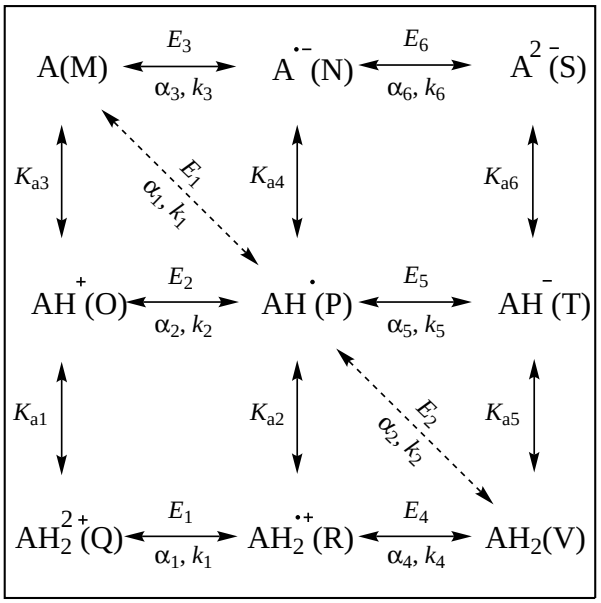

Figure 4.3: "Scheme of squares" for $2H^+$, $2e$ reduction. Solid horizontal and vertical arrows show the stepwise mechanism: horizontal reactions are electrochemical transformations and vertical reactions are protonation/deprotonation of surface bound species. The concerted mechanism is shown by dashed arrow.

The electrochemical reactions described by stepwise and concerted mechanisms (Figures 4.2 and 4.3) are favorably and necessarily accompanied by proton consumption that can affect the local pH of the solution in the proximity of the electrode surface if solution is not fully buffered. The mass transfer of protons is assumed to be exclusively due to diffusion and is described by the Fick's second law of diffusion (equation 4.2).

$$\frac{\partial[\mathrm{H}^+]}{\partial t} = D\frac{\partial^2[\mathrm{H}^+]}{\partial Z^2} \tag{4.2}$$

We assume here that the solution contains a sufficiently high concentration of electroinactive electrolyte and therefore is fully supported.[43] We also assume that the experiments are conducted on a timescale where convection can be neglected.

We next consider a cyclic voltammetry experiment applied to the reduction of A according to scheme 4.1. The potential changes are in agreement with Equation 4.3a before a switching potential (E_s) and E_s and then follows equation 4.3b after the switch potential.

$$E = E_{\mathrm{in}} - vt \tag{4.3a}$$

$$E = E_s + vt \tag{4.3b}$$

where E_{in} is the initial potential and v is a voltage scan rate.

4.2.1 Mathematical Model

One Electron, One Proton Reduction: Stepwise Mechanism

Table 4.1: Dimensionless parameters used for numerical simulation.

Parameter	Expression (Stepwise)	Expression (Concerted)
normal (z) coordinate	$z = Z\sqrt{\frac{vF}{DRT}}$	$z = Z\sqrt{\frac{vF}{DRT}}$
time	$\tau = \frac{tvF}{RT}$	$\tau = \frac{tvF}{RT}$
scan rate	1	1
over potential i	$\eta_{\text{i}} = \frac{F(E-E_{\text{i}}^0)}{RT}$ [a]	$\eta_{\text{i}} = \frac{F(E-E_{\text{i}}^0)}{RT}$
coverage of species i	$\gamma_{\text{i}} = \Gamma_{\text{i}}/\Gamma_{\text{tot}}$	$\gamma_{\text{i}} = \Gamma_{\text{i}}/\Gamma_{\text{tot}}$
concentration of protons	$a = [\text{H}^+]/[\text{H}^+]_0^b$	$a = [\text{H}^+]/[\text{H}^+]^{\star c}$
rate constant	$\Lambda_{\text{i}} = \frac{k_{\text{i}}RT}{vF}$	$\Lambda_{\text{i}} = \frac{k'_{\text{i}}[\text{H}^+]^{\star}RT}{vF}$
equilibrium constant	$\chi_{\text{i}} = \frac{K_{\text{i}}}{[\text{H}^+]_0}$	$\chi_{\text{i}} = \frac{K_{\text{i}}}{[\text{H}^+]^{\star}}$
surface coverage	$\beta = \frac{[\text{H}^+]}{\Gamma_{\text{tot}}}\sqrt{\frac{DRT}{vF}}$	$\beta = \frac{[\text{H}^+]}{\Gamma_{\text{tot}}}\sqrt{\frac{DRT}{vF}}$
Electrode flux	$j = \frac{iRT}{AF^2\Gamma_{\text{tot}}v}$	$j = \frac{iRT}{AF^2\Gamma_{\text{tot}}v}$

[a] These parameters are not independent, see text for details. Note, here we refer to three various concentration of protons in solution: [b] $[\text{H}^+]_0$ initial concentration in a buffered solution, $[\text{H}^+]$ immediate local proton concentration and [c] standard concentration $[\text{H}^+]^* = 1 \times 10^3$ mol/m^3.

The mathematical model of scheme shown in Figure 4.2 has five variables: the surface coverages of species O, P, Q and R are denoted as $\Gamma_{\text{O}}, \Gamma_{\text{P}}, \Gamma_{\text{Q}}, \Gamma_{\text{R}}$ respectively and $[\text{H}^+]_{\text{s}}$ represents the proton concentration at the electrode surface. To formulate a closed system of mathematical equations, five equations must be written down. Two of these are given by the acid dissociation constants:

$$K_{\text{a1}} = \frac{\Gamma_{\text{O}}[\text{H}^+]_{\text{s}}}{\Gamma_{\text{Q}}} \tag{4.4}$$

$$K_{\text{a2}} = \frac{\Gamma_{\text{P}}[\text{H}^+]_{\text{s}}}{\Gamma_{\text{R}}} \tag{4.5}$$

The third equation is the mass conservation law:

$$\Gamma_{\text{tot}} = \Gamma_{\text{O}} + \Gamma_{\text{Q}} + \Gamma_{\text{P}} + \Gamma_{\text{R}} \tag{4.6}$$

where, Γ_{tot} are a total surface coverage.

The electrochemical transformations of surface confined molecules are given by the Butler-Volmer equation 4.7:

$$\begin{aligned} \frac{d\Gamma_{\text{Ot}}}{dt} &= -\Gamma_{\text{O}}(\Gamma_{\text{Ot}}, [\text{H}^+]_{\text{s}}) k_2 e^{-\alpha_2 \eta_2} + \Gamma_{\text{P}}(\Gamma_{\text{Pt}}, [\text{H}^+]_{\text{s}}) k_2 e^{(1-\alpha_2)\eta_2} \\ &\quad -\Gamma_{\text{Q}}(\Gamma_{\text{Ot}}, [\text{H}^+]_{\text{s}}) k_1 e^{-\alpha_1 \eta_1} + \Gamma_{\text{R}}(\Gamma_{\text{Pt}}, [\text{H}^+]_{\text{s}}) k_1 e^{(1-\alpha_1)\eta_1} \end{aligned} \tag{4.7}$$

where, $\eta_{\text{i}} = \frac{F(E-E_{\text{i}}^0)}{RT}$, α_{i} is a transfer coefficient of i^{th} reaction and $\Gamma_{\text{Ot}} = \Gamma_{\text{O}} + \Gamma_{\text{Q}}$, $\Gamma_{\text{Pt}} = \Gamma_{\text{P}} + \Gamma_{\text{R}}$.

The proton concentration at electrode surface can be calculated using Fick's second law of diffusion (equation 4.2) accompanied by the boundary conditions:

$$D\frac{\partial [\text{H}^+]}{\partial Z} = \frac{\partial \Gamma_{\text{O}}}{\partial t} + \frac{\partial \Gamma_{\text{P}}}{\partial t} \tag{4.8}$$

at the electrode surface and $[\text{H}^+] = [\text{H}^+]_0$ in the bulk of the solution.

Independence of Parameters. It should be noted that not all parameters shown in scheme in Figure 4.2 are independent. The potentials E_2^0 and E_1^0 are linked by the Nernst equation:

$$E_1^0 = E_2^0 + \frac{RT}{F} \ln \frac{K_{\text{a1}}}{K_{\text{a2}}} \tag{4.9}$$

Dimensionless Parameters.

We chose the scan rate $\frac{vF}{RT}$ as a time scale for the model. Dimensionless parameters used in this work are presented in Table 4.1. Equations 4.2 - 4.7 can be combined to eliminate variables $\Gamma_{\text{R}}, \Gamma_{\text{Q}}$ and written in the dimensionless form below:

$$\gamma_0 (1 + \frac{\text{a}}{\chi_1}) + \gamma_{\text{P}} (1 + \frac{\text{a}}{\chi_2}) = 1 \tag{4.10}$$

$$\frac{d\gamma_O}{d\tau}(1+\frac{a}{\chi_1})+\gamma_O\frac{da}{d\tau}(\frac{1}{\chi_1}) = -\gamma_O\Lambda_2 e^{-\alpha_2\eta_2}+\gamma_P\Lambda_2 e^{(1-\alpha_2)\eta_2} - \frac{a\gamma_O}{\chi_1}\Lambda_1 e^{-\alpha_1\eta_1}+\frac{a\gamma_P}{\chi_2}\Lambda_1 e^{(1-\alpha_1)\eta_1} \quad (4.11)$$

$$\frac{\partial a}{\partial \tau}=\frac{\partial^2 a}{\partial z^2} \quad (4.12)$$

The dimensionless form of Fick's second law of diffusion (equation 4.12) is accompanied by the dimensionless boundary conditions:

$$\beta\frac{\partial a}{\partial z}=\frac{\partial \gamma_O}{\partial \tau}+\frac{\partial \gamma_P}{\partial \tau} \quad (4.13)$$

at the electrode surface, and $a = 1$ in the bulk of the solution.

Analytical Solution for the Case of Infinitely High Surface Coverage

Limiting case which we consider here is that of infinitely slow mass transport, when only protons situated in the proximity of the surface are involved with the chemical reaction. Here we use a protons surface coverage Γ_H instead of a proton concentration $[H^+]$; note that $\Gamma_H = [H^+] * l$, where l is a layer thickness in which protons can react electrochemically. In the case where the coverage of the electrochemically active species is significantly higher than that of the protons a simple analytical solution was derived for the problem. Equation 4.14 is the mass conservation law for protons adsorbed on surface.

$$\gamma_Q+\gamma_R+\gamma_a=\gamma_{atot} \quad (4.14)$$

Value of γ_{atot} can be evaluated by considering equation 4.14 at the potential sufficiently positive, that the presence of forms P and Q is negligibly small:

$$\gamma_{atot}=\frac{1}{1+\chi_1} \quad (4.15)$$

We further assume that rate of electron transfer is infinitely high:

$$\gamma_P=\gamma_O e^{\theta} \quad (4.16)$$

Combining equations 4.14-4.16 with the mass conservation law for the surface bound specie 4.10

following equation can be derived:

$$\gamma_O = \frac{\chi_1}{(1+e^{-\theta})(1+\chi_1)} \tag{4.17}$$

$$\gamma_O = \frac{\chi_2}{(\chi_2+e^{-\theta}\chi_1)(1+\chi_1)} \tag{4.18}$$

Finally voltammogram can be calculated according to the equation 4.19

$$j = \frac{iRT}{vF^2\Gamma_t A} = \frac{d(\gamma_O+\gamma_Q)}{d\theta} = \frac{e^{\theta}\chi_1(\chi_2(1+e^{\theta})^2+(\chi_1+\chi_2 e^{\theta})^2)}{(1+e^{\theta})^2(1+\chi_1)(\chi_1+\chi_2 e^{\theta})^2} \tag{4.19}$$

One Electron, One Proton Reduction: Concerted Mechanism

The electrochemical reaction is described by a Butler-Volmer type equation:

$$\frac{\partial\Gamma_{tot}}{\partial t} = -k_0\Gamma_A[H^+]e^{-\alpha\eta} + k_b(\Gamma_{tot}-\Gamma_A)e^{(1-\alpha)\eta} \tag{4.20}$$

where, $k_b = k_0[H^+]^*$.[44]

Mass transport is described by Fick's second law of diffusion as given by equation 4.2 accompanied by the boundary condition:

$$D\frac{\partial[H^+]}{\partial Z} = \frac{\partial\Gamma_A}{\partial t} \tag{4.21}$$

Dimensionless Parameters. Dimensionless parameters used here are presented in Table 4.1 and the dimensionless equations are given below:

$$\frac{\partial\gamma}{\partial\tau} = -\Lambda\gamma a e^{-\alpha\eta} + \Lambda(1-\gamma)e^{(1-\alpha)\eta} \tag{4.22}$$

$$\beta\frac{\partial\gamma}{\partial\tau} = \frac{\partial a}{\partial x} \tag{4.23}$$

The dimensionless equation 4.12 describes mass transport.

Two Electron, Two Proton Reductions: Stepwise Mechanism

The mathematical model of a surface bound species as presented in Figure 4.3 has ten variables: nine surface coverages Γ_i and $[H^+]_s$ the proton concentration at the electrode surface. To formulate a closed system of mathematical equations, ten equations must be written down. Six equations are

given by the acid dissociation constants:

$$K_{a1} = \frac{\Gamma_O[H^+]_s}{\Gamma_Q}, K_{a2} = \frac{\Gamma_P[H^+]_s}{\Gamma_R}, K_{a3} = \frac{\Gamma_M[H^+]_s}{\Gamma_O}$$
$$K_{a4} = \frac{\Gamma_N[H^+]_s}{\Gamma_P}, K_{a5} = \frac{\Gamma_T[H^+]_s}{\Gamma_V}, K_{a6} = \frac{\Gamma_S[H^+]_s}{\Gamma_T} \tag{4.24}$$

The seventh equation is the mass conservation law:

$$\Gamma_{tot} = \Gamma_M + \Gamma_N + \Gamma_S + \Gamma_O + \Gamma_P + \Gamma_T + \Gamma_Q + \Gamma_R + \Gamma_V \tag{4.25}$$

The electrochemical transformations of surface confined molecules are given by the equations:

$$\begin{aligned} \frac{d\Gamma_{Ot}}{dt} &= -M(\Gamma_{Ot}, [H^+]_s)k_3 e^{-\alpha_3\eta_3} + \Gamma_N(\Gamma_{Pt}, [H^+]_s)k_3 e^{(1-\alpha_3)\eta_3} \\ &\quad -\Gamma_O(\Gamma_{Ot}, [H^+]_s)k_2 e^{-\alpha_2\eta_2} + \Gamma_P(\Gamma_{Pt}, [H^+]_s)k_2 e^{(1-\alpha_2)\eta_2} \\ &\quad -\Gamma_Q(\Gamma_{Ot}, [H^+]_s)k_1 e^{-\alpha_1\eta_1} + \Gamma_R(\Gamma_{Pt}, [H^+]_s)k_1 e^{(1-\alpha_1)\eta_1} \end{aligned} \tag{4.26}$$

$$\begin{aligned} \frac{d\Gamma_{Tt}}{dt} &= -\Gamma_S(\Gamma_{Ot}, [H^+]_s)k_3 e^{-\alpha_3\eta_3} + \Gamma_N(\Gamma_{Pt}, [H^+]_s)k_3 e^{(1-\alpha_3)\eta_3} \\ &\quad -\Gamma_T(\Gamma_{Ot}, [H^+]_s)k_5 e^{-\alpha_5\eta_5} + \Gamma_P(\Gamma_{Pt}, [H^+]_s)k_5 e^{(1-\alpha_5)\eta_5} \\ &\quad -\Gamma_V(\Gamma_{Ot}, [H^+]_s)k_4 e^{-\alpha_1\eta_1} + \Gamma_R(\Gamma_{Pt}, [H^+]_s)k_4 e^{(1-\alpha_4)\eta_4} \end{aligned} \tag{4.27}$$

where, $\Gamma_{Ot} = \Gamma_M + \Gamma_O + \Gamma_Q, \Gamma_{Pt} = \Gamma_N + \Gamma_P + \Gamma_R, \Gamma_{Tt} = \Gamma_S + \Gamma_T + \Gamma_V$ The tenth equation is Fick's second law of diffusion (equation 4.2) accompanied by the boundary conditions:

$$D\frac{\partial[H^+]}{\partial x} = \frac{\partial\Gamma_O}{\partial t} + 2\frac{\partial}{\partial t}\frac{\Gamma_O[H^+]}{K_{a1}} + \frac{\partial\Gamma_P}{\partial t} + 2\frac{\partial}{\partial t}\frac{\Gamma_P[H^+]}{K_{a2}} + \frac{\partial\Gamma_T}{\partial t} + 2\frac{\partial}{\partial t}\frac{\Gamma_T H^+}{K_{a5}} \tag{4.28}$$

at the electrode surface and $[H^+] = [H^+]_0$ in the bulk of the solution.

Independence of Parameters. It should be noted that not all parameters shown in Figure 4.3 are independent. Here we chose the potentials E_2^0 and E_5^0 to be independent and the rest can be calculated

using the Nernst equation:

$$E_1^0 = E_2^0 + \frac{RT}{F}\ln\frac{K_{a1}}{K_{a2}} \tag{4.29}$$

$$E_3^0 = E_2^0 + \frac{RT}{F}\ln\frac{K_{a4}}{K_{a3}} \tag{4.30}$$

$$E_4^0 = E_5^0 + \frac{RT}{F}\ln\frac{K_{a2}}{K_{a5}} \tag{4.31}$$

$$E_6^0 = E_5^0 + \frac{RT}{F}\ln\frac{K_{a6}}{K_{a4}} \tag{4.32}$$

Dimensionless Parameters. The dimensionless parameters selected are similar to that used in the one electron, one proton model and are presented in Table 4.1. Equations 4.24 - 4.28 are combined to eliminate variables Γ_R, Γ_Q, Γ_V, Γ_M, Γ_N, Γ_S and are written in dimensionless form below:

$$\begin{aligned}
&\frac{d\gamma_O}{d\tau}(1+\frac{a}{\chi_1}+\frac{\chi_3}{a})+\gamma_O\frac{da}{d\tau}(\frac{1}{\eta_1}-\frac{\eta_3}{a^2}) = \\
&-\frac{\chi_3\gamma_O}{a}\Lambda_3 e^{-\alpha_3\eta_3}+\frac{\chi_4\gamma_P}{\mathrm{a}}\Lambda_3 e^{(1-\alpha_3)\eta_3} \\
&-\Gamma_O\Lambda_2 e^{-\alpha_2\eta_2}+\Gamma_P\Lambda_2 e^{(1-\alpha_2)\eta_2} \\
&-\frac{a\gamma_O}{\chi_1}e^{-\alpha_1\eta_1}+\frac{a\gamma_P}{\chi_2}\Lambda_1 e^{(1-\alpha_1)\eta_1}
\end{aligned} \tag{4.33}$$

$$\begin{aligned}
&\frac{d\gamma_T}{d\tau}(1+\frac{a}{\chi_5}+\frac{\chi_6}{a})+\gamma_T\frac{da}{d\tau}(\frac{1}{\chi_5}-\frac{\chi_6}{a^2}) = \\
&-\frac{\chi_6\gamma_T}{a}\Lambda_3 e^{-\alpha_3\eta_3}+\frac{\chi_4\gamma_P}{a}\Lambda_3 e^{(1-\alpha_3)\eta_3} \\
&-\gamma_O\Lambda_2 e^{-\alpha_5\eta_5}+\gamma_P\Lambda_5 e^{(1-\alpha_5)\eta_5} \\
&-\frac{a\gamma_O}{\chi_1}\Lambda_1 e^{-\alpha_1\eta_1}+\frac{a\Gamma_P}{\chi_2}\Lambda_1 e^{(1-\alpha_1)\eta_1}
\end{aligned} \tag{4.34}$$

$$1 = \gamma_O(1+\frac{a}{\chi_1}+\frac{\chi_3}{a})+\gamma_P(1+\frac{a}{\chi_2}+\frac{\chi_4}{a})+\gamma_T(1+\frac{a}{\chi_5}+\frac{\chi_6}{a}) \tag{4.35}$$

The mass transport of protons is given by the Fick's second law of diffusion 4.12 accompanied by boundary condtions:

$$\frac{\partial a}{\partial z} = \frac{\partial\gamma_O}{\partial\tau}+2\frac{\partial}{\partial\tau}\frac{\gamma_O a}{\chi_1}+\frac{\partial\gamma_P}{\partial\tau}+2\frac{\partial}{\partial\tau}\frac{\gamma_P a}{\chi_2}+\frac{\partial\gamma_T}{\partial\tau}+2\frac{\partial}{\partial\tau}\frac{\gamma_T a}{\chi_5} \tag{4.36}$$

at the electrode surface and $a = 1$ in the bulk of the solution.

Two Electron, Two Proton Reductions: Concerted Mechanism

The electrochemical reaction is described by Butler-Volmer equations:

$$\frac{\partial \Gamma_A}{\partial t} = -k_{01}\Gamma_A[H^+]e^{-\alpha_1\eta_1} + k_{b1}\Gamma_B e^{(1-\alpha_1)\eta_1} \tag{4.37}$$

$$\frac{\partial \Gamma_B}{\partial t} = -k_{02}\Gamma_B[H^+]e^{-\alpha_2\eta_2} + k_{b2}\Gamma_C e^{(1-\alpha_2)\eta_2} \tag{4.38}$$

where, $k_{bi} = k_{0i}[H^+]^*$.[44]

Mass transport is described by Fick's second law of diffusion as given by equation 4.2 accompanied by the boundary condition:

$$D\frac{\partial[H^+]}{\partial Z} = \frac{\partial \Gamma_A}{\partial t} - \frac{\partial \Gamma_C}{\partial t} \tag{4.39}$$

Equations 4.37-4.39 are accompanied by the mass conservatiom law:

$$\Gamma_{tot} = \Gamma_A + \Gamma_B + \Gamma_C \tag{4.40}$$

Dimensionless Parameters. Dimensionless parameters used here are presented in Table 4.1 and the dimensionless equations are given below:

$$\frac{\partial \gamma_A}{\partial \tau} = -\Lambda_1\gamma_A a e^{-\alpha_1\eta_1} + \Lambda_1(1-\gamma_A-\gamma_B)e^{(1-\alpha_1)\eta_1} \tag{4.41}$$

$$\frac{\partial \gamma_C}{\partial \tau} = -\Lambda_2(1-\gamma_A-\gamma_C)a e^{-\alpha_2\eta_2} + \Lambda_2\gamma_C e^{(1-\alpha_2)\eta_2} \tag{4.42}$$

$$\beta\left(\frac{\partial \gamma_A}{\partial \tau} - \frac{\partial \gamma_C}{\partial \tau}\right) = \frac{\partial a}{\partial x} \tag{4.43}$$

The Dimensionless equation 4.12 describes mass transport.

4.3 Computational Procedure

4.3.1 Computational Procedure

Fick's second law of diffusion (equation 4.12) is discretised on a grid (defined by equations 4.44, 4.45) which expands away from the electrode surface.

$$z_{i+1} - z_i = h_i \tag{4.44}$$

$$h_i = h_{i-1} \times \gamma \tag{4.45}$$

The standard values of the space mesh are $h_0 = 1 \times 10^{-3}$ and $\gamma = 1.125$. The bulk solution condition is implemented at distance $6\tau_{max}^{1/2}$ from the electrode surface, where τ_{max} is the time of the experiment. Beyond this, the effects of diffusion are not important on the experimental voltammetric time scale.[42] The equations presented in the section *Mathematical Model*, describing electrochemical transformations of surface confound species are essentially nonlinear. We implemented the Newton-Raphson method[45] to solve them. The Newton-Raphson method generates a block-diagonal matrix as shown in scheme 4.46 for the case of the two electron, two proton reaction. First the five diagonal block was converted to a three diagonal block, and then the Thomas algorithm[46] was implemented to solve the linearised system of equations. The program was written in C++.

$$\left(\begin{array}{cccccccc|c}
F_{1,O} & F_{1,P} & 0 & F_{1,a0} & 0 & 0 & . & 0 & 0 & F1_{rhs} \\
0 & F_{2,P} & F_{2,T} & F_{2,a0} & 0 & 0 & . & 0 & 0 & F_{2rhs} \\
F_{3,O} & F_{3,P} & F_{3,T} & F_{3,a0} & 0 & 0 & . & 0 & 0 & F3_{rhs} \\
F_{4,O} & F_{4,P} & F_{4,T} & F_{4,a0} & F_{4,a1} & 0 & . & 0 & 0 & F_{4rhs} \\
0 & 0 & 0 & F_{5,a0} & F_{5,a1} & F_{5,a2} & . & 0 & 0 & F_{4rhs} \\
. & . & . & . & . & . & . & . & . & . \\
0 & 0 & 0 & 0 & 0 & 0 & . & F_{(N+3),a(N-2)} & F_{(N+3),a(N-1)} & F_{(N+3)rhs}
\end{array}\right) \tag{4.46}$$

F_{ij} corresponds to the derivative of i-th equation, by the j-th variable. The discretised equations 4.33, 4.33, 4.35 and 4.36 are F_1, F_2, F_3 and F_4 respectively. The next N equations are generated by the discretisation of Fick's second law of diffusion (equation 4.12) on the expanding grid.

The dimensionless current j was calculated by equation 4.47

$$j = -\frac{d\gamma_{\mathrm{Ot}}}{d\tau} \tag{4.47}$$

for the case of a one electron, one proton reaction and

$$j = -\frac{d\gamma_{\mathrm{Ot}}}{d\tau} + \frac{d\gamma_{\mathrm{Tt}}}{d\tau} \tag{4.48}$$

in case of a two proton, two electron reaction.

4.4 Results and Discussion

4.4.1 One Electron, One Proton Reduction: Stepwise Mechanism

Fully Buffered Solutions

We start from a simple one electron, one proton reduction to show the influence of the mass transport and of the transfer coefficient α on the observed voltammograms. Laviron[20] showed that, assuming infinitely fast mass transport (a fully buffered solution) and $\alpha_{\mathrm{i}} = 0.5$ for all species, the behavior of the 1e, 1H scheme is equal to that of the simple one electron reduction A+$e-$ >B with pH dependent E^0_{app} and k_{app}:

$$E^0_{\mathrm{app}} = E^0_2 + \frac{RT}{F}\ln\frac{K_1([\mathrm{H}^+]+K_2)}{K_2([\mathrm{H}^+]+K_1)} = E^0_2 + \frac{RT}{F}\ln\frac{\chi_1(a+\chi_2)}{\chi_2(a+\chi_1)} \tag{4.49}$$

$$\Lambda_{\mathrm{app}} = \frac{k_{\mathrm{app}}RT}{vF} = \frac{RT}{vF}\frac{k_2 + k_1[\mathrm{H}^+]_0(K_1K_2)^{-1/2}}{(1+[\mathrm{H}^+]_0/K_1)^{1/2}(1+[\mathrm{H}^+]_0/K_2)^{1/2}} = \frac{\Lambda_2 + \Lambda_1 a(\chi_1\chi_2)^{-1/2}}{(1+a/\chi_1)^{1/2}(1+a/\chi_2)^{1/2}} \tag{4.50}$$

The theory of a simple one electron reduction is presented in work by Srinivasan.[47] The current dependence on the potential in the case of infinitely fast electron transfer is given the equation 4.51:

$$j = \frac{iRT}{vF^2\Gamma_{\mathrm{t}}A} = \frac{e^{\eta}}{(1+e^{\eta})^2} \tag{4.51}$$

The peak current and the peak potential are given by the following equations:[47]

$$j_{\mathrm{p}} = \frac{i_{\mathrm{p}}RT}{vF^2\Gamma_{\mathrm{t}}A} = 1/4 \tag{4.52}$$

$$E_p = E_2^0 \tag{4.53}$$

In the limiting case of an irreversible electron transfer, the current dependence on the potential is given by equation 4.54:[47]

$$j = \frac{iRT}{\nu F^2 \Gamma_t A} = \frac{kRT}{\nu F} e^{-\alpha\eta} e^{\frac{kRT}{\alpha\nu F}\exp(-\alpha\eta)} \tag{4.54}$$

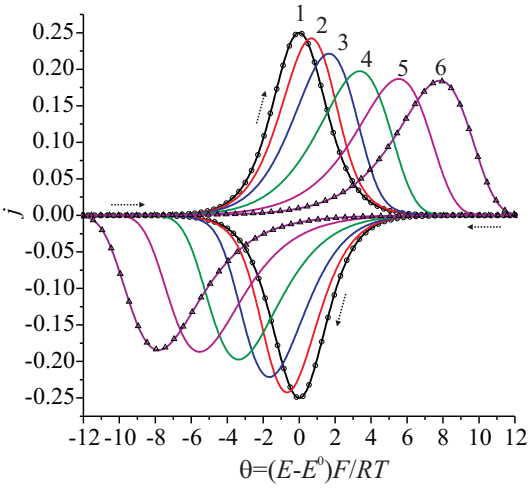

Figure 4.4: Voltammograms simulated for a simple A+$e-$ >B reaction, $E_0 = 0$. Lines 1 and 2, 3, 4, 5, 6 corresponds to the infinitely fast electron transfer and finite rate of electron transfer with Λ =1, 0.316, 0.1, 0.0316, 0.01.

The peak current and the peak potential are given by the following equations:[47]

$$j_p = \frac{i_p RT}{\nu F^2 \Gamma_t A} = \frac{\alpha}{2.718} \tag{4.55}$$

$$E_p = E_f^0 + \frac{RT}{\alpha F} \ln \frac{kRT}{\alpha \nu F} \tag{4.56}$$

Figure 4.5b and 4.5c show the calculated voltammograms for the case of $\alpha_1 \neq \alpha_2$, where the one electron, one proton mechanism (Figure 4.2) cannot be treated as a simple one electron reaction. It is clear that shape of voltammograms are significantly different from those observed in the case of $\alpha_1 = \alpha_2 = 0.5$. Voltammograms calculated for the case $\Lambda_1 \neq \Lambda_2$, when reaction 1 and 2 have different rates of electron transfer exhibit a very asymmetric peak with a shoulder in the direction of scan where symmetry factor is less than 0.5. It has been reported that for some electrochemical systems values of α can be as low as 0.07 and as high as 0.95, such extreme values of transfer coefficients are observed for metal cations reduction,[48] organic systems also can demonstrate values of transfer coefficients significantly deviating from 0.5.[49–51] Therefore equations 4.49 and 4.50 derived by Laviron should be applied to data analysis only if there is confidence that the symmetry factors $\alpha_1 = \alpha_2 = 0.5$. Figure 4.6 shows the calculated voltammograms at various values of pH. Figure 4.6a shows voltammograms calculated in the case of infinitely fast electron transfer, in this case the peak potential gradually shifts with pH according to equation 4.49. Figure 4.6b shows the voltammograms calculated at an intermediate rate of electron transfer $\Lambda_i = 1$ and $\alpha_i = 0.5$. Here the peak to peak separation depends on pH, but the midpoint potential ($E_{p\ forw}$+$E_{p\ back}$)/2) is

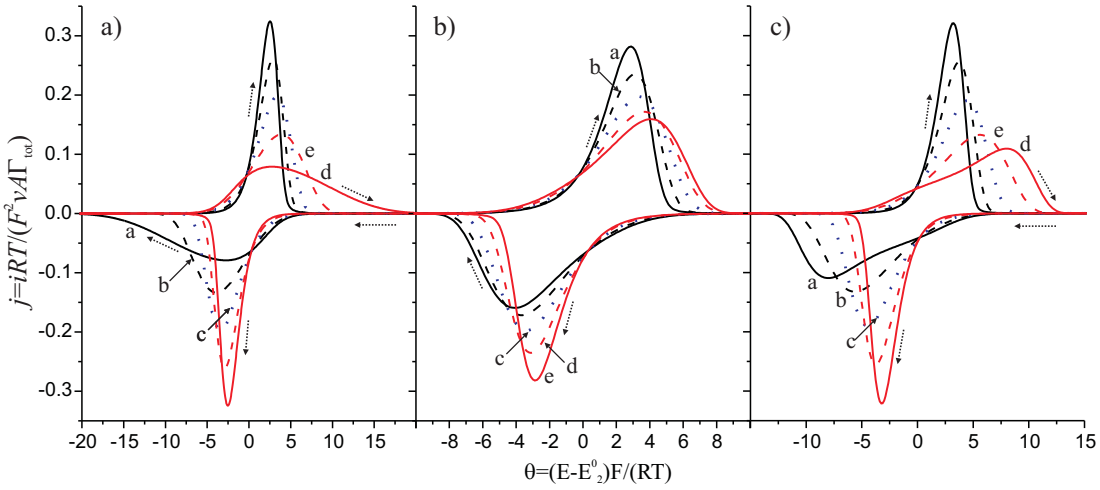

Figure 4.5: Simulated voltammograms for one electron, one proton stepwise reductions (Figure 4.2) a) equivalent of simple A+e $\leftrightarrow$B reaction, $\chi_1 = \chi_2$, $\lambda_1 = \lambda_2 = 0.1$, α_i =0.1(a), 0.3(b), 0.5(c), 0.7(d) and 0.9(e); b) , $\lambda_1 = \lambda_2 = 0.1$, $\chi_1 = \chi_2$, $\alpha_1 = 0.5$, $\alpha_2 = 0.1$(a), 0.3(b), 0.5(c), 0.7(d), 0.9(e); c) $\lambda_1 = 0.1$, $\lambda_2 = 0.01$, $\chi_1 = \chi_2$, $\alpha_2 = 0.5$, $\alpha_1 = 0.1$(a), 0.3(b), 0.5(c), 0.7(d), 0.9(e).

given by equation 4.49. A minimum in the peak current is observed at pH=6. The decrease of the peak current and increase of the peak to peak separation at intermediate pH is observed due to a decrease in $\Lambda_{app} = \frac{k_{app}RT}{\nu F}$ (equation 4.50), such that Λ_{app}(pH=1)=1 (Q$\leftrightarrow$R reaction only observed), Λ_{app}(pH=6)=0.2 (both electrochemical reactions are observed) and Λ_{app}(pH=10)=1 (O$\leftrightarrow$P reaction only observed). Figure 4.6c shows the voltammograms calculated in the case where $\alpha_1 \neq \alpha_2$; here the shape of the voltammogram strongly depends upon the pH of solution. This is due to the fact that rate of both reactions A$\leftrightarrow$P and Q$\leftrightarrow$R depends on the pH.

Infinitely High Surface Coverage

In case of infinitely slow mass transport, when only protons situated in the proximity of the surface are involved with the chemical reaction current versus potential is given by the equation 4.19 derived earlier. Figure 4.7 shows the voltammograms calculated according to equation 4.19. Various types of behavior are observed depending on the values of $\chi_1 = \frac{K_{a1}}{[H^+]_0}$ and $\chi_2 = \frac{K_{a2}}{[H^+]_0}$. If initially only Q present on the electrode surface ($\chi_1 << 1$) then only a single peak is observed and the peak position is given by equation 4.49. If initially only O is present ($\chi_1 >> 1$) at the electrode surface then a single peak is observed and the peak position is independent of χ_1 and χ_2. The observed independence of the peak position is due to virtually no protons being present in system at $\chi_1 >> 1$. At intermediate values

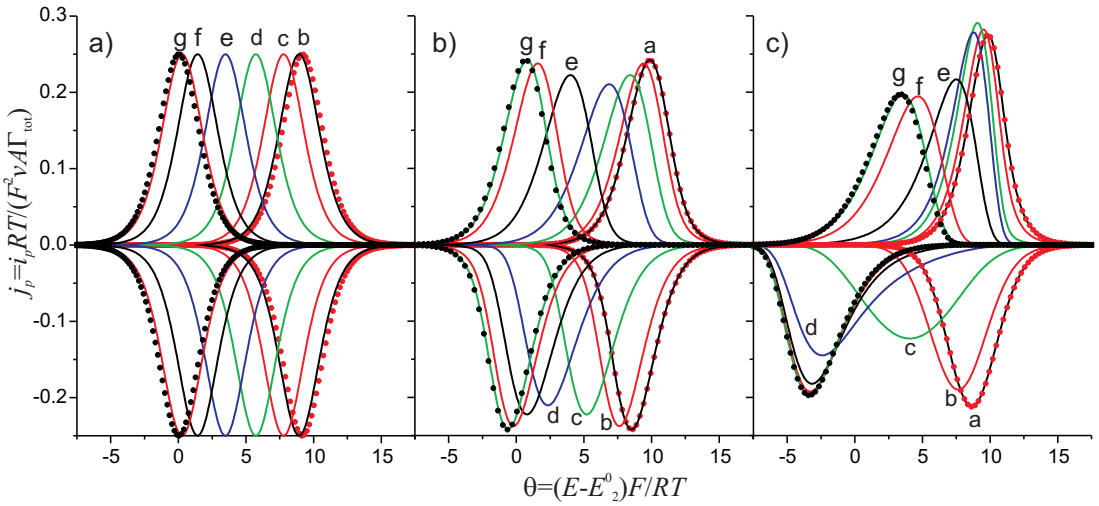

Figure 4.6: Voltammograms simulated for the case of fully buffered solutions, $pKa_1 = 4$, $pKa_2 = 8$. a) Infinitely fast electron transfer; b) $\Lambda_1 = \Lambda_2 = 1$, $\alpha_1 = \alpha_2 = 0.5$; c) $\Lambda_1 = 1$, $\alpha_1 = 0.2$, $\Lambda_2 = 0.1$, $\alpha_2 = 0.5$. Curves (a), (b), (c), (d), (e), (d), and (g) correspond to pH of 2, 4, 5, 6, 7, 8 and 10; black and red dots show voltammograms calculated for the limiting case of very low and very high pH, accordingly.

two separate peaks, two overlapping peaks or a peak with a shoulder (Figure 4.7) may be observed in a voltammogram depending on the ratio of K_{a1}/K_{a2}. All observed shapes of voltammograms can be rationalized by considering the equation 4.49 describing E_{app} dependence on the proton concentration.

Unbuffered Solution

The influence of mass transport on the voltammogram shape can only be observed if protons are either consumed or produced during the electrochemical reaction. Substantial amounts of protons will be produced and/or consumed during electrochemical reaction in all cases except where both $\chi_1 = \frac{K_{a1}}{[H^+]_0}$ and $\chi_2 = \frac{K_{a2}}{[H^+]_0} > 100$ or χ_1 and $\chi_2 < 0.01$. Figure 4.8 shows the voltammograms calculated for the cases where the protonated form Q converts to deprotonated form P (Figure 4.8a), when a mixture of O and Q converts into a fully protonated R and deprotonated P forms (Figures 4.8b and c, correspondingly). In all cases presented in Figure 4.8 a gradual increase of the surface coverage (decrease of dimensionless parameter $\beta = \frac{[H^+]_0}{\Gamma_t}\sqrt{\frac{DRT}{\nu F}}$) changes the voltammograms shape from that observed in a fully buffered solution (equation 4.51) to that observed in the limiting case of infinitely high coverage (equation 4.19). Figure 4.8a shows that on the forward scan only one peak is observed. At low values of the surface coverage the results of numerical simulation are in agreement with

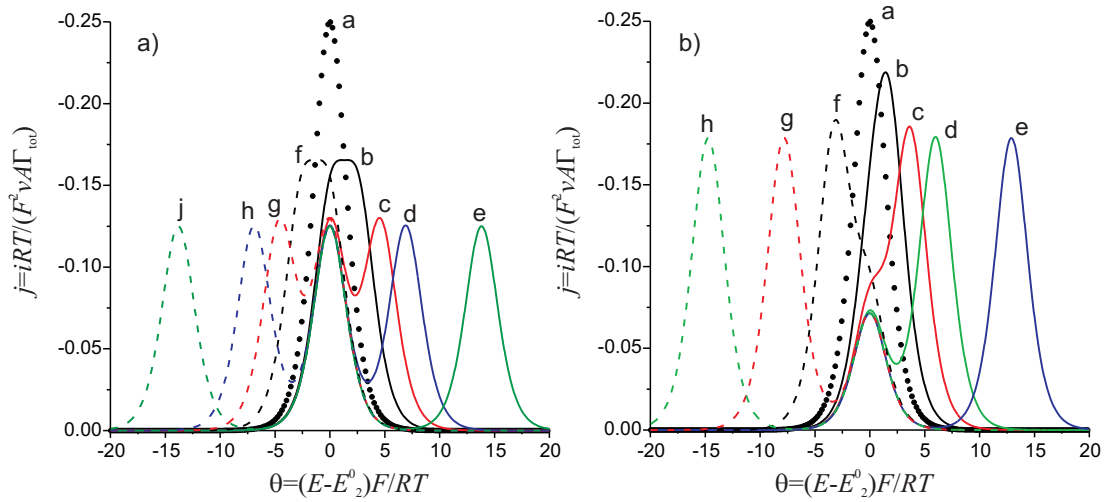

Figure 4.7: Calculated voltammograms in the limiting case of infinitely slow mass transport and infinitely fast electron transfer (equation 4.19). a) $\chi_1 = \frac{K_{a1}}{[H^+]_0} = 1$; line (a) corresponds to $\chi_2 = \frac{K_{a2}}{[H^+]_0} =$ 1, (b) 0.07, (c) 0.01, (d) 10^{-3}, (e) 10^{-6}, (f) 14, (g) 100, (h) 10^3, (j) 10^6. a) $\chi_1 = \frac{K_{a1}}{[H^+]_0} = 0.4$; line (a) corresponds to $\chi_2 = \frac{K_{a2}}{[H^+]_0} = 0.4$, (b) 0.07, (c) 0.01, (d) 10^{-3}, (e) 10^{-6}, (f) 10, (g) 10^3, (h) 10^6. $\chi_1 = \frac{K_{a1}}{[H^+]_0} = 0.4$. Backward sweep is an mirror image of forward scan through potential axis and not shown on the graph.

analytical solution given by equation 4.51. The peak gradually moves to more negative potentials with an increase of surface coverage.

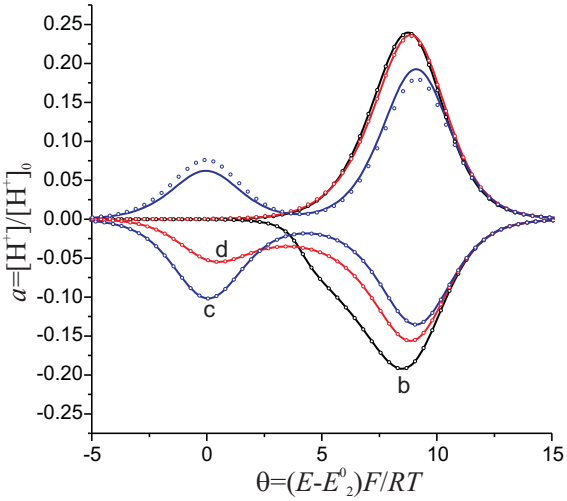

Figure 4.10: Simulated voltammograms $\chi_1 = 1$, $\chi_2 = 10^{-4}$; $\beta = 100$ 0.25 (b), 0.1 (c), 0.031 (d), labeling is as used in Figure 4.9. Solid lines and open circles show voltammograms, where the direction of scan where switched at $\theta = 20$ and $\theta = 10$.

At very high coverage values it is an in agreement with the analytical solution for the case of infinitely slow mass transport (equation 4.19). At intermediate values of surface coverage the backward scan shows two peaks. This behavior can be rationalized in terms of the dimensionless proton concentration $a = \frac{[H^+]}{[H^+]_0}$ adjacent to the electrode surface. Figure 4.9 a) shows the calculated dimensionless concentration of protons $a = \frac{[H^+]}{[H^+]_0}$ in the proximity of the electrode surface. An increase of surface coverage causes an increase in the proton concentration in the proximity of the electrode surface

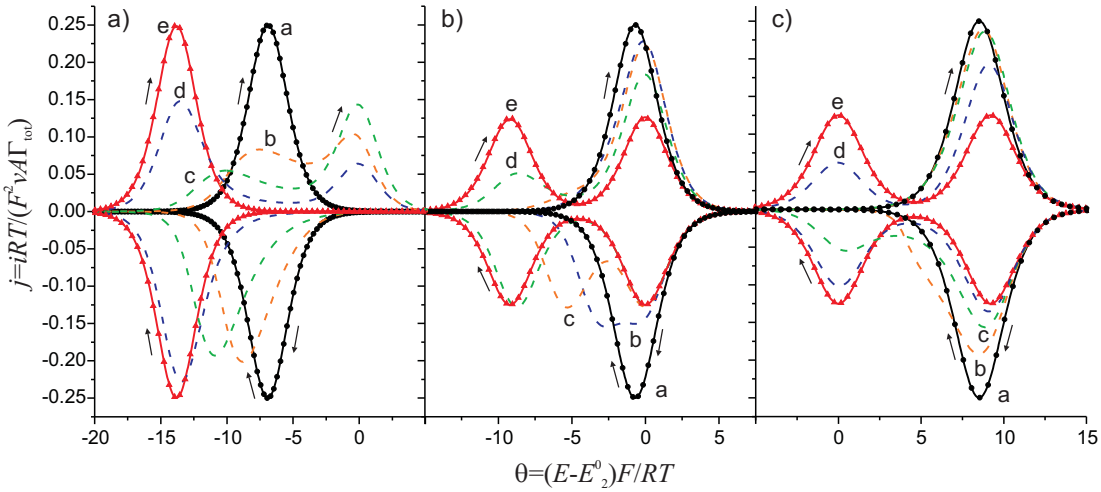

Figure 4.8: Voltammograms simulated at various values of the surface coverage $\beta = \frac{[H^+]_0}{\Gamma_t}\sqrt{\frac{DRT}{\nu f}}$, electron transfer is assumed to be infinitely fast. a) $\chi_1 = \frac{K_{a1}}{[H^+]_0} = 10^{-3}$, $\chi_2 = \frac{K_{a2}}{[H^+]_0} = 10^3$; $\beta = 100$ (a), $\beta = 100$ (a), 0.1 (b), 0.01 (c), 10^{-4} (d), 10^{-8} (e). b) $\chi_1 = 1$, $\chi_2 = 10^4$; $\beta = 100$ (a), 0.032 (b), 3.2×10^{-3} (c), 3.2×10^{-5} (d), 10^{-7} (e). c) $\chi_1 = 1$, $\chi_2 = 10^{-4}$; $\beta = 100$ (a), 0.25 (b), 0.1 (c), 0.031 (d), 10^{-3} (e). Dots and triangles show the voltammograms calculated in the limiting cases of infinitely fast (equation 4.51) and infinitely slow (equation 4.19) mass transport, accordingly.

that shifts E_{app} (equation 4.49) and consequently E_p to more negative potentials. The backward scan starts with a high proton concentration adjacent to the electrode surface; as reaction proceeds the proton concentration drops several orders of magnitude to a value significantly lower than the initial. This shifts E_{app} to more positive values and a second peak is observed at $E \approx E_2^0$ (eqation 4.49). When a mixture of O and Q converts to P (Figure 4.8b) we first observe a splitting of the forward peak into two peaks and further increases in the surface coverage (decrease of β) splits the backward peak. The first peak during the forward scan is observed at $E_p \approx E_{app}$; the electrochemical reduction generates substantial amount of protons (Figure 4.9b) which causes a shift in E_{app} to more negative values where the second peak is observed. The only difference from the previous case is that two peaks are observed only at very high surface loadings. A mechanistic explanation of presence of two peaks in the backward scan is analogous to that presented above for the case of Q transforming into P. When a mixture of O and Q converts to P (Figure 4.8c) the changed proton concentration adjacent to the electrode surface (Figure 4.9c) again causes peak splitting in the forward scan. This is similar to the case considered above and two or one peaks may be observed in the backward scan. Figure 4.9c also shows the concentration of protons in the proximity of the electrode surface as calculated

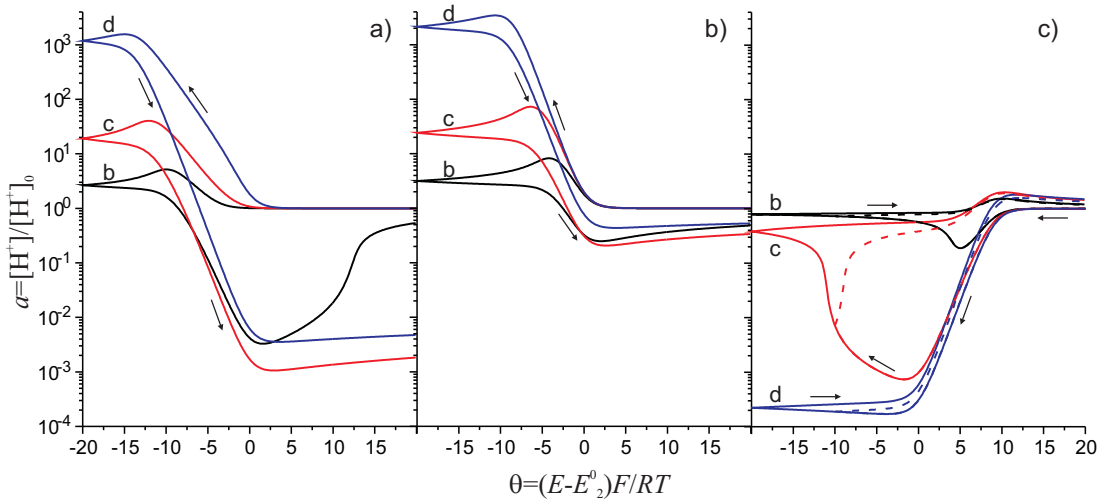

Figure 4.9: Simulated dimensionless concentration $a = \frac{[H^+]}{[H^+]_0}$ of protons in the proximity of electrode surface versus potential at various values of the surface coverage $\beta = \frac{[H^+]_0}{\Gamma_t}\sqrt{\frac{DRT}{vf}}$, electron transfer is assumed to be infinitely fast. a) $\chi_1 = \frac{K_{a1}}{[H^+]_0} = 10^{-3}$, $\chi_2 = \frac{K_{a2}}{[H^+]_0} = 10^3$; $\beta = 0.1$ (b), 0.01 (c), 10^{-4} (d). b) $\chi_1 = 1$, $\chi_2 = 10^4$; $\beta = 0.032$ (b), 3.2×10^{-3} (c), 3.2×10^{-5} (d). c) $\chi_1 = 1$, $\chi_2 = 10^{-4}$; $\beta = 0.25$ (b), 0.1 (c), 0.031 (d). Note here labeling as in Figure 4.8 is applied.

for the case when the direction of scan is switched immediately after the second peak. In this case no time is left for the concentration profile to equilibrate and the first current peak in the backward scan is slightly larger (Figure 4.10) when the direction of the scan is switched further from the peak; this effect is only notable at high surface loadings.

Figure 4.11 and 4.12 depict the peak current and peak potential values versus pH, calculated with parameters values that may be expected for organic molecules adsorbed on a surface. Four regions of behavior are observed depending on the pH value: at low pH (pH $<<$ pKa_1 and $<<$ pKa_2) similar to fully buffered solutions peak potential and peak current are independent of pH; at intermediate values of (pKa_1 $<$ pH $<$$pKa_2$) the peak moves with a potential as in the case of buffered solution, further increase of pH causes peak splitting (forward peak splits if pKa_1 $<$ pKa_2 and backward peak splits if pKa_1 $>$$pKa_2$); finally at high pHs (pH $>>$ pKa_1 and pH $>>$ pKa_2) the peak potential is again independent of the pH and the voltammograms are similar to these observed in the unbuffered solution.

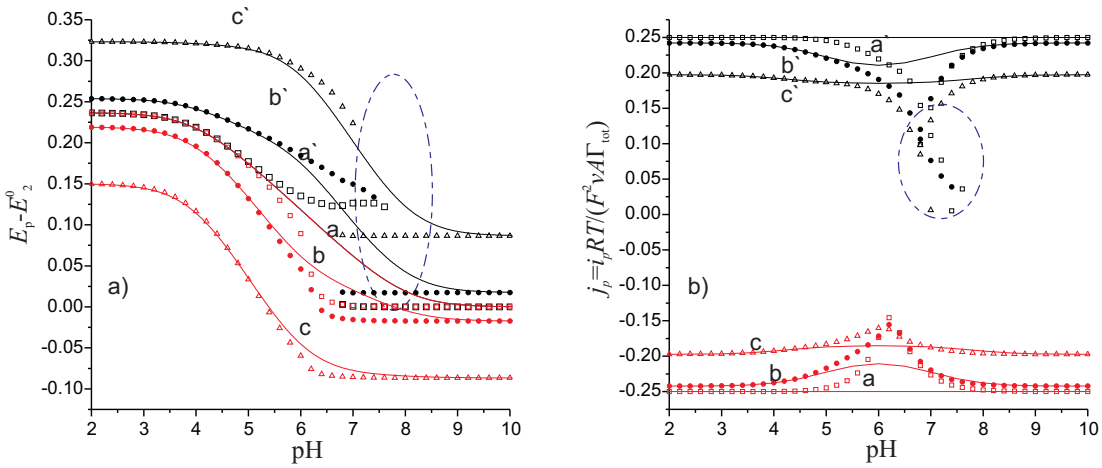

Figure 4.11: The simulated peak current a) and peak potential b) versus pH. $Ka_1 = 10^{-4}$, $Ka_2 = 10^{-8}$, $\Gamma = 2\times10^{-6}\frac{mol}{m^2}$ (a) corresponds to an infinitely fast rate of electron transfer, (b) and (c) correspond to voltammograms calculated with $\Lambda_i = 0.1, \alpha = 0.5$ and $\Lambda_i = 0.01, \alpha = 0.5$, respectively. Solid and scattered lines correspond to a fully buffered and unbuffered solutions, accordingly. Highlight shows region where two peaks during forward scan are observed.

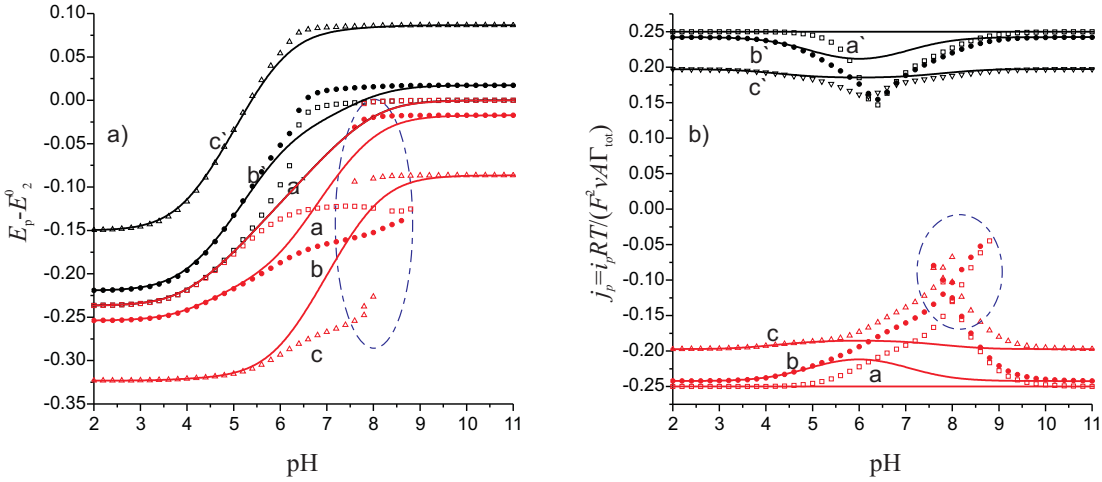

Figure 4.12: The simulated peak current a) and peak potential b) versus pH. $Ka_1 = 10^{-8}$, $Ka_2 = 10^{-4}$, $\Gamma = 2\times10^{-6}\frac{mol}{m^2}$, (a) corresponds to an infinitely fast rate of electron transfer, (b) and (c) correspond to the voltammograms calculated with $\Lambda_i = 0.1, \alpha = 0.5$ and $\Lambda_i = 0.01, \alpha = 0.5$, correspondingly. Solid and scattered lines correspond to a fully buffered and unbuffered solutions, respectively. Highlight shows region where two peaks during forward scan are observed.

4.4.2 One Electron, One Proton Reduction: Concerted Mechanism

Fully Buffered Solution

Assuming an infinitely fast rate of electron transfer, the shape of the voltammogram is given by the equation 4.51, with the peak current described by equation 4.52 and peak potential given by the

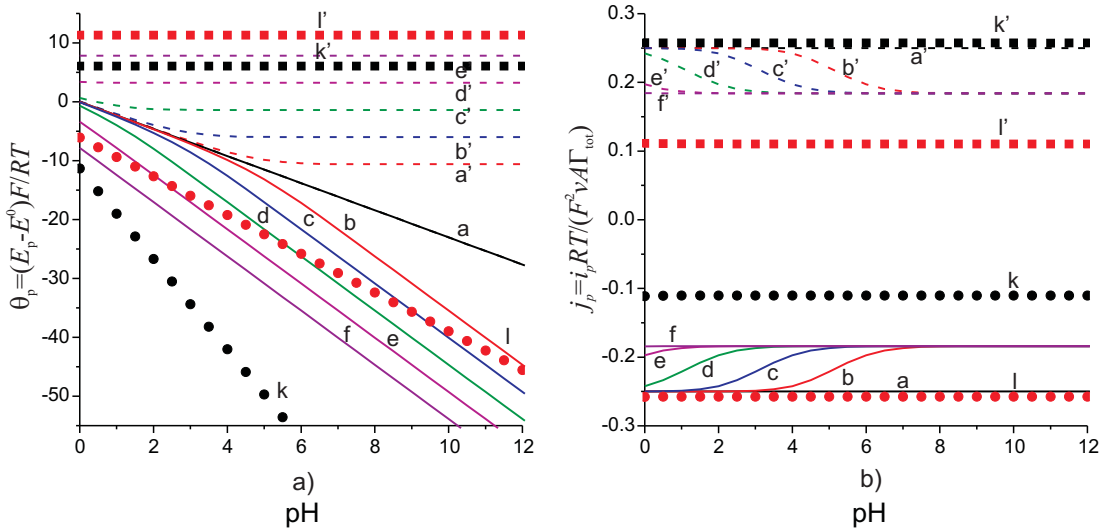

Figure 4.13: The simulated peak potential a) and peak current b) values versus pH. Line (a) corresponds to infinitely fast electron transfer, $\alpha = 0.5$, $\Lambda = \frac{k[\mathrm{H}^+]^* RT}{vF}$=100 (b), 10 (c), 1 (d), 0.1 (e), 0.01 (f). Scatter (k) corresponds to peak values calculated at Λ=0.01, $\alpha = 0.3$ and scatter (l) corresponds to that calculated at Λ=0.01, $\alpha = 0.7$. Symbols with a prime corresponds to a backward scan and that without a prime to forward scan.

equation:

$$E_\mathrm{p} = E^0_\mathrm{f} + \frac{RT}{F} \ln [\mathrm{H}^+]/[\mathrm{H}^+]^* \tag{4.57}$$

where, $[\mathrm{H}^+]^*$ is a standard concentration 1×10^3 mol m^{-3}.

In the limiting case of an irreversible electron transfer, the current dependence on the potential during forward can be derived by substitution of $k = k'[\mathrm{H}^+]$ into equation 4.54:

$$j = \frac{iRT}{vF^2\Gamma_t A} = \frac{k'[\mathrm{H}^+]RT}{vF} e^{-\alpha\eta} e^{\frac{k'[\mathrm{H}^+]RT}{\alpha vF}} \exp(-\alpha\eta) \tag{4.58}$$

The peak current is given by equation 4.55 and the equation for the peak potential for the forward scan can be derived by substitution of $k = k'[\mathrm{H}^+]_0$ into equation 4.56:

$$E_\mathrm{p} = E^0_\mathrm{f} + \frac{RT}{\alpha F} \ln \frac{k'[\mathrm{H}^+]RT}{\alpha vF} \tag{4.59}$$

The backward scan in the case of the fully irreversible reaction remains independent of proton con-

centration with a peak potential given by the equation:

$$E_p = E_f^0 + \frac{RT}{\alpha F} \ln \frac{k'[H^+]^* RT}{\alpha v F} \tag{4.60}$$

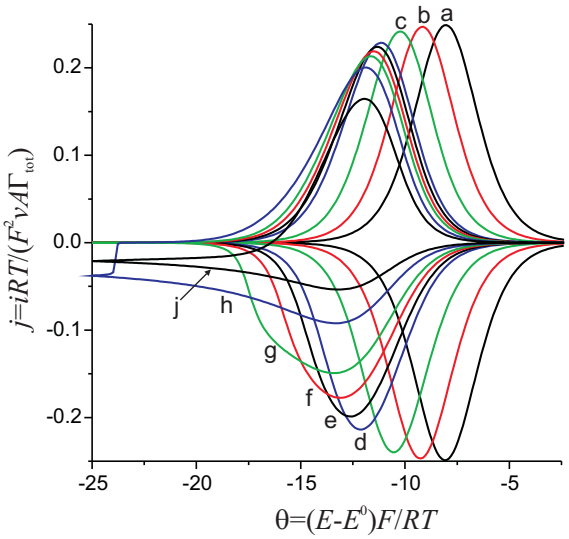

Figure 4.14: Simulated voltammograms for the case of infinitely fast electron transfer, $\beta = \frac{[H^+]}{\Gamma_{tot}} \sqrt{\frac{DRT}{vF}} = 10^5$, curves (a), (b), (c), (d), (e), (f), (g), (h) and (j) corresponds to pH 3.5, 4, 4.5, 5.125, 5.25, 5.375, 5.625 and 5.875, correspondingly.

Figure 4.13 shows the peak current and the peak potential values calculated at various values of the rate of the electron transfer. The calculated peak current and peak potential for the infinitely fast electron transfer are in a good agreement with the analytical values as given by equations 4.57 and 4.52. At low values of the rate of electron transfer $\Lambda = \frac{k'[H^+]^* RT}{vf}$, when the reaction can be assumed to be fully irreversible, the calculated values of the peak current and the peak potential are in agreement with those given by equations 4.55 and 4.59 for the forward scan. The peak current and peak potential for the backward scan are independent of pH and are also in agreement with the analytical results. In the case of slow electron transfer the peak potential dependence on pH is controlled by the symmetry factor α. At intermediate values of the rate of electron transfer $\Lambda = \frac{k'[H^+]^* RT}{vf}$ switch over of behavior is observed: at low pH values when $\Lambda a = \frac{k'[H^+] RT}{vf}$ is high, reversible electron transfer is observed and at high pH values when Λa is low, irreversible electron transfer is observed.

Unbuffered Solution

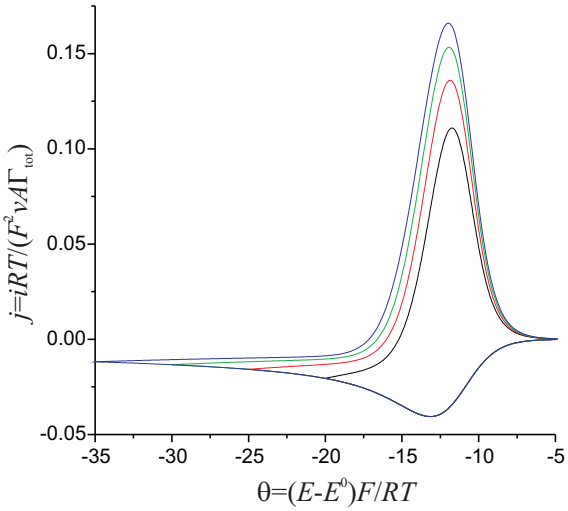

Figure 4.15: Switching potential influence of the back peak, electron transfer is assumed to be infinitely fast, $\beta = \frac{[H^+]}{\Gamma_{tot}}\sqrt{\frac{DRT}{vF}} = 10^5$, pH=6.

Figure 4.14 shows voltammograms simulated in an unbuffered solution. At low pH values when the concentration of protons relative to the surface coverage is high the voltammograms look similar to that of a fully buffered solution. At higher pH when the surface coverage is comparable with the amount of protons available in the solution the voltammogram shape deviates from that observed in a buffered solution - the peak becomes very asymmetric with a long "diffusional tail" at negative overpotentials and decreasing peak current. This alteration in the voltammogram shape is caused by the fact that the rate of the electrochemical reaction is determined by the rate of proton diffusion to the electrode surface, but not the potential. In the region of high pH the back peaks are almost independent of pH; this due to the fact that reaction becomes effectively irreversible, because the rate of the forward reaction proportional to the proton concentration is negligible. The peak height of the back peak here is a function of the switching potential (Figure 4.15) - the further the potential is swept during the forward scan, the higher the backward peak. All of these features make the voltammograms look like an apparent adsorptive stripping voltammetry of protons. Figure 4.16 shows dependence of the peak current and the peak potential calculated for the case of infinitely fast electron transfer on pH for various values of surface coverages β. The shape of the voltammogram is determined by the parameter $\beta a = \frac{[H^+]_0}{\Gamma_{tot}}\sqrt{\frac{DRT}{vF}}$; if $\beta a > 10^5$ the solution can be assumed to be fully buffered, at lower values of βa the finite rate of protons mass transport to the electrode should be considered. Figure 4.17 shows the peak current and the peak potential values calculated in the case of slow electron transfer, where the presence of the reverse reactions are negligible. Here again the solution can be considered fully buffered if $\beta a > 10^5$; in this case peak potential depends on pH as given by equation 4.57 and the peak current is given by the equation 4.52. Here, similar to the case of the infinitely fast electron transfer, the shape of the

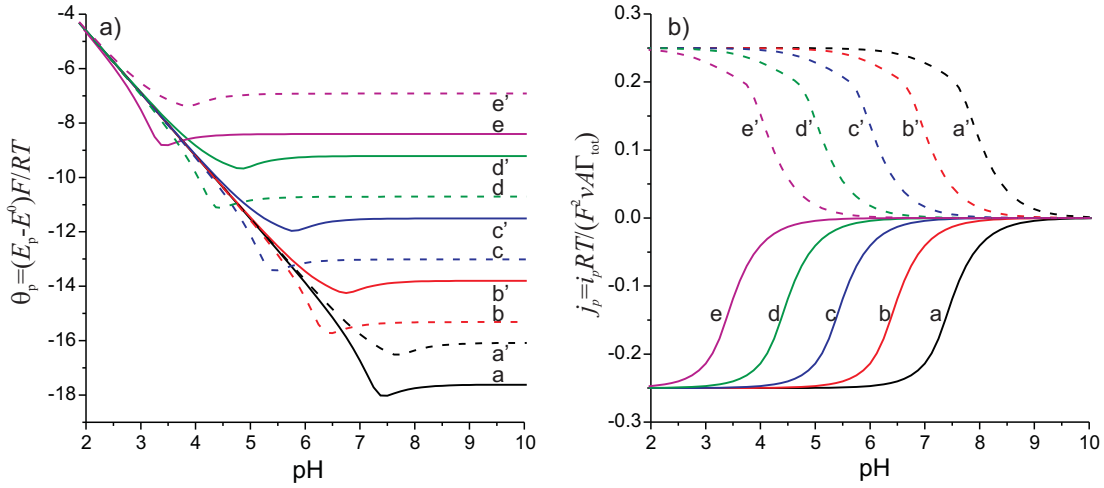

Figure 4.16: The simulated peak potential a) and peak current b) values versus pH, electron transfer is assumed to be infinitely fast, $\beta = \frac{[H^+]^*}{\Gamma_{tot}}\sqrt{\frac{DRT}{vF}} = 10^7$ (a), 10^6(b), 10^5(c), 10^4(d), 10^3(e); lines labeled by symbols with a prime corresponds to a backward sweep.

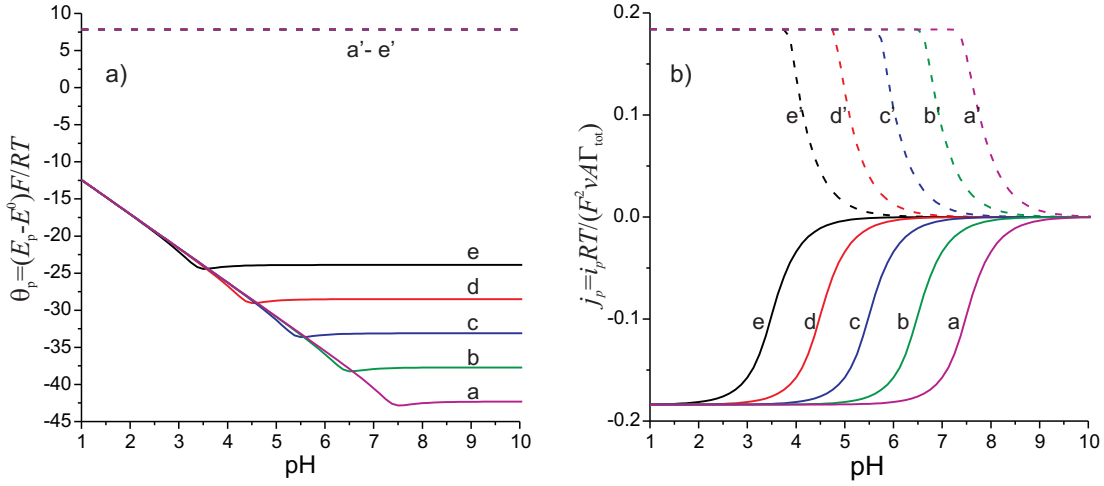

Figure 4.17: The simulated peak potential a) and peak current b) values versus pH, $\Lambda = \frac{k[H^+]^*RT}{vf} = 0.01$, $\beta = \frac{[H^+]^*}{\Gamma_{tot}}\sqrt{\frac{DRT}{vF}} = 10^5$, curves (a), (b), (c), (d), (e), (f), (g), (h) and (j) corresponds to pH 3.5, 4, 4.5, 5.125, 5.25, 5.375, 5.625 and 5.875, correspondingly.

voltammogram is determined by the parameter $\beta a = \frac{[H^+]_0}{\Gamma_{tot}}\sqrt{\frac{DRT}{vF}}$ Figure 4.18 shows the peak current and the peak potential values calculated for the intermediate case when at low pH the electron transfer can be assumed fast and at higher pH rate of the electrochemical reaction decrease due to the decrease of the rate of electron transfer and slow mass transport of protons. Here the voltammograms shape is

a function of both β and a.

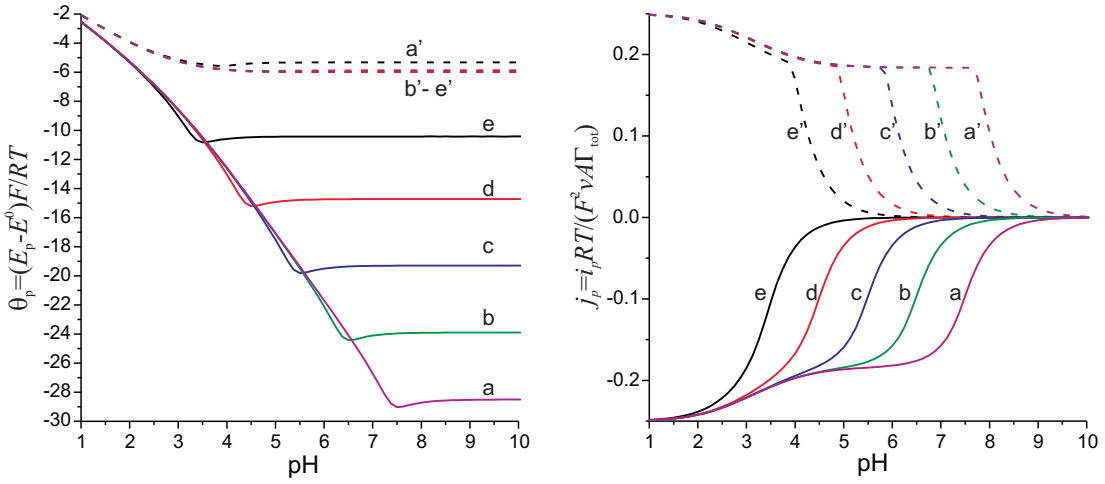

Figure 4.18: The simulated peak potential a) and peak current b) values versus pH, $\Lambda = \frac{k[\mathrm{H}^+]^* RT}{vf} = 10$, $\beta = \frac{[\mathrm{H}^+]}{\Gamma_{\mathrm{tot}}}\sqrt{\frac{DRT}{vF}} = 10^5$, curves (a), (b), (c), (d), (e), (f), (g), (h) and (j) corresponds to pH 3.5, 4, 4.5, 5.125, 5.25, 5.375, 5.625 and 5.875, correspondingly.

4.4.3 Two Electron, Two Proton Reaction: Stepwise Mechanism

Fully Buffered Solution

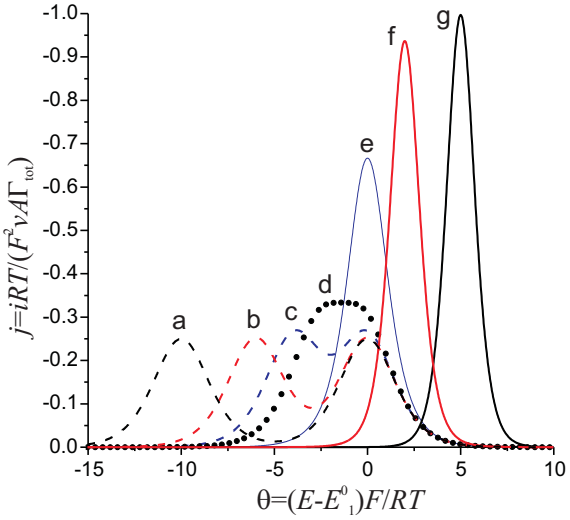

Figure 4.19: Calculated voltammograms in a fully buffered solution for the case of consecutive two electron reduction, the rate of the electron transfer is assumed to be infinitely fast, $(E_{\mathrm{f}}^2 - E_{\mathrm{f}}^1)F/RT = -10$(a), -6(b), -4(c), $-\ln 16$(d), 0 (e), 4(f), 10(g).

Laviron[21] showed that for a two electron, two proton stepwise reduction (Figure 4.3) under the assumption that the solution is fully buffered and $\alpha_i = 0.5$ for all species (i) is equivalent to two consecutive one electron reactions:

$$A \underset{k_{1app}}{\overset{E_{1app}}{\rightleftharpoons}} B \underset{k_{2app}}{\overset{E_{2app}}{\rightleftharpoons}} C \tag{4.61}$$

with apparent values E_{app1}, k_{app1} and E_{app2}, k_{app2} given by the following equations:

$$k_{1app} = \frac{(k_1[H^+](K_1K_2)^{1/2} + k_2 + k_3(K_3K_4)^{-1/2}/[H^+])}{([H^+]K_1 + 1 + (K_3[H^+])^{-1})^{1/2}([H^+]K_2 + 1 + (K_4[H^+])^{-1})^{1/2}} \tag{4.62}$$

$$k_{2app} = \frac{(k_4[H^+](K_2K_5)^{1/2} + k_5 + k_6(K_4K_6)^{-1/2}/[H^+])}{([H^+]K_2 + 1 + (K_4[H^+])^{-1})^{1/2}([H^+]K_5 + 1 + (K_6[H^+])^{-1})^{1/2}} \tag{4.63}$$

$$\frac{FE_{app1}}{RT} = \frac{FE_2^0}{RT} + \ln\frac{[H^+]/K_2 + 1 + K_4/[H^+]}{[H^+]/K_1 + 1 + K_3/[H^+]} \tag{4.64}$$

$$\frac{FE_{app2}}{RT} = \frac{FE_5^0}{RT} + \ln\frac{[H^+]/K_5 + 1 + K_6/[H^+]}{[H^+]/K_2 + 1 + K_4/[H^+]} \tag{4.65}$$

Here we first briefly discuss the theory of a simple two consecutive one electron reactions. In the case where both electrons are transfered infinitely fast the current dependency on potential has a simple analytical expression:[52,53]

$$j = \frac{iRT}{vF^2\Gamma_{tot}A} = \frac{e^{\eta_2}(1 + 2e^{\eta_1} + e^{\eta_1+\eta_2})}{(1 + e^{\eta_2} + e^{\eta_1+\eta_2})^2} = \frac{e^{\eta_1+\Delta\eta}(1 + 2e^{\eta_1} + e^{2\eta_1+\Delta\eta})}{(1 + e^{\Delta\eta+\eta_1} + e^{2\eta_1+\Delta\eta})^2} \tag{4.66}$$

where, $\Delta\eta = \frac{(E_2-E_1)F}{RT}$.

Figure 4.19 show voltammograms calculated according to equation 4.66. If $\Delta\eta < -\ln 16$ only one peak is observed, peak currents and peak potentials are given by the equations:

$$E_p = (E_2 - E_1)/2 \tag{4.67}$$

$$j = \frac{iRT}{vF^2\Gamma_{tot}A} = \frac{2(1 + e^{(E_2-E_1)F/2RT})}{(2 + e^{(E_2-E_1)F/2RT})^2} \tag{4.68}$$

If $\Delta\eta > -\ln 16$ two peaks of the same height are observed, peak current and peak potential are given by the following equations:

$$E_p = E_1 + \frac{RT}{F}\ln(\frac{1}{2}e^{-\Delta\eta}(-8 + e^{\Delta\eta} \pm \sqrt{64 - 20e^{\Delta\eta} + e^{2\Delta\eta}})) \tag{4.69}$$

$$j = \frac{iRT}{vF^2\Gamma_{tot}A} = \frac{e^{\Delta\eta}(-6+e^{\Delta\eta})}{4(-4+e^{\Delta\eta})^2} \tag{4.70}$$

Infinitely High Surface Coverage

Similar to the case of one electron, one proton reaction assuming infinitely fast electron transfer and infinitely high surface coverage the following equation describing compound A the mass conservation law (equation 4.71) and the proton mass conservation (equation 4.72) can be written down.

$$(\frac{\chi_3}{a}+1+\frac{a}{\chi_1})\gamma_O+(\frac{\chi_4}{a}+1+\frac{a}{\chi_2})\gamma_O e^{-\eta_1}+(\frac{\chi_6}{a}+1+\frac{a}{\chi_5})\gamma_O e^{-\eta_1-\eta_2}=1 \tag{4.71}$$

$$\gamma_O(1+e^{-\eta_1}+e^{-\eta_1-\eta_2})+2\gamma_O(\frac{a}{\chi_1}+\frac{ae^{-\eta_1}}{\chi_2}+\frac{ae^{-\eta_1-\eta_2}}{\chi_5})=\frac{2+\chi_1}{1+\chi_1+\chi_1\chi_3} \tag{4.72}$$

These equations were analytically solved in Mathematica 7.0 (Wolfram Research, Inc Champaign,

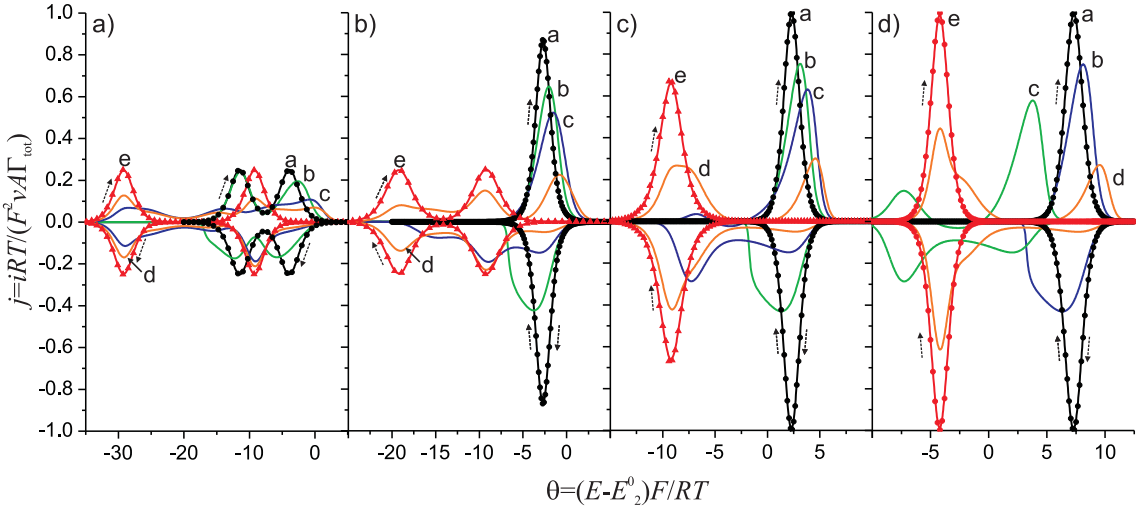

Figure 4.20: Voltammograms simulated at various values of the surface coverage $\beta = \frac{[H^+]_0}{\Gamma_t}\sqrt{\frac{DRT}{vf}}$, electron transfer is assumed to be infinitely fast, K_a corresponds to the NN ($\chi_1 = 10^4, \chi_2 = 10^0, \chi_3 = 10^2, \chi_4 = 10^{-2}, \chi_5 = 10^{-4}, \chi_6 = 10^{-6}$) case. a) $E_5^0 - E_2^0 = -20$, b) $E_5^0 - E_2^0 = -10$, c) $E_5^0 - E_2^0 = 0$, d) $E_5^0 - E_2^0 = 10$. Curves (a), (b), (c), (d) and (e) corresponds to $\beta = 100$, 0.56, 0.1, 0.056 and 10^{-4}, dots shows voltammograms calculated for the case of fully buffered solution, triangles shows voltammograms calculated for the case of infinitely high coverage.

Illinois) and current versus potential were analytically calculated according to formula:

$$j = -\frac{d(\frac{\chi_3}{a}+1+\frac{a}{\chi_1})\gamma_O}{d\eta_1}+\frac{d(\frac{\chi_6}{a}+1+\frac{a}{\chi_5})\gamma_O e^{-\eta_1-\eta_2}}{d\eta_1} \tag{4.73}$$

while differentiating it should be noted that $\eta_2 = \eta_1 + \Delta\eta$.

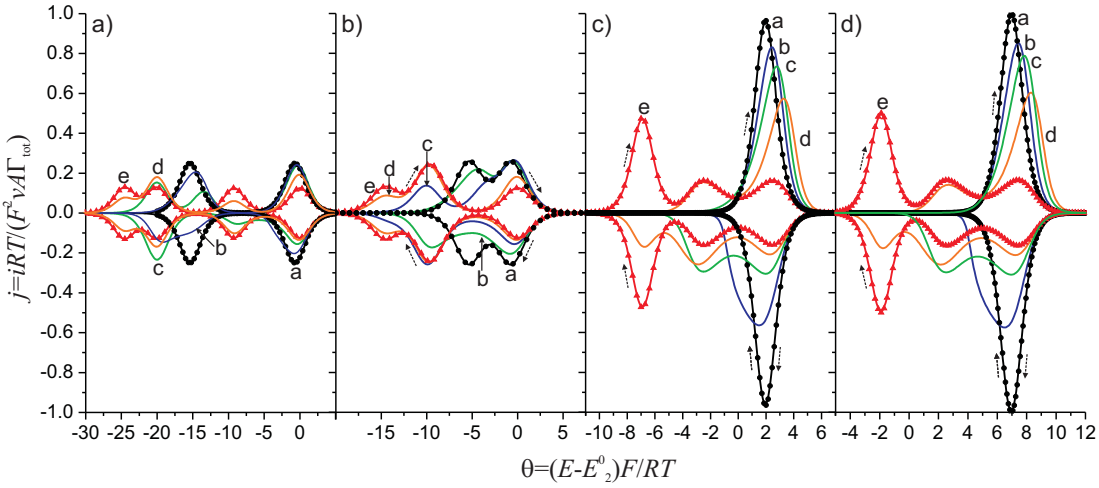

Figure 4.21: Voltammograms Simulated at various values of the surface coverage $\beta = \frac{[H^+]_0}{\Gamma_t}\sqrt{\frac{DRT}{\nu f}}$, electron transfer is assumed to be infinitely fast, K_a corresponds to the SS ($\chi_1 = 10^4, \chi_2 = 10^2, \chi_3 = 10^0, \chi_4 = 10^{-4}, \chi_5 = 10^{-2}, \chi_6 = 10^{-6}$) case. a) $E^0_5 - E^0_2 = -20$, b) $E^0_5 - E^0_2 = -10$, c) $E^0_5 - E^0_2 = 0$, d) $E^0_5 - E^0_2 = 10$. Curves (a), (b), (c), (d) and (e) corresponds to $\beta = 100$, 0.32, 0.1, 0.032 and 10^{-4}, dots shows voltammograms calculated for the case of fully buffered solution, triangles shows voltammograms calculated for the case of infinitely high coverage.

The analytical expression for the current calculated according to equation 4.73 is too bulk to be presented here. Voltammograms calculated according to equation 4.73 are discussed in the section below.

Unbuffered Solutions

Figures 4.20, 4.21, 4.23 and 4.22 show voltammograms calculated at various values of $\beta = \frac{[H^+]_0}{\Gamma_t} = \sqrt{\frac{DRT}{\nu F}}$ at four possible dispositions for the order of the χ_i introduced by Laviron:[21] NN ($\chi_1 > \chi_3 > \chi_2 > \chi_4 > \chi_5 > \chi_6$), SS ($\chi_1 > \chi_2 > \chi_3 > \chi_5 > \chi_4 > \chi_6$), NS ($\chi_1 > \chi_3 > \chi_2 > \chi_5 > \chi_4 > \chi_6$), SN($\chi_1 > \chi_2 > \chi_3 > \chi_4 > \chi_5 > \chi_6$). Voltammograms calculated for the case of an infinitely high surface coverage for all cases of K_i disposition are observed at more negative overpotentials than those calculated in a fully buffered solution; this is due to the fact the electrochemical reactions are followed by significant depletion of the proton concentration adjacent to the electrode surface which makes the reaction less favorable. Voltammograms in fully buffered solutions can exhibit one or two peaks (Figure 4.19) depending on the value of $E^0_2 - E^0_5$; however up to four peaks may be observed in the case of infinitely high coverage. This can be rationalised in the following way: in the section dedicated to stepwise one proton, one electron reduction we showed that the two peaks can be observed at

electrodes with infinitely high coverage, if a doublet of such split peaks is observed then four peaks appear on a voltammogram, if only one of peaks is split than three peaks are observed. The peak potentials can be approximated by combining equations 4.64, 4.65 and 4.67, 4.69. Voltammograms with intermediate values of surface coverage show a gradual change of behavior from that observed in a fully buffered solution to that typical of infinitely high coverage. The value of the surface coverage parameter β need to be changed by a five orders of magnitude to switch from one limiting case to another.

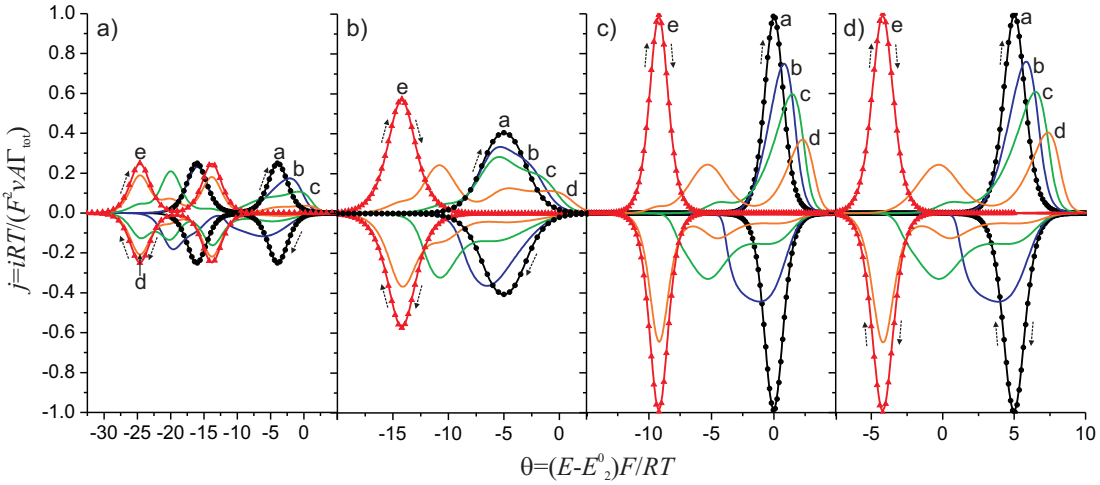

Figure 4.22: Voltammogram simulated at various values of the surface coverage $\beta = \frac{[H^+]_0}{\Gamma_t}\sqrt{\frac{DRT}{vf}}$, electron transfer is assumed to be infinitely fast, K_a corresponds to the NS ($\chi_1 = 10^4, \chi_2 = 10^0, \chi_3 = 10^2, \chi_4 = 10^{-4}, \chi_4 = 10^{-2}, \chi_6 = 10^{-6}$) case. a) $E_5^0 - E_2^0 = -20$, b) $E_5^0 - E_2^0 = -10$, c) $E_5^0 - E_2^0 = 0$, d) $E_5^0 - E_2^0 = 10$. Curves (a), (b), (c), (d) and (e) corresponds to $\beta = 100$, 0.32, 0.1, 0.032 and 10^{-4}, dots shows voltammograms calculated for the case of fully buffered solution, triangles shows voltammograms calculated for the case of infinitely high coverage.

Figure 4.24 shows the peak values calculated for the parameters corresponding to a two electron reduction of AQMS (anthraquoinone 2-monosulfonate) adsorbed on an EPPG (edge plane pirolitic graphite) electrode, experimental details and results of this studies will be published elsewhere.[54] Here at low (pH<3) and high values of pH (pH>11) the electrochemical response in a fully buffered and unbuffered solutions are identical. At low pH the response is identical because the concentration of protons in solution is high enough to assume the solution is self buffered and at high pH reaction occurs without consumption/production of protons as the main forms that are present in solution are A, A^- and A^{2-}. At intermediate pHs the voltammogram shape significantly depends upon the pH(Figure 4.25). At pH=3.75 the forward peak becomes significantly broader and at pH=5 the

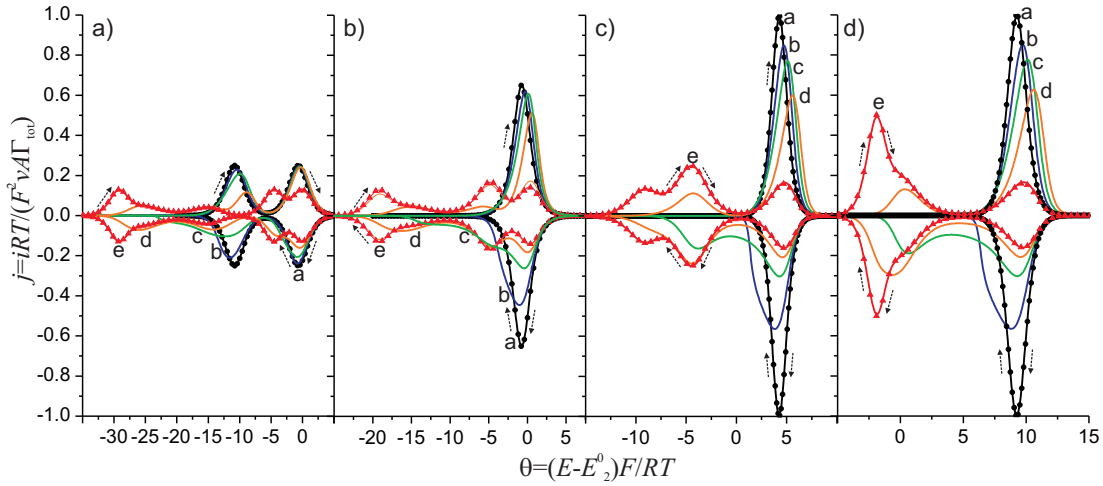

Figure 4.23: Voltammograms simulted at various values of the surface coverage $\beta = \frac{[H^+]_0}{\Gamma_t}\sqrt{\frac{DRT}{vf}}$, electron transfer is assumed to be infinitely fast, K_a corresponds to the SN ($\chi_1 = 10^4, \chi_2 = 10^2, \chi_3 = 10^0, \chi_4 = 10^{-2}, \chi_5 = 10^{-4}, \chi_6 = 10^{-6}$) case. a) $E^0_5 - E^0_2 = -20$, b) $E^0_5 - E^0_2 = -10$, c) $E^0_5 - E^0_2 = 0$, d) $E^0_5 - E^0_2 = 10$. Curves (a), (b), (c), (d) and (e) corresponds to $\beta = 100$, 1, 0.32, 0.1 and 10^{-4}, dots shows voltammograms calculated for the case of fully buffered solution, triangles shows voltammograms calculated for the case of infinitely high coverage.

forward peak is highly asymmetric with a shape which is more common to that found for diffusing species. Two peaks are observed between pH 4.25 and 5 on the forward scan and from pH 4.25 to 6.25 on the backward scan. Figure 4.26 shows the total concentration of oxidised, monoreduced and direduced forms, it is clear that the mechanism of peak splitting here is similar to that discussed in the section for a one electron, one proton reduction, but it is not due to two one electron transfers, with a high concentration of the monoreduced species. Figures 4.25) and 4.26 show that during backward scan at potentials from -0.4 to -0.6 V the electrochemical reaction changes direction, this is due to significant change of apparent potentials (equations 4.64 and 4.65) with a change of the local pH.

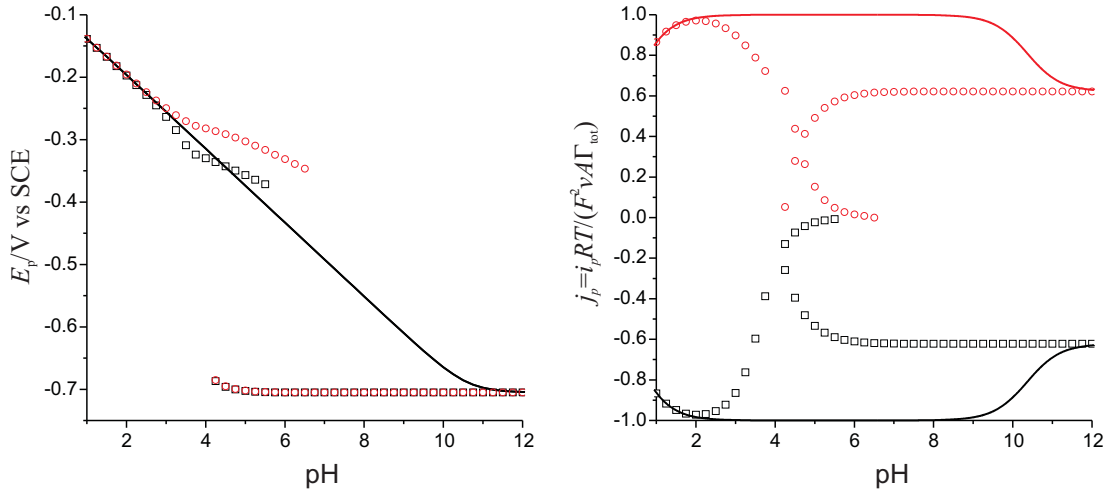

Figure 4.24: Peak current and peak potential simulated at values of parameters corresponding to AQMS adsorbed on EPPG electrode:[54] $E_2^0 = -0.404$ V, $E_5^0 = -0.404$ V, pK_a 2 (0), 3(5.0), 4(5.0), 5(10.4) and 6(10.6) in a fully buffered media (solid lines) and for the case of finite rate of math transport, $\beta = 5 \times 10^3$ (scattered lines, squares and circles correspond to forward and backward scans accordingly). No information on value of pK_{a1} 1 is available in work,[54] but it is known that form M is not present in solution, so pK_{a1} was equal to 4.

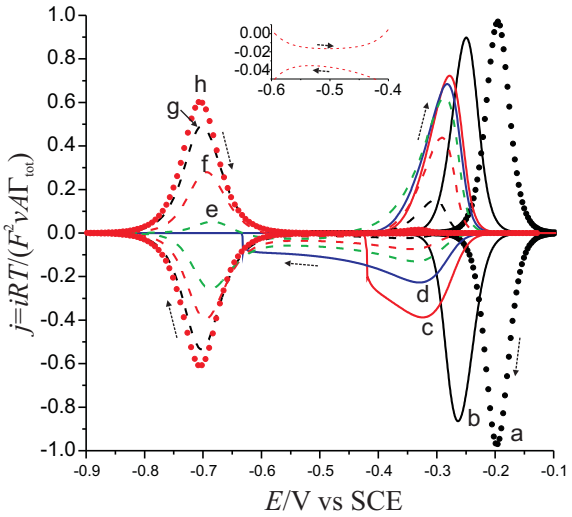

bth

Figure 4.25: Voltammograms simulated at values of parameters corresponding to AQMS adsorbed on EPPG electrode:[54] $E_2^0 = -0.404$ V, $E_5^0 = -0.404$ V, $pK_a1 = 4.0$*, 2 (0), 3(5.0), 4(5.0), 5(10.4) and 6(10.6); $\beta = 5 \times 10^3$. Curve (a) calculated at pH=2, b (3), (c) 3.75, (d) 4, (e) 4.25, (f) 4.5, (g)5 and (h) 6. Inlay shows magnified region around $E = -0.5$ V for the voltammogram calculated at pH=4.5.

4.4.4 Two Electron, Two Proton Reaction: Concerted Mechanism

Fully Buffered Solutions

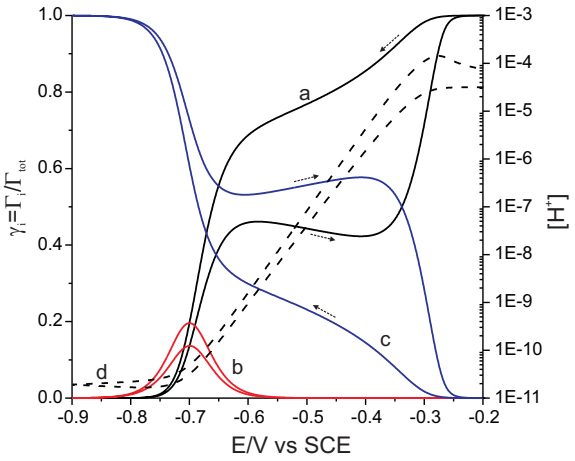

Figure 4.26: Concentration profiles simulated at values of parameters corresponding to AQMS adsorbed on EPPG electrode.[54] Solid curves (a), (b) and (c) corresponds to total concentration of oxidised, once reduced and twice reduced species, dashed line (d) shows local pH nearby electrode surface.

We have shown earlier that theory on concerted electron transfer in a fully buffered solution can be derived from that for a simple one electron reduction. Here a similar theory of a consecutive two electron reduction coupled with protonation in a fully buffered solution is derived from that for a simple two electron reduction.

$$E_{1\mathrm{app}} = E^0_{1\mathrm{f}} + \frac{RT}{F} \ln \frac{[\mathrm{H}^+]}{[\mathrm{H}^+]^*} \tag{4.74}$$

$$E_{2\mathrm{app}} = E^0_{2\mathrm{f}} + \frac{RT}{F} \ln \frac{[\mathrm{H}^+]}{[\mathrm{H}^+]^*} \tag{4.75}$$

and

$$k_{1\mathrm{app}} = k_1[\mathrm{H}^+] \tag{4.76}$$

$$k_{1\mathrm{app}} = k_2[\mathrm{H}^+] \tag{4.77}$$

Hence, the voltammograms shape and peak values in the case of infinitely fast electron transfer are given by the equations 4.66 and 4.67-4.70, accordingly.

Unbuffered Solutions

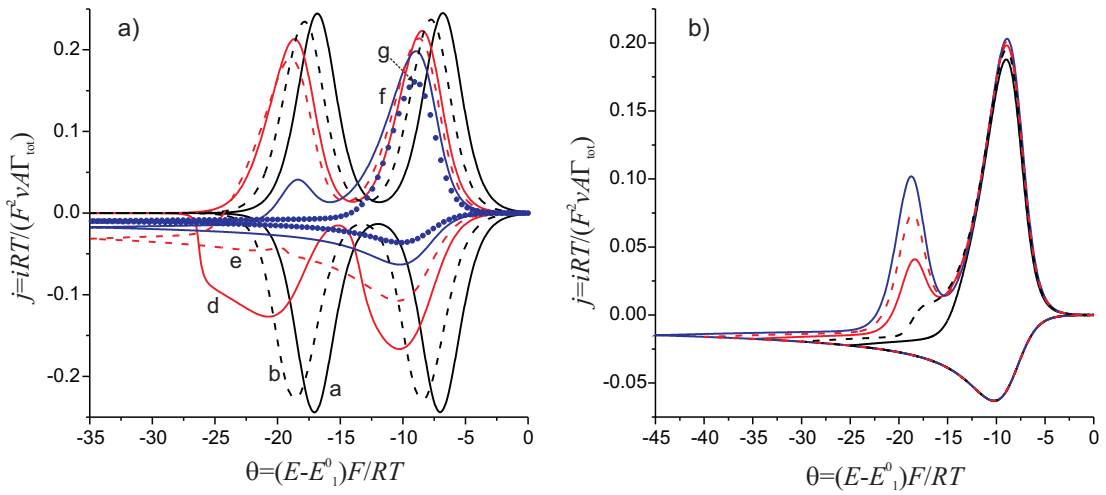

Figure 4.27: Simulated voltammograms for the case of concerted two electron, two proton reduction, electron transfer is assumed to be infinitely fast, $\beta = 10^5$. a) $E_1^0 = E_2^0$, b) $\frac{(E_2^0 - E_1^0)F}{RT} = -10$. Lines (a), (b), (c), (d), (e) and (f) correspond to pH values of 3, 3.5, 4, 4.25, 4.5 and 4.75 respectively. *a) Should be moved to supplementary material/removed in paper version*

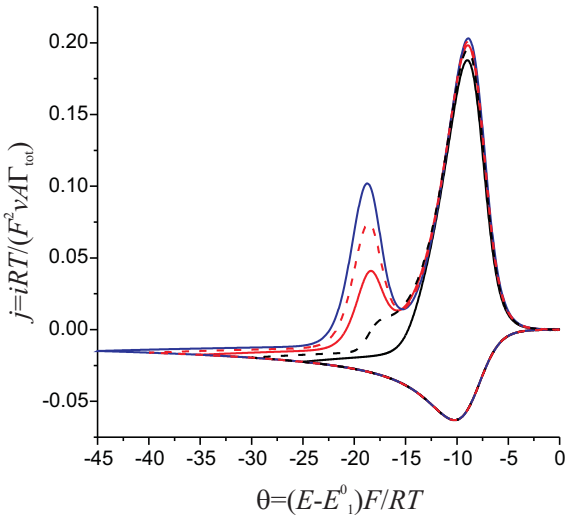

Figure 4.28: Switching potential influence on the back peak, electron transfer is assumed to be infinitely fast, $\beta = \frac{[H^+]^*}{\Gamma_{tot}}\sqrt{\frac{DRT}{vF}} = 5 \times 10^3$, pH=4.5.

Figure 4.27 shows the voltammograms simulated in unbuffered solution. In the case when $E_1^0 = E_2^0$ the peak shape changes with pH similar to that found for a one electron reduction, in the case where the first and second electron transfers are well separated $\frac{(E_2^0 - E_1^0)F}{RT} = -10$ two peaks are observed at low pH. An increase in pH changes the voltammogram shape, with it becoming asymmetric with a long "diffusional tail" at high negative overpotentials, finally the second peak vanishes on the forward scan. The number of peaks observed on the backwards scan depends both upon the value of factor βa and switching potential (Figure 4.28): if the total amount of electrons transfered during forward scan is high enough that the substance AH_2 is formed then two peaks will be observed, in the opposite way if only AH is formed on the forward scan only one peak will be observed on the backward scan.

4.5 Conclusions

First we have extended the theory for a stepwise one proton, one electron reduction of a surface bound species in a fully buffered solution as proposed by Laviron to the general case where the symmetry coefficients α_i can have any value and demonstrated that this has a significant effect on voltammograms shape. Next we propose a simple analytical solution for the limiting case in which electrodes have an infinitely high coverage; in this situation the voltammograms shape is different from that observed in fully buffered media and in particular peak splitting is observed. Further we considered the theory for reduction of a surface bound species coupled with the diffusional mass transport of protons from solution. We have demonstrated that the voltammograms in unbuffered media significantly is different from that observed in fully buffered solutions in particular the forward peak has a shape characteristic of diffusional voltammetry and the backward peak that of stripping voltammetry. We also showed that concerted and stepwise mechanisms results in different types of behavior in unbuffered solutions: peak splitting and the change of peak shape to a highly asymmetric diffusional like waveform is common for stepwise and concerted mechanisms, respectively. Hence voltammetry in unbuffered media may be used to distinguish these mechanisms and to extract kinetic and thermodynamic parameters for systems on interest.

References

[1] Costenin, C. *Chem Rev* **2008,** *108,* 2145–2179.

[2] Huynh, M.; Meyer, T. *Chem Rev* **2007,** *107,* 5004–5064.

[3] Amatore, C.; Gareil, M.; Savant, J.-M. *J Electroanal Chem* **1984,** *176-382,* 377.

[4] Shouji, E.; Buttry, D. A. *J Phys Chem B* **1999,** *124,* 2239–2247.

[5] Laviron, E.; Meunier-Prest, R.; Mathieu, E. *Electroanal Chem* **1994,** *371,* 251-258.

[6] Meunier-Prest, R.; Gaspard, C.; Laviron, E. J. *J Electroanal Chem* **1996,** *410,* 145-154.

[7] Mathieu, E.; Meunier-Prest, R.; Laviron, E. *Electrochim Acta* **1997,** *42,* 331–336.

[8] Mathieu, E.a nd Meunier-Prest, R.; Laviron, E. *Electrochim Acta* **1997,** *42,* 2419–2426.

[9] Laviron, E.; Meunier-Prest, R.; Vallat, A.; Roullier, L.; Lacasse, R. *J Electroanal Chem* **1992,** *341,* 227-255.

[10] Lacasse, R.; Meunier-Prest, R.; Laviron, E.; Vallat, A. *J Electroanal Chem* **1993,** *359,* 223.

[11] Laviron, E.; Vallat, A.; Meunier-Prest, R. *J Electroanal Chem* **1994,** *379,* 427–435.

[12] Dion, D.; Laviron, E. *Electrochim. Acta 1* **1998,** *43,* 2061-2069.

[13] Dion, D.; Meunier-Prest, R.; Laviron, E. *Acta Chem Scan* **1997,** *51,* 411.

[14] Webster, R. D. *Acc Chem Res* **2007,** *40,* 251-257.

[15] Wang, J.; Wang, L.; Wang, Y.; Yang, W.; Jiang, L.; Wang, E. *J Electroanal Chem* **2007,** *601,* 107-111.

[16] Anne, A.; Hapiot, P.; Moiroux, J.; Neta, P.; Savant, J.-M. *J Phys Chem* **1991,** *95,* 2370-2377.

[17] Lebeau, E.; Adeyemi, S. J.; Meyer, T. J. *Inorg Chem* **1998,** *37,* 6476.

[18] Takeuchi, K. J.; Thompson, M. S.; Pipes, T. J.; Meyer, T. J. *Inorg Chem* **1984,** *23,* 1845-1851.

[19] Ho, C.; Che, C.; Lay, T. *J Chem Soc, Dalton Trans* **1990,** 967-970.

[20] Laviron, E. *J Electroanal Chem* **1980,** *109,* 57–67.

[21] Laviron, E. *J Electroanal Chem* **1983,** *146,* 15-36.

[22] Batchelor-McAuley, C.; Li, Q.; Dapin, S.; Compton, R. *J Phys Chem B* **2010,** *114,* 40944100.

[23] Quan, M.; Sanchez, D.; Wasylkiw, M. F.; Smith, D. K. *J Amer Chem Soc* **2007,** *129,* 1284712856.

[24] Guo, S.; Feldberg, S.; Bond, A.; Callahan, M.; Richardt, P.; Wedd, A. *J Phys Chem B* **2005,** *109,* 20641–20651.

[25] Yeo, W. S.; Mrksich, M. *Angew Chem Int Ed* **2003,** *42,* 3121-3124.

[26] Nayak, S.; Yeo, W. S.; Mrksich, M. *Langmuir* **2007,** *23,* 5578-5583.

[27] Hong, H. G.; Park, W. *Langmuir* **2001,** *17,* 2485–2492.

[28] Funt, B. L.; Hoang, P. M. *J Electroanal Chem* **1983,** *154,* 229–238.

[29] Takada, K.; Gopalan, P.; Ober, C. K.; Abruna, H. D. *Chem Mater* **2001,** *13,* 2928-2932.

[30] Sato, Y.; Fujita, M.; Mizutani, F.; Uosaki, K. *J Electroanal Chem* **1996,** *409,* 145–154.

[31] Forster, R. J.; OKelly, J. P. *J Electroanal Chem* **2001,** *498,* 127.

[32] Yu, H.-Z.; Wang, Y.-Q.; Cheng, J.-Z.; Zhao, J.-W.; Cai, S.-M.; Inokuchi, H.; Fujishima, A.; Liu, Z.-F. *Langmuir* **1996,** *12,* 2843-2848.

[33] Trammell, S. A.; Lowy, D. A.; Seferos, D. S.; Moore, M.; Bazan, G. C.; Lebedev, N. *Langmuir* **2007,** *23,* 942-948.

[34] Walsh, D.; Keyes, T.; Hogan, C.; Forster, R. *J Phys Chem B* **2001,** *105,* 2792-2799.

[35] Haddox, R.; Finklea, H. *J Phys Chem B* **2004,** *108,* 1694-1700.

[36] Madhiri, N.; Finklea, H. *Langmuir* **2006,** *22,* 10643–10651.

[37] Jacq, J. *J Electroanal Chem* **1971,** *29,* 149-180.

[38] Petek, H.; Zhao, J. *Chem Rev DOI: 10.1021/cr1001595* .

[39] Hammes-Schiffer, S.; Stuchebrukhov, A. A. *Chem Rev DOI: 10.1021/cr1001436* .

[40] Costentin, C.; Robert, M.; Saveant, J.-M.; Teillout, A. *Proc Nac Am Sci* **2009,** *106,* 11829-11836.

[41] Costentin, C.; Loualt, C.; Robert, M.; Saveant, J.-M. *Proc Nac Am Sci* **2009,** *106,* 18143-18148.

[42] Bard, A. J.; Faulkner, L. R. *Electrochemical Methods: Fundamentals and Applications;* John Wiley and Sons: New York, 2001.

[43] Dickinson, E. J. F.; Limon-Petersen, J. G.; Rees, N. V.; Compton, R. G. *J Phys Chem C* **2009,** *113,* 11157-11171.

[44] Menshykau, D.; Compton, R. G. *J Phys Chem C* **2009,** *113,* 15602-15620.

[45] Press, W.; Teukolsky, S.; Vetterling, W.; Flannery, B. *Numerical Recipes: The Art of Scientific Computing;* Cambridge University Press: 2007.

[46] Atkinson, K. *Elementary Numerical Analysis, 3rd ed;* John Wiley and Sons: New York, 2004.

[47] Srinivasan, S.; Gileadi, E. *Electrochim Acta* **1966,** *11,* 321–335.

[48] Tanaka, N.; Tamamushi, R. *Electrochim Acta* **1964,** *9,* 963–989.

[49] Rees, N. V. *Innovation in Voltammetry,* Thesis, University of Oxford, 2004.

[50] Evans, R. G.; Klymenko, O. V.; Saddoughi, S. A.; Hardacre, C.; Compton, R. G. *J Phys Chem B* **2004,** *108,* 7878–7886.

[51] Clegg, A. D.; Rees, N. V.; Klymenko, O. V.; Coles, B. A.; Compton, R. G. *ChemPhysChem* **2004,** *5,* 1234–1240.

[52] Meunier-Prest, R.; Laviron, E. *J Electroanal Chem* **1996,** *410,* 133-143.

[53] Plichon, V.; Laviron, E. *J Electroanal Chem* **1976,** *71,* 143-156.

[54] Neumann, C. C. M.; Batchelor-McAuley, C.; Compton, R. G. *submitted to Chemistry - A European Journal* .

Chapter 5

Micro-Electrodes and Their Arrays: Diffusional Independence and Applications.

5.1 Introduction

Microelectrode arrays find wide application in electroanalysis due to their high current output as compared to a single microelectrode, whilst showing considerably less background/capacitative currents, as well as significantly enhanced sensitivity, in comparison to macroelectrodes.[1–8] Various techniques[9–11] permits the fabrication of surfaces with a precisely defined geometry at the micro- or nano-scale. Considerable efforts have been devoted to designing new types of arrays containing micro-/nano-electrodes in both regular and random distributions.[4,12–14] A critical factor in the design/fabrication of regular microdisk arrays is the center-to-center separation, d, between nearest neighbor electrodes. This needs to be large enough to avoid the overlap of adjacent diffusion zones but not too large as to result in inefficient use of space.[15] Ideally the behavior of the microelectrode array should be similar to that of a single microelectrode, except in the magnitude of current. This requires that the diffusion layers of the microelectrodes in the array do not overlap. These conditions are referred to as diffusional independence. Such behavior can only be observed at timescales short compared to the time for molecule to diffuse the distance d. Note that earlier simulation work on potential steps or cyclic voltammetry at arrays of microdisks has been reported.[15–17]

In this chapter we use potential step chronoamperometry to investigate both theoretically and experimentally the concept of diffusional independence[15,18] which has been well documented for isolated microelectrodes[19–21] and also used to study microelectrode arrays.[16,17] It is emphasized that the absolute distance d controls the timescale of diffusional independence.

5.2 Mathematical Model

5.2.1 Model of the Electrode Surface

Disk Electrodes, and Their Arrays

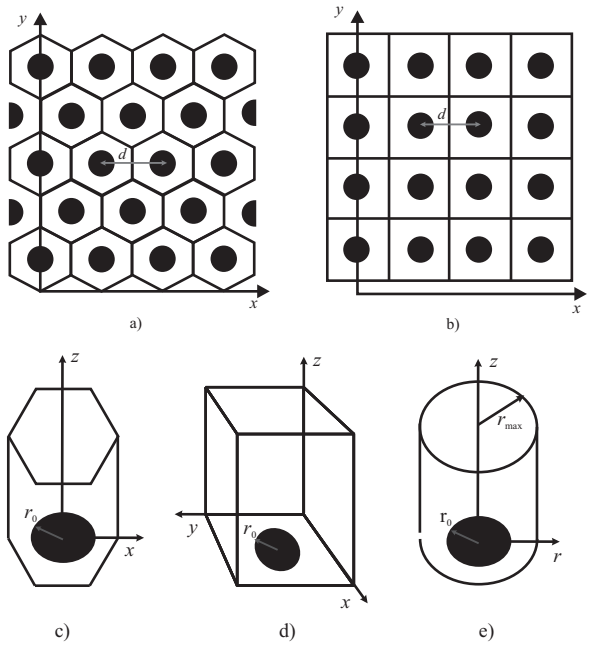

Figure 5.1: Conceptual rendering of hexagonal (a) and cubic (b) arrays of microdisk electrodes; (c) hexagonal and (d) cubic unit cell in Cartesian coordinates; and (e) equivalent diffusion domain in cylindrical coordinates.

The idealized surface is composed of a regular array of microdisk electrodes (Figure 5.1). We consider here two types of arrays: hexagonal and cubic. The diffusion of electrochemically active species to such a surface is complicated because it is intrinsically a three-dimensional problem. However, the problem can be simplified by noting that each electrode belongs to a diffusionally independent region known as a diffusion domain.[22,23] The diffusion domain approximation treats these zones as being cylindrical with a microdisk center situated at the axis of symmetry, thus reducing the problem of diffusion to one of only two dimensions. The approximation is illustrated in Figure 5.1. Figure 5.1c and 5.1d identify unit cells in Cartesian coordinates for hexagonal and cubic arrays. Figure 5.1e shows the diffusional domain in cylindrical coordinates (r,z). Note that the cylindrical coordinate system is defined relative to the single electrode domain. The cylindrical radial coordinate, r, is defined as the distance from the axis of symmetry that runs through the center of the electrode domain. The distance between microdisk centers in arrays is d. The area of cylindrical domain is chosen to be equal to the area of the unit cell in Cartesian coordinates:

$$d^2 = \pi r_{\max}^2 \tag{5.1}$$

for hexagonal and

$$\frac{\sqrt{3}}{3} d^2 = \pi r_{\max}^2 \tag{5.2}$$

for cubic arrays. The total current from the macroelectrode is given by simple multiplication of the current from a single diffusional domain to the total number of domain N_p. Recently it was shown that two dimensional simulations in conjunction with the diffusion domain approach gives results indistinguishable from full three dimensional simulations.[24]

Ring, Ring-Recessed Electrodes, and Their Arrays

The diffusional domain approximation for the array of ring electrodes is illustrated in Figure 5.2. Figure 5.2a and b show the surface in Cartesian coordinates and Figure 5.2c identifies the unit cell in cylindrical coordinates (r,z). The distance between microring centres in array is d. The area of cylindrical domain chosen to be equal to the area of the unit cell in Cartesian coordinates (Equation 5.1).

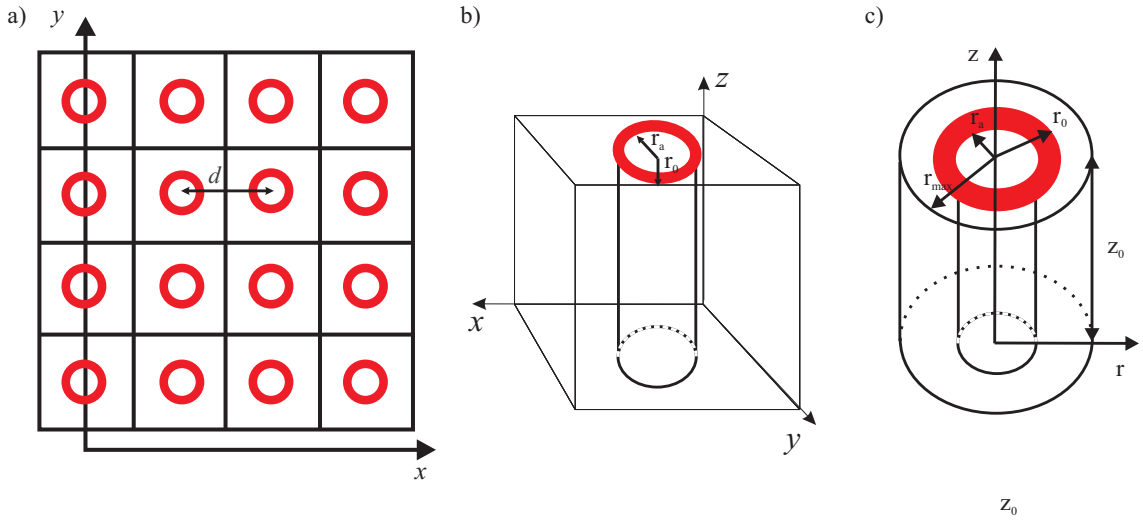

Figure 5.2: (a)Schematic diagram of the unit cell for an array of ring-recessed electrodes; (b) single unit cell in Cartesian coordinates; (c) equivalent diffusion domain in cylindrical coordinates.

5.2.2 Mathematical Model

Equation 5.3 shows the electron transfer reaction at the disc (ring) electrode considered in these numerical simulations. We next consider the potential step experiment applied to the reduction of A at the disc (ring) electrode where the initial condition is zero Faradaic current. Species A and B might have different or equal diffusion coefficients.

$$\mathrm{A} \pm ne^{-} \rightleftharpoons \mathrm{B} \tag{5.3}$$

Table 5.1: Dimensionless parameters used for numerical simulation.

Parameter	Expression normalized to r_0
Radial coordinate	$R = r/r_0$
Normal coordinate	$Z = z/r_0$
Pore depth	$L_{\mathrm{cyl}} = \frac{z_0}{r_0}$
Inner radius of collector ring	$R_{\mathrm{a}} = \frac{r_{\mathrm{a}}}{r_0}$
Radius of diffusion domain	$R_{\max} = \frac{r_{\max}}{r_0}$
Time	$\tau = \frac{Dt}{r_0^2}$
Concentration of species A	$a = [\mathrm{A}]/[\mathrm{A}]_0$
Electrode current	$j = \frac{-i}{4FDn[\mathrm{A}]_0 r_0}$

Mass transport in cylindrical coordinates is described by Fick's second law of diffusion given by equation 5.4:

$$\frac{\partial[\mathrm{A}]}{\partial t} = D_{\mathrm{A}}\left(\frac{\partial^2[\mathrm{A}]}{\partial r^2} + \frac{1}{r}\frac{\partial[\mathrm{A}]}{\partial r} + \frac{\partial^2[\mathrm{A}]}{\partial z^2}\right) \tag{5.4}$$

Note that here we assume that the solution is fully supported[25] and Fick's second law of diffusion adequately describes mass transport in fully supported media when migration can be neglected and if the length scale of the device is larger than *ca* 10 nm.

Table 5.2: Boundary and initial conditions.

Boundary	Condition
Initial concentration	$a = 1$
Bulk solution concentration	$a = 1$
Concentration at electrode	$a = 0$
Axis of symmetry and insulator surface	$\frac{\partial a}{\partial R} = 0$
Diffusion domain border	$\frac{\partial a}{\partial R} = 0$
Insulator surface	$\frac{\partial a}{\partial Z} = 0$

The model is normalized with use of dimensionless parameters which are listed in table 5.1. Mass transport in cylindrical coordinates is given by the dimensionless version of equations 5.4:

$$\frac{\partial a}{\partial \tau} = \frac{\partial^2 a}{\partial R^2} + \frac{1}{R}\frac{\partial a}{\partial R} + \frac{\partial^2 a}{\partial Z^2} \tag{5.5}$$

The boundary conditions for equations 5.5 corresponds to potential step chronoamperometry are summarized in table 5.2.

5.3 Experimental and Computational Details

5.3.1 Computational Procedure

Because of the symmetry of the model, the mass transport equation 5.5 and its accompanying boundary conditions (table 5.2) were solved in the two dimensional space in the region $0 < R < R_{\max}$ and $Z > 0$. The bulk solution condition is implemented at a distance $6\sqrt{\tau_{\max}}$ from the highest point of the electrode, where $\tau_{\max}$ is the duration of potential step experiment. Beyond this the effects of diffusion are not important on the experimental voltammetric timescale.[26,27] The modeling of the ring-recessed electrode is complicated by the presence of singularities at the boundaries between the electrode and the insulators. To calculate the precise values of the current at the electrodes a rectangular expanding grid, similar to that used in previous simulations of electrodes with complicated surfaces[28–31] was utilised. The expanding grid is defined by equations 5.6-5.9.

$$R_{i+1} - R_i = h_i \tag{5.6}$$

$$Z_{i+1} - Z_i = k_i \tag{5.7}$$

$$h_i = \gamma_R \times h_{i-1} \tag{5.8}$$

$$k_i = \gamma_Z \times k_{i-1} \tag{5.9}$$

An exponentially expanding time grid was also used. The standard values of parameters used to simulate current transient on a microdisk were $h_0 = k_0 = 10^{-8}$. For the thin rings, current density becomes extremely high at the electrode edges[32,33] and fine meshes are necessary to meet the required computational accuracy. Standard values of the mesh used in computations were $h_0 = k_0 = 10^{-8}$ and $\gamma_R = \gamma_Z = 1.125$. The alternating direction implicit finite difference method[34] was used in conjunction with the Thomas algorithm[35] to solve the discretized form of the mass transport equation 5.5. The ADI method in conjunction with the Thomas algorithm ideally suits parallel computations, which was implemented by OpenMP. The program was written in C++.

The dimensionless current at ring electrodes of cylindrical symmetry was calculated with formula 5.10.

$$j = \frac{\pi}{2} \int_{R_a}^{1} j' R \mathrm{d}R \tag{5.10}$$

$j' = \frac{\partial a}{\partial Z}$ was calculated with a three point approximation.[36]

5.3.2 Computational Accuracy

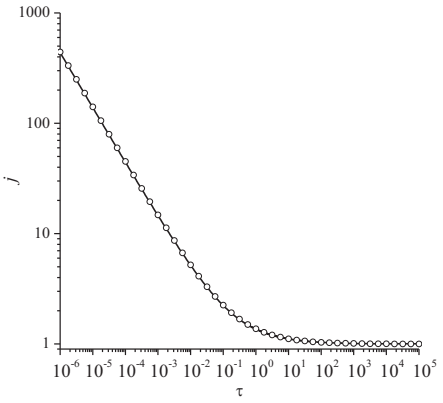

Figure 5.3: Diffusional current versus dimensionless time in the potential step experiment. The solid line is our simulated transient for an isolated single microdisk electrode, the circles here were calculated with ShoupSzabo equation.

To check the convergence of the simulation procedure numerous simulations with different space grids and time steps were run. The calculated current converges with a decrease in the space and time steps, similar to the convergence presented in ref.[37] To validate the procedure, comparisons to the known results for isolated single microdisk electrodes were made. The current in this case is given by the empirical Shoup-Szabo expression (equation 5.11);[19,27] the comparison is presented in Figure 5.3. It is seen that the results perfectly match each other. At short times the current decays in agreement with the dimensionless form of the Cottrell equation (expression 5.12).[27,38]

$$j = 0.7854 + 0.4432\tau^{-1/2} + 0.2146\exp(-0.3912\tau^{-1/2}) \tag{5.11}$$

$$j = \frac{\pi^{1/2}}{4\tau^{1/2}} \tag{5.12}$$

To further validated the procedure and estimate accuracy comparison to known asymptotic solutions at short (equation 5.13) and long (equation 5.14) times were made. Figure 5.4 shows that for all tested ranges of ring thicknesses the deviation did not exceed 0.1 %. Furthermore the current transients calculated at average times are in agreement with those reported in recent computational papers.[32,33]

$$j = \frac{\pi(1+R_a)}{4} + \frac{\pi^2(1-R_a^2)}{\tau^{1/2}} \tag{5.13}$$

$$j = l_0(1 + \frac{l_0}{2\pi^{3/2}\tau^{1/2}})/4 \tag{5.14}$$

where l_0 is the steady-state current at the microring electrode. Szabo[39] proposed an empirical expression for l_0 which is accurate over the whole range of ring thicknesses:

$$l_0 = \frac{\pi^2(1+R_a)}{\ln\left(\frac{32R_a}{1-R_a} + \exp\frac{\pi^2}{4}\right)} \tag{5.15}$$

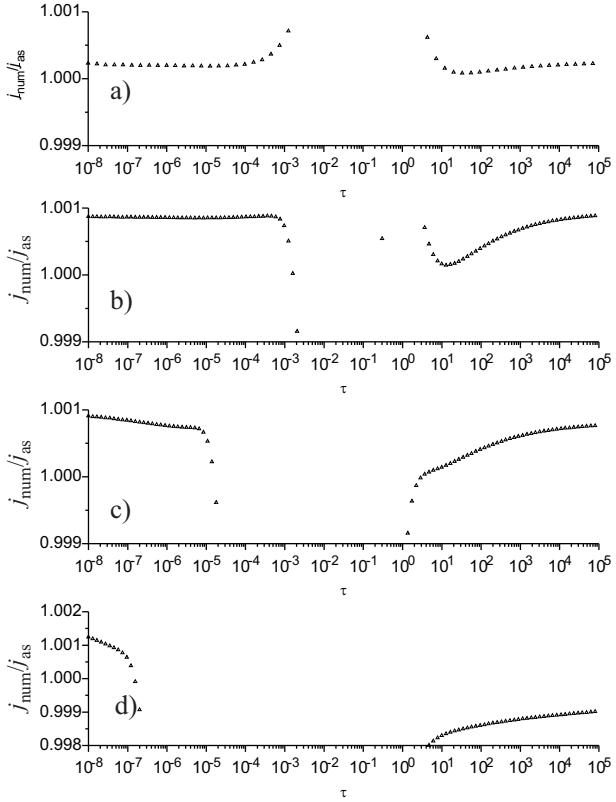

Figure 5.4: Deviation of current calculated numerically from that given by the asymptotic solutions. Disc electrode a), ring electrode R_a=(b)0.9, (c) 0.99, (d) 0.999

5.3.3 Simultaneous Measurement of n[A] and D: procedure

To simulate realistic experimental conditions for current transients calculated according to the procedure in the section above two types of noise were added: (I) normally (Gaussian) distributed noise with zero mean and standard deviation proportional to current (Figure 5.5 a)); (II) uniformly distributed error proportional to the steady state current at the same electrode (Figure 5.5 b)). Generated voltammograms were fitted either with a numerically calculated (tabulated) function generated in simulation or using Shoup-Szabo expression 5.11. Tabulated dimensionless functions have the following

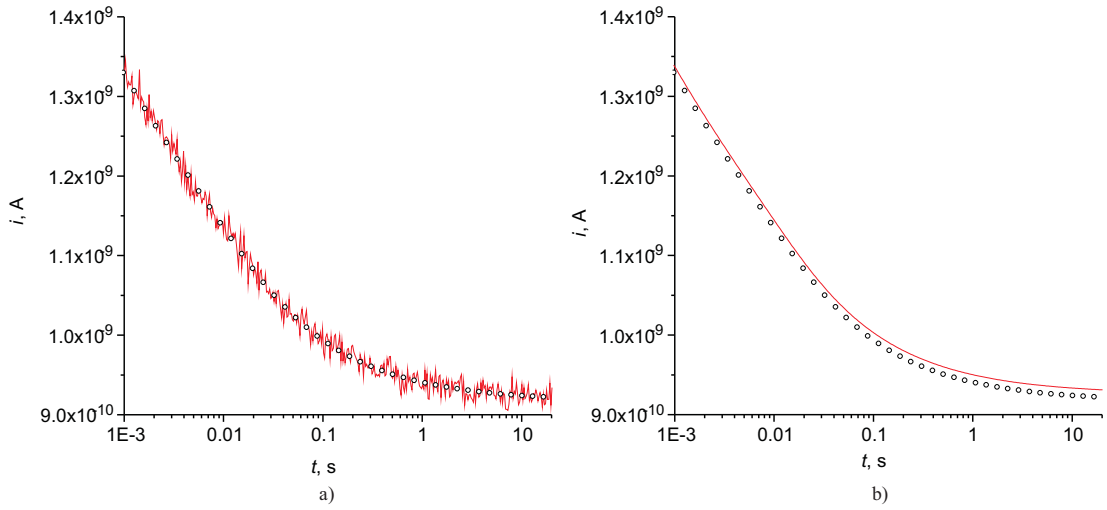

Figure 5.5: Example of voltammograms used to simulate noisy experimental voltammograms, a) normally distributed error with amplitude of 1% of local current, b) unifomly distributed error with amplitude of 1% of steady state current. Open circles correspond to an ideal voltammogram; the solid line corresponds to a voltammogram generated with an added error.

form:

$$j_{\mathrm{i}} = f_{\mathrm{tab}}(\log(\tau_{\mathrm{i}})) \tag{5.16}$$

Values of of D and [A] can be found by non-linear least-square fitting of function 5.17 to experimental data:

$$i = 4FDr_0[\mathrm{A}]f_{\mathrm{interp}}(\log(\frac{tD}{r_0^2})) \tag{5.17}$$

where f_{interp} as in previous work,[40] returns linearly interpolated values between nodes of tabulated function f_{tab}. The number of points in the tabulated function were selected in such a manner that doubling of them has no influence on the values of parameters extracted and was usually equal to a hundred points per decade of time in logarithmic scale.

The software package Origin 8.0 (OriginLab, Northampton, MA) was used to fit the data. The value of r_0 was assumed to be known and was not varied during fitting. Ten sample chronoamperograms were generated with normally distributed error. n[A] and D values extracted from sample transients were averaged and the standard deviation was calculated. In case of uniformly distributed error only one chronoamperogram was generated for each amplitude of the error; n[A] and D were found as well as their standard errors. Two types of datasets were generated: (I) data subset I of 320 points linearly distributed in logarithmic scale from $t = 0.001$ s to $t = 60$ s and (II) data subset II of

160 points linearly distributed in logarithmic scale from $t = 0.01$ s to $t = 20$ s.

5.3.4 Chemical Reagents and Instrumentation

All chemicals used were of analytical grade and were used as received without any further purification. These were: potassium chloride (KCl; Sigma-Aldrich), potassium ferrocyanide ($K_4Fe(CN)_6$; BDH Chemicals Ltd, UK), copper sulfate ($CuSO_4$; Aldrich), sodium sulfate (Na_2SO_4; Aldrich) and hydrochloric acid (HCl; Sigma-Aldrich). All solutions were prepared with deionized water of resistivity no less than 18.2 MΩ cm at 25 ^{0}C (Millipore water system, UK).

Voltammetric experiments were carried out with an μ-Autolab II (Eco-Chemic, Utrecht, The Netherlands) connected to a PC using GPES (version 4.9) software for Windows. All measurements were conducted using a three electrode cell. Iridium microelectrode arrays were used as the working electrode. A saturated calomel electrode (SCE) was used as a reference electrode and a graphite rod as a counter electrode. The pH was monitored using a Hanna Instruments pH 213 Microprocessor pH Meter. The images of microdisk array surfaces were captured with a Sony XC-999P CCD camera attached to an optical OMV-PAR microscope.

Prior to the voltammetric experiments, the system of 0.1 mM $K_4Fe(CN)_6$/0.1 M KCl was degassed using purified N_2. All experiments were conducted at 25 $\pm$ 1 ^{0}C.

Chronoamperometric transients for the oxidation of potassium ferrocyanide were recorded using different sample times: 0.05 s before the potential step and 0.0001, 0.001, 0.01 or 0.05 s after the potential step. The potential was stepped from 0.1 to 0.3 V.

In order to determine the true number of active microelectrodes on each array, copper metal was deposited onto the array surface *via* holding the potential at -0.4 V for 20 s in a solution of 0.05 M $CuSO_4$/0.1 M Na_2SO_4 (pH $\approx$ 3, adjusted with HCl). After copper deposition, the microelectrode surface was imaged with a camera attached to a microscope. This allowed us to undertake a visual count of the active microelectrodes on each array.

5.3.5 Array Fabrication

Photomasks were made in quartz covered by a thin layer of chromium where the patterns to be transferred are defined. Depending on whether these patterns are dark (chromium) or transparent (quartz), the masks are either clear field (also known as bright field) or dark field. Figure 5.6 shows schematic

representations of clear and dark field masks.

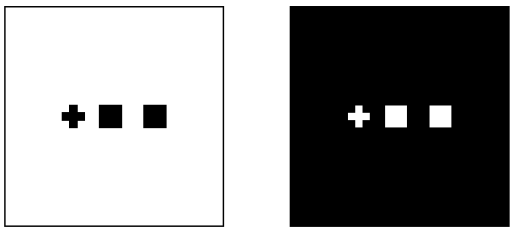

Figure 5.6: Schematic representation of bright- and dark-field photomasks.

Silicon wafers are labeled on the back using a laser engraver, after labelling the wafers are rinsed in deionised water. Next wafers were introduced into a tubular furnace LB45 ASM (ASM, France) at 1000 ^{0}C where 1 micron of silicon oxide was grown. This silicon oxide layer provides the necessary electrical insulation between the silicon and the metals that will become the electrodes.

The next step the creation of iridium structures is shown in Figure 5.7. The metal was patterned using a lift-off technique. First a layer of negative resist was spin coated over the wafer (Figure 5.7.1), which was then exposed to UV light through a clear-field photomask (Figure 5.7.2), photoresist was cross-linked during exposure to UV-light. Unexposed areas were removed in the development step. The reason to use a negative resist in lift-off processes is that the resulting ”T” profile of the resist favours the later removal of the resist after the metal has been deposited.

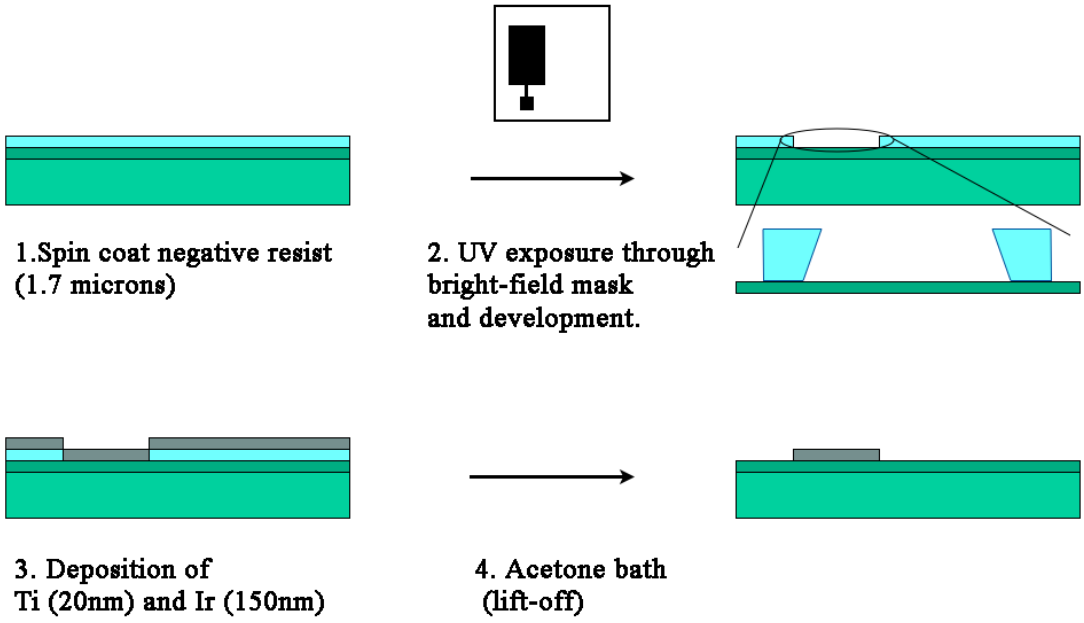

Figure 5.7: Schematic representation of a typical lift-off process.

After developing the resist, a layer of iridium (150nm) on titanium (20 nm) was deposited by

e-beam evaporation (Figure 5.7.3). Following this, the lift-off was done by immersion of the wafers in an acetone bath. The wafers were then rinsed in isopropanol and then in deionised water, which left the iridium electrodes and contacts on the wafers only (Figure 5.7.4).

Next, the gold structures (electrodes and contacts) were defined on the wafers by wet etching as depicted in Figure 5.8.

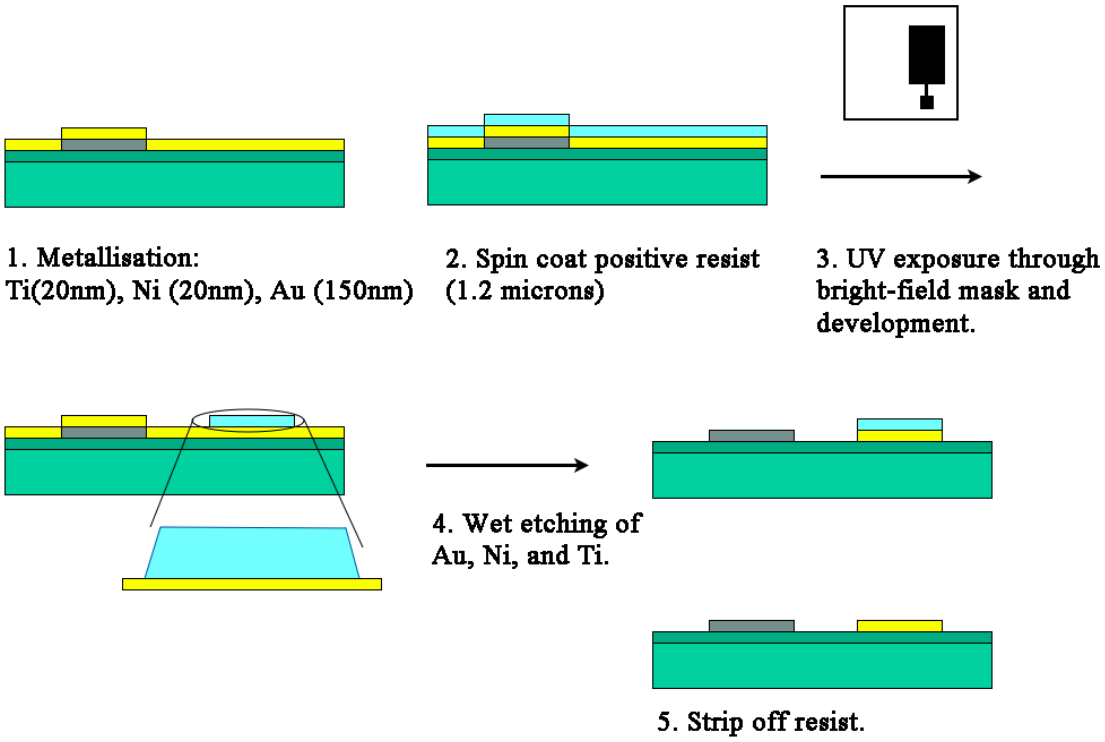

Figure 5.8: Schematic representation of the production of gold structures by wet etching.

The procedure consisted in first depositing a three-layer consisting of (bottom to top) Ti (20nm), Ni (20nm) and Au (150 nm), which were deposited by sputtering (Figure 5.8.1). The role of titanium was to improve adhesion of the subsequent metals on the wafer, and nickel was used as diffusion barrier between gold and titanium to avoid the formation of Ti-Au alloys due to heating of the wafers during the metallisation. After the wafer had been metallised, a layer of positive photoresist was spin-coated over it (Figure 5.8.2). The gold patterns were transferred through a clear-field mask (Figure 5.8.3). The unwanted metal was removed as described: the gold was first etched in an iodine/iodide solution, next nickel was removed in a concentrated nitric acid bath, and finally titanium was removed in HF (Figure 5.4). The wafers were rinsed after each step. Next the excess of resist was stripped in a stripper solution (acetone followed by isopropanol) and the wafers were again rinsed in deionised

water and dried (Figure 5.8.5).

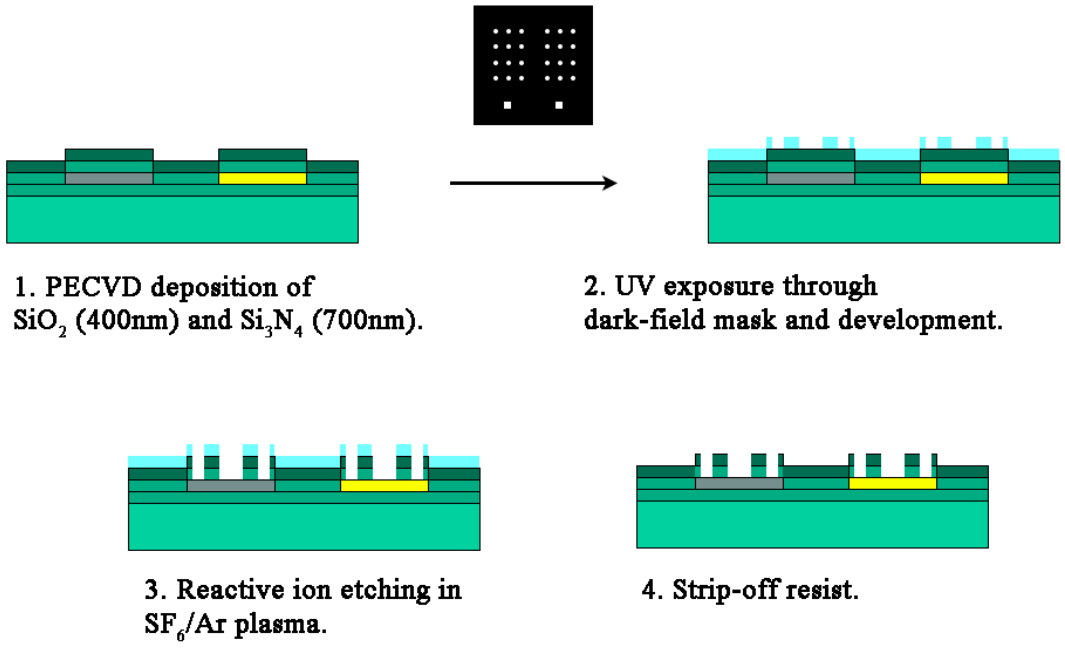

Figure 5.9: Photolithographic patterning of microelectrodes using reactive ion etching.

The wafer now presents areas covered in iridium and gold. In order to pattern the microelectrodes to the desired geometry, a passivation layer was deposited and patterned using plasma enhanced chemical vapour deposition, photolithography, and reactive ion etching, as shown in Figure 5.9. The passivation layer consisted of a double layer of (bottom to top) silicon oxide (400nm) and silicon nitride (700 nm) deposited in an Oxford instruments plasmalab 800Plus (Figure 5.9.1). Following passivation, the wafers were again processed through a new photolithographic step, where the final microelectrode patterns and contacts are defined in a dark-field mask, using a positive photoresist (Figure 5.9.2). Once developed, the resist was hard baked at 115^0C for 30 minutes prior to the dry etching step known as reactive ion etching. The passivation layer was attacked by a reactive plasma in an Alcatel AMS 110DE reactive ion etcher (Figure 5.9.3). Finally, the excess resist was removed in an acetone bath (Figure 5.9.4). The wafers were then rinsed and dried and the fabrication was complete.

The wafers were diced into individual chips using a Load Point AV14 sawing machine. After dicing, the wafers were mounted on custom-made, printed circuit boards to which they were wire bonded (Kulicke&Soffa 4500 manual bonder). Finally, the chips were encapsulated using either

photocurable or thermocurable resins so that the connection wires and pads were protected from the environment.

5.4 Time of Diffusional Independence: Results and Discussion

5.4.1 The Influence of R_{max}

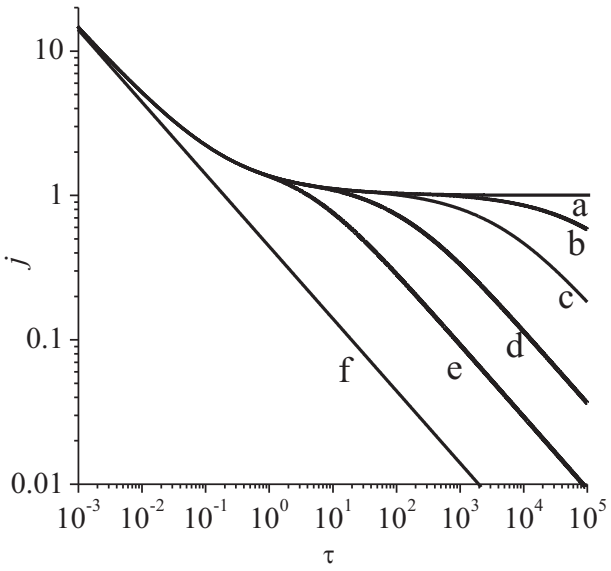

Figure 5.10: Calculated dimensionless current versus dimensionless time in the potential step experiment: (a) non-interacting domains; (b) R_{max} = 50; (c) R_{max} = 13; (d) R_{max} = 10; (e) R_{max} = 5; (f) macroelectrode.

Simulated results for the potential step experiments are presented in Figure 5.10. Values of the dimensionless current per single microdisk in an array are between the values of that from an isolated microdisk (curve (a) in Figure 5.10) and that given by equation (5.12), which corresponds to planar one-dimensional diffusion to a macroelectrode (curve (f) in Figure 5.10).[27,38] Considering Figure 5.10, the higher the value of diffusion domain radius R_{max} the longer the time a microdisk in an array behaves as a diffusionally independent electrode. At long times, in all cases, deviation from the ideal microdisk behavior is observed due to overlapping of diffusional layers between microelectrodes in the array. Figure 5.11 shows concentration profiles calculated for microdisk array with R_{max} = 5. At very small times $\tau < 0.01$ the diffusion is planar and inefficient, and consequently a decrease of current is observed.[27,42] At small times τ = 0.1 (Figure 5.11) and τ = 1 (Figure 5.11) the thickness of the diffusion layer is less than the separation between the electrodes in the array, and the current is similar to that from a diffusionally independent microdisk (Figure 5.11). On further increase of time the thickness of the diffusion layer gets larger and the diffusion layers of the microelectrodes in the array overlap (Figure 5.11); consequently the peak current deviates from the ideal behavior of a single isolated microdisk electrode. Further increase of the diffusion layer thickness with time causes a switch of diffusion type from two-dimensional to effectively one-

dimensional (Figure 5.11) and the current versus time in bi-logarithmic coordinates again has a slope of -1/2, corresponding to planar one-dimensional diffusion (equation 5.12).

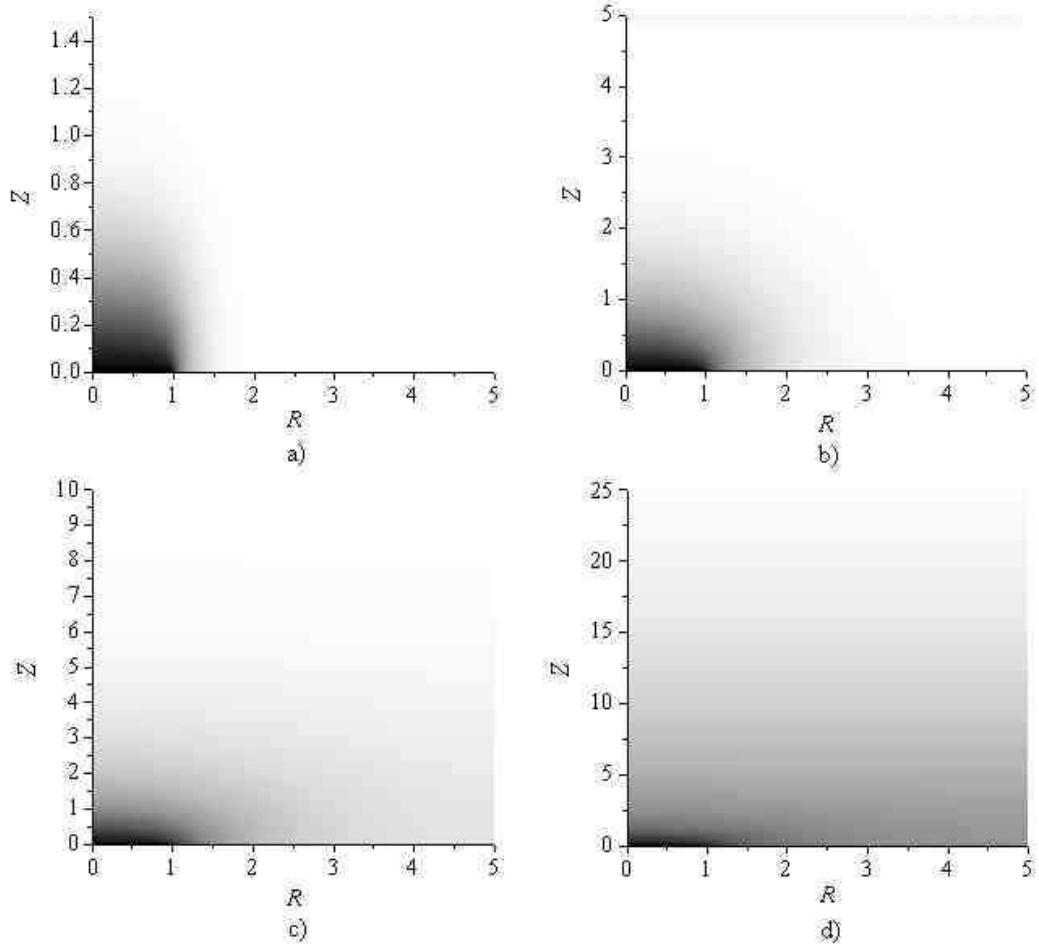

Figure 5.11: Simulated concentration profiles, R_{max} = 5: (a) τ= 0.1; (b) τ= 1; (c) τ = 10; (d) τ= 100. The density of colour identifies the concentration value.

5.4.2 The Influence of the Microdisk Radius and Array Symmetry

We consider here two types of array symmetry: hexagonal and cubic (Figure 5.1a and b). To characterize diffusional independence of microelectrodes in the array we introduce the time when the current reaches 90% of the steady-state current t_{DI} time of diffusional independence:

$$j(t_{DI})/N_p = 0.9 \times j_{ss} \tag{5.18}$$

Table 5.3: Timescale of diffusional independence

	Hexagonal			Cubic		
d/r_0^a	r_0=100 nm	r_0=1 μm	r_0=10 μm	r_0=100 nm	r_0=1 μm	r_0=10 μm
5	6×10^{-5}	0.006	0.6	7.2×10^{-5}	0.0072	0.72
10	4×10^{-4}	0.004	0.4	4.9×10^{-4}	0.049	4.9
50	0.055	5.5	550	0.072	7.2	720

[a] R_{max} values for hexagonal and cubic arrays can be calculated from these data according equations 5.1 and 5.2 respectively.

where, j'_{ss} is the steady-state current at a single microdisk electrode, given by equation 5.19

$$j_{ss} = 4nFDCr_0 \tag{5.19}$$

where, n is the number of electrons transfered, and C is a bulk concentration of electroactive species.

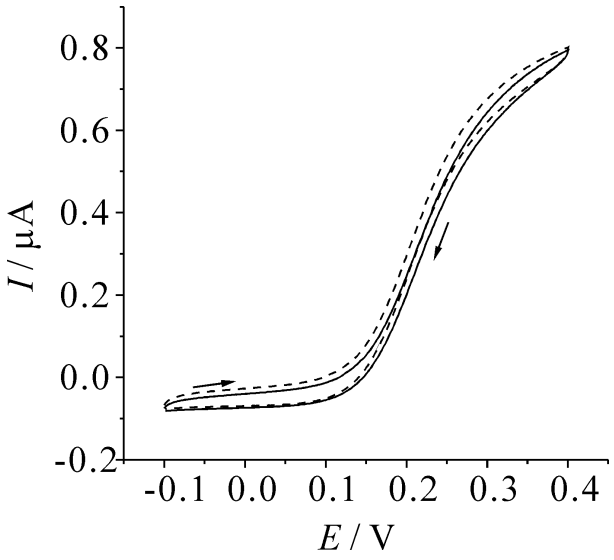

Figure 5.12: Cyclic voltammogram of 1.0 mM ferrocyanide in 0.1 M KCl obtained at an iridium microdisk electrode array. The scan rate is 100 mV s^{-1}. The dashed and solid curves represent respectively cyclic voltammograms obtained before and after chronoamperometric measurements.

In Table 5.3 the time of diffusional independence is presented for hexagonal and cubic arrays for different microelectrode separation distances d, and different microelectrode radii r_0. Table 5.3 shows that a decrease of radius causes a quadratic decrease in the time for diffusional independence; however, it also causes a quadratic decrease of the response time.[43] Arrays with cubic symmetry have a slightly higher time of diffusional independence than hexagonal arrays with similar microdisk separation distance d, but the number of microdisks in the cubic array is smaller and consequently the total current is only 86% (eqation 5.20) of that of a hexagonal array of the same area:

$$N_{pc} = \frac{\sqrt{3}}{2}N_{ph} = 0.86\times N_{ph} \tag{5.20}$$

where, N_{pc} and N_{ph} are the number of microelectrodes in the cubic and hexagonal arrays respectively.

5.4.3 Experimental Validation

Figure 5.12 shows the cyclic voltammograms recorded at 100 mV $s^{-}1$ in 1.0 mM ferrocyanide/0.1 M KCl at a hexagonal iridium microelectrode array (r_0 = 2.5 μm, d = 55 μm, N = 2597). The steady-state current to the iridium array calculated as the sum of the steady-state currents to 2597 diffusionally independent microelectrodes is 1.6 μA, so it is obvious that only some of the microelectrodes in the array contribute to the current. It is known that lithographic procedures commonly lead to a significant number of "dead" electrodes.[44]

To model the transient, the diffusion coefficient of ferrocyanide was taken as 6.5×10^{-6} cm^2 s^{-1}.[42] R_{max} and N were varied to produce the best fit, including under steady-state diffusionally independent conditions subjected to the condition of eqation 5.21. We assume that the presence of electroinactive disks does not significantly affect the symmetry.

$$\pi N R_{max}^2 = 2597 \times \frac{\sqrt{3}}{2} \times d^2 \tag{5.21}$$

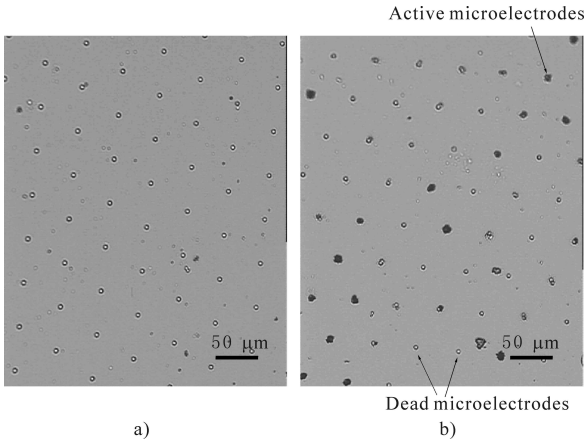

Figure 5.13: Microscopy image of detailed area of iridium microelectrode arrays: (a) before copper deposition; (b) after 20 s of copper deposition at -0.4 V vs. SCE.

The optimized values were N = 900 and R_{max} = 20. The value of N suggest that ca. 35% of the disks are electroactive and that the remainder are dead. To independently verify the value the disks were electroplated with copper, so that copper was only deposited on the active disks.[44] Figure 5.13 shows a fragment of the microdisk electrode array before and after copper deposition. Active electrodes can be visually distinguished from dead. Microscopic investigation of the whole surface showed that ca. 31% of the disks are active, validating the analysis presented above.

Returning to Figure 5.14 we see deviation between theory and experiment both at very short and very long times. The latter is likely due to the increased mass transport efficiency by natural convection for times of 10-100 s,[27] whilst the former is attributed either to kinetic limitation and/or

ohmic losses over the electrode surface.

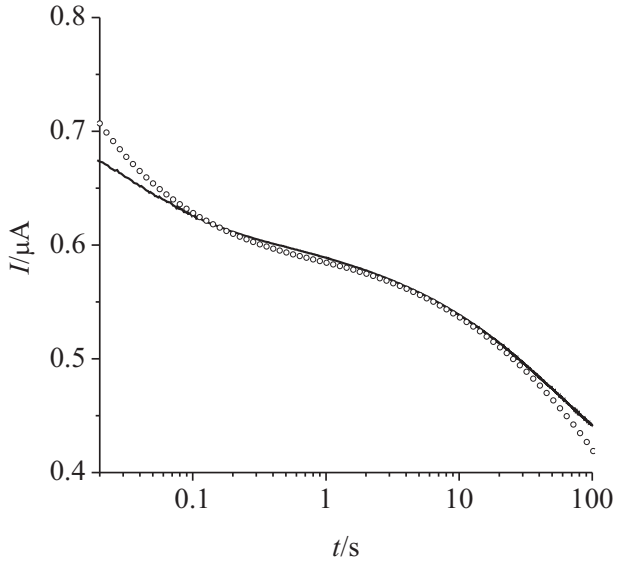

Figure 5.14: Solid line - total current from iridium microelectrode array registered experimentally in a potential step experiment, where the potential is stepped from 0.1 to +0.3 V. Circles represent the best theoretical fit.

5.5 Time of Diffusional Independence: Conclusion

Three different time regimes are observed in a potential step experiment at a microelectrode array. First a rapid ($j \propto \tau^{-1/2}$) decrease of current is seen at short times as is also observed for isolated microdisks. Second a steady-state current is observed and finally a decrease of current is seen at long times. The length of the steady-state period is strongly dependent on the diffusional domain size $R_{\max}$ and for $R_{\max} < 5$ a steady-state regime is not observed. All three regions of behavior were observed experimentally on an iridium microelectrode array. Table 5.3 reports the approximate timescales for diffusional independence. Note that even for electrodes as large as 1 μm the timescale of diffusional independence is less than 10 s unless unusually large separation distances ($>> 100\mu$m) are used. Finally we emphasize that the concept of diffusional independence can only apply to an electrode array for a finite timescale.

5.6 The Sensitive Measurement of Diffusion Coefficients

It has been recognized[21,45] that the measurement of the current-time response accompanying large potential steps at microdisk electrodes applied to electrode process given by Equation 5.3 affects the simultaneous measurements of both the diffusion coefficient of the species A and the product, n[A], being that of the number of electrons transfered and the concentration of A. Such measurements are of value both in the determination of D and of n.[43] In particular if the chronoamperometric transient results from a potential leap from a potential at which no current flows to one corresponding to transport controlled conditions then this discrimination arises because the transient at short time results from planar diffusion so that the current follows a "Cottrellian" behavior and scales with $D^{1/2}n$[A] whereas at longer times, convergent diffusion is established and the current depends on Dn[A]. This change in diffusional characteristics enables the extraction of the D and n[A] values from the analysis of a single transient.

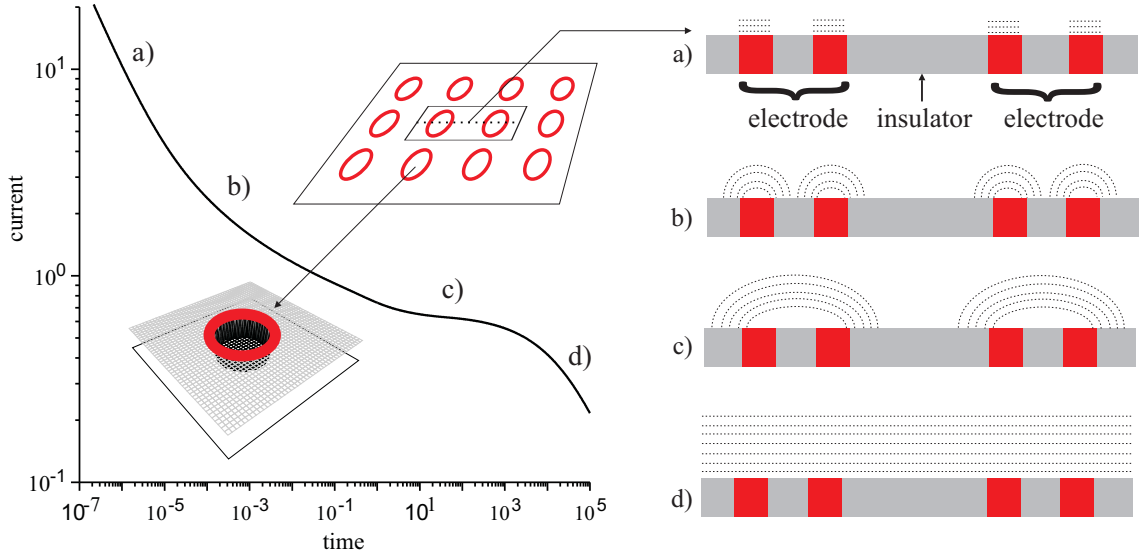

Figure 5.15: Schematic diagram of the electrode surface and current transients at an array of ring electrodes. a) planar diffusion to a ring electrode, Cottrellian behavior; b) convergent diffusion to a ring electrode, microband-like behavior; c) convergent diffusion from outer side of the ring, steady state current; d) planar diffusion to an array of microring, Cottrellian behaviour.

Methodology for the fabrication of microarrays of ring-recessed discs has been reported,[31,46] (Figure 5.15) which in generator-collector mode offers attractive benefits over classical macro-electrode arrangements (ring disc electrodes in particular). The purpose of the current section is to show that similar devices can, with possible significant improvement, be used as an alternative to the mi-

crodisc electrode for the determination of diffusion coefficients without recourse to a knowledge of the concentration of the electroactive species or the number of electrons transferred. In particular, consider an array of microring electrodes, and the application of a potential step to those electrodes so that the current jumps from a value of zero to one of transport limiting character. Again, at short times there will be planar diffusion to each ring electrode. However, in comparison with a disc electrode of the same external radius the duration of the period of "Cottrellian" diffusion will be correspondingly shorter given the ring experiences "edge"diffusion at both its internal and external radii. On the other hand, given material "inside" the internal radius of the ring must diffuse radially as well as normally to the electrode in order to undergo electrolysis. Accordingly the period of "switch over" between the planar diffusion regime whose current scales with $D^{1/2}$ to the fully convergent regime where it follows a direct dependence on D is significantly longer for the ring than the disc. Moreover, by employing arrays of rings if the current transient is recorded for long enough that the diffusional fields of adjacent microrings in the arrays will overlap,[47] the current will start to decrease when the overlap is strong, so that a regime of "Cottrellian" diffusion will again be observed. The schematic current transient is shown for an array in Figure 5.15. By modeling the entire transient over all three regimes a particularly sensitive method of finding D emerges. Furthermore, by using the practical array geometry, as already described, whereby the recessed centre of the ring can contribute to the electrolytic flux (as shown in Figure 5.15) then yet further sensitivity might be obtained from the "reservoir" of extra material in the recessed area causing a lengthening of the switch over period from regime (a) to (c) (see Figure 5.15).

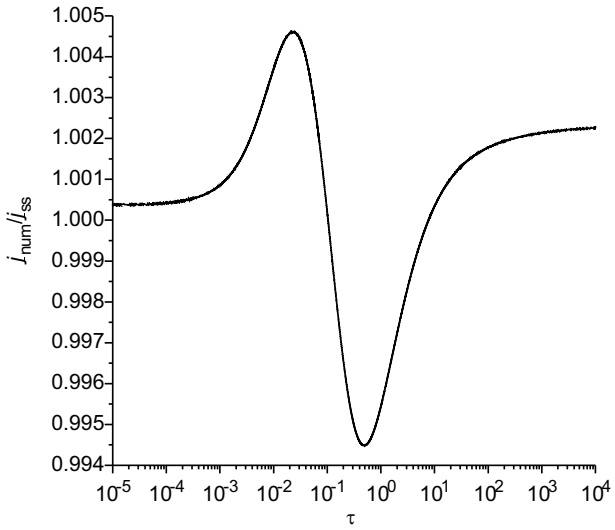

Figure 5.16: Ratio of current calculated numerically (jnum) with accuracy of 0.1 or better (see Figure a) and section Computational Procedure for details) to that given by Shoup-Szabo equation 5.11.

In this section we present the full theory for chronoamperometry at ring and ring-recessed microelectrode arrays and show its applicability to the simultaneous measurement of the D and n[A].

We also propose a generic, accurate and easy to use method of experimental chronoamperometric data analysis. Similar methods have been proposed earlier,[40,48] but never received attention probably due to lack of available tabulated functions, software and computational power. Chronoamperometry at microelectrodes and particularly microdisc electrodes was used to study diffusional processes since the first part of the twentieth century.[49,50] Later a number of equations based on experimental data,[51,52] simulations[53–55] and analytical solutions[56,57] were proposed for the extraction of diffusion coefficients from recorded current transients. Eventually the method became very popular after the work by Shoup and Szabo[19] in which their empirical equation (Equation 5.11) based on short[58,59] and long time[59] asymptotic analytical solution was proposed and utilised. According to Shoup and Szabo: "This expression is accurate to 0.6% for all times."[19] Figure 5.16 shows the ratio of dimensionless current calculated numerically according to the procedure described in the section "*Computational and Numerical Procedures*" to that given by the equation 5.11. The Schupo-Szabo expression is accurate at short times, deviates by 0.6 % at intermediate times and finally deviate by 0.2% at long times.

We show that our proposed method using an array of microring electrodes can be applied to simultaneously measure D and $n[\mathrm{A}]$ in solution. The method is applicable to the analysis of data recorded at single disc and ring electrodes as well as their arrays even in the case of diffusional non-independence of the electrodes. It is also shown that the method extracts more accurate values of $n[\mathrm{A}]$ and D than the Shoup-Szabo expression if applied to chronoamperometric transients at the microdisk electrode.

5.7 The Sensitive Measurement of Diffusion Coefficients: Results and Discussion

5.7.1 Ring Electrodes

Theory of diffusional chronoamperometry on microring electrodes has been considered by a number of earlier researchers.[32,33,39,58,60–64] Asymptotic solutions are available for short time (equation 5.13),[58] $\tau < (1-R_{\mathrm{a}})^2$ and long time[39] (equation 5.14) behavior.

At thin rings at intermediate times $(1-R_{\mathrm{a}})^2 < \tau < R_{\mathrm{a}}^2$ the current might be expected to change with time in a manner similar to that seen at band electrodes. Current transients at band electrodes

were studied by a number of researchers.[64–70] A number of analytical expressions were derived[64–68] to describe quasi-steady state current transients; all the expressions have in common that current scales inversely proportionally to the logarithm of time. Those analytical expressions for band electrodes are not in quantitative agreement with current transients calculated earlier numerically on ring electrodes[32] as well as with results presented here. This is due to the different symmetry of band and ring electrodes as well as the fact that diffusion inside of the ring electrode is convergent for only a limited period of time.

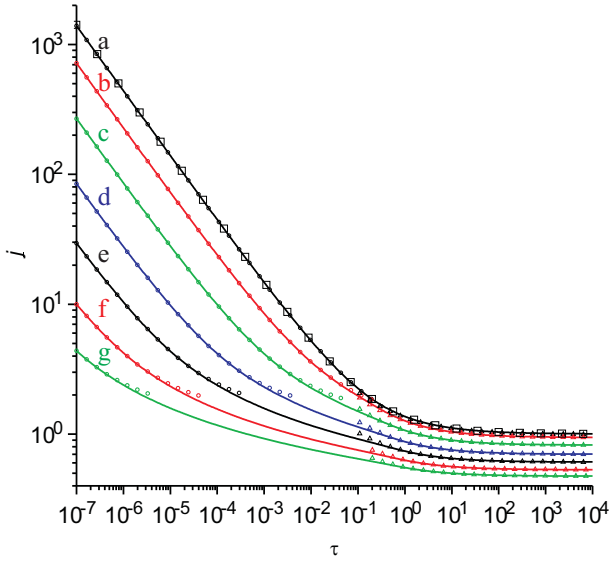

Figure 5.17: Absolute value of calculated dimensionless current at the ring electrode with R_{act}=(a) 0.1, (b) 0.7, (c) 0.9, (d) 0.97, (e) 0.99, (f) 0.997, (g) 0.999. Solid line corresponds to the numerical solution, open squares represent to the asymptotic solution at short time and open triangles to the asymptotic solution at long times, open squares represents current transient at microdisk electrode.

Figure 5.17 shows current transients calculated numerically for various ring thicknesses $R_a = 0.1$ to $R_a = 0.999$. Computational accuracy is illustrated in Figure 5.4, where the deviation of the numerical solution from that given by the analytical equations (j_{as}) 5.13 and 5.14 is presented. For all tested ranges of ring thicknesses the deviation did not exceed 0.1%. Furthermore the current transients calculated at intermidiate times are in agreement with those reported in recent computational papers.[32,33] The current transient at the ring electrode with $R_a = 0.1$ is practically indistinguishable from that for a microdisk. This is expected since the difference in area between the electrodes is just 1% and at intermediate and long times the current density at the centre of either electrode is significantly less than at the outer edge.

Figure 5.18 shows concentration profiles calculated for the ring electrode with $R_a = 0.99$. At very short times ($\tau < 10^{-7}$) the diffusion is almost planar with a minor contribution of convergent diffusion at the electrode edges (Figure 5.18a). Under these conditions the current is proportional to the concentration and to the square root of D (equation 5.13). The diffusion layer grows with time and diffusion becomes fully two dimensional at $\tau = 10^{-3}$ (Figure 5.18b). At longer times ($\tau = 10^{-1}$)

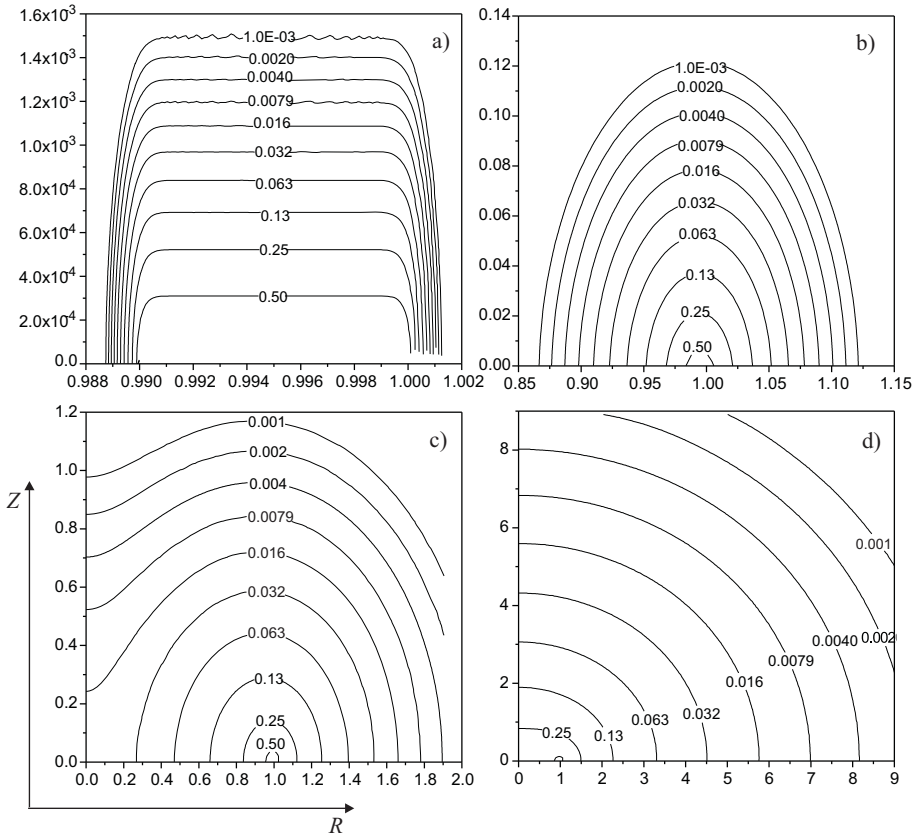

Figure 5.18: Concentration profiles calculated at a flat ring electrode with ring thickness $R_{\text{act}} = 0.99$. τ =(a) 10^{-7}, (b) 10^{-3}, (c) 10^{-1}, (d) 10^{1}.

the diffusion layer reaches the axis of symmetry (Figure 5.18 c)). Finally at very long times ($\tau = 10^{1}$) the diffusion layer looks similar to that of a microdisk electrode, except for some deviation in the proximity of the electrode surface (Figure 5.18d). Under these conditions the steady-state current is proportional to the concentration and to D. The transition from linear diffusion to convergent diffusion takes longer at ring electrodes than it does at disc electrodes.

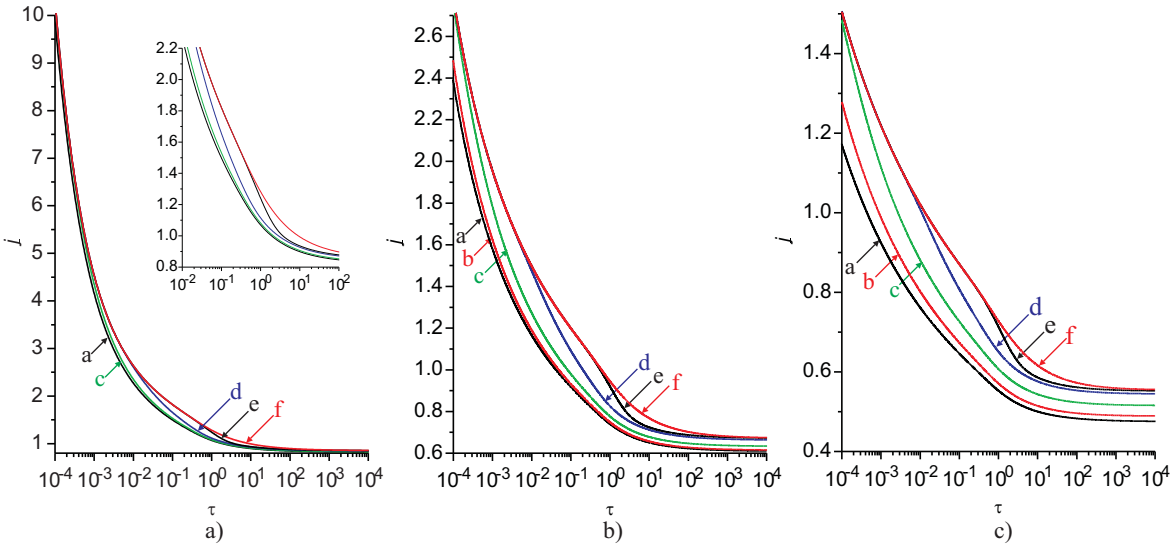

Figure 5.19: Current transients calculated on ring-recessed electrodes. R_{act}=(a)0.9, (b) 0.99, (c) 0.999. L_{cyl}=(a) 0, (b) 10^{-3}, (c) 10^{-2}, (d) 10^{-1}, (e) 1, (f) $+\infty$

5.7.2 Ring-Recessed Electrodes

Figure 5.19 shows current transients calculated for different depth of cylinder recession; recessions as small as $L_{cyl} = 10^{-3}$ are noticeable for a ring with R_{act}=0.999. However for a ring with R_{act}=0.9, a recession of $L_{cyl} = 10^{-2}$ has only a minor effect on the current transient. In general to have an influence on current transients, the recession should be of the order of magnitude of the ring thickness or higher. Figure 5.21 shows concentration profiles calculated at ring-recessed electrodes. At $\tau = 10^{-5}$ at a thick ring, the diffusion is almost planar and the cylindrical hole does not change the concentration profiles significantly (compare with figure 5.18). For thinner rings at this time, the diffusion is radial with a greater contribution from the cylindrical hole. At $\tau = 10^{-3}$ the diffusion to the ring becomes convergent with an observed impact of mass transport from the cylindrical pore. Further increases of time result in the growth of the diffusion layer, and at $\tau = 0.1$, it reaches the axis of symmetry. At these longer times, the diffusion layer above the electrode and insulator surfaces are clearly convergent, and diffusion in the pore is linear.

5.7.3 Array Density Influence

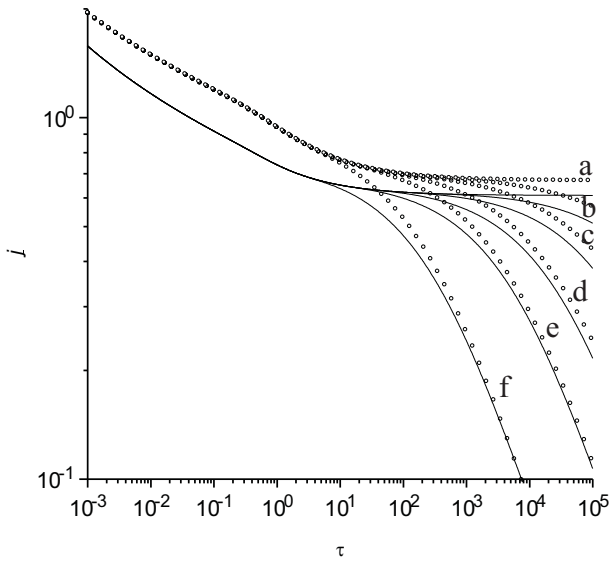

Figure 5.20: Calculated dimensionless current at arrays of ring (solid line) and ring recessed (circles) electrodes with $R_{\max}$(b) 40, (c) 25, (d) 15, (e) 10, (f) 5; a - single ring; $R_{\text{act}} = 0.99$.

Figure 5.20 shows the influence of the diffusion domain radius $R_{\max}$ on the current transients. Similar to arrays of disc electrodes[47] the time of diffusional independence is a function of distance between rings and the diffusion coefficient. Moreover transients on ring recessed electrodes are similar to those on flat electrodes. The diffusional dependence of electrodes in an array can cause a problem if traditional data interpretation is used; e.g. full current transients from microelectrode arrays cannot be fitted with the Shoup and Szabo expression at all times. However if an applied model includes the transition from convergent to linear diffusion, the decay of the current at long times can be used as a source of a useful data. Interpretation of this type of data will be presented in the next section.

5.7.4 Simultaneous Measurement of n[A] and D

Figure 5.5 shows examples of chronoamperograms generated to test the quality of parameter extraction from experimental data. Figure 5.5 a) shows current transients calculated on a disc electrode with a normally distributed error of amplitude of 1% of the local current. Figure 5.5 b) shows a chronoamperogram with a uniformly distributed error of amplitude 1% of the steady state current. Table 5.5 shows parameters extracted with Shoup-Szabo equation as well as that extracted with tabulated functions for ring and disc electrodes. There is now a significant difference between the values of the parameters D and [A] extracted with the Shoup-Szabo expression and the tabulated function for data subset I, which refers the high number of datapoints acquired in a broad time interwal and represented by the dataset of 320 points linearly distributed in logarithmic scale from $t = 0.001$ s to $t = 60$ s. However at data subset II that corresponds to a lower number of datapoints and a narrower time interval and represented by the dataset of 160 points linearly distributed in logarithmic scale from $t = 0.01$ s to $t = 20$ s the Shoup-Szabo expression gives a systematic error of 5% both to the

concentration and diffusion coefficient, while fitting with the tabulated function has no systematic error. A thin ring gives values of both $[A]_0$ and D at the same level of accuracy as a disc electrode, however application of thin ring electrodes is likely be advantageous since the non-faradaic currents at ring electrodes are much smaller than on a disc electrode due to the high difference in electrode area:

$$\frac{A_{\text{ring}}}{A_{\text{disc}}} = (1 - R_{\text{a}})^2 \tag{5.22}$$

that gives 0.0001 for a ring electrode with R_{a}=0.99 whilst the Faradaic current is of the same order of magnitude (Figure 5.17).

Table 5.4: $[A]_0$ and D estimated from noisy voltammograms registered at an array of microring electrodes.[a]

		$R_{\max} = 5$	$R_{\max} = 10$	$R_{\max} = 15$
normal	0.01%	$\frac{.9999}{.0003}, \frac{1.000}{.0004}$	$\frac{.9999}{.0009}, \frac{1.000}{.0009}$	$\frac{.9997}{.0010}, \frac{1.000}{.0010}$
	0.1%	$\frac{1.002}{0.006}, \frac{.9979}{0.0066}$	$\frac{1.002}{0.012}, \frac{.997}{.013}$	$\frac{1.001}{0.0091}, \frac{.9987}{.099}$
	10%	$\frac{.992}{0.037}, \frac{1.013}{0.045}$	$\frac{1.018}{.089}, \frac{.995}{0.1}$	$\frac{1.125}{0.16}, \frac{.91}{0.15}$
constant	0.1%	$\frac{1.001}{.0000}, \frac{.9993}{.0000}$	$\frac{1.000}{.0000}, \frac{1.000}{.0001}$	$\frac{.9996}{.0000}, \frac{1.001}{.0000}$
	1%	$\frac{1.008}{.0004}, \frac{.9928}{.0002}$	$\frac{1.002}{.0004}, \frac{.9995}{.0005}$	$\frac{.9963}{.0003}, \frac{1.005}{.0003}$
	10%	$\frac{1.081}{.0024}, \frac{.9306}{.0023}$	$\frac{1.018}{.0004}, \frac{.9947}{.0045}$	$\frac{.9656}{.0028}, \frac{1.053}{.003}$

[a] Values extracted for data subset I, see section *Simultaneous Measurement of n[A] and D: Procedure* for details. Notations in table are similar to that in table 5.5.

Ring-recessed electrodes can potentially give more accurate values of D and n[A] due to presence of extra information in the current transients (Figure 5.19), but the method of evaluation of parameters quality extraction used here is unable to discretise it (Table 5.5).

Table 5.4 shows values of [A] and D estimated from noisy voltammograms generated at arrays of ring electrodes. Arrays of disc electrodes provide similar quality of data extractions. At arrays with a moderate density ($R_{\max}$=15) of electrodes which are almost diffusionally independent on the time scale of the experiment the quality of parameter extraction is similar to that at single disk and ring electrodes (compare Table 5.5 and Table 5.4). However an increase in the density of the electrodes in the array causes an improvement in the accuracy of parameter extraction from current transients with normally distributed error. This is because a current transients at dense arrays of electrodes

are a function of time at all times, so that gives additional information on the value of the diffusion coefficient and the concentration (see Figures 5.15 and 5.20).

The proposed method of fitting experimental data with a tabulated function can be generalized for the case of solutions containing more than one electrochemically active species. This generalisation is important for the method applicability to real sensors where often several analytical species have to be detected simultaneously either due to difficulty of species separation, or to interest in the concentration of multiple species. Assuming that Faradaic currents from different species are independent and additive, the current registered at electrode is given by the equation 5.23:

$$I = 4Fr_0 \sum_{i=1}^{N} (C_{\mathrm{i}} n_{\mathrm{i}} D_{\mathrm{i}} f(\frac{tD_{\mathrm{i}}}{r_0^2})) \tag{5.23}$$

where, N is a number of electroactive species in solution and $f()$ is a tabulated dimensionless function.

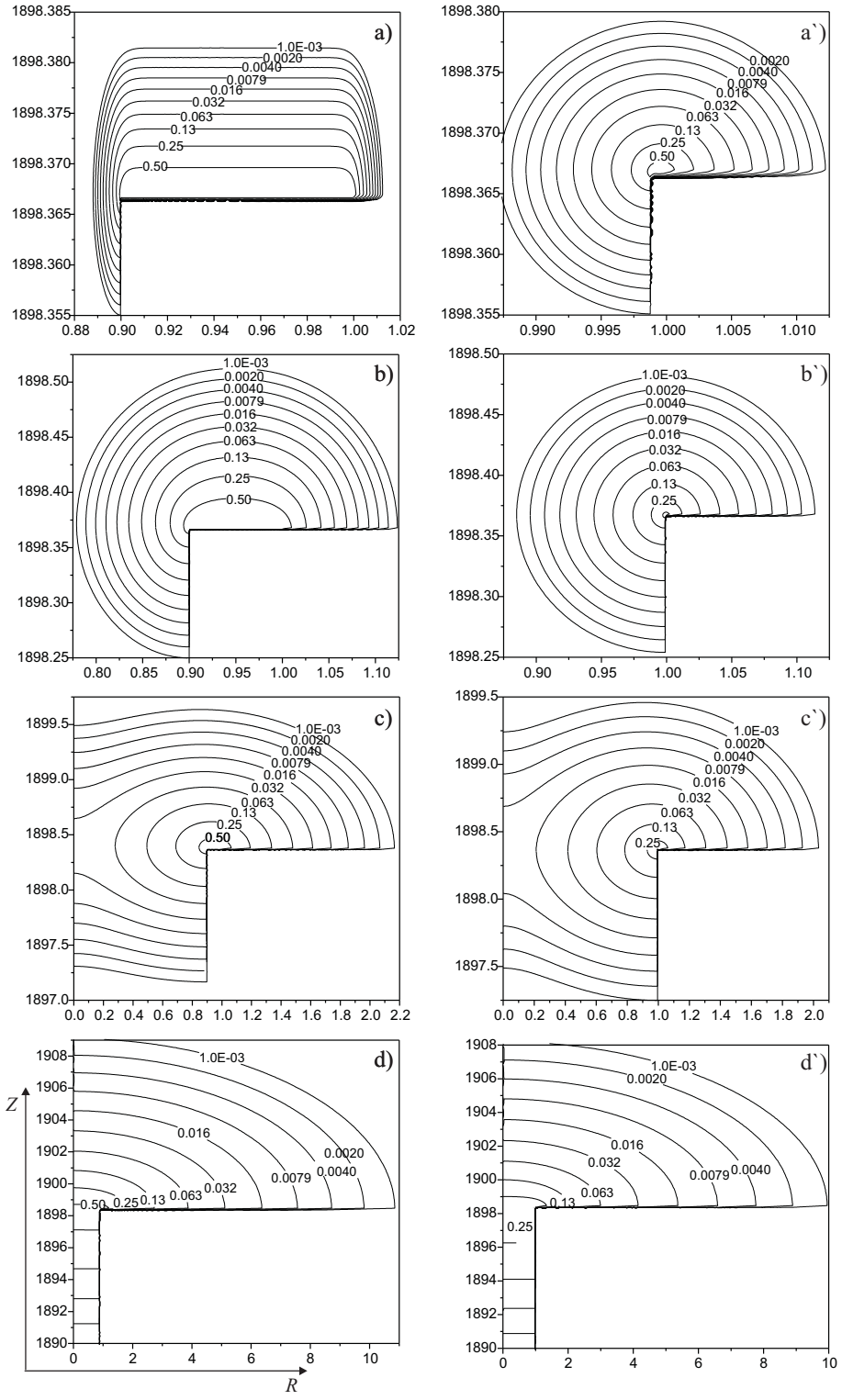

Figure 5.21: Concentration profiles calculated at $\tau =$ (a) 10^{-5}, (b) 10^{-3}, (c) 10^{-1}, (d) 10^{1}; symbol without prime refers to a ring with $R_{\text{act}} = 0.9$, that with prime refers to a ring with $R_{\text{act}} = 0.999$

Table 5.5: $[A]_0$ and D estimated from noisy voltammograms.

		Data subset I[a]				Data subset II[a]			
		$\text{disc}^b_{\text{SS}}$	$\text{disc}^c_{\text{tbl}}$	ring^d	ring^e_{R}	$\text{disc}^b_{\text{SS}}$	$\text{disc}^c_{\text{tbl}}$	ring^d	ring^e_{R}
normal	0.01%	$\frac{1.001}{.0004}, \frac{.9989}{.0004}$	$\frac{1.000}{.0003}, \frac{.9996}{.0004}$	$\frac{.9997}{.0013}, \frac{1.000}{.0014}$	$\frac{.9999}{.0008}, \frac{1.000}{.001}$	$\frac{1.052}{0.000}, \frac{0.954}{0.002}$	$\frac{.9997}{.0016}, \frac{1.000}{0.002}$	$\frac{.9999}{.0027}, \frac{1.000}{.003}$	$\frac{.9997}{.0014}, \frac{1.000}{.002}$
	0.1%	$\frac{1.005}{0.005}, \frac{.9942}{0.003}$	$\frac{1.004}{0.005}, \frac{.9950}{.0050}$	$\frac{1.004}{0.010}, \frac{.997}{.011}$	$\frac{1.002}{.007}, \frac{.998}{.007}$	$\frac{1.054}{0.0015}, \frac{0.952}{0.013}$	$\frac{0.998}{0.013}, \frac{1.003}{0.014}$	$\frac{.9997}{.024}, \frac{1.001}{.025}$	$\frac{.994}{.014}, \frac{1.01}{.01}$
	10%	$\frac{.9623}{0.046}, \frac{1.049}{0.055}$	$\frac{.962}{.045}, \frac{1.049}{0.054}$	$\frac{1.11}{0.12}, \frac{.915}{0.11}$	$\frac{1.02}{0.1}, \frac{1.4}{0.2}$	$\frac{1.052}{0.13}, \frac{0.966}{0.11}$	$\frac{1.01}{0.12}, \frac{1.001}{0.12}$	$\frac{1.03}{0.20}, \frac{1.03}{0.16}$	$\frac{.92}{0.05}, \frac{1.11}{0.06}$
uniform	0.1%	$\frac{.9999}{.0011}, \frac{1.001}{.0013}$	$\frac{.9991}{.0000}, \frac{1.361}{.0000}$	$\frac{.9996}{.0000}, \frac{1.001}{.0000}$	$\frac{.9984}{.0001}, \frac{1.003}{.001}$	$\frac{.9535}{.0004}, \frac{1.053}{.0005}$	$\frac{.9991}{.0000}, \frac{1.002}{0.000}$	$\frac{.9998}{.0000}, \frac{1.000}{0.000}$	$\frac{.9992}{.0001}, \frac{1.002}{.001}$
	1%	$\frac{.9921}{.0011}, \frac{1.018}{.0014}$	$\frac{.9916}{.0000}, \frac{1.018}{.0000}$	$\frac{.9996}{.0000}, \frac{1.000}{.0000}$	$\frac{.984}{.1}, \frac{1.026}{.001}$	$\frac{0.9535}{0.0004}, \frac{1.053}{.0005}$	$\frac{.9911}{.0000}, \frac{1.019}{.0000}$	$\frac{.9981}{.0000}, \frac{1.003}{.0000}$	$\frac{.9918}{.0006}, \frac{1.018}{.001}$
	10%	$\frac{.920}{.001}, \frac{1.20}{.002}$	$\frac{.9226}{.0002}, \frac{1.191}{.0002}$	$\frac{.9669}{.001}, \frac{1.05}{.001}$	$\frac{.925}{.004}, \frac{1.189}{.006}$	$\frac{.9535}{.0004}, \frac{1.053}{.0005}$	$\frac{.9178}{.0002}, \frac{1.198}{0.000}$	$\frac{.9815}{.0003}, \frac{1.034}{.003}$	$\frac{.85}{.01}, \frac{1.30}{.02}$

Values of $[A]_0$ and D extracted from noisy voltammograms presented as fractions, where the first fraction in a row corresponds to $[A]_0$, mol m^{-3} and the second to $D \times 10^9$, m^2 s^{-1}. Numbers in the denominator and numerator are the value itself and the standard deviation. [a] Data subsets I and II correspond to broad and narrow time intervals where the current is, see section *Simultaneous Measurement of n*[A] *and D: Procedure* for details. [b] Values extracted with Shoup-Szabo expression. [c] Values extracted with tabulated function. [d] Values extracted numerically at ring electrode with $R_a = 0.99$.

Table 5.6: $[A]_0$ and D estimated from noisy voltammograms in case of two species presented in solution.[a]

		species 1	species 2
normal	sample 1[a]	$\frac{.966}{.038}, \frac{1.01}{.05}$	$\frac{3.0}{.1}, \frac{0.21}{.02}$
	sample 2[b]	$\frac{.998}{.004}, \frac{0.98}{.03}$	$\frac{.47}{.03}, \frac{0.28}{.08}$
constant	sample 1[a]	$\frac{.83}{.2}, \frac{1.03}{0.1}$	$\frac{3.0}{.2}, \frac{0.26}{.02}$
	sample 2[b]	$\frac{.96}{.25}, \frac{1.0}{.1}$	$\frac{.46}{.25}, \frac{0.35}{.15}$

[a]Notations are similar to that in table 5.5. Sample 1 contains two electroactive species: the first with concentration 1 mol m^{-3} and diffusion coefficient of 1×10^{-9} m^2 s^{-1} and the second 3 mol m^{-3} and 0.2×10^{-9} m^2 s^{-1}. Sample 2 contains two electroactive species: the first with concentration 1 mol m^{-3} and diffusion coefficient of 1×10^{-9} m^2 s^{-1} and the second 0.5 mol m^{-3} and 0.2×10^{-9} m^2 s^{-1} [b].

Table 5.6 shows parameters values extracted from noisy voltammograms containing two electrochemically active species. The error in the values of the extracted parameters is significantly higher than in the case if only one species is present, but sufficient for preliminary quantitative or qualitative analysis.

5.8 The Sensitive Measurement of Diffusion Coefficients: Conclusions

Three different regimes are observed in a potential step experiment on isolated ring electrodes. Similar to microdisk electrodes at short times, planar diffusion is observed whilst at very long times convergent diffusion results in a steady current. Significant differences between ring and disc electrodes are observed at intermediate times - at ring electrodes the transition of planar diffusion to convergent occurs over significantly longer timescales; the thinner the ring the longer the transition. At arrays of the ring electrodes at times longer than that of diffusional independence of rings in an array, a fourth type of diffusion observed - planar diffusion to the array. Recession of the central area inside the ring has an influence on the current transients only only if its height is of the order of magnitude or higher than the thickness. Thin rings become very sensitive to the presence of an internal "pore". A generic method of fitting the experimental current transients is proposed. The method allow the accurate extraction of values of n[A] and D from chronoamperograms recorded at ring and disc electrodes as well as their arrays. The method is more accurate than the use of the Shoup-Szabo expression for a

microdisk electrode and can be applied to the analysis of solution with more than one electroactive species.

Acknowledgments

I would like to thank the Dr. Xing-Jiu Huang who performed experiments and Dr. F. Javier del Campo who provided microarray electrodes.

References

[1] Stett, A.; Egert, U.; Guenther, E.; Hofmann, F.; Meyer, T.; Nisch, W.; Haemmerle, H. *Anal Bioanal Chem* **2003,** *377,* 486-495.

[2] Simm, A. O.; Banks, C. E.; Ward-Jones, S.; Davies, T. J.; Lawrence, N. S.; Jones, T. G. J.; Jiang, L.; Compton, R. G. *Analyst* **2005,** *130,* 1303-1311.

[3] Sandison, M. E.; Anicet, N.; Glidle, A.; Cooper, J. M. *Anal Chem* **2002,** *74,* 5717-5725.

[4] Fletcher, S.; Horne, M. D. *Electrochem Commun* **1999,** *1,* 502-512.

[5] Ordeig, O.; Del Campo, J.; Muoz, F. X.; Banks, C. E.; Compton, R. G. *Electroanalysis* **2007,** *19,* 1973-1986.

[6] Berduque, A.; Lanyon, Y. H.; Beni, V.; Herzog, G.; Watson, Y. E.; Rodgers, K.; Stam, F.; Alderman, J.; Arrigan, D. W. M. *Talanta* **2007,** *71,* 1022-1030.

[7] Arrigan, D. W. M. *Analyst* **2004,** *129,* 1157-1165.

[8] Beni, V.; Arrigan, D. W. M. *Curr Anal Chem* **2008,** *4,* 229-241.

[9] Ben, A. M.; Ondaruhu, T.; Brust, M.; Joachim, C. *Langmuir* **2002,** *18,* 872-876.

[10] Masuda, H.; Watanabe, M.; Yasni, K.; Tryk, D.; Rao, T.; Fiijishima, A. *Advanc Mat* **2000,** *12,* 444-447.

[11] Nayak, B. K.; Gupta, M. C.; Kolasinski, K. W. *Nanotechnology* **2007,** *18,*.

[12] Pagels, M.; Hall, C. E.; Lawrence, N. S.; Meredith, A.; Jones, T. G. J.; Godfried, H. P.; Pickles, C. S. J.; Wilman, J.; Banks, C. E.; Compton, R. G.; Jiang, L. *Anal Chem* **2005,** *77,* 3705-3708.

[13] Huber, C. A.; Huber, T. E.; Sadoqi, M.; Lubin, J. A.; Manalis, S.; Prater, C. B. *Science* **1994,** *263,* 800-802.

[14] Seddon, B. J.; Shao, Y.; Girault, H. H. *Electrochim Acta* **1994,** *39,* 2377-2386.

[15] Davies, T. J.; Compton, R. G. *J Electroanal Chem* **2005,** *585,* 63-82.

[16] Beriet, C.; Ferrigno, R.; Girault, H. H. *J Electroanal Chem* **2000,** *486,* 56-64.

[17] Lee, H. J.; Beriet, C.; Ferrigno, R.; Girault, H. H. *J Electroanal Chem* **2001,** *502,* 138-145.

[18] Streeter, I.; Fietkau, N.; del Campo, F. J.; Mas, R.; Mu´ noz, F. X.; Compton, R. G. *J Phys Chem C* **2007,** *111,* 12058-12066.

[19] Shoup, D.; Szabo, A. *J Electroanal Chem* **1982,** *140,* 237-245.

[20] Amatore, C.; Svir, I. *J Electroanal Chem* **2003,** *557,* 75-90.

[21] Klymenko, O. V.; Evans, R. G.; Hardacre, C.; Svir, I. B.; Compton, R. G. *J Electroanal Chem* **2004,** *571,* 211-221.

[22] Brookes, B. A.; Davies, T. J.; Fisher, A. C.; Evans, R. G.; Wilkins, S. J.; Yunus, K.; Wadhawan, J. D.; Compton, R. G. *J Phys Chem B* **2003,** *107,* 1616-1627.

[23] Amatore, C.; Saveant, J. M.; Tessier, D. *J Electroanal Chem* **1983,** *147,* 39-51.

[24] Guo, J.; Lindner, E. *Anal Chem* **2009,** *81,* 130-138.

[25] Dickinson, E. J. F.; Limon-Petersen, J. G.; Rees, N. V.; Compton, R. G. *J Phys Chem C* **2009,** *113,* 11157-11171.

[26] Svir, I. B.; Klymenko, O. V.; Compton, R. G. *Radiotekhnika* **2001,** *118,* 92-101.

[27] Bard, A. J.; Faulkner, L. R. *Electrochemical Methods: Fundamentals and Applications, 2nd ed.;* John Wiley and Sons: New York: 2001.

[28] Gavaghan, D. J. *J Electroanal Chem* **1998,** *456,* 1-12.

[29] Dickinson, E. J. F.; Streeter, I.; Compton, R. G. *J Phys Chem C* **2008,** *112,* 11637-11644.

[30] Davies, T. J.; Ward-Jones, S.; Banks, C. E.; Del Campo, J.; Mas, R.; Muoz, F. X.; Compton, R. G. *J Electroanal Chem* **2005,** *585,* 51-62.

[31] Menshykau, D.; O'Mahony, A. M.; Del Campo, F. J.; Munoz, F. X.; Compton, R. G. *Anal Chem* **2009,** *81,* 9372-9382.

[32] Amatore, C.; Oleinick, A.; Svir, I. *J Electroanal Chem* **2004,** *564,* 245-260.

[33] Brookes, B. A.; Gavaghan, D. J.; Compton, R. G. *J Phys Chem B* **2002,** *106,* 4886-4896.

[34] Peaceman, D. W.; Rachford, H. H. *J Soc Ind Appl Math* **1955,** *3,* 28-41.

[35] Atkinson, K. *Elementary Numerical Analysis, 3rd ed;* John Wiley and Sons: New York, 2004.

[36] Gavaghan, D. J. *J Electroanal Chem* **1997,** *420,* 147.

[37] Menshykau, D.; Streeter, I.; Compton, R. G. *J Phys Chem C* **2008,** *112,* 14428-14438.

[38] Cottrell, F. G. *Z Phys Chem* **1902,** *42,* 385-431.

[39] Szabo, A. *J Phys Chem* **1987,** *91,* 3108–3111.

[40] Rusling, J. F. *Anal Chim Acta* **1984,** *162,* 393-398.

[41] Menshykau, D.; O'Mahony, A. M.; Cortina-Puig, M.; Javier del Campo, F.; Munoz, F. X.; Compton, R. G. *J Electroanal Chem* **2010,** *647,* 20-28.

[42] Von Stackelberg, M. O.; Pilgram, M.; Toome, V. *Z Elektrochem* **1953,** *57,* 342-350.

[43] Compton, R. G.; Banks, C. E. *Understanding Voltammetry* **2007,** .

[44] Ordeig, O.; Banks, C. . E.; Davies, T. J.; Del Campo, J.; Mas, R.; Munoz, F. X.; Compton, R. G. *Analyst* **2006,** *131,* 440–445.

[45] Paddon, C. A.; Silvester, D. S.; Bhatti, F. L.; Donohoe, T. J.; Compton, R. G. *Electroanalysis* **2007,** *19,* 11-22.

[46] Menshykau, D.; Compton, R. G. *Langmuir* **2009,** *25,* 2519–2529.

[47] Menshykau, D.; Huang, X.-J.; Rees, N. V.; Del Campo, F. J.; Munoz, F. X.; Compton, R. G. *Analyst* **2009,** *134,* 343-348.

[48] Alonso, V.; Camacho, L. *J Chem Educ* **1993,** *70,* A312.

[49] Laitinen, H. A.; Kolthoff, I. M. *J Amer Chem Soc* **1939,** 3344-3349.

[50] Laitinen, H. A.; Kolthoff, I. M. *Nature* **1939,** *144,* 549-550.

[51] Lingane, P. J. *Anal Chem* **1964,** *36,* 1723–1726.

[52] Bard, A. J. *Anal Chem* **1961,** *33,* 11–15.

[53] Flanagan, J. B.; Marcoux, L. *J Phys Chem* **1973,** *77,* 1051–1055.

[54] Kakihana, M.; Ikeuchi, H.; Sat, G. P.; Tokuda, K. *J Electroanal Chem* **1980,** *108,* 381–383.

[55] Kakihana, M.; Ikeuchi, H.; Sato, G. P.; Tokuda, K. *J Electroanal Chem* **1981,** *117,* 201–211.

[56] Soos, Z. G.; Lingane, P. J. *J Phys Chem* **1964,** *68,* 3821–3828.

[57] Heinze, J. *J Electroanal Chem* **1981,** *124,* 73–86.

[58] Oldham, K. B. *J Electroanal Chem* **1981,** *122,* 1–17.

[59] Aoki, K.; Osteryoung, J. *J Electroanal Chem* **1981,** *122,* 19–35.

[60] Cope, D. K.; Tallman, D. E. *J Electroanal Chem* **1990,** *285,* 79–84.

[61] Fleischmann, M.; Bandyopadhyay, S.; Pons, S. *J Phys Chem* **1985,** *89,* 5537–5541.

[62] Fleischmann, M.; Pons, S. *J Electroanal Chem* **1987,** *222,* 107–115.

[63] Symanski, J. S.; Bruckenstein, S. *J Electrochem Soc* **1988,** *135,* 1985–1993.

[64] Senthamarai, R.; Rajendran, L. *J Theor Comput Chem* **2008,** *7,* 205–219.

[65] Senthamarai, R.; Rajendran, L. *Russ J Electrochem* **2008,** *44,* 1156–1161.

[66] Aoki, K.; Tokuda, K.; Matsuda, H. *J Electroanal Chem* **1987,** *235,* 87–96.

[67] Aoki, K.; Tokuda, K.; Matsuda, H. *J Electroanal Chem* **1987,** *230,* 61–67.

[68] Mirkin, M. V.; Bard, A. J. *J Electroanal Chem* **1992,** *323,* 1–27.

[69] Mirkin, M. V.; Bard, A. J. *J Electroanal Chem* **1992,** *323,* 29–51.

[70] Britz, D. *Digital Simulation in Electrochemistry;* Springer-Verlag: Berlin, 3 ed.; 2005.

Chapter 6

Microarrays of Ring-Recessed Disk Electrodes in Generator-Collector Mode

6.1 Introduction

Micro ring-recessed disc electrodes are a particular class of microelectrodes that enable the performance of generator-collector experiments. These experiments use two working electrodes polarised at different potentials. While one electrode, the generator, drives the oxidation or the reduction of a species in solution, the collector electrode potential is set to drive the reverse process. This results in the formation of steep concentration gradients between both electrodes that cause the flux of material from one to the other and give rise to the observation of greatly amplified currents. These extreme rates of mass transport may be used in the study of unstable reaction intermediates[1] or the determination of diffusion coefficients from so called "time-of-flight" experiments.[2] The most common microelectrode geometries used in generator collector experiments are double band,[1] triple band[3] or interdigitated[4,5] electrode arrangements, but other geometries such as paired microdisc systems[6] and micro ring-disc devices are also possible.

Most micro ring-disc systems reported to date are coplanar. Zhao et al. presented the first report of a coplanar micro ring-disc electrode back in 1995.[7] In this work they used a chemical vapour deposition method to grow successive layers of silica and carbon over a carbon microne fiber. A collection efficiency around 95% was reported for a device where a 10 μm (diameter) disc was separated by 2 μm from a ring 4 μm wide. A slightly different construction principle was used in 2002 by Liljeroth and co-workers to develop probes for scanning electrochemical microscopy, SECM.[8] They sealed Pt wires of micrometric diameters inside thin borosilicate glass capillaries. After manually polishing the tip of the resulting microelectrode, they sputtered a thin layer of gold over its surface to form a ring electrode. After providing the microring layer with electrical connection they encapsulated the device using a resin or even nail polish. Such a manual procedure led to reproducibility

issues and lower collection efficiencies. Another route is by sputtering or evaporating a metal over an insulating layer protecting a microfiber.[9] Although these methods usually lead to uneven coverage of the cylindrical substrate, Harvey et al. were recently able to overcome such difficulties by using a sputtering cylindrical hollow target instead of the usual planar ones.[10] Theory for single, inlaid micro-ring disc electrodes was developed by Phillips and Stone in 1997[11] and later by Harvey et al. in 2007.[9] From the above we can conclude that inlaid micro ring-disc devices present one important limitation: the difficulty in their manufacture prevents the construction of regular and controlled arrays. This leads to the consequence that despite the current amplification experienced by the generator electrode, this current typically remains in the low nanoampere range. These problems have been successfully overcome by microband devices of controlled pitch size that can be easily mass-produced by photolithographic techniques, enabling the measurement of currents in the microampere range.

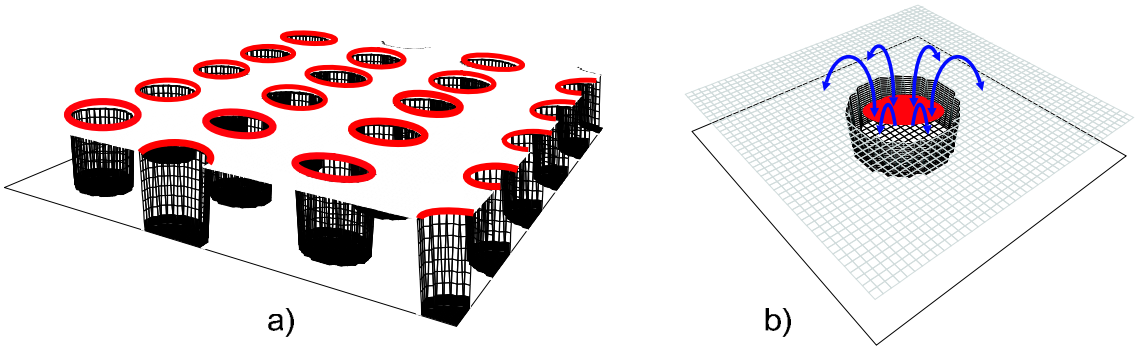

Figure 6.1: Schematic diagram of the electrode surface. a) an array of ring-recessed disk electrodes; b) plane-recessed disk eletrode.

In this work we demonstrate the fabrication of a new device based on disk-ring structures, using standard microfabrication techniques, and where the gap between disk and ring is below the resolution of the photolithographic step. To achieve this, the disks are fabricated recessed with respect to the rings, so the gap between them is controlled by the recess height. This height is nothing else than the thickness of a layer of dielectric material, in the present case a silicon oxide layer, that provides electrical insulation between the disks and the rings above them. Since the deposition of this dielectric layer is independent of the photolithographic step, it is possible in principle to grow very thin layers of oxide over the metal layer featuring the disks, so that nanometric scale gaps can be obtained between discs and rings, regardless of the resolution of our aligner. Another great advantage of this approach is that, since discs and rings are actually on different planes, it is possible to fabricate con-

trolled arrays of identical disc-ring sets. This approach is not common and has never been applied for fabrication of ring-disc arrays, but has been once used to produce interdigitated array electrodes[12,13] and single microcavity device with a ring-generator and tubular nanoband-collector electrode.[14] This is important because although the only disc-ring microelectrodes reported to date are coplanar, the fabrication of regular arrays seems an important challenge, if not impossible, due to the way in which they are produced.[7–10]

We develop the theory of diffusion-controlled currents in a novel micro and nano ring-recessed disc configuration where the disc is recessed with respect to the ring. An important advantage of this geometry is that it is amenable to fabrication by standard photolithographic techniques, thus enabling the construction of arrays where the current is enhanced further. Here we present the theoretical framework describing diffusional mass transport for micro and nano ring-recessed disc electrodes and their arrays, where the disc is recessed with respect to the ring. The work is based on the diffusion domain approach, which has previously been used to successfully describe the behavior of microelectrode arrays of different geometries (discs,[15,16] bands,[17] cylinders,[18] cones[19] and recessed discs[20–22]) and electrochemically heterogeneous surfaces.[23] This work shows the importance of design parameters such as relative radii of the disc and ring as well as depth of recession of the disc below the ring.

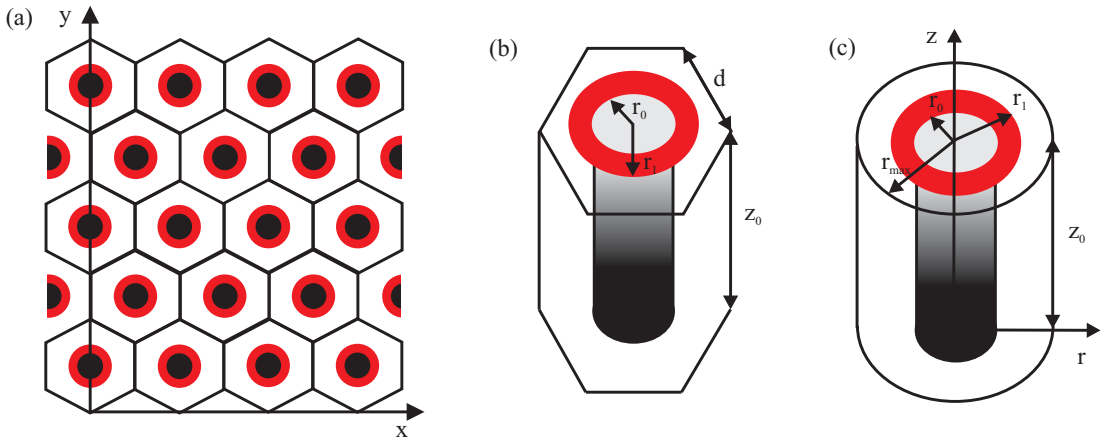

Figure 6.2: (a)Schematic diagram of the unit cell for an array of ring-recessed electrodes; (b) single unit cell in Cartesian coordinates; (c) equivalent diffusion domain in cylindrical coordinates

Further in this work we apply array of generator-collector electrodes to aid in the determination of diffusion coefficients from potential step experiments where potential on the disk is stepted from

the value corresponding to no current to one of diffusion controlled electrolysis whilst the ring is potentiostated to reverse the electrolysis and convert the disk product back to starting material. Three different behaviour zones can be clearly distinguished during generator-collector experiments on fully reversible redox couples. First, at very short times, diffusion to the generator microdisc is mainly planar, because the recessed nature of the microdisc eliminates the possibility of edge diffusion to it. When the material generated by the disc reaches the ring electrode, it is converted back to the starting material and diffuses back towards the disc. After this equilibration period, a true steady-state current is achieved both at the microdisc and the microring electrodes. The duration of this so-called equilibration period is important when the diffusion coefficients of the reduced and oxidised species are different, and the current during this time is extremely sensitive to the ratio of diffusion coefficients. Another important advantage of these devices compared to conventional disc microelectrode arrays is that the steady state currents achieved are true steady state current regardless of the experiment duration, even if the array of disc-ring systems is very densely packed, since the cycling of material between disc and ring reduces the overlap of the diffusional fields of adjacent electrodes.

We next consider devices with a recessed disc acting as a generator electrode and second electrode occupying the entire plane apart from recession (Figure 6.1b) acting as a collector electrode. Such a geometry should provide very high currents and collection efficiencies throughout time-of-flight transients as well as should further simplify the electrode fabrication procedure. We extend the theory for the generator-collector electrodes of the new geometry for the case of a chemical reaction following electrochemical, first and second order chemical reactions are considered:

$$\mathrm{A} \pm e^{-} \leftrightarrow \mathrm{B}$$

$$\mathrm{B} \rightarrow \text{product} : \mathrm{EC}_1$$

or

$$2\mathrm{B} \rightarrow \text{product} : \mathrm{EC}_2$$

We also consider the applicability of the devices for electrochemical sensing and the measurement of the rate constant and diffusion coefficients.

6.2 Mathematical Model

6.2.1 Models of The Electrode Surface

We consider an electrode with an idealized surface as shown in Figure 6.1a. The surface is composed of an "array" of ring-recessed disk electrodes in which the discs are recessed relative to the surrounding rings. We also consider an electrode with an idealized surface as shown in Figure 6.1b. The electrode is composed of a plane-recessed disk electrode in which the disk is recessed relative to the surrounding surface; the latter is covered with a metal layer and acts as an electrode. The disk electrodes act as a "generator". Material is assumed to reach the disk electrode via diffusion through the cylindrical well above it and negligibly otherwise. The diffusion of the electrochemically active species is complicated because it is intrinsically a three dimensional problem. However, the problem can be simplified by noting that each cylindrical well belongs to a diffusionally independent region known as diffusion domain.[24,25] The diffusion domain approximation treats these zones as being cylindrical with a ring-recessed disk electrode center situated at the axis of symmetry, thus reducing the problem to one of only two dimensions. The approximation is illustrated in Figure 6.2. Figure 6.2 a) and b) show the surface in Cartesian coordinates and Figure 6.2 c) identifies the unit cell in cylindrical coordinates (r,z). The cylindrical radial coordinate, r, is defined as the distance from the axis of symmetry that runs through the center of the electrode domain. The cylindrical domain is of equal area to the hexagonal unit cell. The total current from the macroelectrode "array" is given by simple multiplication of the current from a single diffusion domain times the total number of domains N_{p}. Recently it was shown that two dimensional simulations in conjunction with the diffusion domain approach gives results indistinguishable from full three dimensional simulations.[21]

6.2.2 Mathematical model

Equation 6.1 shows the electron transfer reaction at the generator electrode considered in these numerical simulations. Equation 6.2 shows the corresponding reverse electron transfer reaction at the collector electrode. Equations 6.3 and 6.4 describe chemical step following electrochemical for the EC_1 and EC_2 types of reaction. Both species A and B are assumed soluble, but only species A is assumed to be present in the bulk solution; species C is assumed not to take part in any electrochemical

Table 6.1: Dimensionless parameters used for numerical simulation.

Parameter	Expression normalized to r_0
Radial coordinate	$R = r/r_0$
Normal coordinate	$Z = z/r_0$
Time	$\tau = \frac{Dt}{r_0^2}$
Concentration of species A	$a = [\mathrm{A}]/[\mathrm{A}]_0$
Pore depth	$L_{\mathrm{cyl}} = \frac{z_0}{r_0}$
Outer radius of collector ring	$R_1 = \frac{r_1}{r_0}$
Radius of diffusion domain	$R_{\max} = \frac{r_{\max}}{r_0}$
Rate of chemical reaction, EC_1	$q_1 = \frac{k_1 r_0^2}{D_{\mathrm{A}}}$
Rate of chemical reaction, EC_2	$q_2 = \frac{k_2 r_0^2 [\mathrm{A}]_0}{D_{\mathrm{A}}}$
Flux normal to electrode	$j' = \frac{\partial [\mathrm{A}]/[\mathrm{A}]_0}{\partial z/z_0}$
Electrode current	$j = \frac{-i}{4FD[\mathrm{A}]_0 r_0}$

or chemical reactions.

$$\mathrm{Disk} : \mathrm{A} + \mathrm{e}^- \rightleftharpoons \mathrm{B} \tag{6.1}$$

$$\mathrm{Ring(Plane\ electrode)} : \mathrm{B} - \mathrm{e}^- \rightleftharpoons \mathrm{A} \tag{6.2}$$

$$\mathrm{Solution} : \mathrm{B} \xrightarrow{k_1} \mathrm{C} \tag{6.3}$$

or

$$\mathrm{Solution} : 2\mathrm{B} \xrightarrow{k_2} \mathrm{C} \tag{6.4}$$

The rate of electron transfer is described by the Butler-Volmer kinetics:

$$D_{\mathrm{A}} \frac{\partial [\mathrm{A}]}{\partial z}|_{\mathrm{el}} = (k_{\mathrm{f}}[\mathrm{A}] - k_b[\mathrm{B}])|_{\mathrm{el}} \tag{6.5}$$

where k_{f} and k_{b} are given by equations 6.6 and 6.7, consequently and $D_{\mathrm{A}} \frac{\partial [\mathrm{A}]}{\partial z}|_{\mathrm{el}}$ is the diffusional flux of species A to the electrode surface, and

$$k_{\mathrm{f}} = k_0 \exp\left(-\frac{\alpha F}{RT}(E - E_{\mathrm{f}}^0) \right) \tag{6.6}$$

$$k_{\mathrm{b}} = k_0 \exp\left(\frac{(1-\alpha) F}{RT}(E - E_{\mathrm{f}}^0) \right) \tag{6.7}$$

where E_{f}^0 is the formal potential of the A/B couple and k_0 is the standard rate constant of electron transfer.

Table 6.2: Boundary and initial conditions.

Boundary	Condition
Initial concentration	$a = 1$
Bulk solution concentration	$a = 1$
Generator electrode concentration	$a = 0$
Collector electrode concentration	$a = 1$
Axis of symmetry	$\frac{\partial a}{\partial R} = 0$
Diffusion domain border	$\frac{\partial a}{\partial R} = 0$

We next consider the potential step experiment applied to the reduction of A at the disk electrode and we assume that the step is to a sufficiently large potential to assume that the concentration of A is zero at the disk surface. We also assume that the potential at the plane electrode is held at a sufficiently positive value, that the concentration of B is zero at the plane. Mass transport in cylindrical coordinates (Figure 6.2) is described by Fick's second law of diffusion:

$$\frac{\partial[\mathrm{A}]}{\partial t} = D_{\mathrm{A}}\left(\frac{\partial^2[\mathrm{A}]}{\partial r^2} + \frac{1}{r}\frac{\partial[\mathrm{A}]}{\partial r} + \frac{\partial^2[\mathrm{A}]}{\partial z^2}\right) \tag{6.8}$$

$$\frac{\partial[\mathrm{B}]}{\partial t} = D_{\mathrm{B}}\left(\frac{\partial^2[\mathrm{B}]}{\partial r^2} + \frac{1}{r}\frac{\partial[\mathrm{B}]}{\partial r} + \frac{\partial^2[\mathrm{B}]}{\partial z^2}\right) - F_{\mathrm{chem}} \tag{6.9}$$

where, $F_{\mathrm{chem}} = k_1[\mathrm{B}]$ for the EC_1 mechanism and $F_{\mathrm{chem}} = k_2[\mathrm{B}]^2$ for the EC_2 mechanism; we note that alternative parametrisation can also be used for EC_2 mechanism: $F_{\mathrm{chem}} = 2k_2'[\mathrm{B}]^2$, where $k_2' = \frac{1}{2}k_2$.

Note that here we assume that the solution is fully supported[26] and Fick's second law of diffusion adequately describes mass transport in fully supported media when migration can be neglected and if the length scale of the device is higher than *ca* 10 nm.[27,28]

The model is normalized with use of the dimensionless parameters which are listed in table 6.1. Mass transport in cylindrical coordinates is given by the dimensionless version of equations 6.8 and 6.9:

$$\frac{\partial a}{\partial \tau} = \frac{\partial^2 a}{\partial R^2} + \frac{1}{R}\frac{\partial a}{\partial R} + \frac{\partial^2 a}{\partial Z^2} \tag{6.10}$$

$$\frac{\partial b}{\partial \tau} = D_{\mathrm{r}}\left(\frac{\partial^2 b}{\partial R^2} + \frac{1}{R}\frac{\partial b}{\partial R} + \frac{\partial^2 b}{\partial Z^2}\right) - f_{\mathrm{chem}} \tag{6.11}$$

where, $f_{\mathrm{chem}} = q_1 b$ for the EC_1 mechanism and $f_{\mathrm{chem}} = q_2 b^2$ for the EC_2 mechanism.

The boundary conditions for equations 6.10 and 6.11 are summarized in table 6.2.

6.3 Experimental and Computational Details

6.3.1 Computational procedure

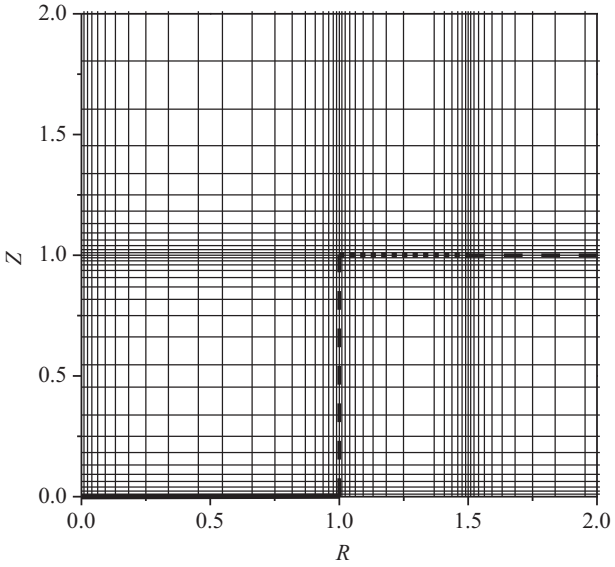

Figure 6.3: Expanding grid used in this work (some lines excluded for clarity). The generator electrode is shown in solid black, the collector electrode is in black squares and the insulator is in black dashes

Because of the symmetry of the model, the mass transport equations 6.10 and 6.11 and its accompanying conditions (table 6.2) were solved in the two dimensional space in the region $0 < R < R_{\max}$ and $Z > 0$. The bulk solution condition is implemented at a distance $6\sqrt{\tau_{\max} * max\{1, D_{\mathrm{r}}\}}$ from the highest point of the electrode, where $\tau_{\max}$ is the time scale of experiment. Beyond this the effects of diffusion are not important on the experimental voltammetric timescale.[29,30] The modeling of the plane-recessed disk electrodes is complicated by the high current densities at the electrodes edge at low values of disc recession in addition to the presence of the reaction layer[31] at high rates of the homogeneous chemical reaction. To calculate the precise values of the current at the electrodes a rectangular expanding grid, similar to that used in previous simulations of electrodes with complicated surfaces[18,19,32–35] was utilized. The expanding grid is defined by equations 6.12-6.15 and as it was used earlier to simulate currents at generator-collector devices.[32,33]

$$R_{\mathrm{i}+1} - R_{\mathrm{i}} = h_{\mathrm{i}} \tag{6.12}$$

$$Z_{\mathrm{i}+1} - Z_{\mathrm{i}} = k_{\mathrm{i}} \tag{6.13}$$

$$h_{\mathrm{i}} = \gamma_{\mathrm{R}} \times h_{\mathrm{i}-1} \tag{6.14}$$

$$k_{\mathrm{i}} = \gamma_{\mathrm{Z}} \times k_{\mathrm{i}-1} \tag{6.15}$$

The nonlinear kinetic term of the second order chemical reaction in equation 6.11 was descretized as shown in equation 6.16.

$$b^{+2} = (b^- + \Delta b)(b^- + \Delta b) = b^{-2} + 2\Delta b b^- + \Delta b \simeq b^{-2} + 2(b^+ - b^-)b^- = 2b^+ b^- - b^{-2} \quad (6.16)$$

where, b^+ and b^- refer to b at the current and previous timesteps respectively.

Furthermore if the distance separating the disk from the ring is small, very fine time steps are required to calculate accurate values of current and an expanding time grid is also used. Standard values of the mesh used in computations were $h_0 = k_0 = 4 \times 10^{-7}$ and $\gamma_R = \gamma_Z = 1.125$.

The alternating direction implicit finite difference method[36] was used in conjunction with the Thomas algorithm[37] to solve the discretized form of the mass transport equations 6.10 and 6.11 with a linearized term in case of the second order chemical reaction as given by equation 6.16. The ADI method in conjunction with the Thomas algorithm ideally suits parallel computations, and was implemented by OpenMP. The program was written in C++.

The dimensionless current at generator and collector electrodes of cylindrical symmetry was calculated with formulas 6.17 and 6.18 respectively.

$$j = \frac{\pi}{2} \int_0^1 j' R \mathrm{d}R \quad (6.17)$$

$$j = \frac{\pi}{2} \int_1^{R_{\max}} j' R \mathrm{d}R \quad (6.18)$$

$j' = \frac{\partial a}{\partial Z}$ was calculated with a three point approximation.[38]

6.3.2 Computational accuracy

To check the convergence of the simulation procedure numerous simulations were run with different space grids and time steps. An example is presented in Figure 6.4. The calculated current converges with the decrease of space and time steps. The convergence in different regions of parameters differs. To calculate accurate values of steady state current at low values of the cylinder depth L_{cyl} and for a low R_1 values fine space and time meshes were required (compare figure 6.4 a) and b)). The whole range of parameters were tested to achieve a final accuracy of at least 0.2% or better.

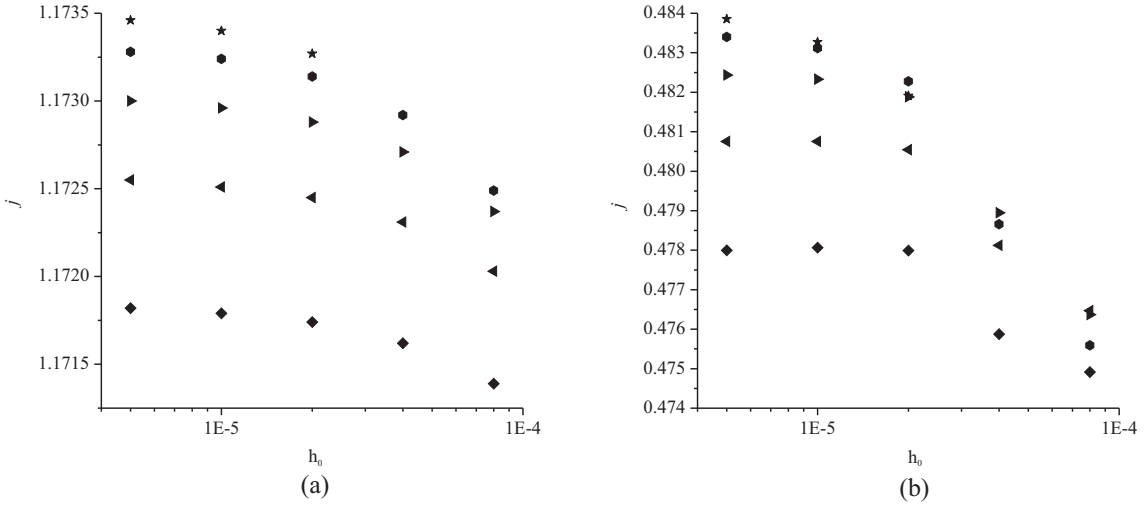

Figure 6.4: Values of the dimensionless steady state current j at the collector electrode for different space grids and time steps. (a) $L_{\mathrm{cyl}} = 1$, $R_1 = 1.05$ and (b) $L_{\mathrm{cyl}} = 0.01$, $R_1 = 1.05$. ♦, ◄, ►, •, ★ shows data calculated with time steps 0.01, 0.005, 0.0025, 0.00125 and 0.000625

6.3.3 Chemical Reagents

N-Hexyltriethylammonium bromide (Aldrich, 99%) was used as purchased for metathesis with lithium bis(trifluoromethyl)- sulfonylimide, and purified by standard literature procedures[39] to yield hexyltriethylammonium bis(trifluoromethylsulfonyl) ($[N_{6,2,2,2}][NTf_2]$). Ferrocene (Aldrich, 98%), tetra-n-butylammonium perchlorate (TBAP, Fluka, Puriss electrochemical grade, >99.99%) and acetonitrile (Fischer Scientific, dried and distilled, >99.99%) were used as received without further purification.

6.3.4 Instrumental

Electrochemical experiments were performed using a computer controlled μ-Autolab potentiostat (Eco-Chemie, Netherlands). A conventional two-electrode system was used for determination of the diffusion coefficient of ferrocene in $[N_{6,2,2,2}][NTf_2]$, typically with a platinum electrode (10 μm diameter) as the working electrode, and a 3.0 mm diameter silver wire as a quasi-reference electrode. The platinum microdisk working electrode was polished on soft lapping pads (Kemet Ltd., U.K.) using alumina powder (Buehler, IL) of size 5.0, 1.0 and 0.3 μm.

The electrode diameter was calibrated electrochemically by analyzing the potential-step voltammetry of a 2 mM solution of ferrocene (Fc) in acetonitrile containing 0.1 M TBAP, with a diffusion coefficient for ferrocene 2.3×10^{-5} cm^2 s^{-1} at 298 K.[40]

The electrodes were housed in a glass cell "T-cell" designed for investigating microsamples of

ionic liquids under a controlled atmosphere.[41,42] The working electrode was modified with a section of disposable micropipette tip to create a small cavity above the disk into which a drop (20 μL) of ionic liquid and a drop (20 μL) of 5 mM Fc in acetonitrile was placed. The RTIL solution was purged under vacuum (Edwards High Vacuum Pump, Model ES 50) for *ca*. 90 minutes, which served to remove trace atmospheric moisture naturally present in the RTIL, and evaporate the acetonitrile so that a concentration of 5 mM Fc remained in the RTIL. All experiments were performed inside a fume cupboard, in a thermostated box (previously described by Evans *et al*.)[43] which also functioned as a Faraday cage. The temperature was maintained at 298 ($\pm$ 1.0) K.

An array of ring-recessed disk electrodes was used to compare the theoretical generator/collector model outline in Section6.2.2 with experimental data. The electrode array was rinsed well with water and dried with nitrogen. The Fc/[$N_{6,2,2,2}$][NTf_2] solution used at the platinum electrode was removed from the cavity above the disk using a micropipette and dropped onto the surface of the electrode array. Experiments were performed in a faraday cage at room temperature.

6.3.5 Microdisc and Micro Array Chronoamperometric Experiments

Chronoamperometric transients at the platinum electrode (10 μm diameter) were achieved using a sample time of 0.01 s. After pre-equilibration for 20 seconds, the potential was stepped from a postion of zero current to a chosen potential after the oxidative peak of ferrocene, and the current was measured for 5 s. The software package Origin 7.0 (Microcal Software Inc.) was used to fit the experimental data. The equations proposed by Shoup and Szabo[44] (below) were imported into the non-linear curve fitting function.

$$I = -4nFDcr_{\mathrm{d}}f(\tau) \tag{6.19}$$

$$f(\tau) = 0.7854 + 0.4432\tau^{-\frac{1}{2}} + 0.2146\exp(-0.3912\tau^{-\frac{1}{2}}) \tag{6.20}$$

where n is the number of electrons transferred, F is the Faraday constant, D is the diffusion coefficient, $[A]_0$ is the initial concentration of parent species, r_0 is the radius of the disk electrode, and τ is the time. The equations used in this approximation are sufficient to give D and c within an error of 0.6 %.

The value for the radius (previously calibrated) was fixed, and a value for the diffusion coefficient and the product of the number of electrons and concentration was obtained after optimization of the experimental data.

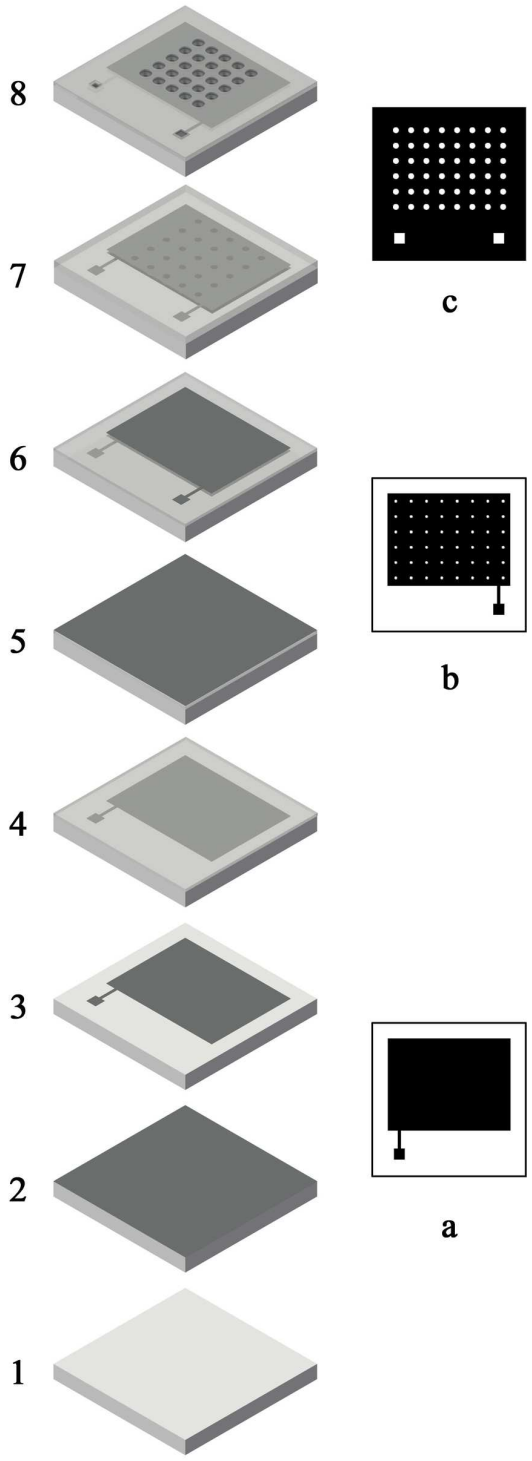

Figure 6.5: Schematic representation of main steps in the fabrication process (1-8) and mask types used (a-c).

Double potential step chronoamperometric transients at the platinum electrode (10 μm diameter) were achieved using a sample time of 0.01 s. The solution was pretreated by holding potential at a point of zero current for 20 s, after which the potential was stepped to a position after the oxidative peak for Fc, and the current was measured for 5 s. The potential was then stepped back to a point of zero current, and the current response measured for a further 5 s. In order to extract diffusion coefficients from these transients, the first potential step was fitted as before using the a nonlinear curve fitting function in the software package Origin 7.0 (Microcal Software Inc.) following eqns 6.19 and 6.20 as proposed by Shoup and Szabo. To model the second potential step, a computer simulation program (described by Klymenko et al.)[45] was employed. Values of D and $[A]_0$ obtained from Shoup and Szabo[44] analysis of experimental data were input into simulation software and values of D for the reverse step were varied until the best fit between theoretical and experimental data was achieved.

Bipotentiostat chronoamperometry was performed on the ring-recessed disk electrode array to oxidise and reduce Fc. The microdisk array was used as a generator electrode to oxidise Fc to Fc^+, and the microring array was

used as the collector electrode to reduce Fc^+ to Fc. The solution was pretreated by holding potential at a pont of zero current for 20 s, after which the potential on the microdisk array was stepped to potential after the oxidative peak for Fc. The current was measured for 0.5 s at a sample time of 0.001 s, and then for 20 s at a sample time of 0.004 s. Simultaneously the potential was stepped back to a point after the reduction of Fc^+ to Fc on the microring array. The current was measured under the same conditions as that of the microdisk array.

6.3.6 Array Fabrication Procedure

Microelectrode arrays were fabricated by using standard photolithographic techniques as follows. A 1 micron thick layer of thermal oxide was grown on 4-inch diameter silicon wafers to provide electrical insulation to the microelectrodes (Figure 6.5.1). Next the bottom metal layer was deposited by sputtering (Figure 6.5.2). This metal layer consisted of 25 nm Ti, 25 nm Ni and 125 nm Au. The Titanium was used to promote adhesion of the gold over the silicon oxide. Nickel was used as a diffusion barrier to avoid contamination of the gold by titanium due to the high temperatures achieved during sputtering. Next, a positive photoresist was deposited by spin coating over the gold. This photoresist was developed after contact-UV insolation through a clear field mask (Figure 6.5.a). Following this, the bottom metal areas and the contacts were defined in a wet-etching step (Figure 6.5.3). The excess photoresist was stripped once these patterns had been defined, and a thin silicon oxide layer (ca. 1 micron) was grown over the wafers (Figure 6.5.4). This oxide layer provided electrical insulation and provided the separation between the discs and the rings in the final device. Following the deposition of the intermediate oxide layer, a second metal layer was deposited and patterned in the same way as the previous one (Figure 6.5.5-6). The only special feature of this second metal layer was that it featured ”holes” corresponding to the underlaying microdiscs (Figure 6.5.b). This way the top gold layer will also be used as mask during the final etching steps. Following this second metallisation, a passivation layer was deposited over the wafers to provide electrical insulation to the devices. This passivation layer consisted of 200nm of silicon oxide and 400 nm of silicon nitride (Figure6.5.7).

The next steps of the fabrication were critical, as it involved opening the contacts and defining the rings and discs in the top and bottom metal levels, respectively.

A positive photoresist was spin coated over the surface of the nitride face of the wafers. A dark

field chromium mask featuring disks was used to pattern the microrings on the top metal layer (Figure 6.5.c). After the photoresist was developed, the silicon nitride and oxide over the top metal layer was etched by reactive ion etching, RIE. During this step, the top metal layer served as mask and thus the intermediate oxide layer between metal levels could also be etched (Figure 6.5.8). The trouble with this approach is that the RIE may damage the gold and therefore the time of attack must be carefully controlled in order not to "burn" the top metal level. As a result of this and also of the fact that the different passivating layers present slight inhomogeneities depending on the position of the wafer in various ovens, intermediate silicon oxide is not successfully removed from all the disc-ring systems, and hence there are a low number of active microdiscs compared to more common microelectrode arrays. After the RIE step, the excess resin was stripped in acetone and the wafers thoroughly rinsed in deionised water. The wafers were then diced into individual chips, which were subsequently attached, wire-bonded and encapsulated on suitable print circuit board strips.

6.4 Current Collection Efficiency: Results and discussions

6.4.1 Isolated Ring-Recessed Disk Electrodes

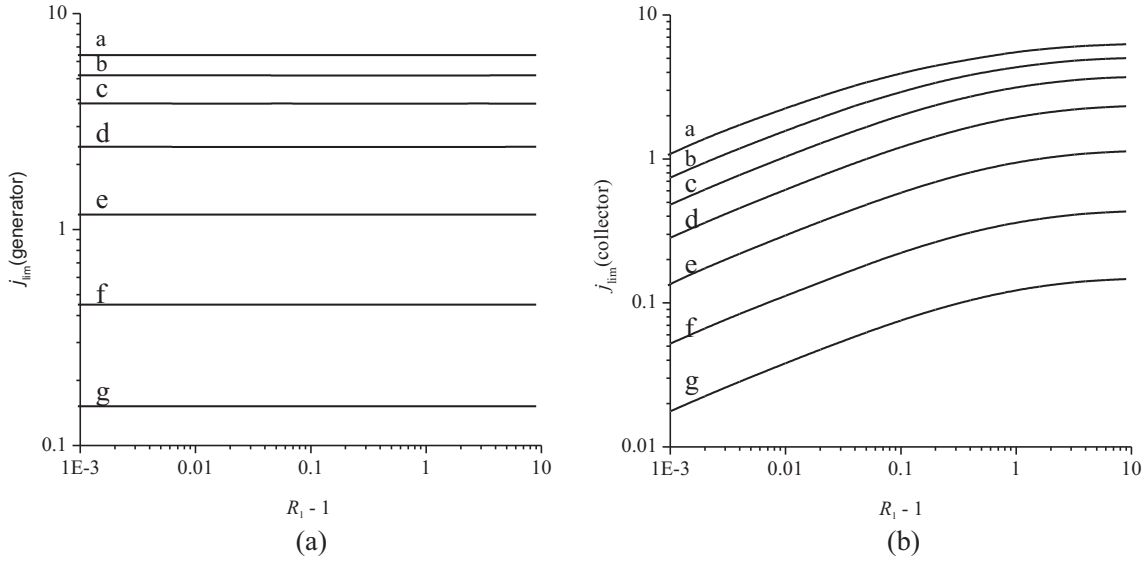

Figure 6.6: Limiting dimensionless current (a) at the generator and (b) the collector electrodes. L_{cyl} =0.01 (a), 0.0316 (b), 0.1 (c), 0.316 (d), 1 (e), 3.16 (f), 10 (g)

Figure 6.6 shows the dimensionless current at the generator (disc) and collector (ring) electrodes. The current on the generator electrode is independent of the radius of the collector electrode. However

in the absence of a collector electrode the limiting current is significantly less.[20] Figure 6.7 shows the flux density at the generator and collector electrodes calculated at different values of R_1. The current density on the generator and collector electrodes is almost independent of R_1; most of the current is collected at the edge. The current on the collector electrode depends on its radius. A decrease of radius causes a decrease of current. Figure 6.8 shows the concentration profiles calculated for different values of R_1 and L_{cyl}. It is seen that the concentration profiles are almost independent of the radius of the collector electrode R_1 planes. However, both currents on the generator and collector electrodes strongly depend on the depth L_{cyl} (figure 6.6) corresponding to the distance between the disc electrode and the ring electrode. At low values of the depth L_{cyl} the efficiency of mass transport and the currents on both the generator and collector electrodes increase significantly (figure 6.8). The

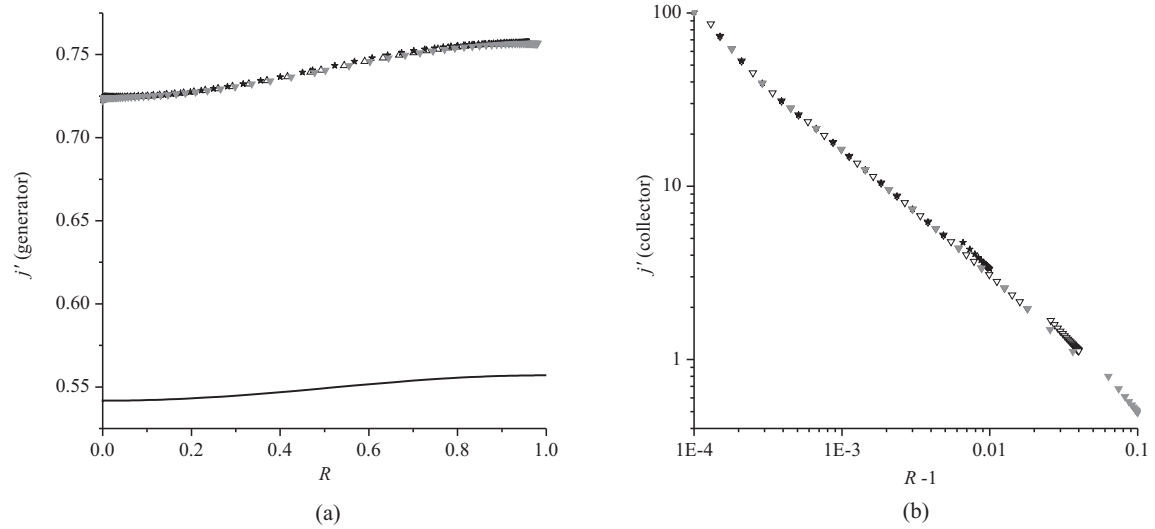

Figure 6.7: Dimensionless flux normal to electrode surface distance along the cylindrical radial coordinate R (a) at the generator and (b) the collector electrodes. Stars, black triangles and open triangles represent the flux versus radii at the collector electrode with radii R_1 =1.01, 1.04 and 1.1 respectively. The solid line represents the current at a electrode with similar geometry, but without a collector ring

figure of merit for generator-collector systems is the collection efficiency N,[1,3,46–55] which is defined as the ratio of current on the collector (ring) electrode to that on the generator (disc):

$$N = \frac{i_{col}}{i_{gen}} \tag{6.21}$$

The collection efficiency is presented in figure 6.9. At values of the depth L_{cyl} higher than 0.1 the current collection efficiency essentially does not depend on the cylinder depth. At low values of L_{cyl} the current collection efficiency increases. Over all ranges of parameters an increase of radius of the

collector electrode causes an increase in N. At $R_1 = 2$ more than 90% of current is collected. This value is considerably greater than found for classical generator/collector systems such as the ring-disc electrode,[48–50,54] the wall jet,[46,47] the rotating ring disc electrodes[50] disc or the double chanel electrode,[56] but is similar in value to some other micro generator/collector systems.[1,3,51–53,57]

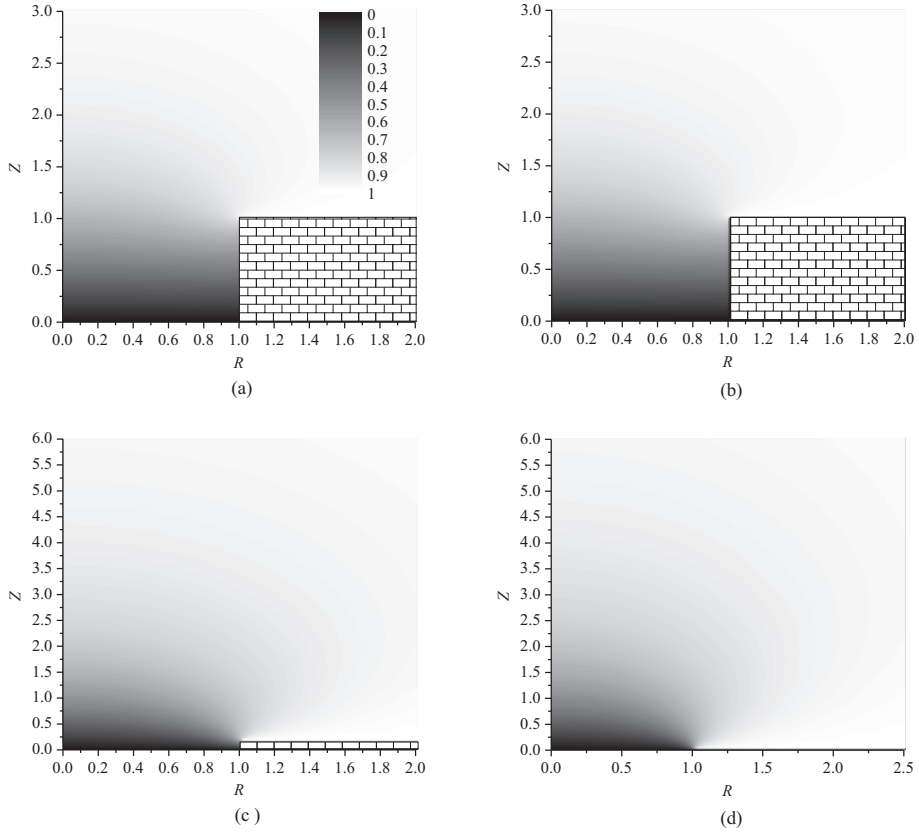

Figure 6.8: Concentration profiles calculated at steady state. (a) $L_{cyl} = 1$, $R_1 = 1.01$; (b) $L_{cyl} = 1$, $R_1 = 4.2$; (c) $L_{cyl} = 0.1$, $R_1 = 1.01$; (d) $L_{cyl} = 0.01$, $R_1 = 1.01$.

6.4.2 Arrays of ring-recessed disk electrodes

Figure 6.10 shows the current at the collector electrode and the collection efficiency at different values of R_{max}. The current at the generator electrode is almost independent of R_{max} and is not presented here. It is clear that the current at the collector is independent of R_{max} at low values of R_1 but depends slightly on R_{max} at higher values. In contrast microdisk arrays (without rings) where the behavior strongly depends on R_{max}.[30,58] This difference is observed at steady state since the electroactive species diffuses to the generator electrode not from bulk solution but rather primarily from the collector electrode (figure 6.15).

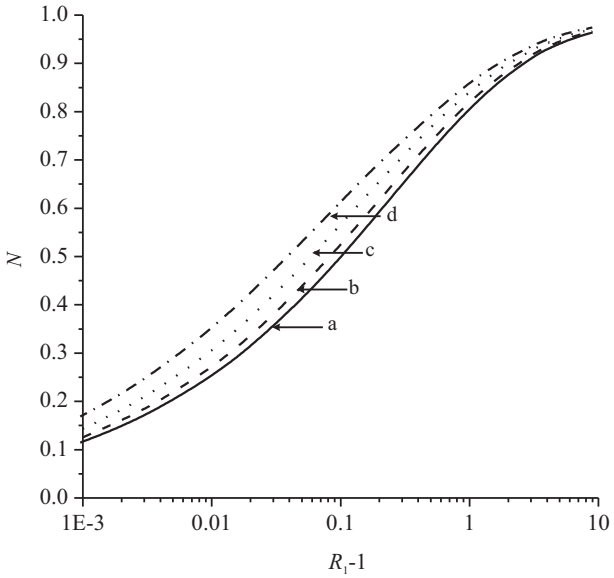

Figure 6.9: Collection efficiency as a function of R_1 for $L_{cyl} = 10$ a, $L_{cyl} = 0.1$ b, $L_{cyl} = 0.0316$ c, $L_{cyl} = 0.01$ d;

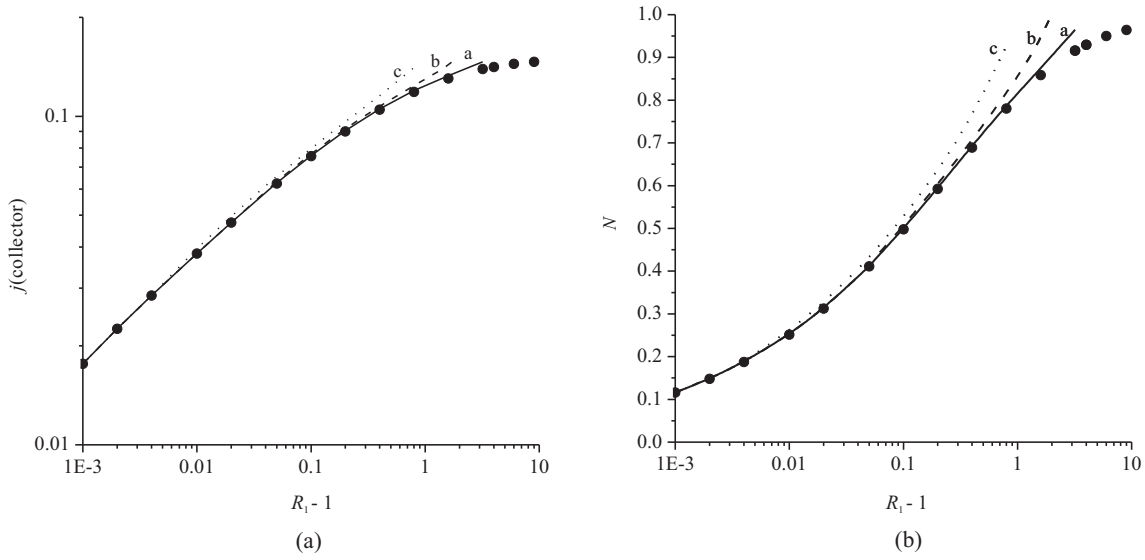

Figure 6.10: Influence of R_{max} on the current at (a) the collector electrode and (b) collection efficiency, $L_{cyl} = 10$. $R_{max} = 5$ (a); $R_{max} = 3$ (b); $R_{max} = 2$ (c)

6.5 Current Collections Efficiency: Conclusion

We have presented a rigorous study of the diffusional mass transport at micro and nano- ring-recessed disc structures where the disc is recessed with respect to the ring. The diffusion domain approach has been used to turn an inherently three dimensional problem, as is the case of an array of multiple

ring-recessed disc systems, into a more manageable two dimensional case. It has been found that the parameters with the most significant impact on the current collection efficiency of the device are the pore depth parameter L_{cyl}, which relates to the recess height, and R_1, which relates the size of the collector ring. The numerical technique is limited for values of L_{cyl} below 0.01 due to meshing and time stepping issues. Nevertheless, collection efficiencies over 90% have been shown to be possible under this configuration, which is in the same range as previously shown for interdigitated microband electrodes operated in generator-collector mode. Another finding is that when operated so that the microdisc acts as the generator and the ring as collector, the size of the diffusion domain is not critical because most of the current observed arises from the diffusional exchange between the disc and the ring. This is an important difference compared to microdisc-only arrays where microelectrode inter-central distance is a key parameter affecting device performance, as diffusional independence between adjacent microdiscs is always desireable but not always achieved. Note that diffusional independence between microdisks in an array is a time dependent property. However the results presented here for the generator-collector system are valid for steady state conditions. For the case of a microdisc array and potential step chronoamperometry experiment steady state regime is observed only for $R_{max} > 5$.[16] In the present case, this is not so, and provided that the ring electrode is sufficiently large ($2 < R_1 < 10$), then one should not expect significant shielding between neighbouring microdiscs regardless of inter-centre separation.

6.6 Current Transients: Results and Discussions

6.6.1 Isolated Ring-Recessed Disk Electrodes: Theory

Equal Diffusion Coefficients

Figure 6.11 shows current transients and concentration profiles calculated on ring-recessed disk electrodes. At short times ($\tau < 10^{-4}$) diffusion to the generator electrode (disk) is planar (Figure 6.11 b) and the current corresponds to that predicted by the Cottrell equation; no current is at that time observed on the ring (generator) electrode. At $\tau > 10^{-3}$ the electrogenerated species B reaches the collector electrode (Figure 6.11 c) and an increase of current on it is observed. However, the diffusion to the collector electrode is still planar and the current scales inversely with square root of time. With further increase of time the thickness of the diffusional layer increases (Figure 6.11 d))

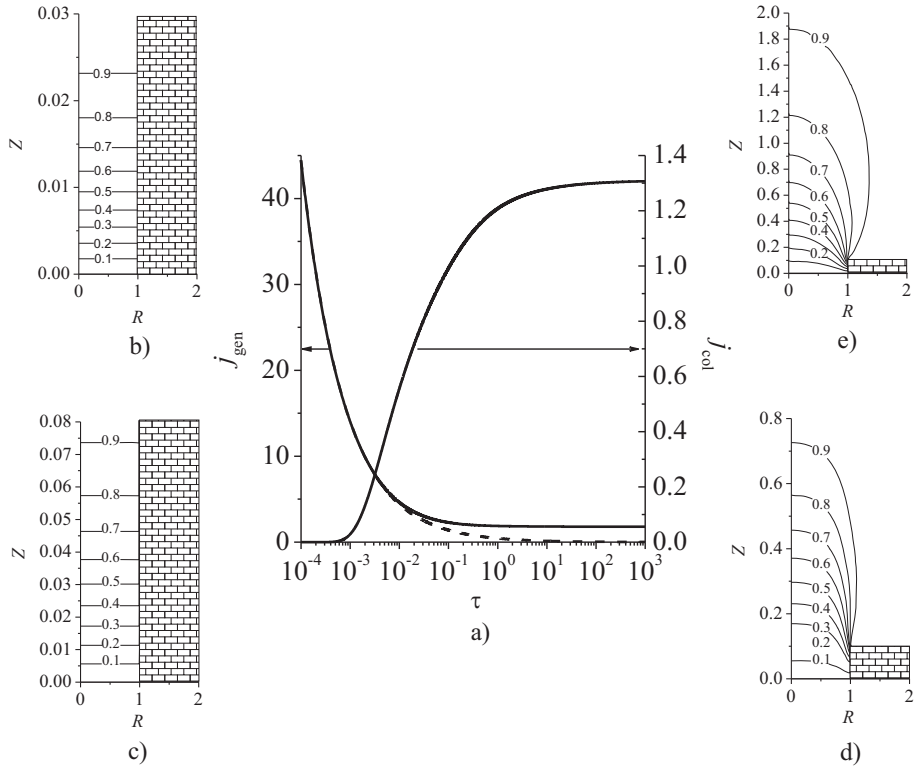

Figure 6.11: a) Calculated dimensionless current at generator and collector electrodes (solid lines) versus dimensionless time in the potential step experiment, dashed line represents current transient given by the Cottrell equation, $L_{cyl} = 0.1$. b), c), d), e) Concentration profile at $\tau = 10^{-4}$, 10^{-3}, 0.1, 100 correspondingly

and the current on the collector electrode grows. Current on the generator electrode is not described by the Cottrell equation anymore but decays slowly because of the convergent diffusion. At very long times ($\tau > 10^3$) steady state currents are observed at both generator and collector electrodes and the concentration profile does not changes over the the time (Figure 6.11 e).

Figure 6.12 shows the influence of the cylinder depth L_{cyl} on the current transients on the generator and collector electrodes. An increase of ring to disc separation causes an increase of time scale for which the generator electrode behaves as a macroelectrode. This is because the sides of the well surrounding the disc constrain the diffusion to being one dimensional, similar behavior was observed before on the disc recessed electrodes.[20,21,59,60] At the same time increase of the parameter L_{cyl} causes increased delay of the current appearing at the collector electrode. Increasing the cylinder depths/recess heights have a decreasing effect on the steady state current both on generator and collector electrodes.

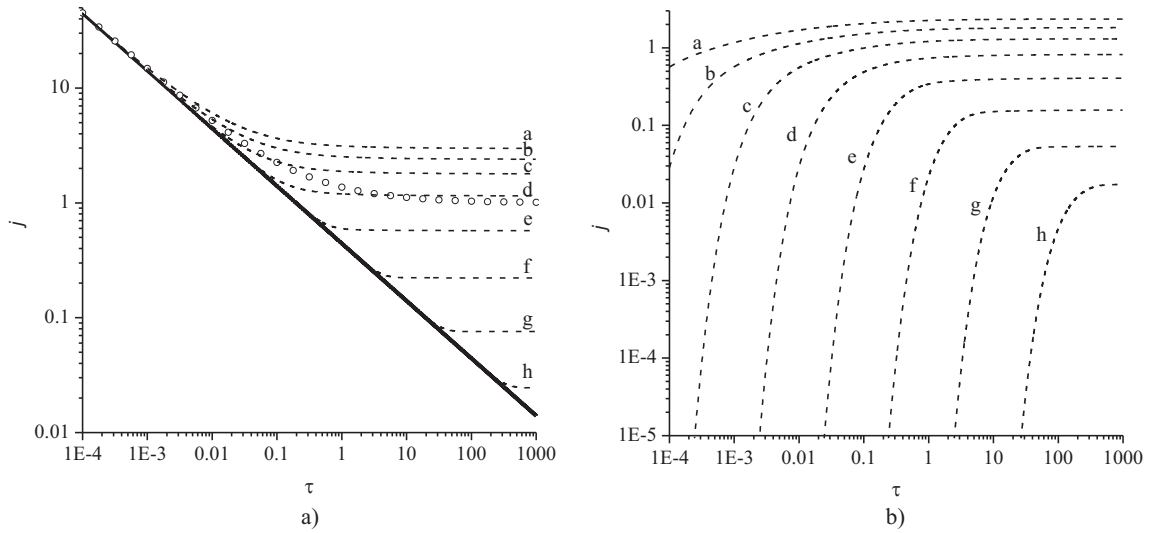

Figure 6.12: Absolute value of calculated dimensionless current at generator a) and collector b) versus dimensionless time in the potential step experiment, single electrode, $R_1 = 1.1$. Solid and dotes lines corresponds to current at macro- and microelectrodes. Dashed lines represents current at recessed generator-collector electrodes with L_{cyl} =0.01 (a), 0.032 (b), 0.1 (c), 0.32 (d), 1 (e), 3.2 (f), 10 (g), 32 (h).

Unequal Diffusion Coefficients.

Figure 6.13 shows current transients calculated for the case of unequal diffusion coefficients. Current transitions on both generator and collector electrodes is sensitive to the ratio of the diffusion coefficients D_{r}. If the diffusion coefficient of the reduced species B is less than that of the initial form A, then the current at the generator electrode will show a "delay" compared with the case of equal diffusion coefficients. The current on the generator electrode goes through a minimum and before it reaches the steady state value if the diffusion coefficient of reduced species B is less than that of the initial form. If the diffusion coefficient of the reduced form is higher than that of oxidised then it reaches collector electrode faster than in case of equal diffusion coefficients. Consequently current at the collector electrode rises faster (time of flight $\sim L_{\mathrm{cyl}}^2/D_{\mathrm{r}}$). However supply of electroactive species to generator electrode is limited by the slow diffusion of oxidised form (time of flight $\sim L_{\mathrm{cyl}}^2$). Slow generation of reduced species on the disc electrode causes a decrease of current on collector electrode, consequently the current on it goes through the maximum until the steady state is reached. The value of the steady state current on both generator and collector electrode depends on the geometry of the ring-disk electrode and on the diffusion coefficient of the initial species A, but is not affected by the value of the diffusion coefficients of reduced species B (D_{B}).

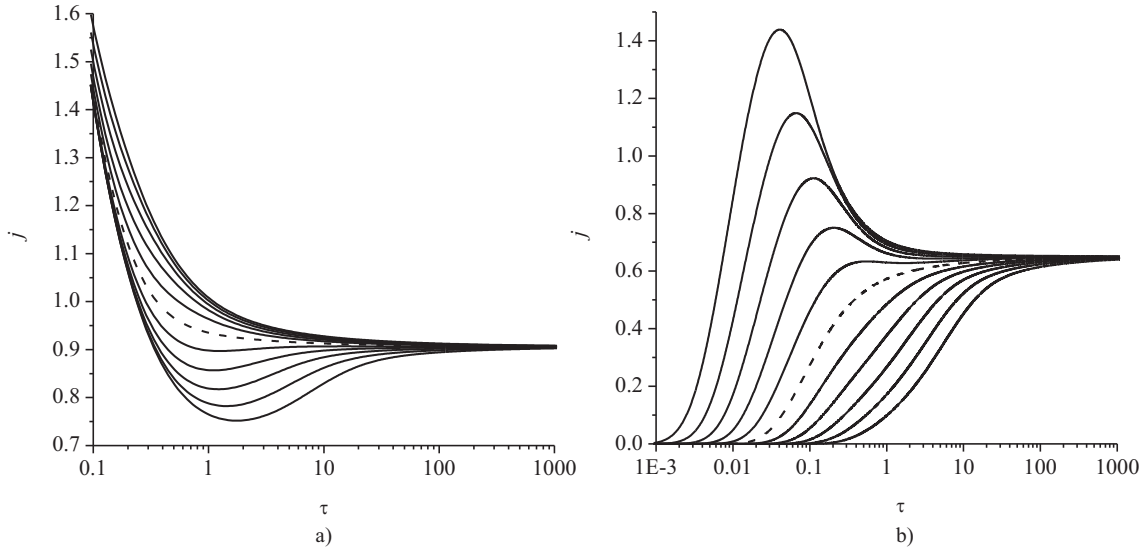

Figure 6.13: Absolute value of calculated dimensionless current at generator a) and collector b) electrodes versus dimensionless time in the potential step experiment, single electrode, $R_1 = 1.1$, $L_{cyl} = 0.5$. Dashed line represents case of equal diffusion coefficients, solid lines represents results of modeling with unequal diffusion coefficients. D_r have values of 0.1, 0.16, 0.25, 0.40, 0.63, 1.6, 2.5, 4.0, 6.3, 10 from the lowest to the highest line.

6.6.2 Effect of the Array Density

Table 6.3: Steady state current and time of diffusion independence on disks electrodes and generator-collector electrodes* within the array.

	microdisk			generator-collector		
$\frac{d}{r_0}$	r_0=100 nm	r_0=1 μm	r_0=10 μm	r_0=100 nm	r_0=1 μm	r_0=10 μm
5	6E-5; 1.5E-7**	6E-3; 1.5E-8	0.6; 1.5E-9	∞; 3E-7	∞; 3E-8	∞; 3E-9
10	6E-4; 3.9E-8	0.04; 3.9E-9	4; 3.9E-10	∞; 7.4E-8	∞; 7.4E-9	∞; 7.4E-10
50	0.055; 1.5E-9	5.5; 1.5E-10	550; 1.5E-11	∞; 3E-9	∞; 3E-10	∞; 3E-11

* Geometry of the generator collector electrode is definite by the next parameters L_{cyl}=0.1, $R_1 = R_{max}$, area of the electrode array is 1 mm^2. ** The first number is time, s of diffusional independence of electrodes within the array, the second number is the values of current, A from the microelectrode array.

Figure 6.14 shows the influence of the diffusion domain radius on the current transients. It is clear that the current on the generator electrode is almost independent of the diffusion domain radius. This is contrary to the behavior of a flat array of microelectrodes (in the absence of the collector) where the current dramatically depends on the diffusion domain radius[16] and timescale of the experiment. It was shown that the nano or microelectrode in the array with any separation of electrodes within the array can be assumed to be diffusionally independent, only for limited time, after which the

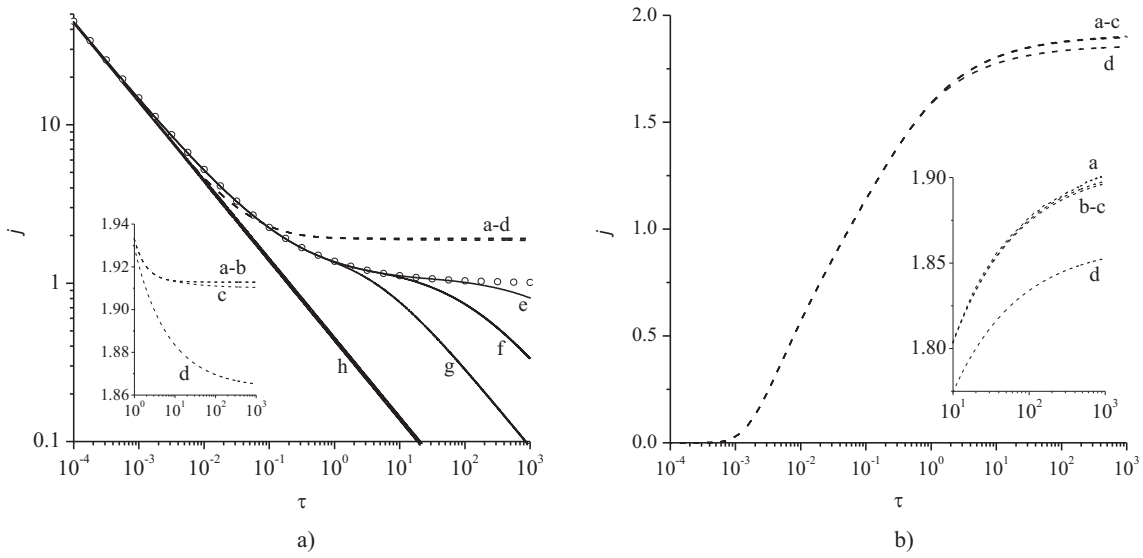

Figure 6.14: Influence of diffusional domain radius on current transients. $R_1 = 1.1$ and $L_{cyl} = 0.1$. a) circles corresponds to single microelectrode, solid line h corresponds to macroelectrode, solid lines g, f and e corresponds to microelectrodes in the array with $R_{max} = 5$, 10 and 13 correspondingly, dashed lines a and b, c, d represents current on generator at single recessed generator-collector device and the array of generator-collector device with R_{max} =10, 5 and 2 correspondingly. b) dashed lines a and b, c, d represents current on collector at single recessed generator-collector device and the array of generator-collector device with R_{max}=10, 5 and 2 correspondingly.

array as a whole behaves as a macroelectrode[16] (see solid curves on figure 6.14). This dramatic difference can be understood in terms of the concentration profiles presented in figure 6.8. This shows the concentration profile for an analite at flat microelectrode array and also for ring-recessed disk electrode. The size of the diffusional layer on the array of flat microelectrodes increases with time, however on the generator-collector system it increases significantly only at very short times, which makes the microelectrodes in the array diffusionally independent at all but the very longest timescales of the experiment. In table 6.3 duration and values of the steady state currents from an array of microdisks and an array of generator collector electrodes are presented.

It is clear that the generator-collector electrodes have greater advantages over the ordinary arrays of microdisks when the radius of the electrode is small as can be judged from table 6.3. At these values of the radius, the duration of steady state currents on array of microelectrodes is too short, however on arrays of the generator-collector electrodes due to the diffusional independence of electrodes within the array the current does not deviate from the steady state value over time. Furthermore use of generator-collector electrodes allows dense packing of electrodes in the array without loss of the duration of steady state current.

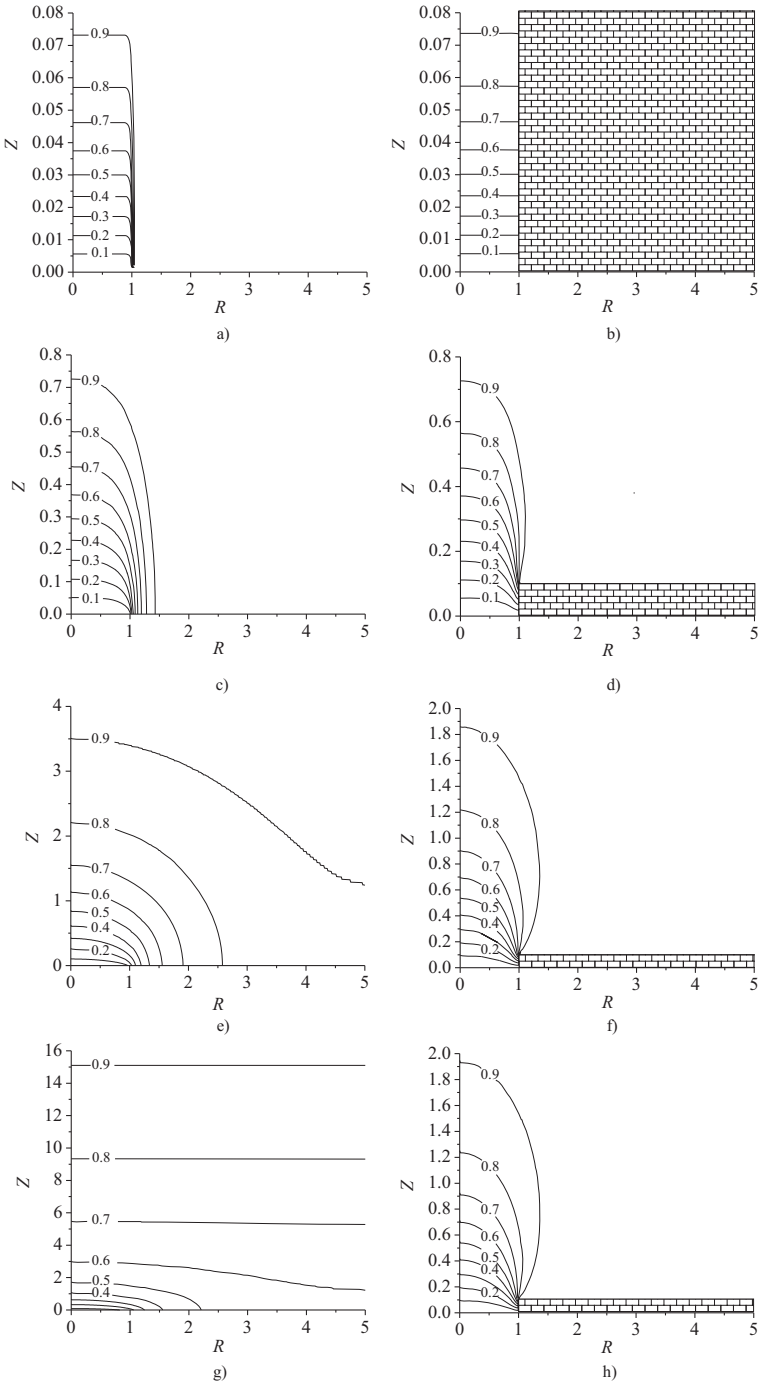

Figure 6.15: Simulated concentrations profiles, at array of microelectrodes (a), c), e), g)) and recessed generator-collector (b), d), f), h)): $\tau = 0.001$ a) and b), $\tau = 0.1$ c) and d), $\tau = 10$ e) and f), $\tau = 100$ g) and h)

6.6.3 Array Characterisation

Figure 6.16 shows images of the fabricated array obtained to confirm its geometry. The ring-recessed disc microelectrode arrays were characterised by profilometry using a P15 KLA Tencor instruments perfilometer mounting a low force head. The tip used was a 2mm diamond stylus tip with a 60 cone angle. These measurements allowed the determination of the various passivation layers. The height of the top nitride and oxide passivation layer was 710 +/- 50 nm, and the disc recess height relative to the rings was 1.50 microns Figure 6.16 a. In addition, confocal microscopy was also used to obtain a 3D optical images of the devices shown in Figure 6.16 b. For these measurements, a PLμ non-contact confocal imaging profiler system attached to a Nikon microscope using a 50x magnification lens was employed, and controlled using PLμ proprietary software (Sensofar, Spain). The same software was used to analyse the images and extract topological data. Confocal measurements were in good agreement with perfilometric measurements. Optical microscopy was also used to verify the diameter of the discs and rings making up the arrays, which were 10 microns for disk diameter and 30 microns for ring diameter (Figure 6.16 b). Figure 6.16 c shows the whole array, the number of ring-recessed disc electrodes in the array is 130.

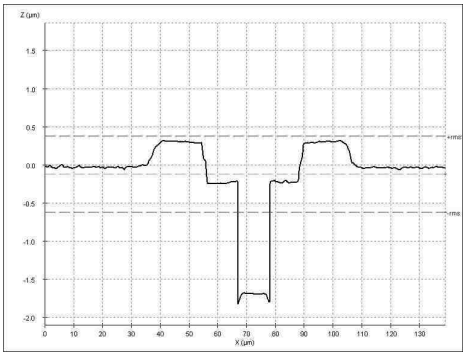

a)

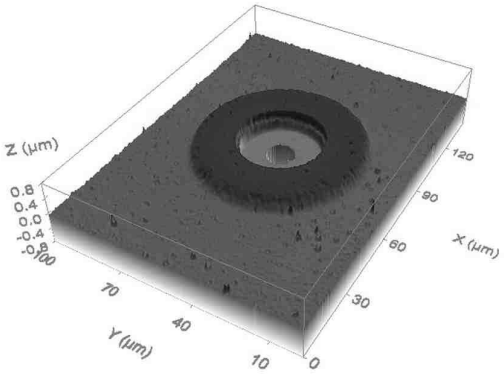

b)

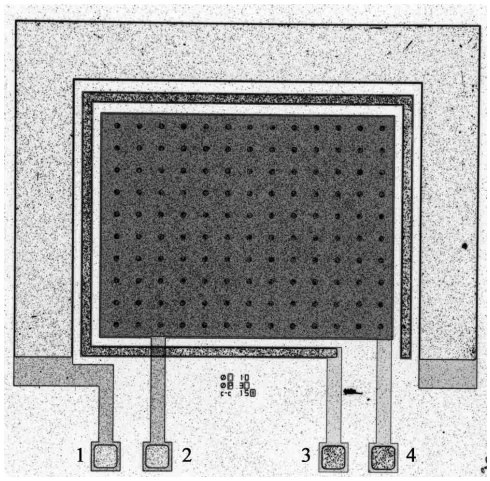

tbh c)

Figure 6.16: a) Perfolimetry profile. b) Confocal microscopy image showing, in detail, a typical ring-recessed disc electrode in an array. The disc diameter, which is also the ring inner diameter, is 10 microns. The ring outer diameter is 30 microns. The disc recess height is approximately 1.6 microns c) Optical microscope image of the chip type used in this work. The chip features 4 electrodes. From left to right, 1 is a large electrode that can be used as auxiliary electrode. 2 corresponds to the recessed microdiscs, 3 is a thin microband intended for use as quasi-reference electrode and 4 connects to the top microring electrodes.

6.6.4 Experimental Validation

Diffusion Coefficient Measurements

Figure 6.17a shows a cyclic voltammogram of the oxidation and reduction of ferrocene (Fc) and ferrocenium (Fc^+) respectively in $[N_{6,2,2,2}][NTf_2]$ at 100 mV s^{-1} at 10 μm diameter Pt electrode the solution was purged under vacuum for 90 min. Ferrocene is oxidized by one-electron to ferrocenium at a peak potential of +0.14 V vs Ag, and reduced back to ferrocene at a peak potential of +0.05 V vs Ag, corresponding to eqn 6.22.

$$[Fe(C_5H_5)_2] \rightleftharpoons [Fe(C_5H_5)_2]^+ + e^- \tag{6.22}$$

Double potential step chronoamperometry was carried out to calculate diffusion coefficients of Fc and its oxidized species, Fc^+. The potential was stepped from -0.1 V to +0.4 V to oxidise Fc to Fc^+, and then stepped back to -0.1 V to reduce Fc^+ to Fc. The transient obtained is shown as the solid line in Figure 6.17. The diffusion coefficient, D and concentration, c of neutral Fc was determined from analysis of the experimental data for the first potential step using Shoup and Szabo[44] approximations. A computer simulation program[45] was used to model the second potential step to give D_{Fc^+}. The

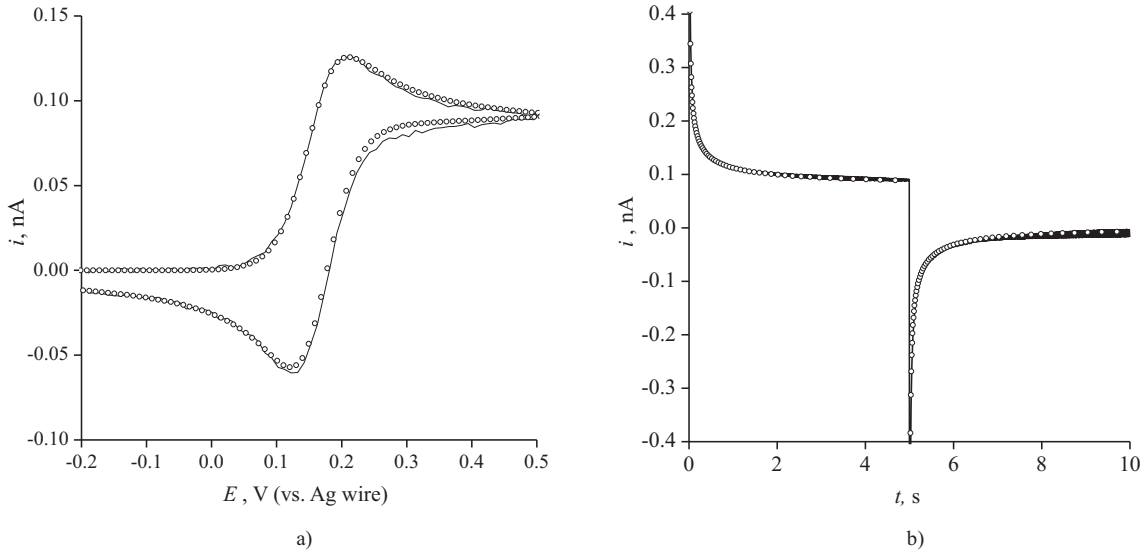

Figure 6.17: a) Cyclic voltammogram of ferrocene in $[N_{6,2,2,2}][NTf_2]$ at 10 μm Pt electrode vs Ag wire at 100 mV $s^{-}1$. b)Double-step chronoamperometry of Fc in hexyltriethylammonium bis(trifluoromethylsulfonyl)amide ($[N_{6,2,2,2}][NTf_2]$) at microdisk platinum electrode (10 μm diameter) *vs* silver wire for duration 5 s at sample time 0.01 s. Experimental data is shown as a line and theoretical fit is plotted as cycles.

value for D_{Fc} was calculated to be 10.0×10^{-12} m^2 s^{-1} which is consistent with previous observations reported for other RTILs.[43,61] The value for D_{Fc^+} was calculated to be 5.50×10^{-12} m^2 s^{-1}. The ratio $D_{Fc}/D_{Fc^+} \neq 1$, suggesting that the neutral Fc species diffuses more quickly than the charged Fc^+ species through the ionic liquid media, an effect similar to that observed for oxygen/superoxide in RTIL[62] The same Fc/RTIL solution used to determine the above diffusion coefficient and concentration values, was dropped onto the electrode array surface. The solution had previously been purged under vacuum for 90 min. and was used without further degassing.

Generator Collector Mode

The array was immersed in a solution of Fc of known concentration. Figure 6.18 shows a bipotentiostat chronoamperometric transients using the microdisk array as the generator and the microring array as the collector. The potential on the microdisk array was stepped from -0.1 V to +0.4 V to oxidise Fc to Fc^+ and potential on the microring array was kept at -0.1 V to reduce Fc^+ to Fc. The transients obtained are shown as the solid line in Figure 6.18. The diffusion coefficients of Fc and Fc^+ and the concentration of the Fc in solution have been previously determined at the platinum electrode and are known.

To model the transient at generator and collector electrode, diffusion coefficients and concentration values were used as determined in double step chronoamperometry shown in figure 6.17. The geometry of the array were used as determined from microscopy (figure 6.16) and the number of active generator-collector electrodes N were varied. The optimised value of active generator-collector microelectrodes was N=26. The fraction of the active electrodes is 20% which is less than the typical value of active electrodes in conventional microdisk electrodes arrays.[16,63] This is due to deficiencies in the final etching step of the fabrication process. Presumably, due to slight inhomogeneities in oxide layer thicknesses, the reactive ion etching has not been able to open all the microdisks and hence the low active number. To show that the theoretical model presented above adequately describes fabricated arrays of the generator-collector electrodes in the presence of dead devices we consider different types of dead devices. Devices with an inactive ring and an inactive disc do not contribute to the recorded current and they do not distort current transients from neighbouring electrodes due to diffusional independence of the generator-collector system (Figure 6.14); devices with a dead disc and an active ring do not generate any current due to absence of electroactive species at the ring elec-

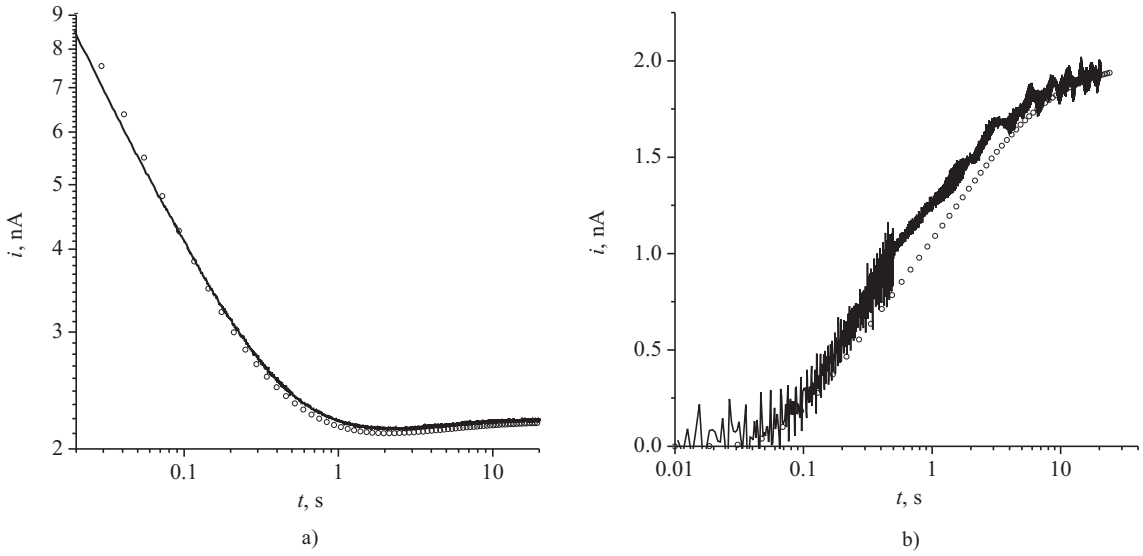

Figure 6.18: Bipotentiostat chronoamperometry of Fc in $[N_{6,2,2,2}][NTf_2]$ at ring-recessed disk electrode array for a) generator electrode and b) collector electrode, experimental data is shown as a line and theoretical fit is plotted as cycles. $D_{Fc}=10.0\times10^{-12}$, $D_{Fc^+}=5.50\times10^{-12}$, N=26.

trode; finally devices with an active disc only can distort the current, but voltammograms and current transients recorded at ring only and disc only modes suggest that the number of active rings is significantly higher than number of active discs, consequently the presence of such a devices is negligible. It is clear that the theoretical fit is in good agreement with the experimental data. Particularly, the theoretical fit represents well one-dimensional diffusion to microdisk at short times when the Fc^+ has not yet reached the collector electrode (Figure 6.15 b). It also describes well the region of times where diffusion is converged and Fc^+ reduced to Fc at the collector electrode and diffuses back to the generator (Figure 6.15 d and f). The fit predicts the feature that current transient on the generator electrode goes through the minima and finally it gives accurate values of steady state current on generator and collector electrodes. This shows that two dimensional simulations in conjunction with the diffusion domain approach gives accurate description of a full three dimensional problem of mass transport at ring-recessed disk electrodes, taking into account sensitivity of current transients, particularly the depth of minima/maxima and the time of flight to the ratio of diffusion coefficients (Figure 6.13). Consequently we conclude that the method can be applied to simultaneous determination of diffusion coefficients of red/ox couple.

6.7 Current Transients: Conclusions

Three different time regimes are observed in a potential step experiment on ring-recessed disk electrode. First a rapid decrease of current on generator similar to that on macroelectrode and no-current on the collector is observed at short times. This is followed by the region where current at the collector grows and current at the generator "equilibrates". Finally a true steady state current is observed on both generator and collector electrodes. All three regions of behavior were observed experimentally on a fabricated array of generator-collector array. The theoretical fit agrees well with the experimental data, therefore diffusional domain approach can be used to model arrays of ring-recessed disc electrodes. Currents in the steady state mode are almost independent of the distance between electrodes in the array, but sensitive to the distance between disk and ring L_{cyl}. Steady state currents is also insensitive to the ratio of diffusional coefficients, but the modeling of current transients on the generator and collector electrodes allows the determination of diffusion coefficients to both oxidised and reduced forms simultaneously. The use of arrays of ring-recessed disk electrodes in generator-collector mode has advantages over conventional arrays of disk electrodes, such as higher currents at a single microelectode in an array. The number of electrodes on the array can also be increased, as smaller interelectrode distances are possible. As well as this, the disks in the array are not restricted by size as true steady-state behavior is observed over a wide range of scales.

6.8 EC_1 and EC_2 Reactions: Results and Discussions

6.8.1 First Order Kinetics

Figure 6.19 shows current transients calculated at the generator-collector device with a disc recession of $L_{\mathrm{cyl}} = 0.1$. In the limiting case of a slow chemical reaction, the current at the generator and collector electrodes converges to that reported earlier[33] in the absence of chemical reaction at the ring-disc electrode in the generator-collector mode. In the limiting case of the very fast chemical reaction the current at the generator electrode is equal to that at the recessed disc electrode[20,60] and the current at the collector electrode is negligible (Figure 6.19 a) and b)). At short times ($\tau < L_{\mathrm{cyl}}^2$) when the diffusion layer of chemical A has not yet reached the collector electrode the current at the generator electrode scales with time according to the dimensionless Cottrell equation 6.23 and is independent of the rate of the chemical reaction. The concentration profile computed for the case of

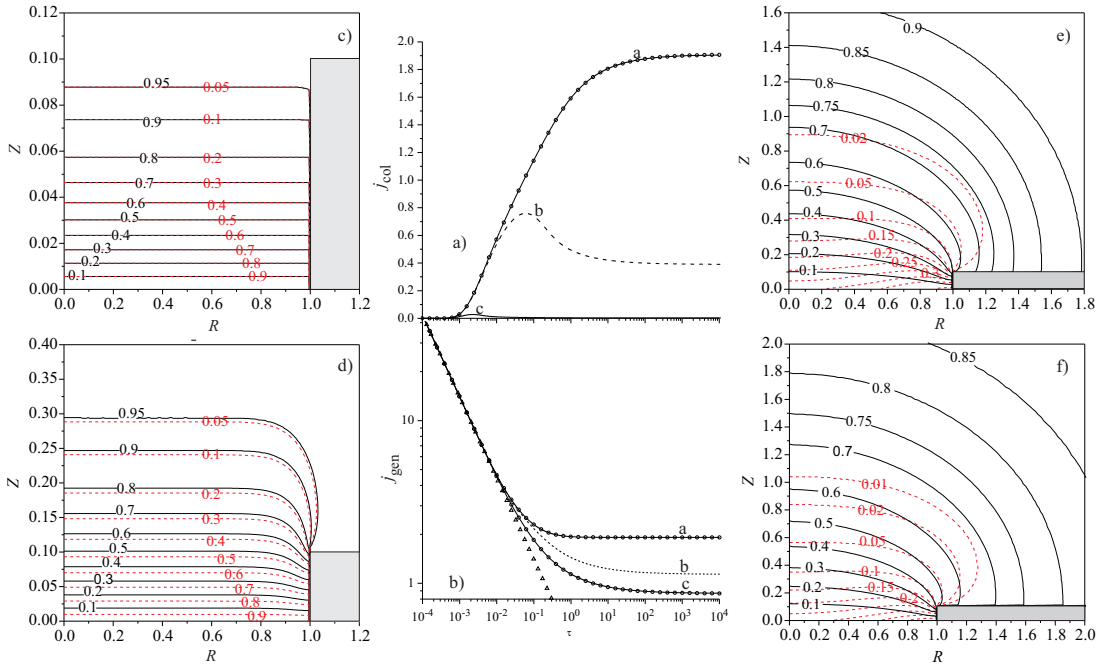

Figure 6.19: Current transients and concentration profiles at the generator-collector electrode, first order chemical kinetics, $L_{cyl} = 0.1$. a) current transient at the collector electrode, open circles represent the limiting cases of the infinitely slow and fast reactions, the solid line "a" represents calculated current transients at $q_1 = 10^{-4}$, the dashed line "b" $q_1 = 10$ and the solid line "c" $q_1 = 10^3$ b) current transient at the generator electrode; the labeling is similar to that at a), open triangles represent current given by the Cottrell equation. c), d), e) and f) show concentration profiles calculated at times $\tau = 0.001$, 0.01, 1 and 100; the rate constant of the chemical reaction $q_1 = 10$, and the solid line shows the concentration of A and the dashed line the concentration of B.

the equal diffusional coefficients, D_r=1 are shown in Figure 6.19 c). At $\tau = 0.001$ diffusion is almost planar, the impact of the chemical reaction is negligible.

$$j = \frac{\pi^{1/2}}{4\tau^{1/2}} \tag{6.23}$$

At longer times the species B reaches the collector electrode (Figure 6.19 d)) and the current at this electrode increases. The current at the generator deviates from that given by the Cottrell equation since the diffusion is no longer confined to the well but extends beyond it; the impact of the chemical reaction becomes noticeable at times $\tau \approx \ln(2)/q_1$ and the mass conservation law [A]+[B]=$[A]_0$ (D_r=1) significantly not fulfilled. Further increase of time ($\tau = 1$ and 100 Figures 6.19 e) and f)) causes an increase of the diffusion layer thickness of A and B. A's diffusion layer thickness is larger than B's, because species B cannot diffuse far away from the generator electrode since it is captured at

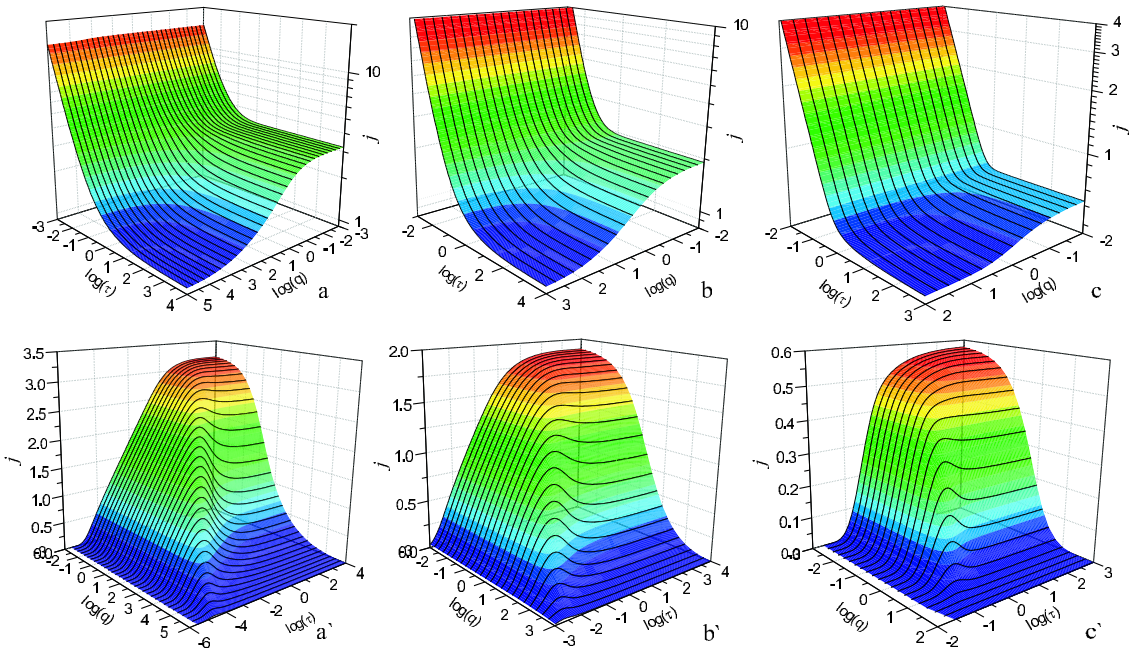

Figure 6.20: Current transients at the generator-collector electrode, for the case of first order chemical kinetics. (a, a') L_{cyl}=0.01; (b, b') L_{cyl}=0.1; (c, c') L_{cyl}=1. Graphs labeled with/without a symbol with an asterisk refer to the current transient at the collector/generator electrodes.

the collector electrode and decaying in the chemical reaction. The time necessary to reach steady state in the presence of a follow up chemical reaction is longer than in its absence of it due to the prolonged growth of the diffusion layer and it's higher thickness (compare Figure 6.19 with that presented in ref.[33]). This suggests that the current registered at the generator-collector electrode should be sensitive to the density of the electrodes in an array; this will be discussed below. Figure 6.20 shows current transients calculated at various rate constants q_1 of the chemical reaction as well as disc recession L_{cyl}. Steady state currents at the generator and collector electrodes as well as the peak current at the collector electrode decrease gradually with an increase of the rate constant of the chemical reaction. The observed maximum is caused by the interplay of the above discussed mass transport and rate of the chemical reactions. The time at which the peak current is reached decreases with an increase of the rate of the chemical reaction q_1; this is in agreement with the equation giving the half life of the transformation $\tau_{1/2} = \ln(2)/q_1$. The depth of recession of the disc is an important parameter that has an influence on maximum and minimum values of the rate constant of the chemical reaction that can be detected on the considered electrode, at L_{cyl}=0.01 the rate constant q_1 can be measured in the range of 0.01 to 10^4, at L_{cyl}=0.1 the rate constant q_1 in the range of 0.01 to 10^3 and finally at L_{cyl}=1

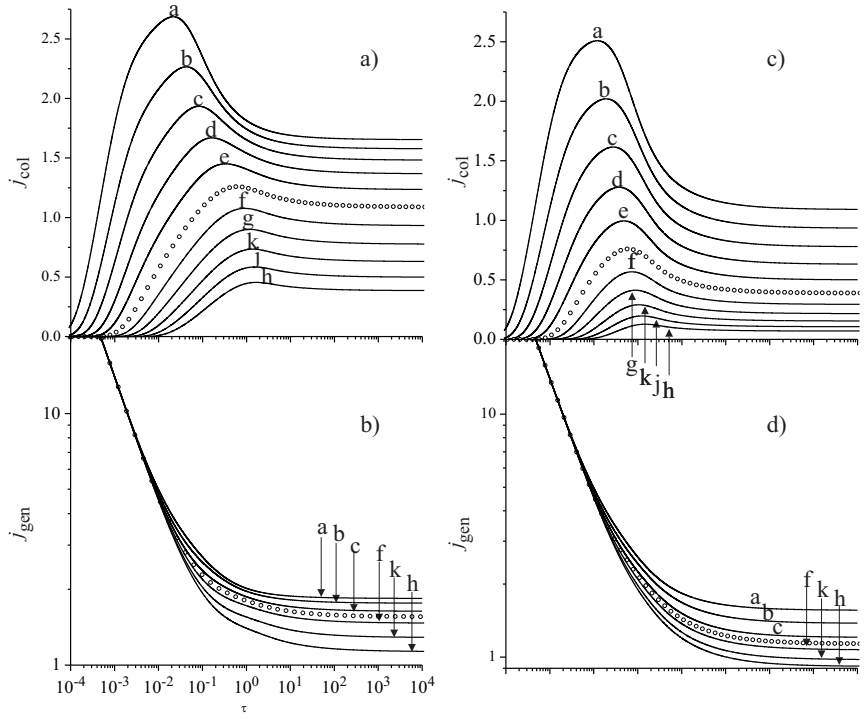

Figure 6.21: Influence of the ratio of the diffusion coefficients D_r on the current transients, for the case of first order chemical kinetics, $L_{cyl} = 0.1$. a) and b) show the current at the collector and generator electrodes, for $q_1 = 1$; c) and d) show the current at the collector and generator electrodes, for $q_1 = 10$. Lines a, b, c, d, e, f, g, h, j, k corresponds to D_r=10, 6.3, 4, 2.5, 1.6, 0.63, 0.4, 0.25, 0.16, 0.1 and open circles shows the current transient at D_r=1.

the rate constant q_1 can be measured in the range of only 0.01 to 1. Here and further the criteria for the minimum rate constant that can be extracted is that steady-state current at generator and/or collector electrodes is deviate by 1% or higher from that in the absence of the reaction, criteria for the maximum rate constant is that steady-state current at the collector electrode is 0.1% or higher of that at the generator electrode.

Figure 6.21 shows the influence of the ratio of the diffusion coefficients D_r on the current transients at generator and collector electrodes. The current transients both on the generator and collector electrodes are sensitive to the ratio of diffusion coefficients D_r. Contrary to the current transients at the generator-collector electrodes in the absence of the chemical reaction[32] the steady state current depends on the ratio of the diffusion coefficients D_r and no minimum is observed on the generator electrode at $D_r < 1$ at substantial rate constants for the chemical reaction.

6.8.2 Second Order Kinetics

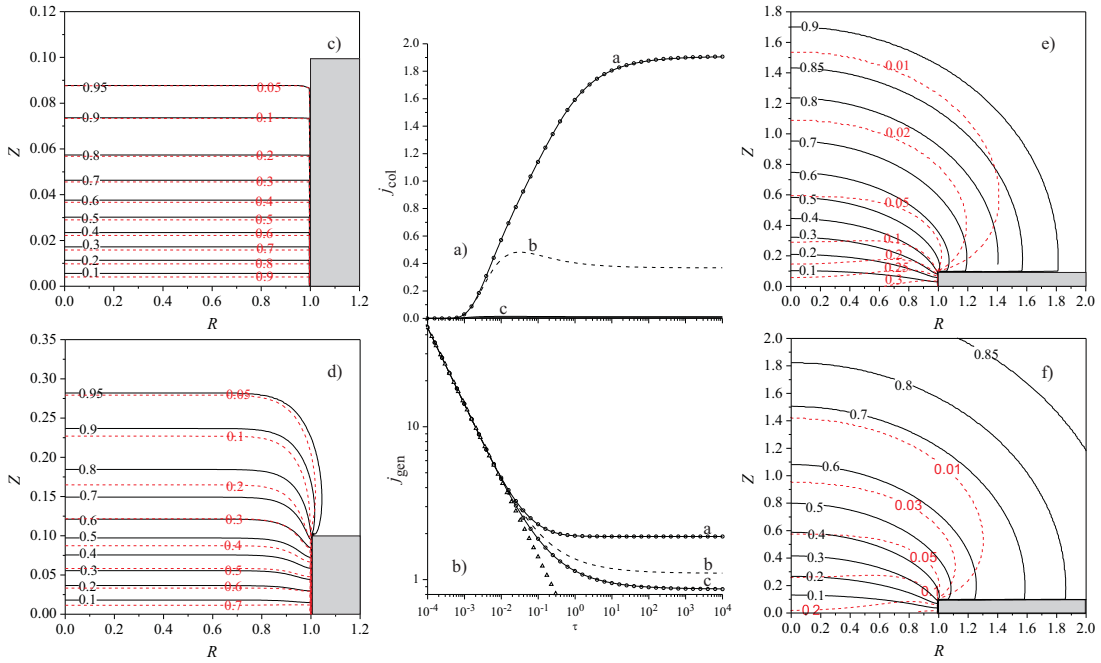

Figure 6.22: Current transients and concentration profiles at the generator-collector electrode, for the case of second order chemical kinetics; $L_{cyl} = 0.1$. a) current transient at the collector electrode, open circles represents the limiting cases of infinitely slow and fast reaction, the solid line *a* represents the calculated current transients for $q_2 = 3.2 \times 10^{-3}$, the dashed line *b* $q_2 = 100$ and the solid line *c* for $q_2 = 3.2 \times 10^3$ b) current transient at the generator electrode; the labeling is similar to that for a) above, the open triangles represent the current given by the Cottrell equation. c), d), e) and f) shows concentration profiles calculated at times $\tau = 0.001$, 0.01, 1 and 100, for the rate constant of the chemical reaction $q_2 = 100$; the the solid line shows concentration of A and the dashed line the concentration of B.

Figure 6.22 shows current transients calculated at the generator-collector device with a disc recession of $L_{cyl} = 0.1$ for the case of a second order follow-up reaction. Analogously to the first order chemical reaction case (above Figure 6.19) the current transients at the generator and collector electrodes converge to limiting cases at high and low values of the rate constants of the chemical reaction (Figure 6.22 a) and b)). At short times ($\tau < L_{cyl}^2$) diffusion is planar and the diffusion layer of the chemical B has not yet reached the collector electrode. The current at the generator electrode scales with time according to dimensionless Cottrell equation 6.23 and is independent of the rate of the chemical reaction. The concentration profile in Figure 6.19 c) shows that impact of the chemical reaction is substantial and the mass-conservation law [A]+[B]=[A]$_0$ (D_r=1) is not fulfilled even approximately near the generator electrode at times as short as at $\tau = 0.001$. At τ=0.01 diffusion

becomes convergent, species B reaches the collector electrode (Figure 6.22 d)) and the current at the generator electrode approaches the maximum. Similar to the case of the first order reaction a further increase of time causes growth of the diffusion layer, but here the diffusion layer of species B expands further (compare Figure 6.19) due to the fast fall of the rate of the second order reaction with a decrease of the concentration. Figure 6.23 shows current transients calculated at various rate

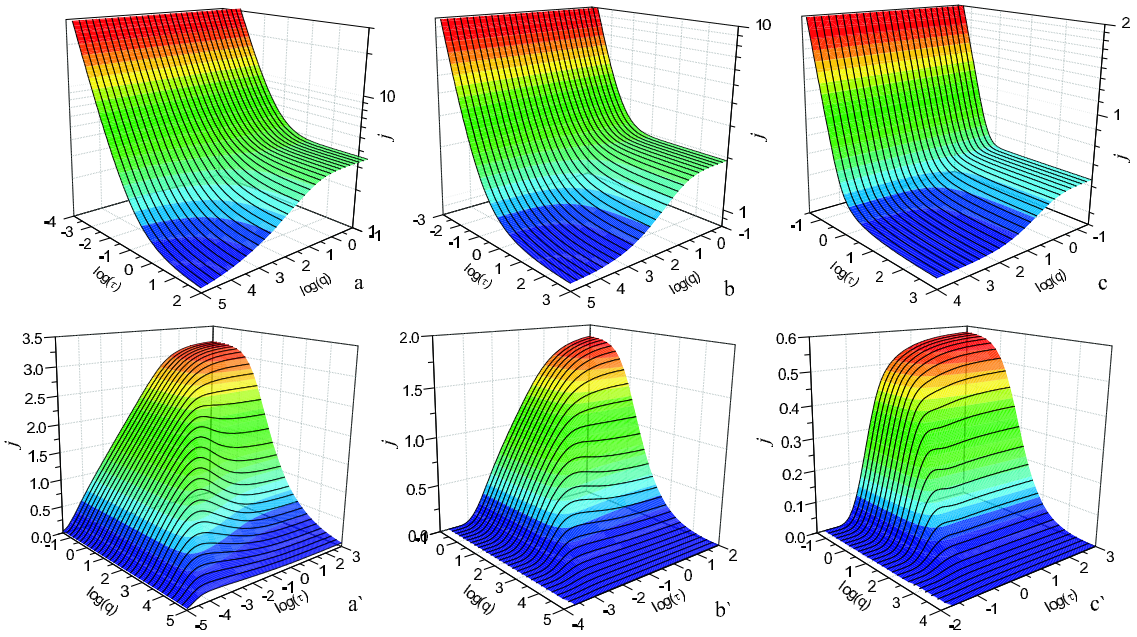

Figure 6.23: Current transients at the generator-collector electrode, for the case of second order chemical kinetics. a, a‘ L_{cyl}=0.01; b, b‘ L_{cyl}=0.1; c, c‘ L_{cyl}=1. Graphs labeled with/without a symbol of an asterisk refer to the current transient at the collector/generator electrodes respectively.

constants q_2 of the chemical reaction as well as disc recession L_{cyl}. The steady state currents at generator and collector electrodes as well as the peak currents at the collector electrode decrease gradually with an increase of the rate constant of the chemical reaction. Here the peak on the transient is less pronounced than in case of the first order chemical reaction (Figure 6.20). The time at which the peak current is reached decreases with an increase of the rate of the chemical reaction q_2 which is in agreement with the half-life under homogeneous conditions of $\tau_{1/2} = 1/q_2$. The recession of the disc is an important parameter that influences the maximum and minimum values of the rate constant of the chemical reaction that can be detected. At L_{cyl}=0.01 the rate constant q_1 can be measured in the range of 1 to 10^6, at L_{cyl}=0.1 the rate constant q_2 in the range of 1 to 10^5 and finally at L_{cyl}=1 the rate constant q_1 can be measured in the range of only 0.1 to 10^4.

Figure 6.24 shows the influence of the ratio of the diffusion coefficients D_r on the current tran-

sients at generator and collector electrodes. The current transients both on the generator and collector electrodes are sensitive to the ratio of diffusion coefficients D_r. Contrary to the current transients at the generator-collector electrodes in the absence of the chemical reaction1 and similar to that in the presence of a first order chemical reaction the steady state current depends on the ratio of the diffusion coefficients D_r and no minimum is observed on the generator electrode at $D_r < 1$ at substantial rate constants for the chemical reaction.

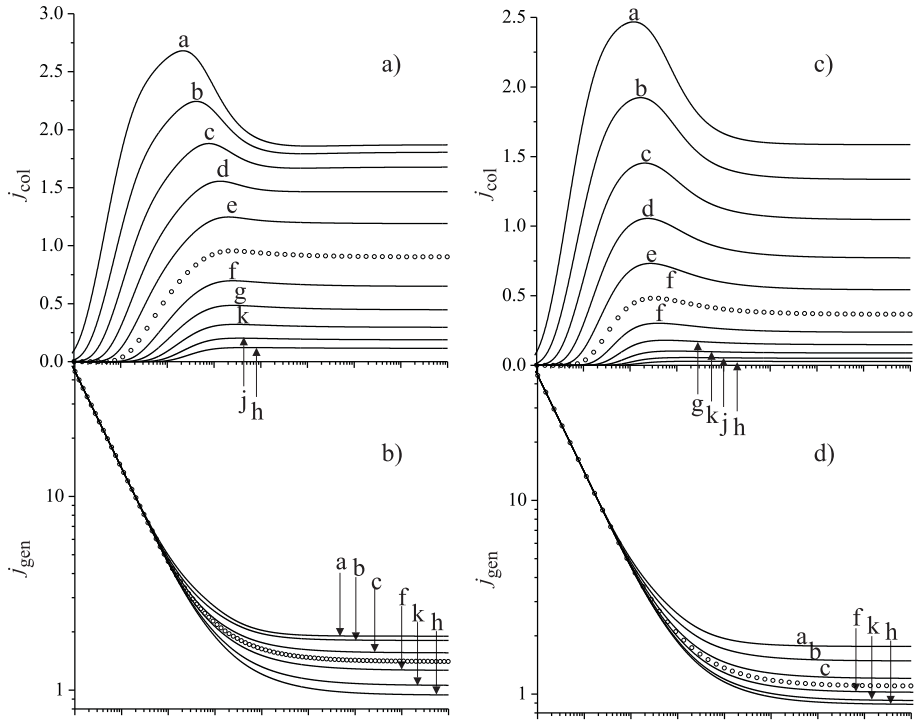

Figure 6.24: Influence of the ratio of the diffusion coefficients D_r on the current transients, for the case of second order chemical kinetics, and $L_{cyl} = 0.1$. a) and b) show the current at the collector and generator electrodes for $q_1 = 1$; c) and d) show the current at the collector and generator electrodes for $q_1 = 10$. Lines a, b, c, d, e, f, g, h, j, k corresponds to D_r=10, 6.3, 4, 2.5, 1.6, 0.63, 0.4, 0.25, 0.16, 0.1 and the open circles show the current transients at D_r=1.

6.8.3 Arrays of generator-collector electrodes.

Next we consider arrays of plane-recessed disc electrodes. Figure 6.25 shows the influence of the electrode density in the array. Here again contrary to the case where no chemical reaction is present[33] the generator-collector electrodes do not behave independently at all timescales, but behave similarly to arrays of microdisk electrodes[16] diffusional independence of electrodes in the arrays is a function of time and array geometry. However it is also function of the rate constant of the chemical reaction.

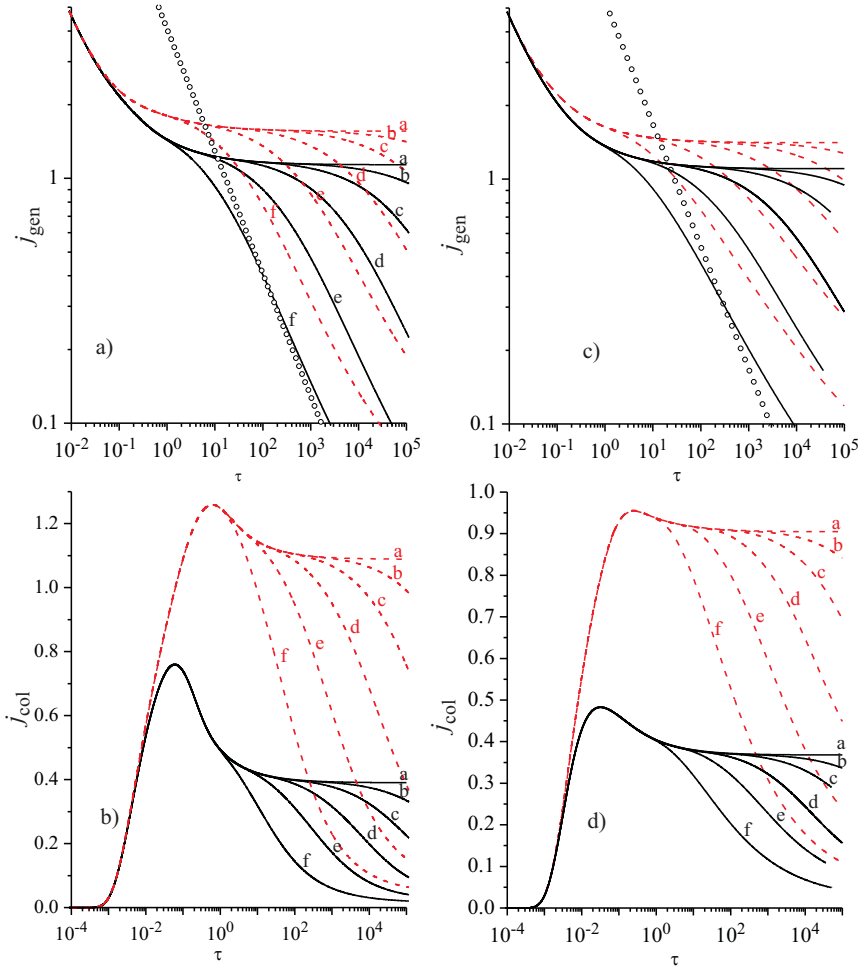

Figure 6.25: Influence of the electrode density in the array on current transients, $L_{cyl} = 0.1$. a) and b) show current transients at the generator and collector electrode respectively in the presence of the first order chemical reactions; dashed line - $q_1 = 1$, solid line - $q_1 = 10$; c) and d) show current transients at the generator and collector electrodes respectively in the presence of second order chemical reactions; dashed line - $q_1 = 10$, solid line - $q_1 = 100$. Curves a and b, c, d, e, f correspond to the single generator-collector device and array of the electrodes with $R_{max} = 40$, 20, 10, 5, 2.5 respectively. Open circles represent currents given by the Cottrell equation.

At long times both in the case of second and first order chemical reactions current decays, the slope in bilogarithmic coordinates depends on the rate constant of the chemical reaction and is smaller than Cottrellian. The current transients at long times at arrays of generator-collector electrodes contain important information about the rate constant of the chemical reaction and fitting of long time transients together or separately from the short time transients can be used to extract the value of the rate constant.

6.9 EC_1 and EC_2 Reactions: Conclusions

The results presented above show that current transients at the proposed generator-collector devices and their arrays are sensitive to the mechanism of the chemical reaction and the rate constant of the chemical reaction as well as ratio of the diffusion coefficients D_r and should be suitable for their simultaneous determination. The value of the rate constant that can be measured with a single device spans across six orders of magnitude. Table 3 shows real values of the rate constant that can be extracted with the proposed generator-collector devices. It should be noted though that presented values are calculated for a single generator-collector device, application of arrays of generator-collector devices should not change significantly range of the rate constants available for the measurement,[64] although later is advantageous due to the higher currents generated. For the second order chemical reaction rate constant values as high as diffusion controlled can be measured.

6.10 Acknowledgments

I would like to thank Dr. Aoife O'Mahony who performed experiments and Dr. F. Javier del Campo who supplied microarray electrodes, performed their characterisation and provided detailed information and figures for Array Fabrcication subsection.

References

[1] Fosset, B.; Amatore, C.; Bartelt, J.; Michael, A.; Wightman, R. *Anal Chem* **1991,** *63,* 306-314.

[2] Feldman, B. J.; Feldberg, S. W.; Murray, R. W. *J Phys Chem* **1987,** *91,* 6558-6560.

[3] Fosset, B.; Amatore, C.; Bartelt, J.; Wightman, R. *Anal Chem* **1991,** *63,* 1403-1408.

[4] Aoki, K.; Morita, M.; Niwa, O.; Tabei, H. *J Electroanal Chem* **1988,** *256,* 269-282.

[5] Niwa, O.; Morita, M.; Tabei, H. *Anal Chem* **1990,** *62,* 447-452.

[6] French, R.; Collins, A. M.; Marken, F. *Electroanal* **2008,** *20,* 2403-2409.

[7] Zhao, G.; Giolando, D. M.; Kirchhoff, J. R. *Anal Chem* **1995,** *67,* 1491-1495.

[8] Liljeroth, P.; Johans, C.; Slevin, C. J.; Quinn, B. M.; Kontturi, K. *Electrochem Comm* **2002,** *4,* 67-71.

[9] Harvey, S. L. R.; Parker, K.; O'Hare, D. *J Electroanal Chem* **2007,** *610,* 122-130.

[10] Harvey, S. L. R.; Coxon, P.; Bates, D.; Parker, K. H.; O'Hare, D. *Sens Actuators B* **2008,** *129,* 659-665.

[11] Phillips, C. G.; Stone, H. A. *J Electroanal Chem* **1997,** *437,* 157-165.

[12] Niwa, O.; Morita, M.; Tabei, H. *J Electroanal Chem* **1989,** *267,* 291–297.

[13] Ivanic, R.; Rehacek, V.; Novotny, I.; Breternitz, V.; Spiess, L.; Knedlik, C.; Tvarozek, V. *Vacuum* **2001,** *61,* 229–234.

[14] Vandaveer IV, W. R.; Woodward, D. J.; Fritsch, I. *Electrochim Acta* **2003,** *48,* 3341–3348.

[15] Davies, T. J.; Ward-Jones, S.; Banks, C. E.; Del Campo, J.; Mas, R.; Munoz, F. X.; Compton, R. G. *J Electroanal Chem* **2005,** *585,* 51-62.

[16] Menshykau, D.; Huang, X.-J.; Rees, N. V.; Del Campo, F. J.; Munoz, F.; Compton, R. G. *Analyst* **2009,** *134,* 343-348.

[17] Streeter, I.; Fietkau, N.; del Campo, F.; Mas, R.; Mu´ noz, F. X.; Compton, R. G. *J Phys Chem C* **2007,** *111,* 12058-12066.

[18] Dickinson, E. J. F.; Streeter, I.; Compton, R. G. *J. Phys. Chem. C* **2008,** *112,* 11637-11644.

[19] Dickinson, E. J. F.; Streeter, I.; Compton, R. G. *J Phys Chem B* **2008,** *112,* 4059-4066.

[20] Menshykau, D.; Compton, R. G. *Langmuir* **2009,** *25,* 2519–2529.

[21] Guo, J.; Lindner, E. *Anal Chem* **2009,** *81,* 130-138.

[22] Amatore, C.; Oleinick, A. I.; Svir, I. *J Electroanal Chem* **2006,** *597,* 77-85.

[23] Davies, T. J.; Moore, R. R.; Banks, C. E.; Compton, R. G. *J Electroanal Chem* **2004,** *574,* 123-152.

[24] Amatore, C.; Saveant, J. M.; Tessier, D. *J Electroanal Chem* **1983,** *147,* 39-51.

[25] Brookes, B. A.; Davies, T. J.; Fisher, A. C.; Evans, R. G.; Wilkins, S. J.; Yunus, K.; Wadhawan, J. D.; Compton, R. G. *J Phys Chem B* **2003,** *107,* 1616-1627.

[26] Dickinson, E. J. F.; Limon-Petersen, J. G.; Rees, N. V.; Compton, R. G. *J Phys Chem C* **2009,** *113,* 11157-11171.

[27] Cui, S. *J Chem Phys* **2005,** *123,* 054706-054706.

[28] Xue, J.; Zou, X.; Xie, Y.; Wang, Y. *J Phys D: Appl Phys* **2009,** *42,* 105308-105308.

[29] Svir, I. B.; Klymenko, O. V.; Compton, R. G. *Radiotekhnika* **2001,** *118,* 92-101.

[30] Bard, A. J.; Faulkner, L. R. *Electrochemical Methods: Fundamentals and Application;* John Wiley and Sons: New York, 2001.

[31] Britz, D. *Digital Simulation in Electrochemistry;* Springer: Berlin, 2008.

[32] Menshykau, D.; Javier del Campo, F.; Munoz, F.; Compton, R. *Sens Actuators, B* **2009,** *138,* 362-367.

[33] Menshykau, D.; O'Mahony, A. M.; del Campo, F. J.; Munoz, F. X.; Compton, R. G. *Anal Chem* **2009,** *81,* 9372-9382.

[34] Gavaghan, D. J. *J Electroanal Chem* **1998,** *456,* 1-12.

[35] Davies, T. J.; Compton, R. G. *J Electroanal Chem* **2005,** *585,* 63-82.

[36] Peaceman, J.; Rachford, H. *J Soc Ind Appl Math* **1955,** *3,* 28-41.

[37] Atkinson, K. *Elementary Numerical Analysis, 3rd ed;* John Wiley and Sons: New York, 2004.

[38] Gavaghan, D. J. *J Electroanal Chem* **1997,** *420,* 147.

[39] Bonhôte, P.; Dias, A.-P.; Papageorgiou, N.; Kalyanasundaram, K.; Grätzel, M. *Inorg Chem* **1996,** *35,* 1168-1178.

[40] Sharp, M. *Electrochim Acta* **1983,** *28,* 301-308.

[41] Schröder, U.; Wadhawan, J. D.; Compton, R. G.; Marken, F.; Suarez, P. A. Z.; Consorti, C. S.; de Souza, R. F.; Dupont, J. *New J Chem* **2000,** *24,* 1009-1015.

[42] Silvester, D. S.; Aldous, L.; Hardacre, C.; Compton, R. G. *J Phys Chem B* **2007,** *111,* 5000-5007.

[43] Evans, R. G.; Klymenko, O. V.; Price, P. D.; Davies, S. G.; Hardacre, C.; Compton, R. G. *ChemPhysChem* **2005,** *6,* 526-533.

[44] Shoup, D.; Szabo, A. *J Electroanal Chem* **1982,** *140,* 237-245.

[45] Klymenko, O. V.; Evans, R. G.; Hardacre, C.; Svir, I. B.; Compton, R. G. *J Electroanal Chem* **2004,** *571,* 211-221.

[46] Albery, W. J.; Brett, C. M. A. *J Electroanal Chem* **1983,** *148,* 201-210.

[47] Albery, W. J.; Brett, C. M. A. *J Electroanal Chem* **1983,** *148,* 211-220.

[48] Albery, W. J.; Compton, R. G.; Hillman, A. R. *J Chem Soc, Faraday Trans* **1978,** *74,* 1007-1019.

[49] Albery, W. J.; Drury, J. S. *J Chem Soc, Faraday Trans* **1972,** *68,* 456-464.

[50] Albery, W. .; Bruckenstein, S. *Trans Faraday Soc* **1966,** *62,* 1920-1931.

[51] Postlethwaite, T. A.; Hutchison, J. E.; Murray, R.; Fosset, B.; Amatore, C. *Anal Chem* **1996,** *68,* 2951-2958.

[52] Amatore, C.; Da Mota, N.; Lemmer, C.; Sella, C.; Thouin, L. *Anal Chem in press* .

[53] Ghanem, M. A.; Thompson, M.; Compton, R. G.; Coles, B. A.; Harvey, S.; Parker, K. H.; O'Hare, D.; Marken, F. *J Phys Chem B* **2006,** *35,* 17589-17594.

[54] Macfie, G.; Compton, R. G. *J Electroanal Chem* **2001,** *503,* 125-132.

[55] Nekrasov, L. N. *Soviet electrochemistry* **1987,** *23,* 145-152.

[56] Alden, J.; Compton, R. G. *J Electroanal Chem* **1996,** *415,* 1-12.

[57] Amatore, C.; Da Mota, N.; Sella, C.; Thouin, L. *Anal Chem* **2007,** *79,* 8502-8510.

[58] Compton, R. G.; Banks, C. E. *Understanding Voltammetry;* World Scientific: Singapore, 2007.

[59] Amatore, C.; Oleinick, A. I.; Svir, I. *J Electroanal Chem* **2006,** *597,* 77–85.

[60] Amatore, C.; Oleinick, A. I.; Svir, I. *Anal Chem* **2009,** *81,* 4397–4405.

[61] Rogers, E. I.; Silvester, D. S.; Poole, D. L.; Aldous, L.; Hardacre, C.; Compton, R. G. *J Phys Chem C* **2008,** *112,* 2729-2735.

[62] Evans, R. G.; Klymenko, O. V.; Saddoughi, S. A.; Hardacre, C.; Compton, R. G. *J Phys Chem B* **2004,** *108,* 7878–7886.

[63] Ordeig, O.; Banks, C. E.; Davies, T. J.; Del Campo, J.; Mas, R.; Munoz, F. X.; Compton, R. G. *Analyst* **2006,** *131,* 440–445.

[64] Menshykau, D.; O'Mahony, A.; Cortina-Puig, M.; Javier del Campo, F.; Munoz, F.; Compton, R. *J Electroanal Chem* **2010,** *647,* 20-28.

Chapter 7

Conclusions

This theses presents modeling of various electrochemical systems, with an emphasis on the diffusional transport towards the electrode surface. In particular in this theses following systems are considered: cyclic and stripping voltammetry at rough and scratched electrodes; voltammetry at electrodes covered with electroactive and electro-inactive layers; voltammetry of surface-bound species which undergoes proton-coupled electrochemical reduction; chronoamperometry at micro-electrodes and their arrays; microarrays of ring-recessed disc electrodes in generator-collector mode.

Diffusional cyclic voltammetry experiment performed under the standard conditions was found to be insensitive surface roughness produced by the deliberate polishing and/or scratching. Electrode morphology has a greater effect on stripping voltammetry. The influence of electrode roughness on stripping voltammetry depends on the model of electron transfer, stripping voltammetry of bulk layers was found to be extremely sensitive to the electrode morphology.

Deposition of eletroactive and electro-inactive layers over the electrode surface could significantly change diffusional regime towards the electrode surface. Two models of electro-inactive layer has been proposed: a uniform layer and a porous layer. Both of these under certain conditions depicted in this theses change diffusional regime from that charachterestic for a bare macroelectrode, this result in an altered shape of cyclic voltammograms registered at the modified electrode. Analysis of voltammograms registered in a broad range of scanrates let to distinguish uniform and porous layers as well as to extract model parameters. Presence of the electroactive layer over the electrode surface also significantly change observed shape of voltammograms, in particular it causes decrease of the peak-to-peak separation and increase of the peak current. These can often be misinterpreted as an "electrocatalysis". Randles-Sevcik plots should be used to distinguish increase of the rate constant of the electron transfer from a change of the diffusional regime.

Voltammetry of surface-bound species which undergoes proton coupled electrochemical reduction is studied for two mechanisms of electron transfer: concerted and stepwise. In both cases voltammograms simulated in an unbuffered solution significantly differ from that in a buffered solution.

Limited rate of protons diffusion towards the electrode surface results in a votlammograms with a split peak in case of stepwise mechanism and voltammograms with a wave shape characteristic for diffusional voltammetry during the forward scan and that characteristic for the stripping voltammetry during the backward scan.

Theory of chronoamperometry on disc and ring-recessed microelectrodes and their arrays is reported. Three and four different regimes of transient current versus time can be observed at microelectrode arrays of disc and ring electrodes, accordingly. These regimes are charaterised by the various types of diffusion: planar diffusion to a microelectrode, converged diffusion (two types at ring electrode) to microelectrode and planar diffusion to an array of microelectrodes. It is also emphasised that microelectrode in the array can be considered as a diffusionally independent only for a limited period of time. Further a generic, accurate and easy to use method of experimental chronoamperometric data analysis is proposed. It is shown that the method can be applied to the simultaneous measurement of the diffusion coefficient D and the product nC, where n is the number of electrons transferred and C is the concentration of electroactive analyte.

Finally, fabrication, characterization, and use of arrays of ring-recessed disk generator-colector microelectrodes are reported. Three different time regimes are observed in a potential step experiment on ring-recessed disk electrode, electrodes are shown to be truly diffusionally independent in the array. All three regions of behavior were observed experimentally on a fabricated array of generator-collector electrodes. The theoretical fit agrees well with the experimental data. The use of arrays of ring-recessed disk electrodes in generator-collector mode has advantages over conventional arrays of disk electrodes, such as higher currents at a single microelectode in an array. The number of electrodes on the array can also be increased, as smaller interelectrode distances are possible. The current transients at the plane-recessed disk electrodes and their arrays in the generator-collector mode are shown to be sensitive to the mechanism of the chemical reaction, the rate constant of the chemical reaction as well as the diffusion coefficients of electrochemically active couple.

All these projects demonstrate that computational electrochemistry is a mature field. The role of modelling in electrochemistry dramatically increased during past two decades and will continue to grow as increased coomputational power as well development of computational methods let now to build comprehensive and realistic models. These models should be used to quantify and descritise verbal models, extract quantitative data from experiment and finally reduce and direct experimental

screening.